Structure Pharmaceutics Based on Synchrotron Radiation X-Ray Micro-Computed Tomography

Xianzhen YIN

Submitted for the Degree of

Doctor of Philosophy

Faculty of Life Sciences

University of Bradford

2016

Abstract

Xianzhen Yin

Structure Pharmaceutics Based on Synchrotron Radiation X-Ray Micro-Computed Tomography

From Characterization to Evaluation and Innovation of Pharmaceutical Structures

Drug delivery systems (DDS) are essentially pharmaceutical products for human therapy, typically involving a mixture of active ingredients and excipients. Based upon quantitative characterization of structure, the thesis introduces the concept of classifying the architecture of DDS into four levels by their spatial scale and the life time period. The primary level is recognised as the static structure of the whole dosage form with a size from μm to cm with the final structure generated by formulation design. The secondary level categorises the structures of particles or sub-units to form a DDS with sizes from nm to mm as key units in processing such as mixing, grinding, granulation and packing; The tertiary level represents the dynamic structures of DDS during the drug release phase in vitro or in vivo incorporating the structure size range from nm to mm, which undergo changes during dissolution, swelling, erosion or diffusion. The spatial scale for the quaternary level is defined as the meso or micro scale architecture of active and non-active molecules within a DDS with sizes from Å to μm for the molecular structure of drug and excipients.

Methods combining X-ray tomography, image processing, and 3D reconstructions have been devised and evaluated to study systematically pharmaceutical structures and correlate them with drug release kinetics of DDS. Based on the quantitative structural information of pharmaceutical intermediates and dosage forms, it is possible now to correlate structures with production processing, behaviour and function, and the static and dynamic structures of DDS with the release kinetics. Thus, a structure-guided methodology has been established for the research of DDS.

List of Publications

First Author #，Corresponding Author *

1. **Xianzhen Yin**[#], Tiqiao Xiao, Ashwini Nangia, Shuo Yang, Xiaolong Lu, Haiyan Li, Qun Shao, You He, Peter York, Jiwen Zhang[*]. In situ 3D topographic and shape analysis by synchrotron radiation X-ray microtomography for crystal form identification in polymorphic mixtures. Scientific Reports, 2016, doi:10.1038/srep24763

2. **Xianzhen Yin**[#], Li Wu[#], Ying Li[#], Tao Guo, Haiyan Li, Tiqiao Xiao, Peter York, Ashwini Nangia, Shuangying Gui, Jiwen Zhang[*]. Visualization and quantification of deformation behavior of clopidogrel bisulfate polymorphs during tableting. Scientific Reports, 2016, DOI: 10.1038/srep21770

3. Shuo Yang[#], **Xianzhen Yin**[#], Caifen Wang[#], Haiyan Li, You He, Tiqiao Xiao, Lixin Sun, Jiasheng Li, Peter York[*], Jun He[*], Jiwen Zhang[*]. Release Behaviour of Single Pellets and Internal Fine 3D Structural Features Co-define the In Vitro Drug Release Profile[J]. The AAPS journal, 2014, 16(4): 860-871

4. **Xianzhen Yin**[#], Haiyan Li[#], Zhen Guo, Li Wu, Fangwei Chen, Marcel de Matas, Qun Shao, Tiqiao Xiao, Peter York*, You He*, Jiwen Zhang*. Quantification of the relative importance of swelling and erosion in the controlled release of poorly water-soluble drugs using statistical modeling and synchrotron radiation X-ray computed microtomography. AAPS J 2013, 15(4):1025-34

5. **Xianzhen Yin**[#], Haiyan Li[#], Ruihao Liu, Jing Chen, Junqiu Ji, Jun Chen, Qun Shao, Tiqiao Xiao, Peter York[*], You He[*], Jiwen Zhang[*]. Fractal structure determines controlled release kinetics of monolithic osmotic pump tablets. J Pharm Pharmacol 2013, 65 (7): 953-959

6. Ruihao Liu[#], **Xianzhen Yin**[#], Haiyan Li, Qun Shao Peter York, You He, Tiqiao Xiao*, Jiwen Zhang*. Visualization and quantitative profiling of mixing and segregation of granules using synchrotron radiation X-ray microtomography and three dimensional reconstruction. Int J Pharm 2013, 445(1-2):125-133

7. Haiyan Li[#], **Xianzhen Yin**[#], Junqiu Ji, Lixin Sun, Qun Shao, Peter York, Tiqiao Xiao, You He*, Jiwen Zhang*. Microstructural Investigation to the Controlled Release Kinetics of Monolith Osmotic Pump tablets via Synchrotron Radiation X-ray Microtomography. Int J Pharm 2012, 427(2):270-275

8. Li Wu[#], Lebing Wang, Shuxian Wang, Tiqiao Xiao, Men Chen, Qun Shao, Peter York, Vikaramjeet Singh, **Xianzhen Yin**[*], Jingkai Gu[*], Jiwen Zhang[*]. Three dimensional structural insight of laser drilled orifices in osmotic pump tablets. European Journal of Pharmaceutical Sciences, 2016, 93(1):287-294

9.. Li Wu, **Xianzhen Yin**, Zhen Guo, Yajun Tong, Jing Feng, Peter York, Tiqiao Xiao, Min Chen[*], Jingkai Gu[*], Jiwen Zhang[*]. Hydration induced material transfer in membranes of osmotic pump tablets measured by synchrotron radiation based FTIR. European Journal of Pharmaceutical Science, 2016, 84: 132-138.

10. **Xianzhen Yin**[#], Li Wu, You He, Zhen Guo, Xiaohong Ren, Qun Shao, Jingkai Gu, Tiqiao Xiao, Peter York, Jiwen Zhang*. 3D Structural Investigation of Solid Dosage Forms, Chapter 12 in "Computational Pharmaceutics: Application of Molecular Modeling in Drug Delivery" (Editor: Dr Defang Ouyang and Dr Sean C. Smith). John Wiley & Sons Limited, 2015.

To my adorable son, GuoGuo

To my dear wife, Xiaomin Guo for her constant support and encouragement

To my loving parents, for their guidance and motivation throughout my life

.

Acknowledgements/ Dedications

Table of Contents

List of Figures

List of Tables

Glossary

2D - Two dimensional

2.5D – 2.5 dimensional

3D - Three dimensional

μCT - micro computed tomography

AFM - Atomic force microscopy

APIs - Active pharmaceutical ingredients

CA - Cellulose acetate

CCD - Charge-coupled device

CLP - Clopidogrel bisulphate

CT - Computed tomography

DDSs - Drug delivery systems.

DSC - Differential scanning calorimeter

DSD - The distance between sample and detector

EOP - Elementary osmotic pump tablet

FTIR - Fourier transform infrared spectroscopy

HPMC - hydroxypropyl methylcellulose

MOTS - Monolithic osmotic tablets

MRI - magnetic resonance imaging

OPDDS – Osmotic pump drug delivery systems

OCT – Optical coherence tomography

PAM– Photoacoustic imaging

PEG - Polyethylene glycol)

PPOP - Push-pull osmotic pump tablet

PXRD - Powder X-ray diffraction

PVP/VA - Polyvinylpyrrolidone vinylacetate co-polymer

SSRF- Shanghai Synchrotron Radiation Facility

SR-μCT - Synchrotron Radiation micro-Computed Tomography

SEM - Scanning electron microscope

TEM - Transmission electron microscopy

TPI - Terahertz pulsed imaging

US – ultrasonography, ultrasound imaging

XRD - X-ray diffraction

Chapter 1

Introduction

1.1 Drug Delivery Systems and Structure

For the purpose of the treatment, cure, prevention, diagnosis of disease or enhanced physical or mental well-being, active pharmaceutical ingredients (APIs) should be transported in the body safely to achieve their therapeutic effect [1]. To achieve this, it is required that APIs are formulated and assembled into suitable deliverable dosage forms for convenient administration to patients. Drug delivery technologies have been introduced to modify drug release profiles, absorption, distribution and elimination of drugs for the benefit of improving product efficacy and safety, as well as patient convenience and compliance. Pharmaceutics is the subject which provides the underpinning scientific knowledge concerned with the transformation of drug substance, via formulation, into dosage forms and the various manufacturing processes used to provide high- quality, efficacious and safe medicines.

Drug Delivery Systems (DDSs): Drug delivery is approached via various DDSs and is heavily integrated with dosage form and route of administration. The common routes of administration include the preferred non-invasive peroral (through the mouth), topical (skin), transmucosal (nasal, buccal/sublingual, vaginal, ocular and rectal) and inhalation routes [2]. DDSs should be considered as the completed forms of the pharmaceutical preparation in which prescribed doses of medication are included and be designed to achieve the delivery of drugs to target sites of pharmacological action. Procedures involved during the development of DDS include those concerning drug preparation, route of administration, site targeting, metabolism, and toxicity testing. For oral administration, DDSs are designed to resist action by gastric fluids, prevent vomiting and nausea, reduce or alleviate any undesirable taste and smells,

achieve a high concentration of drug at the target site, and/or produce a delayed or long-acting drug effect.

Structure: The different types of dosage forms are usually classified by the specific structure, the route of administration, the physical form and size of the dosage unit. The various dosage forms can be considered across different scales of scrutiny and size (see Figure 1) - from the molecular to the macro level [3].
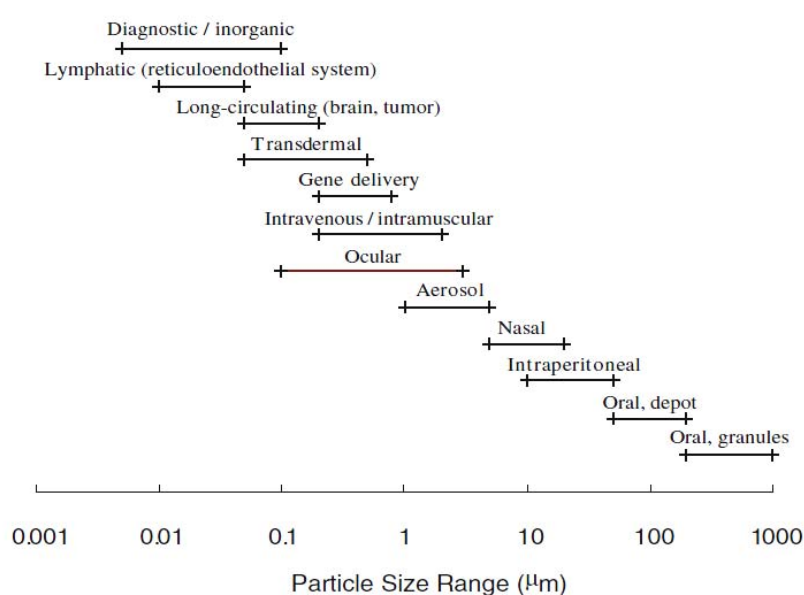
Figure 1 *Particle size range for different dosage forms [3].*

For clinical applications, the final pharmaceutical structures can be divided into numerous conventional types - solutions, emulsions, suspensions, semi-solids, and solids. During the processing of materials into final dosage forms, other intermediate structures can be found - crystals, powders, granules etc. Of the range of marketed drug delivery systems, solid dosage forms are the most common forms and provide the vast majority of marketed medicines. Solid dosage forms are usually classified by the static and dynamic structure before and during release, the typical forms including powders, pellets, granules, tablets and capsules, with the structural features of these forms and the corresponding

dynamic changes due to phenomena such as hydration, swelling, and diffusion during drug release and dissolution playing dominant roles in determining the quality and performance of the medicines.

1.2 Primary Factors Defining the Structure of DDS

1.2.1 The Properties of APIs and Excipients

Most drugs are marketed as tablets, capsules or pellets. During manufacturing, APIs are transformed into dosage units with particular characteristics. Besides the APIs, non-medicinal functional substances, called excipients are added to enhance the drug form, quality, and efficacy. For the proper design and formulation of these major dosage forms, it is essential that fundamental physical, chemical, biologic and other characteristics of APIs and excipients to be used in fabricating the product are determined. This information should be considered as important both in product design and formulation development. Properties of APIs define the design space and the properties of excipients mainly determine the architecture of the dosage form.

Properties of APIs that should be taken into account in the design of formulations include: a) the solubility of the drug which affects the bioavailability, the rate of drug release into dissolution media and the therapeutic efficiency of the pharmaceutical product; b) the dissociation content which is important since solubility and consequently absorption, can be altered by orders of magnitude with changing pH; c) partition coefficient (oil/water) which is a measure of the lipophilic/ hydrophilic balance and has been shown to be a contributing factor for the rate and extent of drug absorption; d) the dissolution rate of the drug, especially when it is the rate limiting step in the absorption process; e) crystal

properties and polymorphism - polymorphs generally have different melting points, x-ray diffraction patterns and solubility even though they are chemically identical. Differences in the dissolution rates and solubility of different polymorphic forms of a given drug are commonly observed; f) size and surface morphology of the drug particles influence the flow and the mixing efficiency of powders and granules. Size can also be a factor in stability with fine materials relatively more open to attack from atmospheric oxygen, the humidity, and interacting excipients than are coarse materials.

Excipients are commonly used: a) to bulk up formulations as "bulking agents," "fillers," or "diluents", enabling convenient and accurate dispensing of a drug substance in formulation; b) to serve various therapeutic-enhancing purposes, such as facilitating drug absorption or solubility, or other pharmacokinetic considerations; c) to aid in the handling of the active substance concerned such as by facilitating powder flow or non-stick properties, in addition to aiding drug stability such as prevention of denaturation over the expected shelf life.

1.2.2 Pharmaceutical Processing

Pharmaceutical manufacturing processing usually consists of a series of unit operations executed in batch mode or in a continuous manufacturing operation to produce the desired quality product. Unit operations involve physical or chemical changes, such as mixing, milling, granulation, drying, compression, and coating. Process parameters are key factors in determining the structure of DDS, and when parameters have been adjusted both the external morphology and the inner fine structure of DDS are changed.

For solid dosage forms, typical processes employed which affect the architecture of the DDS include: a) mixing - to reduce composition variability in multi component powder blends; b) wet granulation - to create agglomerates, or granules, of powder blends; c) dry granulation - through roller compaction; d) mass transfer - for holding materials and conveying them; e) size reduction and milling - to reduce the particle size of raw materials, particularly APIs, or to reduce the size of granules generated by either wet or dry granulation; f) drying - a ubiquitous process in the handling and preparation of pharmaceuticals, which may be defined as the vaporization and removal of water or other liquid from a solution, suspension, or other solid-liquid mixture to form a dry solid; g) evaporation - may be defined as the removal of a solvent from a solution by vaporization but is usually restricted to the concentration of solutions by boiling; h) tableting - the compaction of powder blends to form a hard compact; i) encapsulation, enclose granules or powders of APIs and excipients into capsules; j) coating – frequently carried out for tablets that have an unpleasant taste, or to make easier to swallow, modify release behaviours, and extend the shelf-life of components that are sensitive to moisture or oxidation.[4]

1.3 Structure Characterization Methods

The conventional ways to evaluate pharmaceutical solid structures can be divided into two categories: a) indirect determination, e.g., using melting which provide some detail of structural differences of crystalline materials, powder X-ray diffraction to characterize the molecular arrangement in crystals, nitrogen adsorption measurement to obtain the pore structure parameters of solid dosage forms [5]; and b) imaging methods which include two dimensional observation, e.g., microscopy, scanning electron microscope and transmission electron

microscope. As shown in Figure 2, the ability of a light source to penetrate a certain maximum depth determines the size and dimension of a sample that can be examined, with analytical methods based on different disciplines achieving different spatial resolutions.
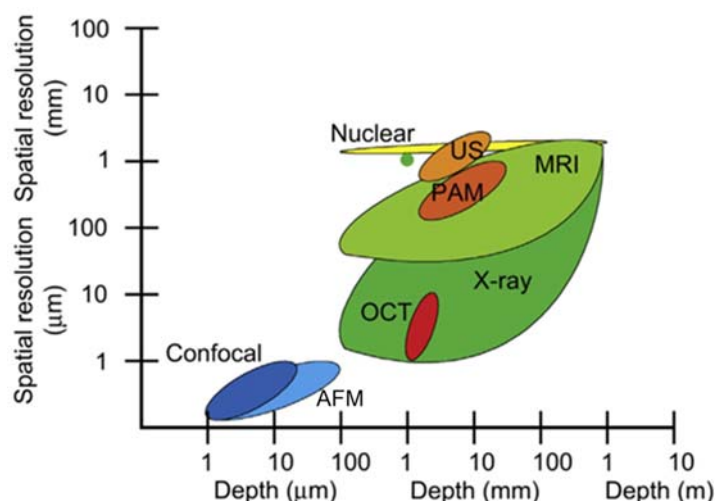
Figure 2 *Light source used in Imaging methods*

1.3.1 2D Methods

Optical Microscopy: The optical microscope, the oldest design of microscope, is easy to use for observation of the structure of dosage forms over a wide range of resolution. The structural detail can be directly observed by eye or captured by normal light-sensitive cameras to generate a micrograph. Based on the captured images of dosage forms, quantitative analysis can be performed.

SEM: The scanning electron microscopy (SEM) is a type of electron microscope that produces images of a sample by scanning it with a focused beam of electrons. The electrons interact with atoms in the sample, producing various signals that can be detected and that contain information about the sample's surface topography and composition. The electron beam is generally scanned in a raster scan pattern, and the beam's position is combined with the detected signal to

7

produce an image. SEM can achieve resolution down to nanometer scale. Specimens can be observed in high vacuum, in low vacuum, and (in environmental SEM) in wet conditions. SEM is the most widely used method to observe the external surface structures of pharmaceutical dosage forms and powders, such as morphology, particle size distribution [6].

TEM: Transmission electron microscopy (TEM) is a microscopic technique in which a beam of electrons is transmitted through an ultra-thin (usually the thickness is about 100~200 nm) specimen. An image formed by the interaction of the electrons transmitted through the specimen is magnified and focused onto an imaging device, such as a fluorescent screen, on a layer of photographic film, or to be detected by a sensor such as a CCD camera. TEMs are capable of imaging at a much greater resolution than light microscopes, owing to the small de Broglie wavelength of electrons. This enables fine detail - even as small as a single column of atoms, which is thousands of times smaller than the smallest resolvable object in a light microscope to be examined. TEM forms a major analytical method in a range of scientific fields, in both the physical and biological sciences. TEMs find application in cancer research, virology, materials science as well as pollution, nanotechnology, and semiconductor research.

AFM: Atomic force microscopy (AFM) or scanning force microscopy (SFM) is a high-resolution type of scanning probe microscopy, with demonstrated resolution in the order of a fraction of a nanometer. AFM is one of the foremost tools for imaging, measuring, and manipulating matter at the nanoscale. The information is gathered by "feeling" the surface with a mechanical probe. Piezoelectric elements that facilitate tiny but accurate and precise movements on (electronic) command enable precise scanning. In some variations, electric potentials can

also be scanned using conducting cantilevers. In more advanced versions, currents can be passed through the tip to probe the electrical conductivity or transport of the underlying surface. AFM has been used to study surface adhesion and morphology as a function of relative humidity (RH) for monoclinic acetaminophen [7].

However, most of the above mentioned methods are not true 3D approaches. Techniques such as SEM, Raman, ATM, ultrasound, vibrational spectroscopy and near infrared spectroscopy are generally applied for 2D observation. These methods reveal only structural information about the surface or inner region just below the surface, and in order to observe internal structures, samples must be sectioned or cut which destroys their original 3D structure.

1.3.2 3D and 2.5D imaging

Magnetic resonance imaging (3D): Magnetic resonance imaging (MRI) is an imaging technique used primarily in medical settings to produce high quality images of the inside of the human body. MRI is based on the principles of nuclear magnetic resonance (NMR), a spectroscopic technique used by scientists to obtain microscopic chemical and physical information about molecules. MRI started out as a tomographic imaging technique, that is it produced an image of the NMR signal in a thin slice. However MRI has advanced beyond a tomographic imaging technique to a volume imaging technique. Magnetic resonance imaging uses a back projection technique similar to that used in CT. The magnetic resonance imaging primarily images the NMR signal from the hydrogen nuclei. The proton possesses a property called spin which can be thought of as a small magnetic field, causing the nucleus to produce an NMR signal. A quantitative

ultra-fast MRI technique, together with 19F NMR spectra and 1D 19F profiles has been applied to study the dissolution process of commercial HPMC matrix tablets [8].

Raman Imaging (2.5D): Raman imaging combines the beneficial properties of Raman spectrometry, such as negligible sample preparation and sharp vibrational bands, with the power of high-resolution chemical imaging in detecting patterns and heterogeneity in analysed samples. The micro-spectrometric techniques apply two approaches, global imaging and point mapping techniques, for characterizing an area. Both techniques provide a hypercube of data with two spatial and one spectral dimension. Raman imaging method has been used to characterize the effect of different manufacturing technologies on properties of tablets, such as API and excipient distribution, polymorphism, tablet strength, and estimated API content [9].

Terahertz imaging (2.5D and 3D): Terahertz radiation consists of electromagnetic waves within the ITU-designated band of frequencies from 0.3 to 3 terahertz and wavelengths range from 1 mm to 0.1 mm. Terahertz radiation is unique in that it can penetrate into and through a number of materials, such as polymers, ceramics, and amorphous pharmaceutical materials. Images or chemical data can be extracted from the reflected or transmitted radiation. Also, many crystalline materials have characteristic spectral features in the terahertz range. Recently, terahertz radiation has been used in pharmaceutical applications such as polymorph identification and quantification, phase transition monitoring, and characterization of hydrate forms [10-12].

Ultrasound (3D): Ultrasound imaging refers to the application of sound waves of frequencies greater than 20 kHz and up to the values in excess of 25 MHz. They are used in many applications including plastic welding, medicine, jewelry cleaning, and nondestructive testing. For a nondestructive test, ultrasonic waves give the ability to "see through" solid/opaque material and detect surface or internal flaws without affecting the material adversely. Ultrasonic wavelengths can be focused, reflected, and refracted and are transmitted through air, water, and solids such as steel by high-frequency particle vibrations. When waves are transmitted in solid objects, the directed energy is reflected by boundaries between materials and also any cracks or voids in solid materials. These reflected waves, caused by internal defects, can be compared to the reflected waves from the external surfaces, enabling the size and severity of internal defects to be identified.

Micro Computed Tomography (3D): X-ray micro-computed tomography (µCT), a powerful non-invasive investigative technique, has been applied to observe the three dimensional structure of various objects and has great potential for providing information of the microstructure of particulate based solid dosage forms. In contrast to conventional techniques, the µCT technique allows non-invasive, visualization of internal and microstructural details at micron scale resolution [13, 14]. The physical principle is the interaction of ionizing radiation, such as X-rays with matter, where, in the energy range typically used for CT imaging, the so-called photon-effect including absorption, diffraction and scattering builds the main interaction mechanism.

With the ongoing development of CT systems, this technique can operate at many different levels of resolution in combination with novel image processing

algorithms and analytical techniques. These new techniques have enabled this methodology to be applied in a range of new applications.

1.4 Objective of the Dissertation

1.4.1 Grey box in pharmaceutics

A key challenge, attracting increasing attention from pharmaceutical scientists, is to provide mechanistic understanding of the behaviour of drug substances and functional formulation components at all stages of the transition of a drug substance from a powdered state into final dosage forms and deliver optimal bio-performance of the medicine in patients. As shown in Figure 3, APIs and excipients are processed by different unit operations within a set of parameters into the specific form of DDS with a deliverable structure. Then the pharmaceutical properties including physical, chemical and biological characteristics are analysed and the disintegration, dissolution and drug release profile of the DDS evaluated. For current scientific researches and industrial applications, a quality strategy is implemented by the control of key attributes of material input characteristics and processing parameters. In many cases, optimizing the processing parameters is based on empirical experimentation and experience without systematic discipline. For the prediction of the target DDS quality from the input attributes and processing parameters theoretical or multi-variable analytical models are required. The construction of these models is dependent upon a huge database from well-designed experiments and thorough analysis. However, the mechanism of how the raw material attributes and the processing parameters affect the quality and pharmaceutical behaviours of dosage forms remain a 'black box' with only a corner as yet uncovered.
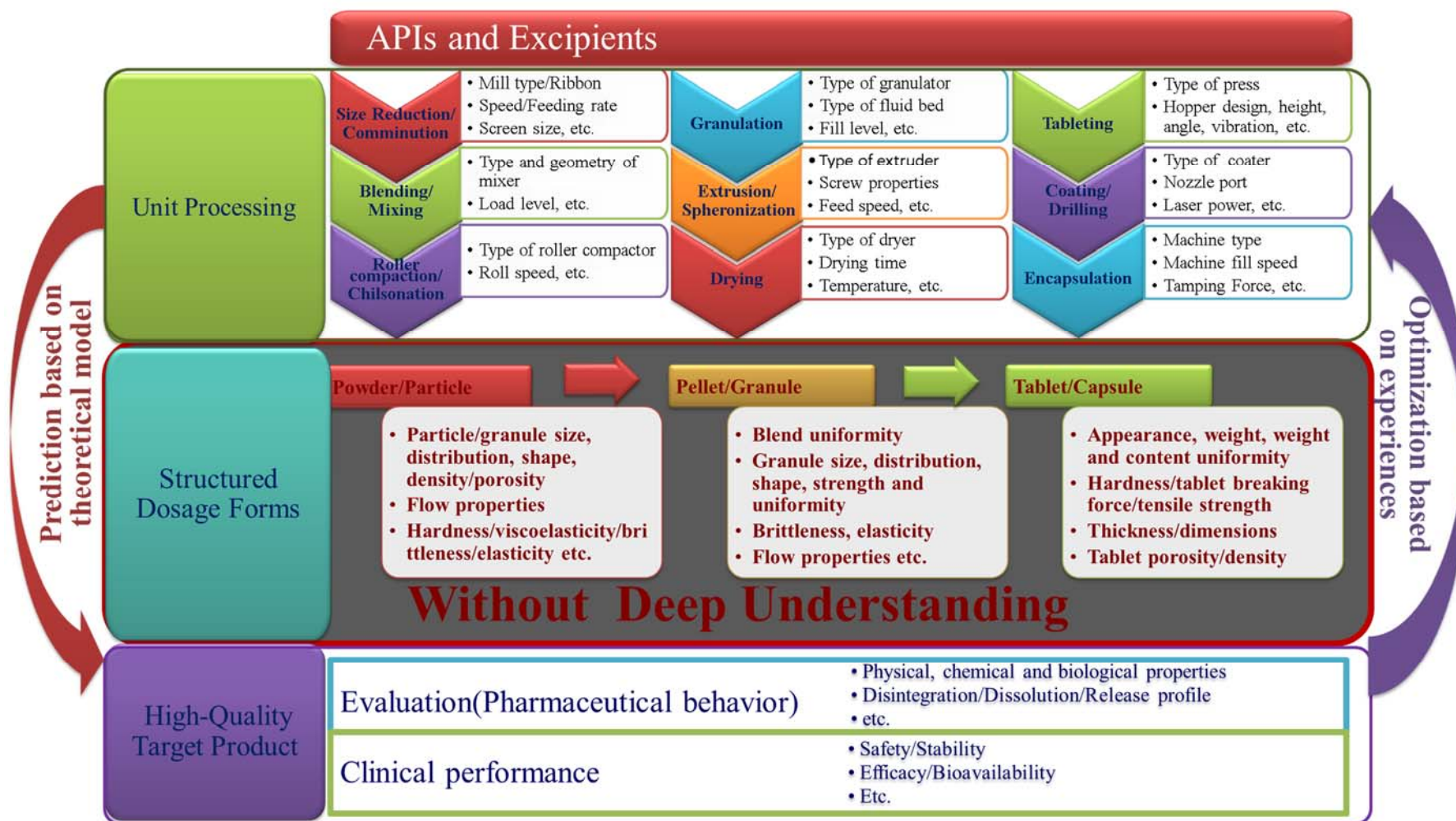
Figure 3 *Processing, Structures and Pharmaceutical Behaviours of DDS*

13

1.4.2 SR-µCT and 3D reconstruction technique

In pharmaceutical research, non-invasive high resolution data are essential for extracting and rendering the finest structural information and to minimize the partial volume effect typical of medical CT scanners. Nonetheless, the major limitation of laboratory µCT equipment is that pharmaceutical samples of only up to a few centimetres in diameter can be examined. The current 'ideal' system for imaging highly (re)mineralized objects of pharmaceutical interest is synchrotron radiation-based micro-computed tomography (SR-µCT).

Synchrotron Radiation and Synchrotron Radiation Light Source ：

Synchrotron radiation is an electromagnetic radiation from radially accelerated charged particles. It is produced in synchrotrons with bending magnets, undulators, or wigglers. It resembles cyclotron radiation except for being generated by accelerating ultrarelativistic particles including electrons forced to travel in a curved path by a magnetic field. In theory, the relativistic speed will change the observed frequency due to the Doppler effect by the Lorentz factor, γ. Relativistic length contraction then bumps the frequency observed in the lab by another factor of γ, thus multiplying the GHz frequency of the resonant cavity that accelerates the electrons into the X-ray range. The radiated power is given by the relativistic Larmor formula while the force on the emitting electron is given by the Abraham–Lorentz–Dirac force. The radiation pattern can be distorted from an isotropic dipole pattern into an extremely forward-pointing cone of radiation. Synchrotron radiation is the brightest artificial source of X-rays. The planar acceleration geometry appears to make the radiation linearly polarized when observed in the orbital plane, and circularly polarized when observed at a small angle to that plane. Amplitude and frequency are focused to the polar ecliptic[15,

16]. Synchrotron radiation may be artificially achieved in synchrotrons or storage rings or naturally by fast electrons passing magnetic fields. When the circulating electron beam is deflected by the bending magnets in the storage ring, an intense flux of electromagnetic radiation has been generated. Synchrotron radiation is characteristically polarized, emitted in a narrow cone and has frequencies ranging over the entire electromagnetic spectrum.[15]

Figure 4 *Shanghai Synchrotron Radiation Facility*

Synchrotron radiation may occur in accelerators either as a nuisance, causing undesired energy loss in particle physics contexts, or as a deliberately produced radiation source for numerous laboratory applications. In the 1960s and 1970s, the advantages of using synchrotron radiation for spectroscopy and diffraction have been realized by an ever-growing scientific community. Accelerators were initially built for particle physics research, and synchrotron radiation was used in "parasitic mode" when bending magnet radiation had to be

extracted by drilling extra holes in the beam pipes. The first storage ring commissioned as a synchrotron light source was Tantalus, at the Synchrotron Radiation Center, first operational in 1968. [17] As accelerator synchrotron radiation became more intense and its applications more promising, devices that enhanced the intensity of synchrotron radiation were built into existing rings. Third-generation synchrotron radiation sources were conceived and optimized from the outset to produce brilliant X-rays. Fourth-generation sources that will include different concepts for producing ultrabrilliant, pulsed time-structured X-rays for extremely demanding, and also yet-to-be-conceived, experiments are under consideration.

Bending electromagnets in accelerators were first used to generate this radiation, but to generate stronger radiation, other specialized devices – insertion devices – are sometimes employed. The third-generation synchrotron radiation sources are typically reliant upon these insertion devices, where straight sections of the storage ring incorporate periodic magnetic structures (comprising many magnets in a pattern of alternating N and S poles) which force the electrons into a sinusoidal or helical path. Thus, instead of a single bend, many tens or hundreds of "wiggles" at precisely calculated positions add up or multiply the total intensity of the beam. These devices are called wigglers or undulators. The main difference between an undulator and a wiggler is the intensity of their magnetic field and the amplitude of the deviation from the straight line path of the electrons. There are openings in the storage ring to let the radiation exit and follow a beam line into the experimenters' vacuum chamber. A great number of such beamlines can emerge from modern third-generation synchrotron radiation sources.

Shanghai Synchrotron Radiation Facility, SSRF (Figure 4), is a third-generation of synchrotron radiation light source, and is an invaluable tool for the Chinese scientific research and industry communities. Up to now, SSRF is the biggest scientific platform for science research and technology development in China.

In contrast with micro CT, the SR-μCT (Figure 5) uses the synchrotron radiation X-ray as a light source to achieve high-speed imaging, intensive strength, high spatial resolution (to sub-micron or nano-scale), noninvasive fluoroscopy, to be able to scan, quantitatively evaluate and visualize the 3D structure of DDS. The advanced performance of SR-μCT is due to a number of factors. Include - the wide X-ray energy region 1~>200keV photon energy which can be generated; high intensity of beam: the total power is 600 KW, which is tens of thousands times higher than that of X-tubes; reduced time of obtaining the experimental data; high brilliance: brilliance which is hundreds of times higher than that of X-tubes; the synchrotron light is fully polarized. As a result, SR-μCT is an increasingly important tool to research the structure of biological molecules, medical molecules and dichromatic magnetic materials [18].
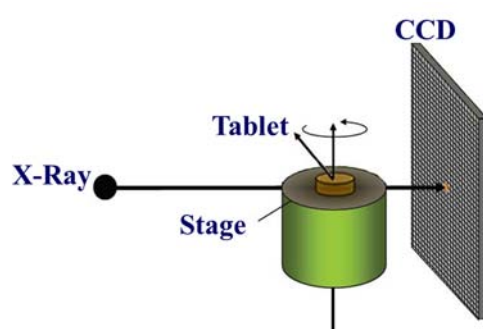
Figure 5 *SR-μCT scanning*

3D Reconstruction： 3D reconstruction from multiple images is the creation of three-dimensional models from a set of images. It is the reverse process of obtaining 2D images from 3D scenes. The essence of an image is a projection of a 3D scene onto a 2D plane, during which process the depth is lost. The 3D point corresponding to a specific image point is constrained to be on the line of sight. From a single image, it is impossible to determine which point on this line corresponds to the image point. If two images are available, then the position of a 3D point can be found as the intersection of the two projection rays. 3D reconstruction is the process of capturing the shape and appearance of real objects.

Tomographic reconstruction is a type of multidimensional inverse problem where the challenge is to yield an estimate of a specific system from a finite number of projections. The mathematical basis for tomographic imaging was laid down by Johann Radon. A notable example of applications is in computed tomography (CT) where cross-sectional images of patients are obtained in a non-invasive manner. In practice for tomographic image reconstruction, often a stabilized and discretized version of the inverse Radon transform is used, known as the filtered back projection algorithm (Figure 6).
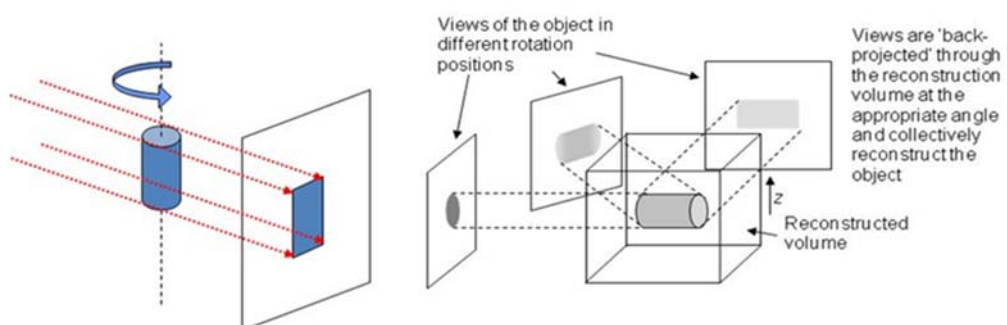
Figure 6 *Back-projection reconstruction*

Methods combining X-ray tomography, image processing and 3D reconstructions to study the architecture and drug release kinetics of DDS have been developed and are detailed in this thesis

1.4.3 Architecture and properties, behaviour and functions

The concept that architecture determines the function is often described in terms of cells and their constituents, which has contributed to the rapid development of biology and life science over the last several decades. Shapes and physicochemical characteristics of proteins, cells, tissue and organs relate to their specific function. The links between structure and function can also be observed in pharmaceutics. The drug release behaviours of DDS are mainly determined by the static architecture and dynamic change such as disintegration, erosion, diffusion, degradation, swelling and etc. [19]. The intermediate structure of the solid dosage unit also plays an important role in the function and effectiveness of final drug products. Characterization of particles is an important requirement for pre-formulation and formulation studies since particle morphology, size, shape, mechanical properties can influence the selection of other formulation ingredients and selection of specific production processes. Drug particle size can influence a range of important performance criteria, such as powder flow and mixing, dosage unit content uniformity, dissolution rate, bioavailability, stability, and thus has an important role in the formulation, processing and ultimately therapeutic efficiency in patients. Thus, manufacturers producing a particulate based medicine need to understand and quantify any differences between batches of particulate materials for product development and quality control purposes.
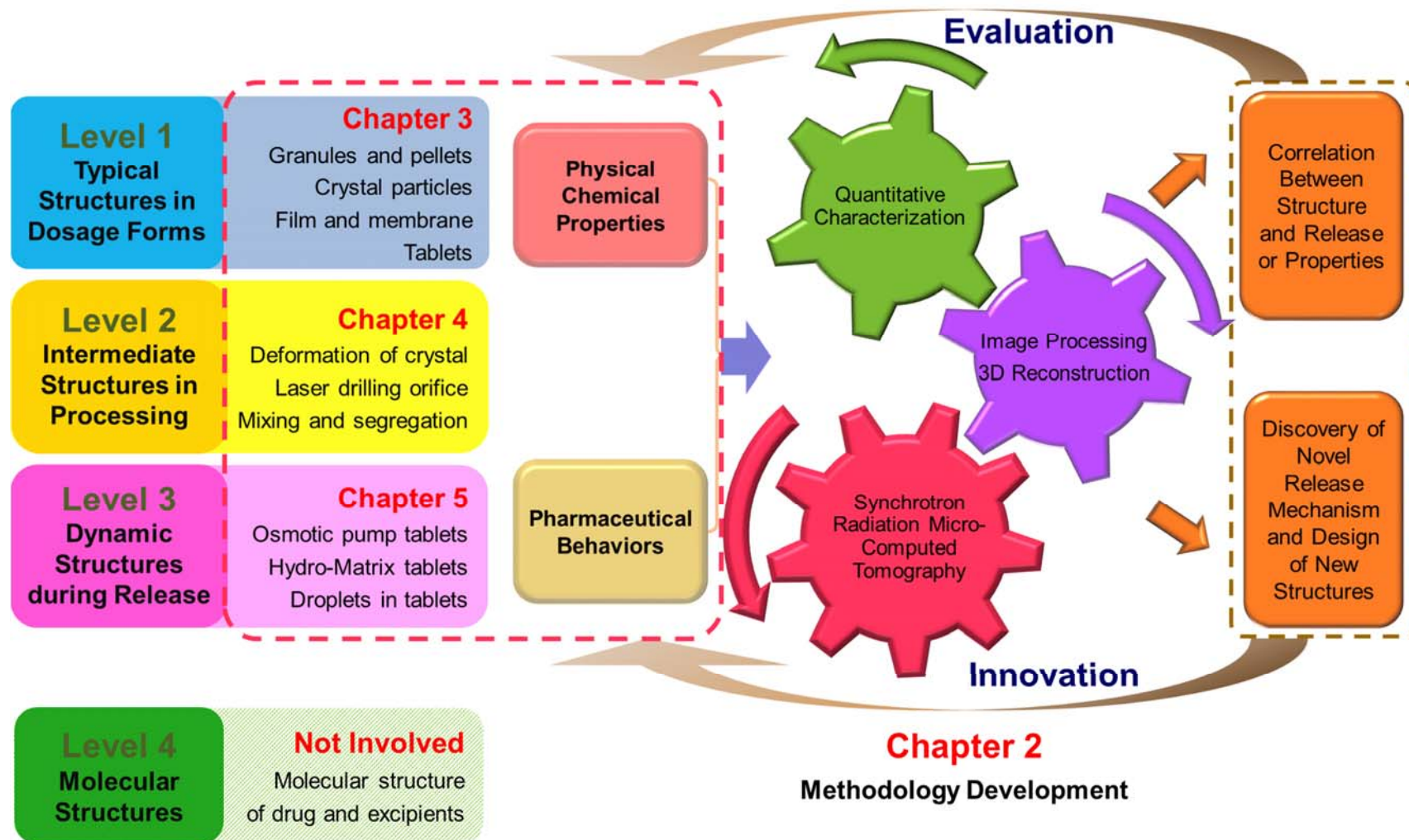
Figure 7 *Framework of thesis and the four levels of drug delivery system architectures*

The research of this thesis has focused on creating and developing a strategy for applying the µCT technique for investigating the morphology and internal structure of solid dosage forms and powders at different levels or architecture (see Figure 7). As a result, the whole spatial information on a particular powder or solid dose unit can be obtained by this method. In addition, distributions of geometric characteristics describing size, shape, and spatial arrangement of the particles can be estimated after imaging and analytic separation of data of the individual particles [20] [21]. This powerful method has been employed to provide detailed morphological information such as pore shape, spatial distribution, and connectivity of porous particles which can be correlated with the dissolution properties of the drug delivery system [22, 23]. It is also shown that the µCT combined with discrete element method (DEM) can be used to investigate particle packing in a process of pharmaceutical tablet manufactured by powder compaction [24]. In this dissertation, the powerful three dimensional (3D) research tool, the SR-µCT technique has been applied to demonstrate its potential for DDS research to explore the world of fine internal structures and the dynamic behaviours in architecture oriented drug release kinetics. The structure of thesis is visualized in Figure 7.

Methodology design for quantitative characterization of structure:

Methods based on 3D reconstruction for the quantitative evaluation of the irregular micro-structures of DDS as well as particles from intermediate processing are researched and developed. In addition, new methods for SR-µCT imaging of the pharmaceutical samples devised to present the full details of the surface morphology and the internal 3D structure, including the image processing

method, 3D reconstruction method, and construction and optimization of 3D models.

Characterization of DDS and DDS component structures:

After consolidating the theoretical and methodological parts of imaging and structural analysis, systematic methods and applied research are carried out for typical drug delivery systems at different dimensional scales. The unique sample preparation methodologies developed are compared to other preparations measured by synchrotron radiation. Since most of the sample ingredients are organic substances, optimization procedures have focussed on such samples for synchrotron radiation imaging to optimize the resolution, imaging parameters on the contrast and calculation methods. After CT measurement, the true three-dimensional structure of prepared samples have been obtained by reconstruction. In addition, new software to determine the fractal dimension is considered to be useful to link material fractal dimension with pharmaceutical properties as the drug release rate to achieve quantitative analysis of the irregularity for complex structures.

Interpretation of the dosage form structure:

The quantitative structural studies are performed for the fine structure of large-size dosage forms, such as drug crystals, powders of the formulated particles and tablets on a wide spatial scale from submicron to 5000 μm and combined with the release features of drug delivery systems to create a structure-based drug delivery theory and methodology. The structural studies cover the entire 'life span' of the drug delivery systems, from material selection, formulation design, process optimization to patient administration and drug release in vitro

and in vivo. Based on a SR-µCT three-dimensional reconstruction, image analysis, quantitative characterization, data mining, modelling and simulation technologies are combined to conduct cross-scale, multi-level networking and dynamic structure research for drug delivery systems and establish the structural pharmaceutical research system. Following the concept of Quality by Design (QbD), the quality of the final products is established from the structural pharmaceutical formulation research to develop more controllable novel drug delivery systems.

Pharmaceutical structures to be investigated:

The methodologies used to examine the range of samples are described and validated in chapter 2. Correlation between the micro-structures of interest, the ISO-Surface model construction and 3D steric quantitative parameters and the pharmaceutical relevant characteristics and the properties of DDS are explored. Where alternative experimental and analytical procedures are required for specific sample types, these are introduced in the later Chapters and further details provided in the Appendices.

Chapter 3 reports on examination of DDS samples at Level 1 architecture includes spherical granules, irregular granules, pellets of multi-unit DDS, crystals and agglomerated crystal particles of polymorphs, osmotic pump controlled release tablets and hydrogel matrix sustained release tablets.

In Chapter 4, investigation of DDS samples at level 2 architecture was reported. The intermediate structures include blend granules during mixing, blend granules during shaking, deformation behaviour of crystal particles during

compaction, orifices for osmotic pump tablets after laser drilling were studied for the evaluation of pharmaceutical processing.

Chapter 5 focus on the level 3 architecture and the relationship between dynamic structures and drug release behaviours. Samples include single pellet of multi-unit DDS, osmotic pump tablets and hydrogel matrix tablets during release. Based on the quantitative characterization of the changing structures to the reveal the dominant release mechanism. More importantly, the developed dynamic computed tomography methods was used for the *in-situ* testing of novel osmotic pump tablet.

Although the methods and principles include the procedure and workflow of preparation of samples, image acquisition, parameters optimization, image processing and 3D reconstruction were described generally in the section of methodology development. The detailed information related with the particular samples tested in the foregoing chapters was provided respectively and included in the Appendix section to avoid much repetitive descriptions in the main part of thesis.

a) Particles, granules and pellets. The blend homogeneity and segregation of binary mixtures are investigated using frequency distribution of a particle structure based statistical model. The internal fine structures of granules and microspheres are quantitatively characterized and correlated with the single pellet release characteristics or release profiles of the microspheres.

b) Polymorphs of drug crystals. Polymorphism denotes the existence of more than one crystal structure of a substance, and is of great practical and theoretical interest for the chemical and pharmaceutical industries. In many cases, it is

challenging to produce a powder with all particles chemically pure and of the same crystal form and to establish a sensitive detection method for the identification of crystal form in a mixture of polymorphs.

c) Osmotic pump tablets. Investigation of the internal 3D steric microstructure uncovered the drug release mechanism of the monolith pump controlled release systems. The fractal dimensions of tablet core structures calculated based on the box counting method are used to link the irregular internal structure of an osmotic pump tablet with its drug release kinetics.

d) Gel matrix tablets. Investigation of the quantification of swelling and erosion in the controlled release tablets of a poorly water-soluble drug has enabled a model of 3D release kinetics to be established.

Chapter 2

Methodology Development for 3D

Structural Characterization

2.1 Materials and equipment

2.1.1 APIs and Excipients

a) CLP I and CLP II, Clopidogrel bisulphate (purity of 99.9%) were provided by Shenyang Pharmaceutical University (Shenyang, China).

b) Acetaminophen with purity of 99.45% was provided by Anhui Fengyuanlikang Pharmaceutical Co., Ltd., (China).

c) PVP/VA (Plasdone® S630) was purchased from Shanghai Chineway Pharmaceutical Tech Co., Ltd. (Shanghai, China)

d) Gelatin capsule shells of different size were provided by Xinchang Hechang Co., Ltd. (Zhejiang, China).

e) Starcap 1500® Co-Processed Starch Excipient, was provided by Shanghai Colourcon Coating Technology Limited (China).

f) Microcrystalline cellulose granules (Celphere®), were supplied by Anhui Shanhe Pharmaceutical Excipients Co., Ltd.(China).

g) Octadecanol, was supplied by Hunan Erkang Pharmaceutical Co., Ltd.

h) Eudragit E100 (PMA) was supplied by Hanghai Chineway Pharmaceutical Tech. Co., Ltd.,(China)

i) Sodium phosphate monobasic dihydrate, sodium hydrogen phosphate and phosphoric acid were provided by Sinopharm Chemical Reagent Co., Ltd., (China).

j) Captopril was gifted by Changzhou Pharmaceutical Factory Co., Ltd., (China).

k) Lactose (Ludipress® LCE) was provided by BASF (Germany).

l) Sodium chloride was provided by Ciji Medicine Pharmacy (China).

m) Magnesium stearate was provided by Anhui Sunhere Pharmaceutical Excipients Co., Ltd., China.

n) Cellulose acetate (398-10NF) was provided by Easter Chemical Company (USA).

o) Polyethylene glycol (4000 g/mol) was purchased from Sichuan Hanhua Pharmaceutical Excipients Co., Ltd. (China).

p) The other chemical reagents used were all of the analytical grade and purchased in China.

2.1.2 Marketed drug delivery systems

a) Felodipine sustained-release tablets (Linuo; each tablet containing 5 mg of felodipine) with orifices drilled on both the upper and lower, were supplied by Hefei Lifeon Medication Group (Hefei, China).

b) Felodipine extended release tablets (Plendil®, each tablet containing 5 mg of felodipine, lot number: 1010014) were produced by AstraZeneca PLC, China. In addition to the active ingredient felodipine, the tablets contained the following inactive ingredients: cellulose, red and yellow oxide, lactose, polyethylene glycol, sodium stearyl fumarate, titanium dioxide, and other ingredients.

c) Tamsulosin hydrochloride (TSL) sustained release capsules were purchased from Astellas Pharma China Inc. (Shenyang, China). In addition to the active ingredient of tamsulosin hydrochloride, the pellets contained the following

inactive excipients: methacrylic acid copolymer, microcrystalline cellulose, triacetin, polysorbate 80, sodium lauryl sulfate, calcium stearate (http://www.accessdata.fda.gov/drugsatfda_docs/label/ 2005/020579s016lbl.pdf). The mixture of all substance was granulated after the addition of the aqueous liquid material to form pellets, which can be classified as typical matrix cores pellets, according to the patent (European Patent EP0533297).

2.1.3 Analytical equipment and other devices

a) Bruker D8 Advance powder diffractometer (Bruker, Germany) equipped with a 2.2 kW sealed Cu X-ray source, a graphite monochromator to filter out the Cu K β radiation, and a NaI (TI) scintillation detector. The XRD patterns were measured on using Cu-Ka radiation (I = 1.5418 Å). The voltage and current were 40 kV and 40 mA,respectively. Reflection mode was used in the 2θ range of 3-40° with a scan speed of 15° min^{-1} (step size 0.025°, step time 0.1 s) with a LynxEye detector. All the data were acquired at ambient temperature (20℃). The data were imaged and integrated with RINT Rapid and diffraction peaks-analyzed with Jade 6.0 software from Rigaku. Calibration of the instrument was performed using a Corindon (Bruker AXS Korundprobe) standard.

b) Chinese Pharmacopoeia Dissolution Apparatus II (Tianjin TDTF Technology Co., Ltd., China).

c) Freeze dryer FD5-3, China-GOLD SIM(Beijing) InternationalCo. Ltd., (China).

d) Agilent 1260 series HPLC system (Agilent Technologies Inc., China).

e) G6460 tandem mass spectrometer (Agilent Technologies Inc., China) equipped with an atmospheric pressure chemical ionisation (APCI) module.

f) Luna C18 column (150 mm×4.6 mm, 5 µm, Phenomenex)

g) SEM, Hitachi S520 device (Hitachi, Japan)

h) Inverted phase contrast microscopy (TS-100F, Nikon, Japan).

i) Particle sizing system (Camsizer XT, Retsch, Germany).

j) X-ray digital camera 4008 pixel× 2672 pixel with direct coupled (micro) fiber-optic (photonics Science Ltd, Robertsbridge, UK) in Figure 8.

Figure 8 *X-ray digital camera from Photomic Science*

k) Diffraction-limited microscope optics (1.25×, 2×, 4×, 10× and 20× magnification)

l) High-resolution 2048 pixel× 2048 pixel CCD camera (pco.2000, PCO AG, Kelheim, Germany) in Figure 9.

Figure 9 *High resolution CCD camera from PCO AG*

m) Lu2SiO5: Ce scintillator (10 μm thickness)

n) YAG:Ce scintillator (200 μm thickness)

o) Laboratory Shaker (MS 3 digital, IKA, Germany).

p) Spraying system (Spray gun, W-71, Iwata, Japan).

q) Dissolution apparatus (ZRS-8G, Tianjin Haiyida Co., Ltd., China).

r) High-resolution 2048 pixel × 2048 pixel sCMOS camera (ORCA Flash 4.0Scientific CMOS, Hamamatsu K.K, Shizuoka Pref., Japan). The physical pixel size was 6.5 μm in Figure 10.
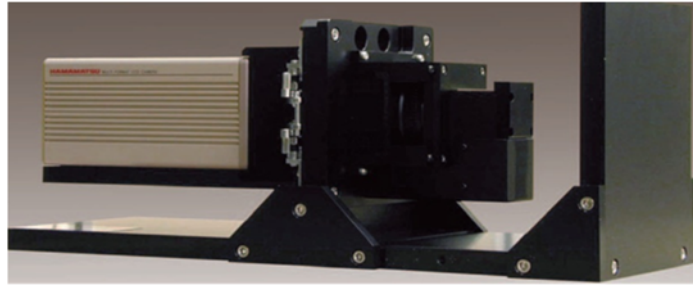
Figure 10 *High resolution sCMOS camera from HAMAMATSU*

s) 6-Axis Positioning Stage for the holding of sample form PI (Physik Instrumente) LP, USA and Kohzu Precision co. Ltd, Japan in Figure 11.

Figure 11 *High precision positioning stages*

t) Synchrotron radiation facility and resource

As a third generation synchrotron radiation facility, the SSRF provided large tuning range (10-100keV), monochrome and high flux X-ray and started its user operation in May 2009. The X-ray Imaging and Biomedical Application Beamline (BL13W1) is composed of a 1.9 Tesla wiggler, 6 set of filters for high heat load reducing, and double crystal monochromator cooled with liquid nitrogen. X-rays are derived from an electron storage ring with an accelerated energy of 3.5 GeV, and an average beam current of 180 mA. The light source is hybrid-type wiggler with periodic length 14 cm and the number of the period is 8. Maximum K-value is designed to be 24.8 at minimum wiggler magnet gap of 17 mm. The

fundamental radiation covers the energy range from 8.0 to 72.5 keV by tuning the gap from 17 to 35 mm. At the end station, sets of digital X-ray detectors are employed with the pixel size range from 0.165 to 13 micrometers. Imaging methods of microscopic computer tomography (micro-CT, Figure 12), in-line phase contrast imaging (IL-PCI) and X-ray fluorescence imaging are provided for scientific researches on high Z and low Z samples in the field of biomedical, material, archaeology, environmental science. Spatial resolution of 0.8 μm and time resolution of 1 ms can be achieved.
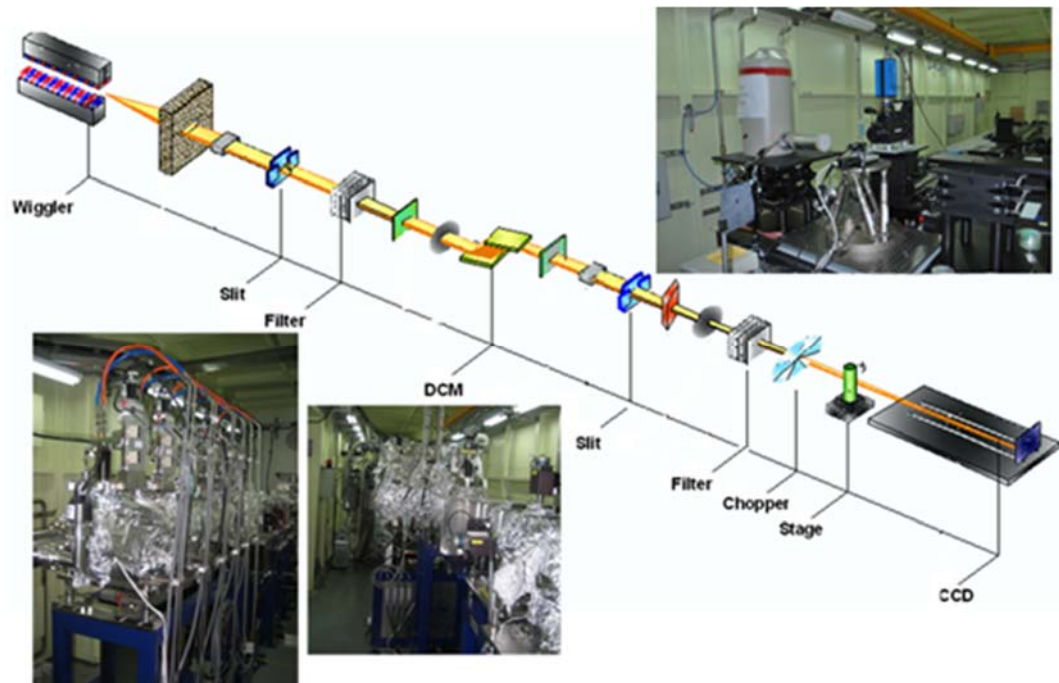
Figure 12 *The beam line for X-ray imaging and biomedical application at Shanghai Synchrotron Radiation Facility*

Where the Wiggler is an insertion device used for the generation of synchrotron radiation, slits and choppers are used to shut down the beam as necessary, filters for selective transmission of light, DCM to monochromatize the X-ray, a sample stage and CCD to capture the images. The SR-μCT tomographic images of prepared samples were acquired at a relatively low energy. The size of the beam was approximately 45 mm (horizontal) × 5 mm (vertical) and a

double-crystal monochromator with Si (111) and Si (311) crystals was used to monochromatize the X-rays. The monochromatized has a flux density about 5.8 × 10^{10} ph/s/mm^2 at 16 KeV and the energy resolution was Δ E/E = 5 × 10^{-3}.

2.1.4 Software and Workstation

a) X-TRACT SSRF CWS x64 (Version 6.5 Commonwealth Scientific and Industrial Research Organization, Australia, http://www.ts-imaging.net/Default.aspx) is an image analysis and processing application with functionality targeting researchers working in imaging science and technology fields, especially in optical, electron and X-ray microscopy and astronomy. It was developed by international cooperation with the CSIRO in Australia. With these software packages, phase contrast reconstruction, fast micro CT reconstruction and other image processing are achieved. Remote data processing and transfer have also been realized.

b) VGStudio Max (Version 2.1, Volume Graphics GmbH, Germany) provides unique functionality for precise and fast analysis of voxel data, visualization and analysis of CT data in combination with the optional add-on modules.

c) Image Pro Analyser 3D (Version 7.0, Media Cybernetics, Inc., USA)

d) Image Pro Premier (Version 9.0, Media Cybernetics, Inc., USA)

e) Amira (Version 6.0, Konrad-Zuse-Zentrum für Informationstechnik Berlin (ZIB, Germany, FEI, Inc. SAS, USA) 3D software platform for visualizing, manipulating, and understanding biomedical data coming from all types of sources and modalities.

f) ImageJ (Version 1.49, National Institute of Health, USA)

g) Matlab (2013a, Mathwork. Inc., USA)

h) PITRE: a CPU based software package that supports phase retrieval for propagation-based phase-contrast imaging/tomography (PPCI/PPCT), extracting apparent absorption, refractive and scattering information from DEI, and CT reconstruction. H-PITRE, CT reconstruction software accelerated by GPU

i) DCM: software for the data-constrained modelling and characterization of material compositional microstructure and properties, developed by CSIRO (http://research.csiro.au/dcm)

j) PASW Statistics version 18.0 (Polar Engineering and Consulting)

k) Dell Precision M6800 Workstation (Windows 7 64bit SP1, DirectX 11, Core i7-4900MQ @ 2.80GHz Quadcore, Dell Motherboard 0XD1M5 Intel Haswell, 32 GB Samsung DDR3L 1600MHz , SSD IT LCS-512M6S 2.5 7mm 512GB, GPU Nvidia Quadro K5100M 8 GB)

l) Microsuper Workstation (Windows 7 64bit SP1, DirectX 12, Xeon 2650 @ 2.20GHz Octacore × 2, Supermicro Motherboard X9Di, 64 GB Kingston DDR3 1600MHz , SSD Intel 480GB, GPU Nvidia Quadro M5000M 8 GB)

2.2 Synchrotron radiation and micro-computed tomography

2.2.1 Preparation of samples

In order to evaluate temporal changes in pharmaceutical DDS microstructures, optimum samples should be prepared. Several critical factors such as X-ray absorption intensity, water content, stability of samples, containers,

statistical significance, size of samples and parallel control of experiment can have a marked effect on the SR-µCT test and data generated.

X-ray absorption intensity

The intensity values associated with the different features of an SR-µCT image are determined by the X-ray transmission measured by an X-ray detection system, which is dependent on the material's atomic mass and the energy of X-rays [14, 25]. Different elements in pharmaceutical samples have different X-ray absorption intensity. To identify the targeted element precisely, other elements in pharmaceutical samples used for the SR-µCT test need to be identified and distinguished. The physical nature of samples, however, does affect its X-ray absorption over and above its bulk density. For instance, porosity either above the system resolution limit or at sub-voxel levels will result in differences in X-ray absorption that will be seen as different grey levels, and this will be in turn depend on variables such as the distributive characteristic of the porosity, the point-spread function of the X-ray source, and the pixel size of the camera.

The complexity of sample interfaces

Material interfaces also need to be considered, as the degree of complexity will determine how detectable the boundary will be. In some instances, where mixing of materials is extensive, a fairly diffuse boundary may be imaged; in other instances, the interface may be less complex giving rise to sharper delineations. In other cases, the porosity and, hence localized density, may be affected by sample interactions occurring at boundaries.

Density and density distribution

Density sensitivity is an important issue to be taken into consideration when performing SR-μCT scans. The basic density of the materials being imaged is clearly a major factor. If two adjacent materials have a similar density then they may not be differentiated unless some other properties such as different hydration levels act to modify their base density.

Water content

Water will interfere with imaging. Samples should contain as little water as possible. Owing to this interference imaging acquisition using SR-μCT technique, samples containing water must be dried prior to image acquisition. Three methods have been considered for the pretreatment of the samples in SR-μCT experiments: (a) drying in an oven, (b) freeze-drying, and (c) absorbing as much liquid as possible with filter paper and storage at room temperature over silica gel. For methods (a) and (c) for certain samples such as the matrix gel tablets samples tend to shrink, and the gel formed on the surface of the tablet core would collapse causing changes to the internal gel structure during the imaging process. However for these samples, the freeze-drying method was found to maintain the microstructure of the hydration layer as much as possible due to its rapid cooling process. For these samples, it is considered that the freeze-drying method caused minimal change to the structure of the tablet core and was selected for all further work.

Stability of samples

Consideration was also given to the stability of sample components. The energy of X-ray in SR-μCT is high and will heat samples, and some may undergo

physical and chemical changes. Therefore, samples used for SR-µCT scan are required to have good thermal stability.

Size of samples

Image resolution should be chosen primarily according to the absorption of samples. Higher resolution indicates a smaller acquisition window. Thus, limited by the acquisition windows during the SR-µCT test, the size of samples should be carefully considered.

Choose of containers

In this study, samples used for SR-µCT scan need to be positioned in certain containers such as plastic tube and capsule shells. These containers require the features of rigidity, thinness, weak X-ray absorption and homogeneous structure.

Fixation of samples

To capture enough image information, the sample stage will rotate 180 ° during the SR-µCT scan. Rotation of the sample stage could lead to unexpected movement of samples, especially for the powder and granule samples. Thus, samples should be rigidly fixed.

Number of samples

A different number of samples are required to be examined depending on the specific investigation target. If the study objective is a focus on the macroscopical action, such as investigation of granular systems, samples of a large number granules should be chosen. In contrast, when for sample microscopical internal structures are being investigated tens of granules may be

sufficient on condition that the results have statistical significance. In order to recognize two or multi-component systems in each granule by SR-µCT, a diluent with weak absorption can be added to separate each granule. When quantifying swelling and erosion in felodipine extended release tablets for example, 18 tablets were taken and divided into nine groups, each containing two tablets and a standard dissolution test was carried out. At 0.5, 1.0, 2.0, 3.0, 4.0, 5.0, 6.0, 7.0, and 8.0 h, two tablets were removed from the dissolution medium and prepared for further testing [25].

Samples of dynamic process studies

It would be advantageous to visualize the internal structure of materials post-manufacturing and focus for example on dynamic properties of pore structure and porosity changes during drug dissolution and diffusion from tablet samples. SR-µCT can produce 3D images of materials with a voxel size of around several micrometres cubed, allowing the visualization of internal and microstructural details with different X-ray absorbencies. Whilst in vitro dissolution test is usually used to evaluate the drug release behaviour of DDS, such as tablets. SR-µCT can be used to evaluate the temporal changes in the pharmaceutical microstructure during drug release. For metal element containing active pharmaceutical ingredients with relatively high densities, such as ferrous sulphate, tablets containing these materials can be imaged directly using the SR-µCT technique during dissolution testing. The dissolution medium will not influence either the imaging or the visualization of the microstructure of the tablet core. However, for non-metallic drugs with similar density to the dissolution medium, such as felodipine, that do not have metallic elements in their molecular structure, the dissolution medium will interfere with the imaging [26].

Unfortunately, most drugs are not metallic compounds. Therefore, for studying drug dissolution effects dynamically, tablets taken out from the dissolution medium must be dried prior to the image acquisition. In published research, tablets are first frozen in liquid nitrogen or ultralow temperature refrigerator then dried using a freeze dryer [27]. In the studies reported in this thesis, in order to maintain the shape of the tablets from dissolution testing, swollen tablets were carefully removed using small spoons together with about 2 mL of the medium and placed individually in 24-well plates with 2 mL of the corresponding dissolution medium added to maintain the original shape of the tablets. The 24-well plates containing the tablets in various states of hydration and erosion were then immediately placed into the ultra-low-temperature refrigerator at −80°C for 12 h. After this process, the tablets were freeze-dried over a period of 24 h at −50 °C and 10 mTorr using a freeze dryer. These tablets were then kept in the dry cabinet under ambient temperature (relative humidity of 20%) for further SR-µCT tests and were not reused in dissolution tests [28].

This method has also been evaluated to dry the felodipine monolith osmotic pump tablet prior to image acquisition. However, due to the special structure of the monolith osmotic pump tablet and the fact that the volume expansion of water during the phase transition from liquid to ice during freezing leading to the internally dissolved solution and suspension content of the drug in the tablet core being forced out through orifices, this procedure was not used. Furthermore, the remains of the tablet cores are mainly gels, and the formation of water crystals at low temperature may destroy the internal microstructure.

2.2.2 Image acquisition

Accurate and precise experimental results based on the high quality images acquired during the CT scans are essential. In order to guarantee the precision, it is imperative to optimize the parameters according to the objective of experiment and the properties of prepared samples. The various parameters requiring consideration are as follows:

a) The resolution of images is determined both by the magnification of the lens and the pixel size of CCD. As the CCD is fixed, the higher resolution means a smaller area of acquisition window. There is thus a trade-off between the size of the whole sample and the expected resolution required to examine the smallest component in the microstructure.

b) The photon energy of synchrotron X-rays have a range of 1~>200 KeV which has potential for damaging the samples. For the selection of X-ray energy, factors such as the sample components, molecular weights, density of materials and the thickness of sample should be considered.

c) The exposure time affects the X-ray photon number reaching the detector. When the exposure time increases, the flux of CCD to capture a projection will be raised. A CT scan with an unsuitable exposure time will not generate highquality images. A long exposure time may lead to an overexposure that would affect the contrast between materials and increase the scan time of every sample. In the case of underexposure, the signal-noise ratio will be reduced. In addition, the radiation dose should be taken into account as a long time exposure to X-ray can result in deformation of sample and radiation damage.

d) The distance between sample and detector (DSD) is a key factor in in-line phase contrast SR-µCT, and especially useful for the imaging of materials with low-Z elements and low-density. Within a certain distance, longer DSDs provide an improved phase contrast which benefits distinguishing materials with small difference in density that cannot be distinguished by the absorption contrast method.

e) The number of projections is typically determined by the size of the sample and the precision required for the experiment. During the scanning, the sample rotates 180° and projections will be captured at certain angles. More projections will enhance the quality and restrain any artefacts (i.e. misleading or confusing alteration in data or observation, commonly found in experimental science, resulting from flaws in technique or equipment). however, more projections will lengthen the scanning time and will lead to potential radiation damage as mentioned above.

Prepared samples need to be positioned in a suitable container and attached to the sample stage to prevent any unexpected movements during scans. Axis adjustment of the sample stage is also necessary to make sure that there is no deviation in the horizontal direction during sample rotation. After X-ray penetration through the sample, the projections are magnified by diffraction-limited microscope optics and digitized by a CCD camera. For each acquisition, a certain number of projection images over 180° sample roration are taken. Light field images (i.e. X-ray illumination on the beam-path without the sample) and dark-field images (i.e. X-ray illumination off) are also collected during each acquisition, for corrections due to electronic noise and variations in the X-ray source brightness.

Table 1 Parameters of SR-μCT scans for different samples.

Samples	X-ray Energy /Kev	DSD /cm	Resolution / μm	Projections /pic	Exposure time /ms
Cellulose pellets and starch granules	13	25	13.00	630	1000
Tamsulosin sustained release pellets	16	12	3.70	720	3000
Clopidogrel polymorphs crystal particles	16	12	3.70	720	2000
Clopidogrel polymorphs crystal tablets	16	12	3.70	720	2000
Felodipine osmotic pump tablets	13	25	5.92	900	4000
felodipine HPMC gel matrix tablet	13	10	9.0	720	4000
Laser drilling orifices	18	10	3.25	720	1000
Droplet driven osmotic pump tablet	18	10	3.7	720	2000
Dynamic CT	18	10	6.5	230	2

2.2.3 Phase contrast and phase retrieval

In order to investigate the distribution of low Z materials in samples, the propagation-based imaging (PBI) method can be used for phase contrast imaging for the simplest experimental implementation. The imaging parameters should be optimized according to preliminary experiments and references. From the theoretical complex refractive index detail, it is required that to enhance the phase contrast X-rays with a lower energy should be selected for imaging (Figure 13). For interrogating various sample properties including composition, density and proportions, samples were scanned at low energy for achieving the balance between the penetration ability and the higher flux to reduce the imaging times.

In order to enhance the contrast to show a small difference in density, the sample-to-detector distance was also adjusted appropriately.
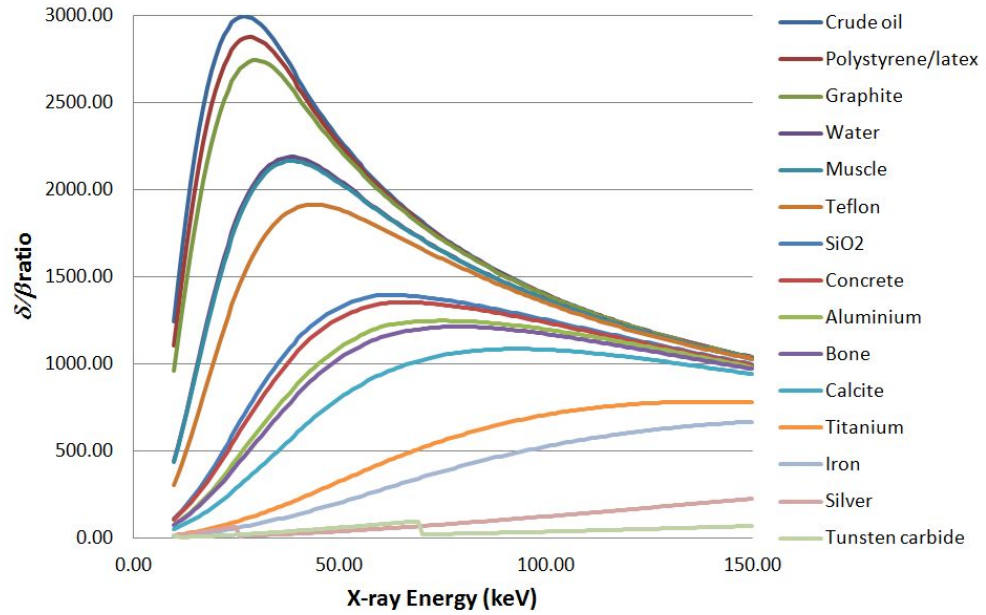
Figure 13 *The delta/beta ratio for a range of materials between 10-150 keV x-ray energy*

The projected images for the samples were reconstructed using the X-TRACT SSRF CWSx64 (CSIRO, Commonwealth Scientific and Industrial Research Organization, Australia, http://www.ts-imaging.net) to perform a direct filtered back projection algorithm. To enhance the quality of reconstructed slices, propagation-based phase contrast extraction was carried out. In phase contrast imaging, the amplitude and phase of X-rays are affected by the interaction of the wave with matter and the forward diffraction is formally be described by the complex refractive index (n) of the medium as

n = 1 - δ - iβ

The refractive index δ results in a phase shift, and the absorption index β is linked to the linear absorption coefficient μ. The theoretical values of β and δ were

calculated with the X-ray attenuation properties model of DCM (software for the data-constrained modelling and characterization of material compositional microstructure and properties, which was developed by CSIRO, http://research.csiro.au/dcm). The larger sample-to-detector distances increased the contrast primarily due to the contribution from differences in the refractive properties across the sample in addition to differential absorption. In combination with Homogeneous Transport of Intensity Equation (TIE-Hom) phase retrieval achieves high quality reconstructed 3D images. The value of β can be accurately reconstructed with TIE-Hom and conventional CT reconstruction from a single projection image per view angle. In contrast, the accuracy of reconstruction of δ depends strongly on the choice of the "regularization" (δ/β) parameter in TIE-Hom. During phase extraction, the parameter of δ/β can be adjusted to theoretical values. After phase retrieval and reconstruction, the calculated β in the images must be truncated and rescaled to a grey value of 0 to 255 (8 bit grey level) [29].

2.2.4 The 3D reconstruction and quantitative characterization

3D reconstruction from reconstructed slices is used for the creation of three dimensional models. The projections were converted to reconstructed slices using a filtered back-projection algorithm. In order to enhance the quality of reconstructed slices, a phase retrieval algorithm is included for phase contrast extraction. The 3D rendered data were analysed with commercially available software such as VGStudio Max (Volume Graphics GmbH, Germany), Amira (Visualization Sciences Group, France) and Image Pro Analyser 3D (Media Cybernetics, Inc., USA) to obtain qualitative and quantitative information. After segmentation, slices were all converted into black and white images by removal of the background and noise. Then 3D ISO-Surface models were constructed

with segmented slices. The surface level, surface range and the simplification parameters were adjusted to optimize the models. Then all objects in the samples were extracted to calculate the steric parameters.

As the model construction and analysis are compute-intensive tasks, the reconstructed slice stacks were converted into 8-bit greyscale format and cropped for accuracy and computational efficiency. Then, the resized slices of samples were processed to enhance quality, reduce noise and analysed to determine the threshold grey values to distinguish different materials and micro-structures. In most case the quantitative criterion to distinguish the objects of interest is the grey value, but for some samples with ultra-complex structures or challenging material contents, the morphological information will be more suitable. All samples in the same group experiments were processed with consistent parameters to ensure that all result can be compared quantitatively.

The optimized 3D models provide full detail of the surface morphology, as well as the internal 3D structure. Based on the difference in grey value between materials, objects or micro-structures of interest can be extracted from the 3D models by segmentation. With the ISO-Surface model many 3D steric quantitative parameters can be calculated. The names and descriptions of these parameters are listed below:

Volume: *Volume of object in calibrated units;*

Surface area: *Surface area of object in calibrated units;*

Width: *Size of bounding box in X direction;*

Height: *Size of bounding box in Y direction;*

Depth: *Size of bounding box in Z direction;*

Centre X: *X coordinate of the centre of object;*

Centre Y: *Y coordinate of the centre of object;*

Centre Z: *Z coordinate of the centre of object;*

Box Volume: *Volume of object's bounding box (V = W * H * D);*

Box ratio: *Ratio between maximum and minimum size of the bounding box. (R = Max / Min);*

Volume fraction: *Ratio of object's volume to the box volume (R = Vobj / Vbox);*

Diameter: *Equivalent diameter of object;*

Sphericity: *Sphericity of object, calculated as 6 volumes of object divided by equivalent diameter and surface area of object. For a spherical object this parameter equals 1, for all other shapes it is less than 1;*

Radius (max): *Maximum distance between an object's centroid and surface;*

Radius (min): *Minimum distance between an object's centroid and surface;*

Radius Ratio: *Ratio between Radius (max) and Radius (min);*

Feret (max): *Maximum distance between two parallel planes enclosing an object;*

Feret (min): *Minimum distance between two parallel planes enclosing an object;*

Feret Ratio: *Ratio between Feret (max) and Feret (min);*

Surface deviation: *is calculated as the deviation of end points of a triangle normal. The calculations are done as follow: all triangle normal vectors of the surface are normalized (length set to 1) and the average distance from the mean position of the end-points to all*

other vectors is calculated. A uniform surface will have a deviation of 0, and the maximum deviation of 1.336 will occur for a sphere.

These parameters enable additional parameters such as porosity, specific surface area and roughness to be calculated which help to further describe the morphology of the sample. Relationships can then be explored between all the structural parameters and correlated with the properties of the sample, which include the drug content, drug release kinetics and how is the pharmaceutical processing affectting the structure. In addition, multivariate analysis, data mining, and modelling methods can be introduced to construct statistical models.

2.3 Dynamic computed tomography method

Drug substances and DDS ingredients are usually low Z materials. In order to study drug release characteristics in situ, monochromatic-beam-based high-contrast quantitative dynamic CT needed to be devised and developed. When conventionally white beam is used to realize dynamic CT, the quantitative properties of the sample are lost. In this study, monochromatic beam based phase-contrast quantitative dynamic CT has been established with a millisecond time resolution and a spatial resolution of 6.5 μm. The developed method is able to record continuously 200 seconds of a dynamic process by adapting a sCMOS sensor based detector and introducing compressed sensing (CS) theory into CT reconstruction. Additionally with the phase retrieval algorithm implemented, quantitative information of the sample is extracted for further analysis.

Compressed sensing (also known as compressive sensing, compressive sampling, or sparse sampling) is a signal processing technique for efficiently acquiring and reconstructing a signal, by finding solutions to underdetermined

linear systems. Compressed sensing is based on the concept that, through optimization, the sparsity of a signal can be exploited to recover it from far fewer samples than are required by the Shannon-Nyquist sampling theorem. The possibility of recovery depends on two conditions. The first is sparsity, which requires the signal to be sparse in some domain. The second one is incoherence which is applied through the isometric property which is sufficient for sparse signals. Total variation can be seen as a non-negative real-value function defined in the space of real-value functions (for the case of functions of one variable) or in the space of integrable functions (for the case of functions of several variables). In image reconstruction, it is applied as total variation regularization where the underlying principle is that signals with excessive details have high total variation and that removing these details, while retaining important information such as edges, would reduce the total variation of the signal and make the signal subject closer to the original signal in the problem.

For the purpose of image reconstruction, minimization models are used. The current CS Regularization models attempt to address this problem by incorporating sparsity priors of the original image, one of which is the total variation (TV). Conventional TV approaches are designed to give piece-wise constant solutions. This method, though fast, subsequently leads to over-smoothing of edges resulting in blurred image edges. TV methods with iterative re-weighting have been implemented to reduce the influence of large gradient value magnitudes in the images. This has been used in computed tomography (CT) reconstruction as a method known as edge-preserving total variation [30]. This method would have 2 stages: the first stage estimates and refines the initial orientation field - which is defined as a noisy point-wise initial estimate, through

edge-detection, of the given image. In the second stage, the CS reconstruction model is presented by utilizing a directional TV regularizer.

The incorporation of compressive sensing reduced the number of projections required while maintaining image quality. Combined with a rapid sCMOS detector, the data acquisition process is speeded up, which makes X-ray dynamic-CT more practicable. Moreover, a phase retrieval algorithm based on one set of projections was developed to provide quantitative information of the sample. During data processing, GPU-CUDA based parallel computing architecture is employed to process the massive SR-µCT data. As a result, in-situ investigation on the drug delivery dynamics can be carried out at SSRF, while the microstructures of the pharmaceutical preparations with quantitative and high-contrast information, were revealed three dimensionally.

The methodology developed for investigating the dynamic microtomography, focuses on improving the time resolution and the high spatial resolution. The generation and evolution of the microstructures during drug release process, especially at its initial state, is critical to the investigation on the driving mechanism of the drug release process. High spatial resolution and high contrast imaging form the basis of achieving quantitative analysis (Figure 14).
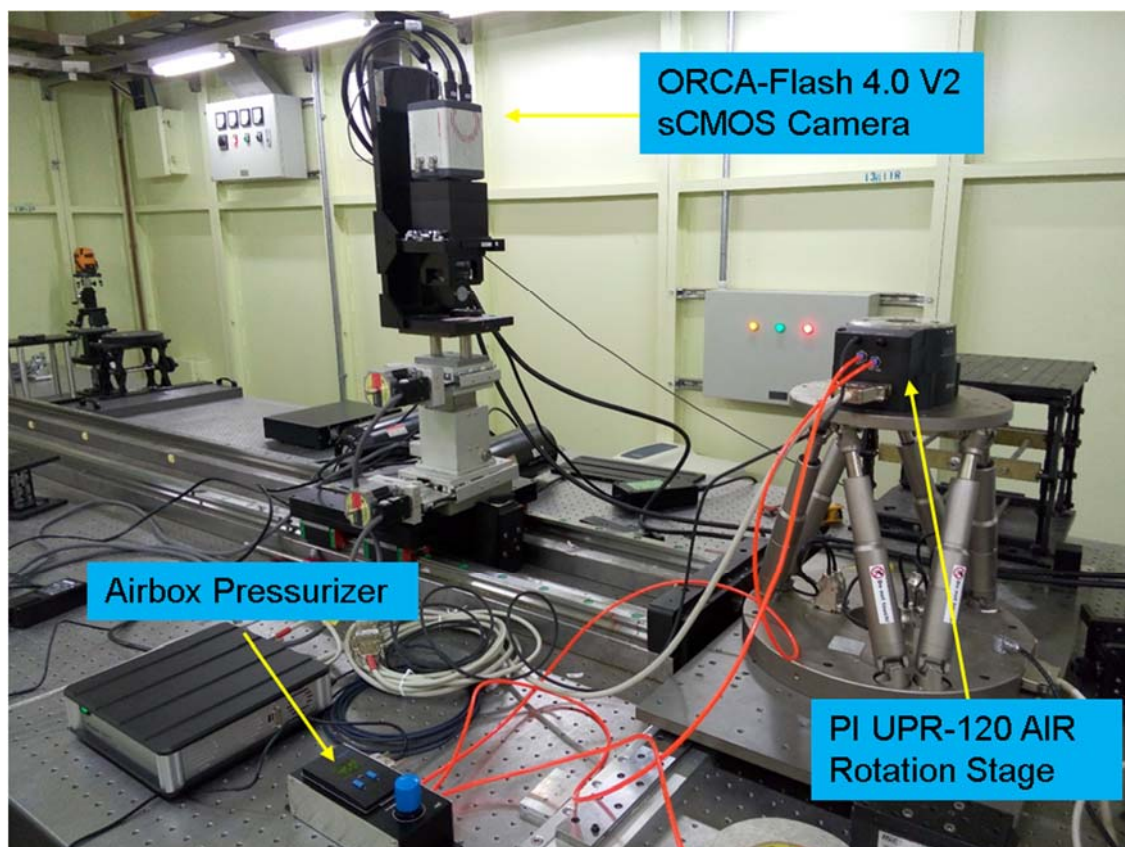
Figure 14 *Experiment condition for dynamic CT*

Improving the time resolution: The rate of change of the microstructures during drug release is relatively fast, and tracking of microstructure changes in a short time is crucial to the research on the correlation between structure and release kinetics. Practical approaches include decreasing the exposure time and reducing the number of projections.

Improve the contrast: Since the active ingredient and excipients of conventional pharmaceutical preparations are weak absorbing organic materials, improving the discrimination among different materials is critical for studying the internal drug distribution of the preparations. The investigation on the release mechanism of the drug formulation also needs in situ determination on the structure changes during the release process. Therefore, the discrimination between material

preparation and the dissolution medium needs to be further improved by reducing the distance of dissolution medium that the X-ray needs to penetrate.

Phase retrieval: Single image based phase retrieval is used for component-resolving imaging for samples of mixtures. Considering the duality effect of the binary mixed substances, derived phase-absorb duality Bronnikov algorithm and phase-absorb duality Born approximation algorithm are applied to improve quantitative accuracy of phase retrieval. The anti-noise ability of phase retrieval algorithm was optimized, taking into account the sample constituents, statistical noise and structural noise.

General comments

In this Chapter, SR-µCT imaging methodology is described for quantitative characterization of the structure. Principles of the synchrotron radiation imaging include the preparation of samples, optimization of imaging parameters and the evaluation of image quality are described. Protocols and workflow of data analysis especially image processing and 3D reconstruction have been established. In the next chapter, the developed methodology will be applied to define the quantitative evaluation of irregular micro-structures of DDS as well as particles from intermediate processing to demonstrate the potential of the new methods for quantitative analysis in describing the detail of the surface morphology and the internal 3D structure of solid pharmaceutical structures.

Chapter 3

Characterization of Typical

Pharmaceutical Structures

- Quantification of Irregular and

Complex Structures

3.1 The structure of pharmaceutical particulates

3.1.1 Spherical microcrystalline cellulose core pellet and irregular starch granules

Granule Morphology Characterization by SR-µCT

The individual granular systems of microcrystalline cellulose and starch are characterized using SR-µCT(detailed information please refer to: S 1 Granule sample preparation and reconstruction). Highly resolved tomographic images with high quality phase contrast were derived for each single particle after 3D reconstruction. During image segmentation, a region growth algorithm was implemented to separate particles in contact with each other. Then, four particles of each granular system were randomly selected to show the morphologies and spatial information (Figure 15). As can be seen, the morphologies of the microcrystalline cellulose and starch granules are markedly different. As expected, compared with the irregular shaped starch granules, the microcrystalline cellulose granules show a regular spherical profile.
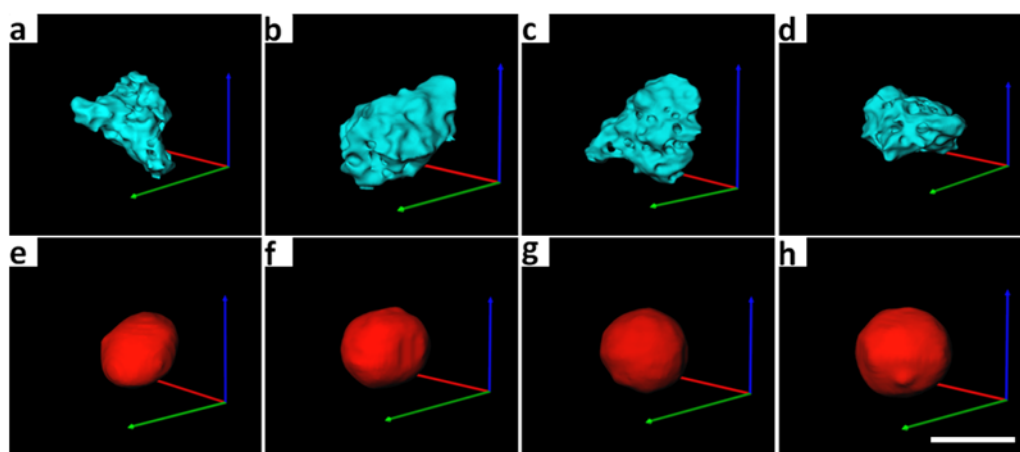
Figure 15 *The morphologies of randomly selected four particles imaged by SR-µCT.*

(a) particle 1, (b) particle 2, (c) particle 3 and (d) particle 4 of the starch granules, (e) particle 1, (f) particle 2, (g) particle 3 and (h) particle 4 of the microcrystalline cellulose granules, the scale bar is 1000 μm.

The characteristics of the two types of particles as determined by SR-μCT also differ in many parameters (Table 2, Table 3). The equivalent diameter is defined as the diameter of a ball of equivalent volume. Width, height and depth represent the side lengths of a minimum sized bounding box for a particle. Depending on the measuring method applied, the particle size is derived from different physical properties (i.e. volume, surface area and equivalent diameter). The results show that the microcrystalline cellulose granules have a smaller particle size compared with the starch granules. In attempting to describe the shape of particles, several parameters including box ratio, volume fraction and sphericity are introduced. Box ratio is the ratio between maximum and minimum side length of the bounding box (box ratio value≥1; values closer to 1 the more spherical the granule). The volume fraction is defined as the volume of a particle divided by the volume of its bounding box (the volume fraction value of a sphere is 0.52; the closer to a value of 0.52 the more spherical the granule). As can be seen, the microcrystalline cellulose and the starch granules differ in that the former is more spherical, whereas the latter is more irregular shaped, with results showing good agreement with the 3D image (Figure 15). These analyses confirm that the characteristics of both spherical and non-spherical granules, including particle size and shape information, can be measured efficiently by SR-μCT. Furthermore, since characterizing individual granule is an important requirement, this investigative process carried out supports this ambition.

Table 2 The characteristics of starch granules obtained by SR-μCT.

starch granules	a	b	c	d
Volume / μm^3	1.40E+08	1.52E+08	1.96E+08	1.46E+08
Surface area /μm^2	1.34E+06	1.40E+06	1.65E+06	1.37E+06
Diameter /μm	646.39	634.87	739.00	686.67
Width /μm	689.18	713.24	765.25	678.43
Height /μm	644.33	660.08	712.19	683.38
Box ratio	0.49	0.51	0.49	0.46
Volume fraction	24.78	25.46	27.70	25.14
Sphericity	0.97	0.98	0.99	0.98

Table 3 The characteristics of microcrystalline cellulose granules obtained by SR-μCT.

microcrystalline cellulose	a	b	c	d
Volume /μm^3	6.36E+08	7.09E+08	1.05E+09	1.13E+09
Surface area /μm^2	8.98E+06	7.38E+06	1.04E+07	1.27E+07
Diameter /μm	1066.93	1106.28	1260.21	1292.61
Width /μm	1712.91	1568.80	1867.80	2301.87
Height /μm	2006.54	1321.27	1656.59	1933.99
Box ratio	1.58	1.19	1.13	2.00
Volume fraction	0.15	0.25	0.18	0.22
Sphericity	0.40	0.52	0.48	0.41

Granular system analysis using statistical methods

Based on characteristic data of about 50 particles, the individual granular systems are described by means of frequency distributions. The individual granular system is highly homogeneous in that the frequency distributions of volume, surface area and sphericity are similar in both upper and lower levels (Figure 16, Figure 17). In comparison with the microcrystalline cellulose granules,

most starch granules are larger with broader volume and surface area distributions. For this reason, the frequency distributions of volume and surface area are not suitable to be applied to distinguish between the two different granular systems. However, the frequency distributions of sphericity are markedly different, lying within relatively narrow ranges (Figure 16c, g, Figure 17c, g). Thus, the microcrystalline cellulose and starch granules can be distinguished from mixed systems by calculating the frequency distribution of sphericity. Depending on the sphericity of each granule, the reconstructed images of granular systems are displayed with different colours. The colour scheme has been chosen such that yellow to red illustrates an increasing and high sphericity whereas green to dark blue corresponds to an increasing and low sphericity. Images show that the individual granular systems are highly homogeneous (Figure 16d, h, Figure 17d, h). The two species have markedly different sphericity, with the yellow to red regions demonstrating higher sphericity of the microcrystalline cellulose granules as compared to the green to blue regions of starch ones.

It is not possible to determine accurately the physical characteristics of all particles since a number of particles cross the boundary of the image. As large particles run a higher risk to cross the boundary, removing all boundary particles from the analysis may induce a bias. In our study, the boundary particles were excluded from the system manually. A minus-sampling edge correction was also applied such that all particles having their centre of the bounding box inside the observation window are completely contained in the image. The statistical evaluation is then confined to these particles.
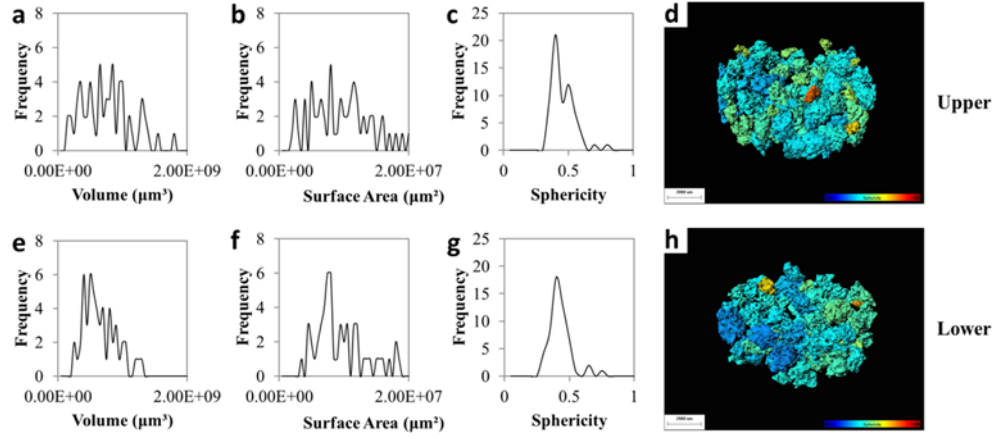
Figure 16 *The frequency distribution and 3D images of individual starch granular system.*

(a-d): Frequency distribution profiles of volume (a), surface area (b) and sphericity (c) and 3D image (d) for starch granules in the upper level of the cylindrical vessel. (e-h): Frequency distribution profiles of volume (e), surface area (f) and sphericity (g) and 3D image (h) for starch granules in the lower level of the cylindrical vessel, the scale bar is 2000 μm and the standard jet colormap indicates the sphericity range from 0.0 to 1.0.
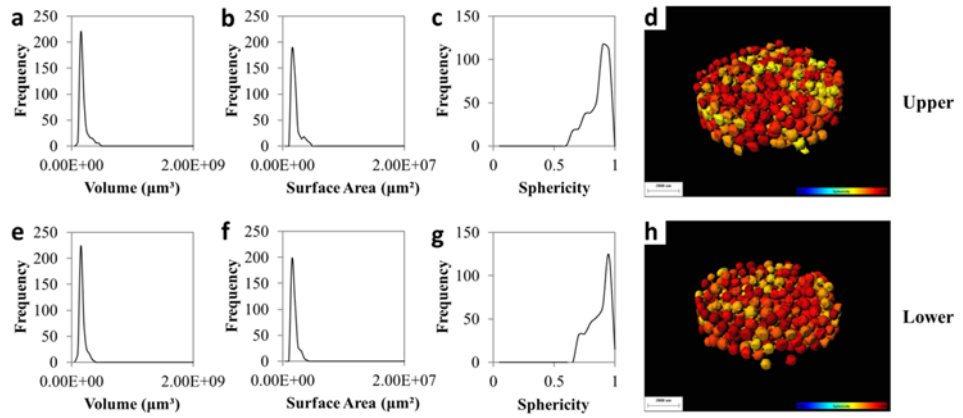
Figure 17 *The frequency distribution and 3D images of individual microcrystalline cellulose granular system.*

(a-d): Frequency distribution profiles of volume (a), surface area (b) and sphericity (c) and 3D image (d) for microcrystalline cellulose granules in the upper level of the cylindrical vessel. (e-h): Frequency distribution profiles of volume (e), surface area (f) and sphericity (g) and 3D image (h) for microcrystalline cellulose granules in the lower level of the cylindrical vessel, the scale bar is 2000 μm and the standard jet colormap indicates the sphericity range from 0.0 to 1.0.

3.1.2 Pellets of multi-particulate dosage form

Multi-particulate solid dosage formulations contain numerous discrete particles (e.g., pellets and granules) that are filled into hard gelatine capsules or compressed into tablets, forming a single dose unit. Multi-unit dosing forms have gained considerable popularity over conventional single unit products for controlled release technology due to the following advantages: a) rapid dispersion in the gastrointestinal tract to maximise drug absorption, reducing peak plasma fluctuations and minimize potential side effects without lowering drug bioavailability; b) reducing susceptibility of dose dumping than reservoir- or matrix-type single-unit dosage forms; c) flexibility during product development because pellets containing different drug substances can be blended to formulate a single dose form. However, although several technologies for the production of multi particulate systems have been designed, thus far the mainstream technologies used industrially are still based on spray-drying, spheronization, and film-coating technology. Limitation of process variables caused by multiple formulation steps can act as technical hurdles in manufacturing reproducibility and reduced product safety and efficacy [31].

Visualisation of surface morphology and internal 3D structure

Tomographic imaging techniques help improve our understanding of the quality, performance and release mechanisms of pharmaceutical dosage forms. In these studies, as mentioned previously the full 3D image is not recorded directly; instead, it is obtained by reconstructing 2D image cross-sections and stacking the reconstructed slices (for detailed information on S 2 Imaging and quantitative characterization of single pellets see S 2). The high-resolution 3D

images obtained from SR-µCT refer in this section to a model that reproduces the morphology and microstructure of a pellet (Figure 18a); the 3D rendering model displays comprehensive detailed structural information on all pellets in the sample. From 2D slice and reconstructed 3D model, voids in pellets are clearly identified. The voids are spherical in shape which is thought to be caused by the volatilization of binder solution in the drying process. A porous pellet and a solid pellet are randomly selected to show the morphological and microstructural information (Figure 18b). The differences in the shape, size, morphology and internal structure of each pellet are clearly visualised, although it was difficult to distinguish the solid pellets from those with voids using only the apparent morphology. Internal void could not be detected without the CT technology.
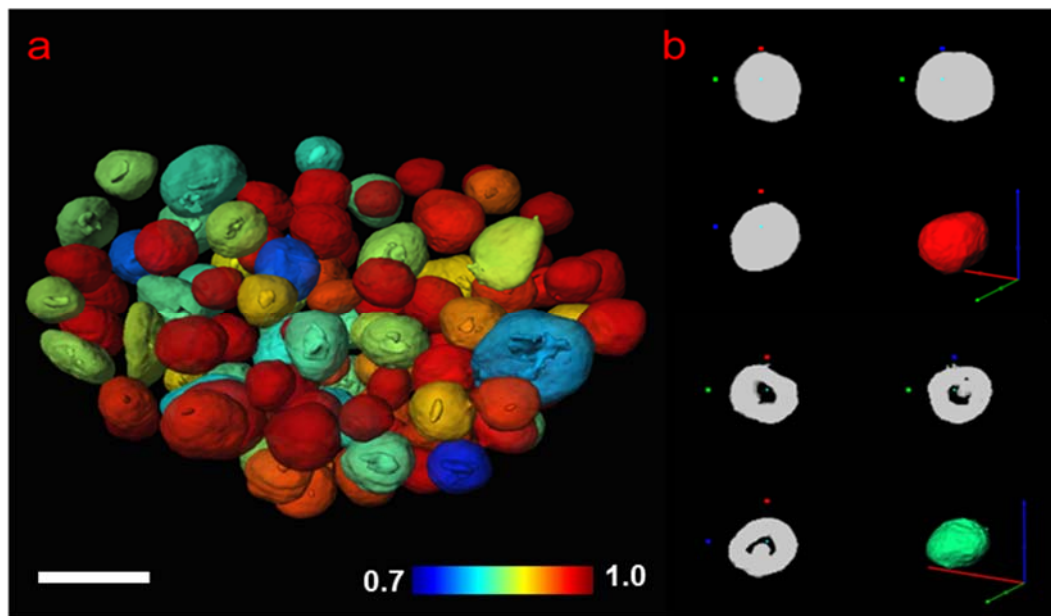
Figure 18 *Characterisation of the pellets.*

 a The reconstructed 3D model of pellets imaged using SR-µCT showed the sphericity with the blue to red regions demonstrating incrementally higher sphericity; b a typical solid pellet and one with a void, the scale bar is 1000 µm and the standard jet colormap indicates the sphericity range from 0.7 to 1.0.

3D Parameter Calculations

The traditional measurement methods for the specific surface area of powdered materials are gas adsorption [32] and the ethylene glycol monoethyl ether method. SR-µCT in contrast provides three-dimensional topographic images on the sub-micrometer scale. Therefore, pellet properties, such as the diameter, the surface roughness and the internal void, can be extracted from these images, clearly visualised and used to calculate the volume and specific surface area for each pellet.

The ability to visualise the microstructures of the individual pellet from the results of the CT scans and 3D reconstructions from samples containing many individual pellets is valuable when investigating the drug release mechanism. When attempting to describe the pellets, approximately 40 steric quantitative parameters can be obtained from the reconstructed model. The most important ten parameters that are closely related to the release profile have been selected by principle component analysis (PCA) and are listed in Table 4. Here the diameter is the diameter of a ball with an equivalent volume and the void fraction is the volume of the void divided by that of the pellet.

Table 4 The names, descriptions and the units of the 3D Parameters

3D parameters	Description	Units
Volume	Volume of the whole pellet	μm^3
Surface area	Surface area of whole pellet	μm^2
Diameter	Equivalent diameter of whole pellet	μm
Sphericity	A measure of how spherical an object is	Dimensionless
Volume of void	Volume of the void	μm^3
Surface area of void	Surface area of the void	μm^2
Void fraction	The volume of voids over the total volume	%
Specific surface area	The surface area per unit volume	μm^{-1}
Surface area without void	Surface area of the pellet without void	μm^2
Drug content in unit volume	The amount of drug in unit volume	$ng/\mu m^3$

Based on the data above, the pellets were different in size and shape from one another within the approximately 1000 pellets in each Tamsulosin sustained release capsule. The total capsule fill of pellet particles is described using a frequency distribution (Figure 19) which shows that the size (volume, surface area and diameter) distributions have a wide range and do not exhibit Gaussian distributions. In addition, most pellets have a value close to 1 for sphericity, while some pellets are still irregular. The specific surface area of most pellets is between 0.007 and 0.035 μm^{-1}. Approximately 50% of the pellets are solid, and the other half have voids with variable volumes and surface area distributions.
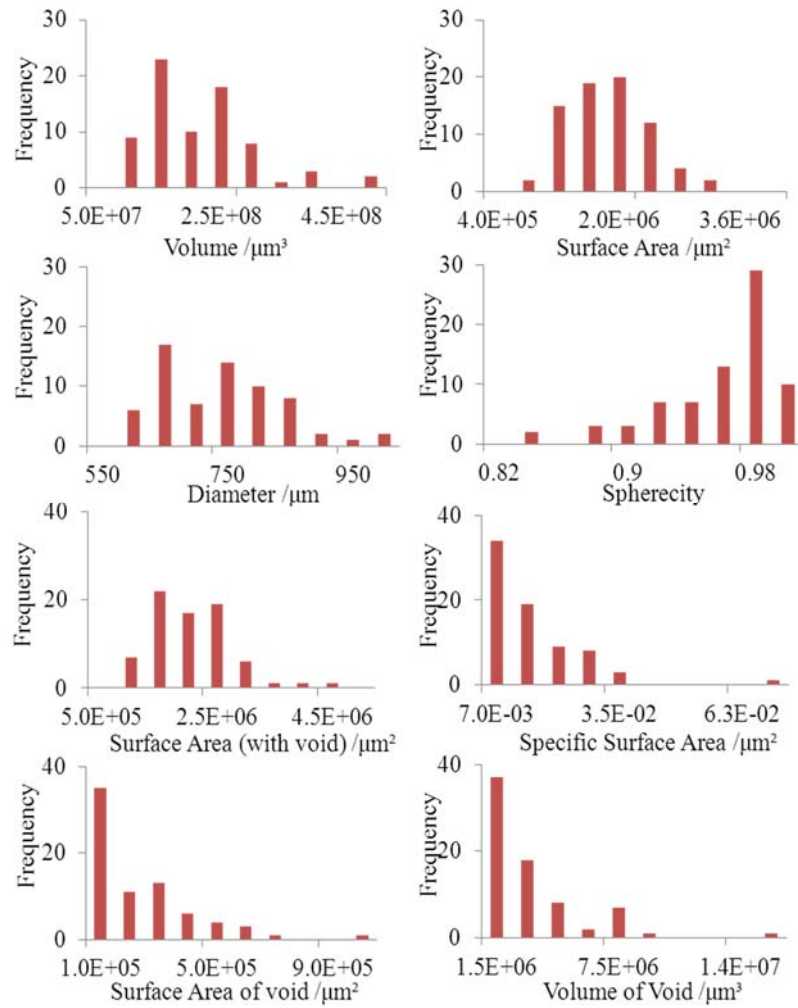
Figure 19 *The frequency distribution for different parameters of the pellets*

In Figure 20, the blue domains represent the pellets with small surface areas, and red domains represent large surface areas. The smaller pellets (with respect to surface area and volume) were more spherical. A few pellets were ovoid in overall shape due to the deformation under pressure during the pellet formation and coating processes. The deviations in size decreased when the particles were more spherical. However, no strong correlation was detected between the void fraction and the other parameters. For example, the void fraction distribution and the diameter showed a random tendency without a significant co-relationship (Figure 20 b).
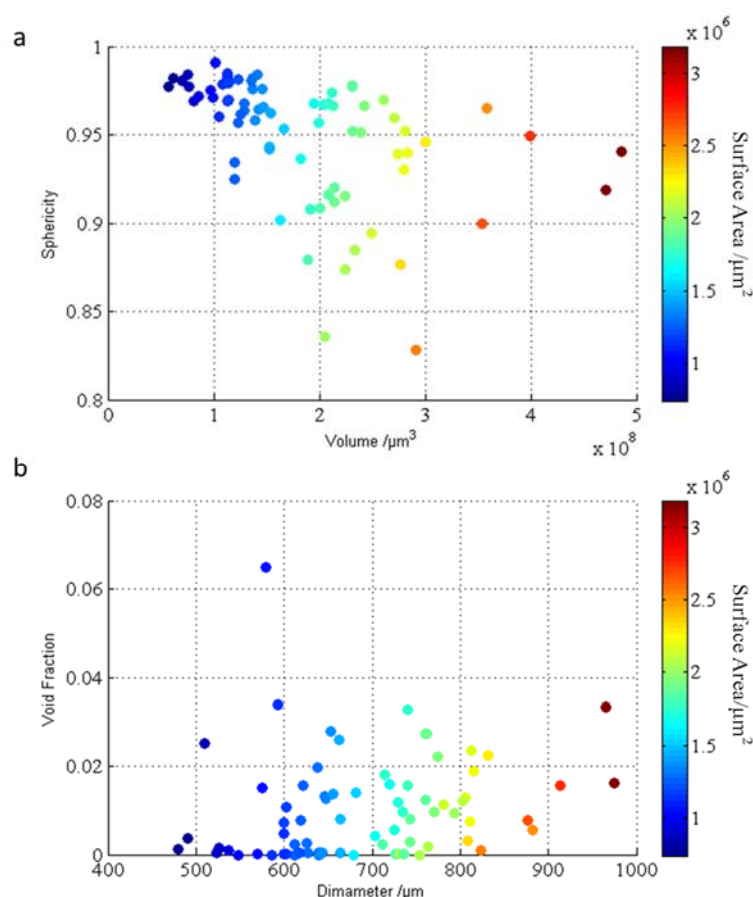
Figure 20 *Correlation between (a) pellet volume and sphericity, (b) diameter and void fraction.*

The colour coding (bar on the right) referred to the surface area of the pellet.

In summary, based on the SR-μCT technique, detailed information regarding the surface morphology, internal 3D structure and quantitative pore characteristics of the pellets were clearly visualised from the 2D monochrome X-ray CT images and reconstructed 3D tomography images.

3.2 Crystal form identification in polymorphic mixtures

Polymorphism is the ability of the atoms and/or molecules of solid material to exist in more than one crystal structure, and can potentially be found in many crystalline materials including polymers, minerals, and metals. Polymorphism is of great theoretical and practical interest for the pharmaceutical industries, since

different polymorphs of the same compound exhibit diverse physicochemical properties of solubility, dissolution rate, stability, and mechanical properties, thereby influencing the bioavailability and therapeutic efficiency of the formulated drug products[33, 34]. Many polymorphic drug substances approved by the regulatory authorities are for one specific polymorph of the compound [35]. However, individual polymorphs may convert to another during manufacturing process and storage, particularly when a metastable form is used and a resulting more stable polymorph is likely to exhibit a lower dissolution rate. Since an amorphous form is thermodynamically less stable than the crystalline form, spontaneous crystallization from an amorphous drug substance may also occur [36, 37]. Therefore, the investigation of crystal polymorphism of active pharmaceutical ingredients (APIs) is of increasing importance to the pharmaceutical industry, either in the early stage of drug discovery research or in the development and manufacture of a drug delivery system.

Several techniques can be applied to identify and characterize solid-state forms and polymorphic composition of APIs in raw materials and dosage forms, such as X-ray diffraction (XRD), thermal methods (including differential scanning calorimetry (DSC), thermal gravimetric analysis (TGA) and isothermal microcalorimetry (IMC)), vibrational spectroscopy (including mid-infrared (IR), near-infrared (NIR), Raman, and terahertz pulsed spectroscopy (TPS)), solid state NMR (SS-NMR), atomic force microscopy (AFM), optical and electron microscopy [38-41]. Whilst powder X-ray diffraction (PXRD) has increasingly been regarded as the definitive test for the crystallographic identification of polymorphs, it can only be used to quantify non-crystalline or second component crystalline material down to levels of 5% [33]. In addition, its use for quantitative

analysis is often marred for samples with complex scattering patterns, since the isolation of the diffraction peaks of the APIs and excipients peaks may be difficult and some low intensity peaks may exist in the background because of the effect of residual solvent in the sample, factors which may interfere with the interpretation of results[33].

For clopidogrel bisulphate (CLP), six polymorphs are known, but only two (form I and form II) are used as therapeutic agents. Form II as well as several solvate forms and amorphous form of the substance are patented, but Form I is now out of patent control and available for generic product development and marketing[42, 43]. As clopidogrel bisulphate polymorphs comprise an enantiotropic system, and Form II is the thermodynamically more stable form at room temperature[44], there is a potential for the occurrence of Form II in Form I both in the production steps and during the storage period. Thus, a suitable analytical technique for the detection and quantification of low levels of the stable form II in the metastable Form I material is needed. A recent publication has reported on the quantitative analysis of clopidogrel bisulphate polymorphs by X-ray powder diffraction[42]. The authors used whole powder pattern decomposition as well as classical direct methods for quantification in the range of 10-80% Form I in Form II. The limit of detection using both methods is in the range of 1-2% of phase content in the mixture. A previous study utilized transmission FT-IR spectroscopy for the quantitative measurement of clopidogrel bisulphate polymorphs[43], by using unique peaks of the forms in the analytical range of 10-90% Form I in Form II. Low levels of Form II in Form I are undetectable because characteristic bands of Form II are not visible in the IR spectra of the mixture below 30%. Recently, vibrational spectroscopic methods

have been developed for quantitative analysis of Form II of clopidogrel bisulphate in Form I and Form II polymorphic mixtures. Results show that both IR and Raman spectroscopy combined with chemometrics are suitable to quantify low levels of Form II in Form I, down to 2 and 3%, respectively, a limit of detection less than 1%[44].

However, it is still a great challenge to identify quantitatively the polymorphs in multi-component mixtures, or with binary mixtures in which the crystalline form of interest is present at a low level. Microscopic methods based on the image acquisition followed by a suitable image-analysis scheme to extract morphological details may be useful tools to quantify the trace amount of polymorphs by morphology. These approaches are likely to prove especially powerful for the characterization of minor phases in mixtures and, provided that a suitable crystallite can be located, the analysis can be performed on exceptionally small amounts of material. The particular value of these methods lies in the possibility it offers for combining imaging, diffraction and spectroscopic data from the same sample, with the potential for simultaneous acquisition of different data types. For example, in scanning mode, direct imaging of the crystal lattice can be coupled with spectroscopic analysis to yield chemical information at the unit cell level; in imaging mode, the technique is routinely used for the identification and characterization of defect structures; and in diffraction mode, detailed investigations of both symmetry and crystal structure are possible [45, 46].

The present study employed synchrotron radiation X-ray computed microtomography (SR-μCT) to devise and develop an accurate and sensitive method for identification and quantification of polymorphs, using forms I and II of clopidogrel bisulphate (CLP) crystal particles as a model (detailed information please refer to: S 3 Crystallographic analysis and reconstruction of CLP polymorphs particles). The SR-μCT was first employed to visualize the morphology and to identify qualitatively CLP I and CLP II. The steric parameters of CLP polymorph particles, such as size, sphericity and surface properties were calculated. Then a new parameter, VBP (Volume bias percentage) was derived which eliminated interference from any other excipients present to achieve the quantitative identification of polymorphs with an in-situ 3D view.

3.2.1 CLP polymorphs characterization

The XRPD profiles of CLP I and II are shown in Figure 21, and these are in good agreement with those reported in literatures [43, 47]. The optical microscopy and SEM images in Figure 21 indicate that particles of the two polymorphs are all polycrystalline rather than individual larger single crystals, but the primary particles within the polycrystalline assemblies of CLP-I particles are smaller and more spherical, in contrast with the larger columnar single primary crystalline units of CLP-II which form an irregular and rough surface for the polycrystalline assembly.
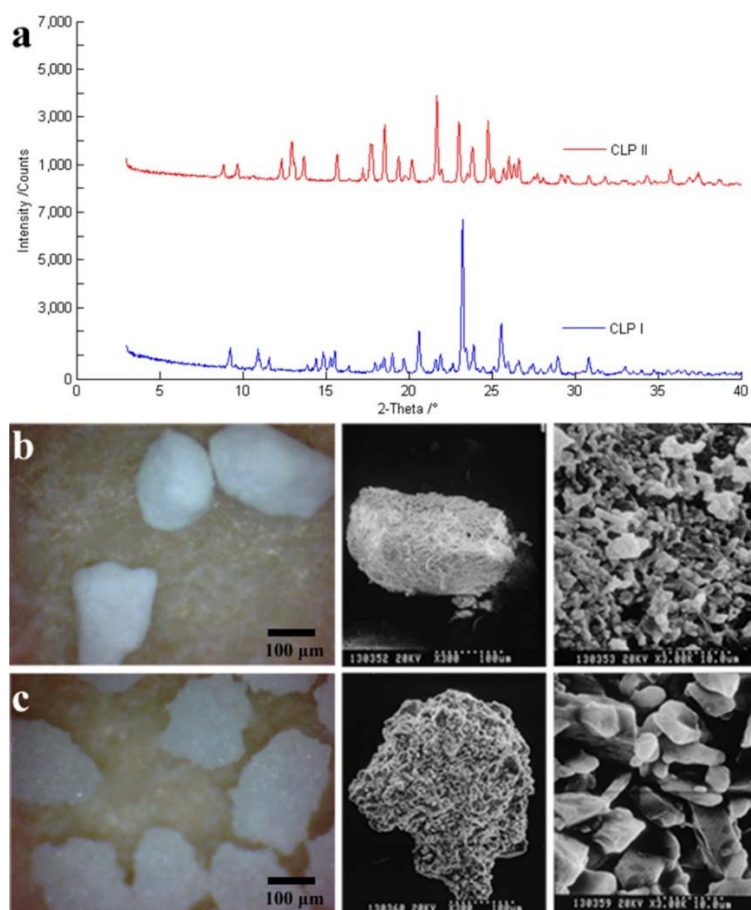
Figure 21 *PXRD and morphology of CLP I and CLP II crystal particles.*

(a) PXRD, (b) optical microscopy and SEM morphology of CLP I, (c) optical microscopy and SEM morphology of CLP II.

Quantitative characterization of the polymorphs.

Based on the analysis of grey values, all of the crystal particles in the sample were extracted by the grey level segmentation. Then the highly resolved tomographic images of CLP I and CLP II with high quality phase contrast were derived for each single particle after 3D reconstruction as shown in Figure 22. Both samples had hundreds of individual microcrystalline particles, which were coloured with pseudo-colour according to the volumes of particles. Then, four particles of each crystal form were randomly selected to show the morphologies and spatial information (Figure 22). As can be seen, the morphologies of the CLP

69

I and CLP II differ from each other. The particle shapes of the two crystal forms were all irregular but the surface of CLP II exhibited a greater degree of topographical roughness than CLP I, a finding which is in good agreement with that shown in the optical microscopy and SEM images.
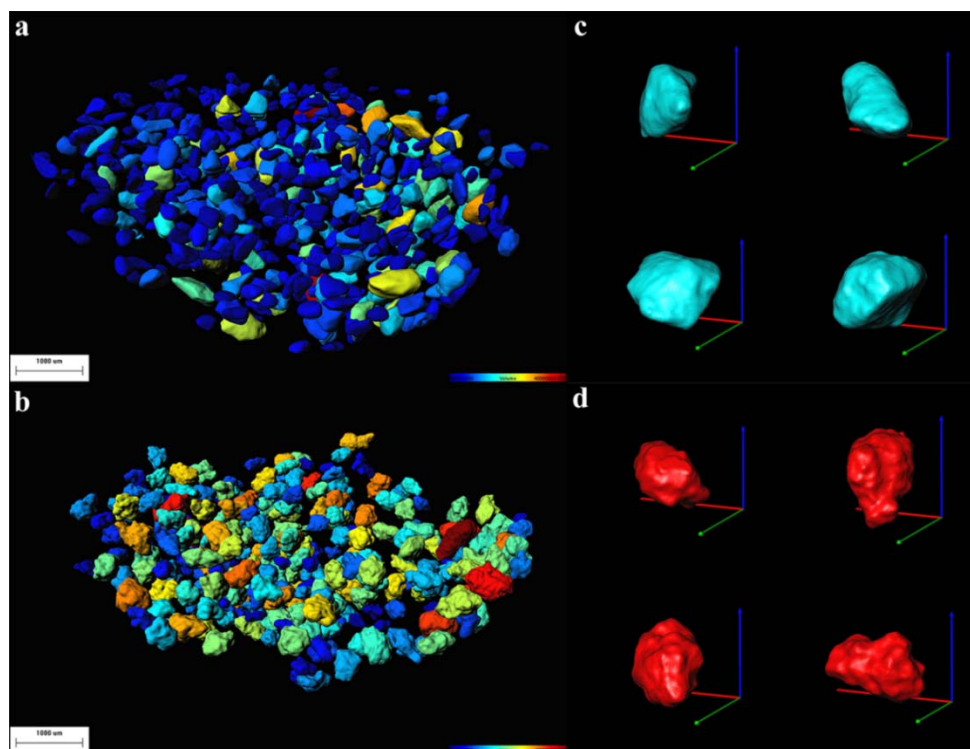
Figure 22 *3D images of individual CLP I and CLP II microcrystalline particles in the capsule after extraction and construction.*

(a) Particles of CLP I and (b) particles of CLP II. Morphologies of randomly selected four particles (c) particles of CLP I and (d) particles of CLP II, the scale bar is 1000 μm and the standard jet colormap indicates the volume range from 6E5 to 2E7.

Based on characteristic data of single particles, the individual primary particles clusters of CLP I and CLP II are described by means of the frequency distribution of volume, surface area, diameter, box ratio, volume fraction, sphericity, radius min and Ferret min, as shown in Figure 23. In comparison with the CLP I particles, the diameter distribution shows that the particle cluster of CLP

II has a larger average diameter, although both clusters were all fractionated with standard sieves prior to scanning (CLP I from 150 µm to 400 µm, CLP II from 200 µm to 400 µm,). This finding is likely to be caused by the difference in morphological properties between the two crystal forms, as can be seen from Figure 23. The CLP I microcrystalline particles are all oblate objects with relatively smooth surfaces in contrast to those of CLP II which are all much more irregular, rough and complex. The particle cluster of CLP I exhibits a wider distribution range in volume, surface area and diameter. The distribution of box ratio indicates that the microcrystalline particles of CLP II are thinner and flatter, and the particle cluster of CLP I shows low values in volume fraction and sphericity as the shape of the particles is more regular. The CLP I particles are narrow and flat in shape with a relatively smooth surface. In comparison with the particle cluster of CLP I, the CLP II shows a smaller radius min and larger Feret min indicating that the shapes of particles are more irregular and have deep voids and pores present on the surface.
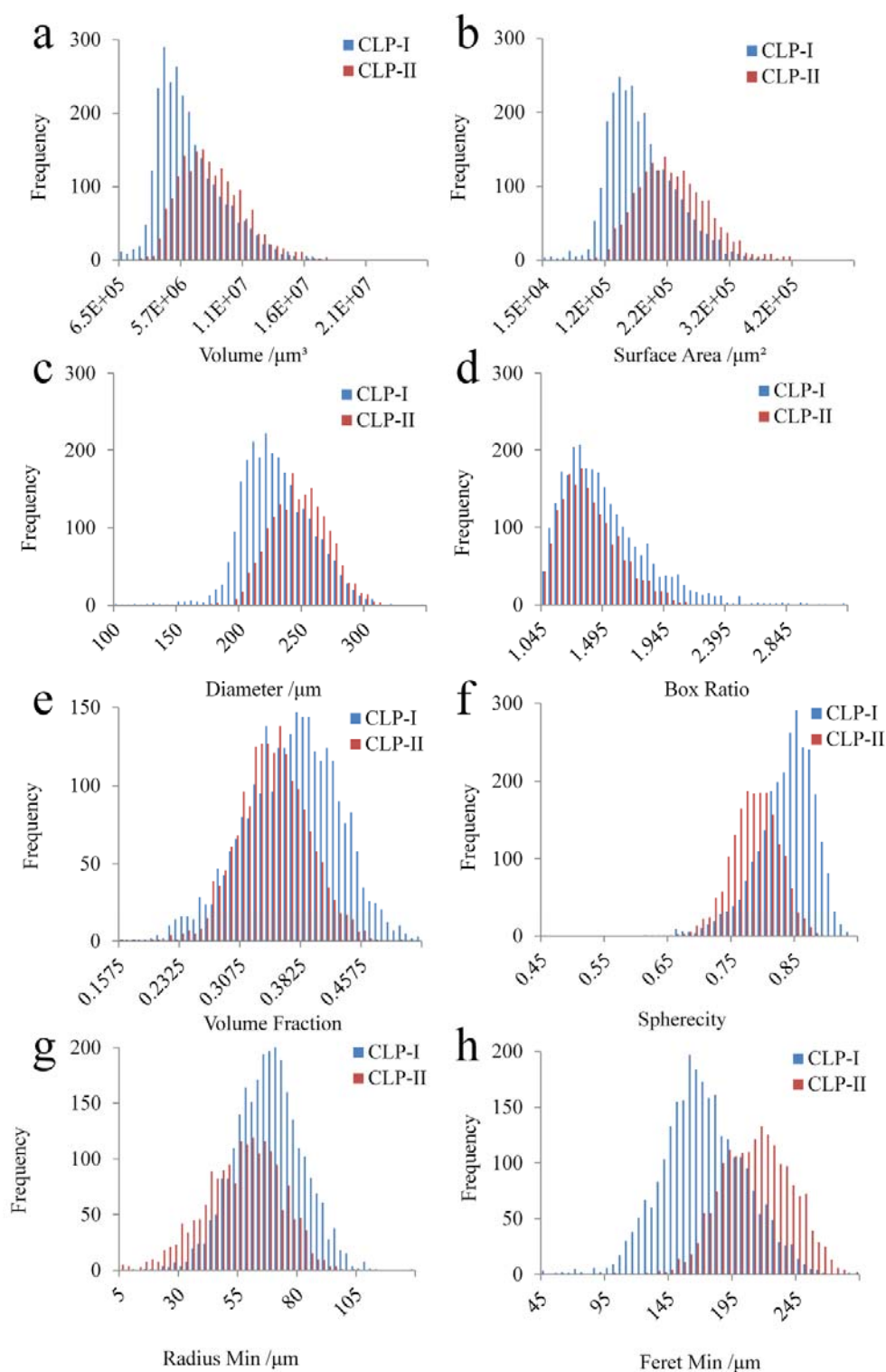
Figure 23 *Number frequency distribution profiles of individual CLP I and CLP II microcrystalline particles.*

(a) Volume, (b) Surface area, (c) Diameter, (d) Box ratio, (e) Volume fraction, (f) Sphericity, (g) Radius min, (h) Feret min (n = 4544).

3.2.2 Quantitative analysis of the surface morphology

In order to establish a quantitative method to identify CLP I and II, relationships between the 3D steric parameters have been investigated. As shown in Figure 24a, the equivalent diameters and the surface area of particles and the trend lines of CLP I and CLP II show a standard cubic relationship, and a degree of differentiation. As the exponential index in the fitting equation for CLP I is 1.992 and close to 2, the integer for a perfect relationship between the diameter and surface area for a sphere. In contrast, the corresponding value for CLP II is 2.1454, higher than for CLP I and larger than 2, demonstrating that the surface of CLP II is more complex and irregular.
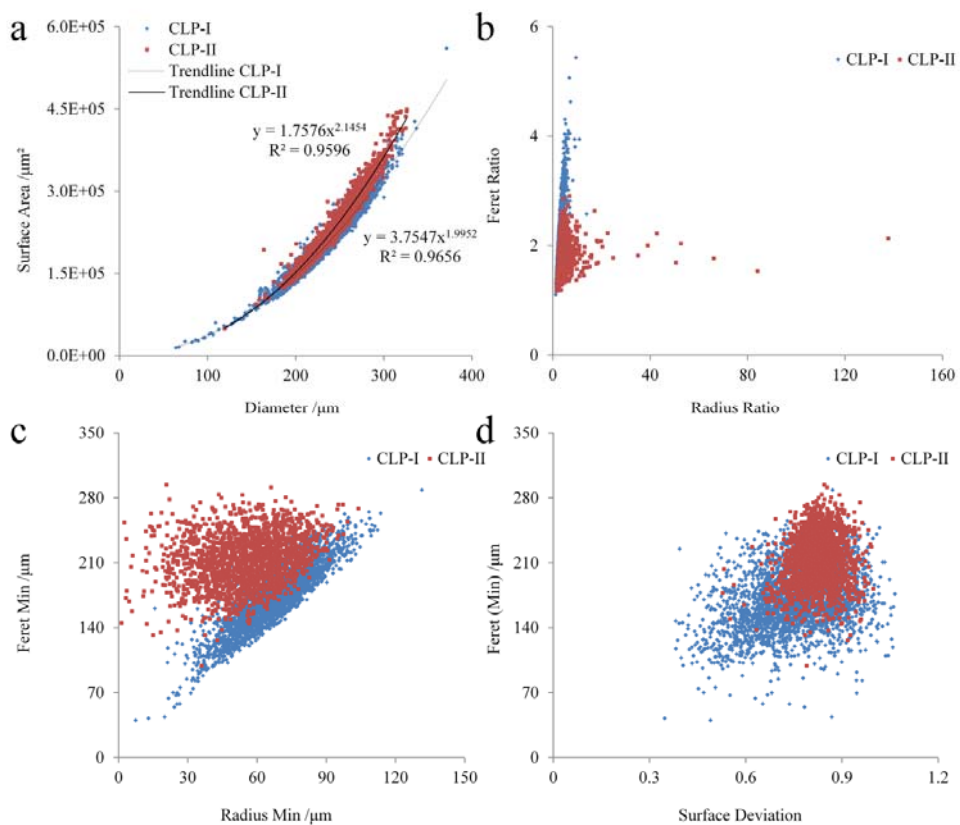
Figure 24 *Relations between different 3D steric parameters.*

(a) Relation between diameter and surface area, (b) Radius ratio and Ferret ratio, (c) Radius min and Ferret min, (d) Surface deviation and ferret min (n = 4544).

73

The same tendency can also be seen from Figure 25 b, c and d, especially the correlation between the Feret min and the Radius min. The correlation for CLP I shows a good linear relationship which indicates that the CLP I microcrystalline particles are regular with a flat facet, whilst on the other hand, the Feret min of CLP II particles has a higher value than the radius min due to the coarser surface and pores distributed on the surface of particle. Furthermore, these findings obtained from the morphological parameters are consistent with the SEM result. However, data for CLP I and II in these correlations are all overlapping and require separation to achieve direct and quantitative polymorphic identification. Thus, new quantitative parameters and methods are needed to be created, developed and validated to characterize the roughness and pattern of surfaces.

3.2.3 Crystal form classification based on surface morphology patterns

A crystal or crystalline solid is a solid material whose constituent atoms, molecules, or ions are arranged in an ordered pattern extending in all three spatial dimensions form a periodic arrangement. In addition to their microscopic structure, large crystals are usually identifiable by their macroscopic geometrical shape, consisting of flat faces with specific characteristic orientations.

An ideal crystal is a single crystal with a perfectly regular lattice in regular shapes, consisting of flat faces (also called facets) which are oriented in a specific way. In reality, a crystal particle's external shape is determined by the crystal structure (which restricts the possible facet orientations), the specific crystal chemistry and bonding (which may favour some facet types over others), and the

conditions under which the crystal is formed. In practice and common use, individual particles are composed of a number of smaller crystals – a microcrystalline assembly - and are not regular in morphology. Therefore, we propose a hypothesis: that the surface morphology of typical particles composed of microcrystals has a high specificity which is different from other polymorphs of the same chemical compound. Thereby the shape pattern of the surface is closely related and determined by the crystal form as polymorphs frequently exhibit some difference in single crystal shape and the aggregation mode whereby single crystals form microcrystalline assemblies. It is proposed that these patterns can be used for the classification of the polymorph.

In order to classify quantitatively the crystal form based on the morphological property of particles, a new method has been developed for the characterization of the pattern of the particles' surfaces. At first, after the 3D model construction, every particle in the sample was extracted individually and moved into a sufficiently empty computing space; secondly, the original 3D model was processed by the low pass filter algorithm at the degree of $9\times9\times9$ (the quantitative analysis of surface pattern indicated that the sizes of pores distributed on the surface were close to $9\times9\times9$) for smoothing the surface to generate a new smoothed 3D model; then the smoothed model was sliced into a stack of 2D slices, and the original slice was subtracted from the new stack; finally, the residual part after subtraction was used to construct the deviation model. The sum volume of all objects in the model divided by the volume of original model was defined as the Volume Bias for the characterization of surface roughness (Figure 25).
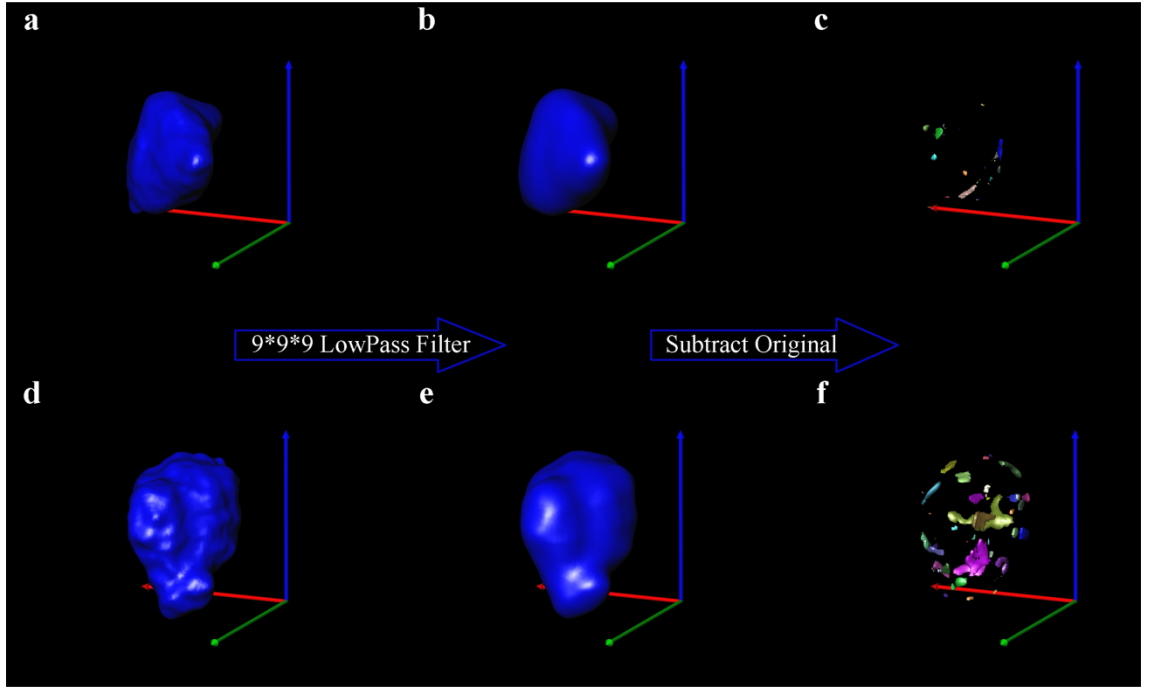
Figure 25 *Quantitative characterization of the particles' surface pattern.*

The original 3D model of the CLP I (a) and CLP II (d) particles, the 3D model of the CLP I (b) and CLP II (e) particles after smooth with 9*9*9 low pass filter algorithm, volume bias of the CLP I (c) and CLP II (f) particles.

$$VBP = \sum_{i,j,k \in Mask}[Lowpass_{Averaging\ 9\times9\times9}(SA) - SA]_{i,j,k} / \sum_{i,j,k \in Mask} SA_{i,j,k} \times 100\% \quad \textbf{Eq. (1)}$$

Where

   VBP is the Volume Bias Percentage based on Surface Smoothing.

   SA is the original 3D matrix of crystal particle.

   $\sum_{i,j,k \in Mask} SA_{i,j,k}$ is the volume of crystal particle above the threshold value.

   $Lowpass_{Averaging\ 9\times9\times9}(SA)$ is the lowpass filtering of 3D matrix of

crystal particle with the averaging algorithm at the size of $9\times9\times9$.

   In the experiment, totally 4544 (include 2710 particles of CLP I and 1834 particles CLP II) particles have been scanned, and the respective VBP values were calculated. As shown in Figure 26, the VBP values clustered into two classes with values of CLP II generally higher than those of CLP I. The volume bias values

76

of CLP I have a narrow distribution range, and most are close to 0. In contrast, the distribution of volume bias values of CLP II is wide and several particles have high values. After analysis, the highest 1% of CLP I and the lowest 1% of CLP II (totally 45 particles include 27 CLP I and 18 CLP II) VBP values were used to calculate an average value. In this way the average value of 0.004915 has been obtained and was selected as the threshold value for the classification of two crystal polymorphs. The overall accuracy is 99.91% (4 particles misidentified out of the total of 4544) as there are 2 CLP I and 2 CLP II particles misidentified by the VBP value. As listed in the Table 5, the one by one matching analysis indicates the average accuracy was 99.82±0.21 % at 9 different polymorphic mix ratios. The lowest detectable limit has been found to be 1%.
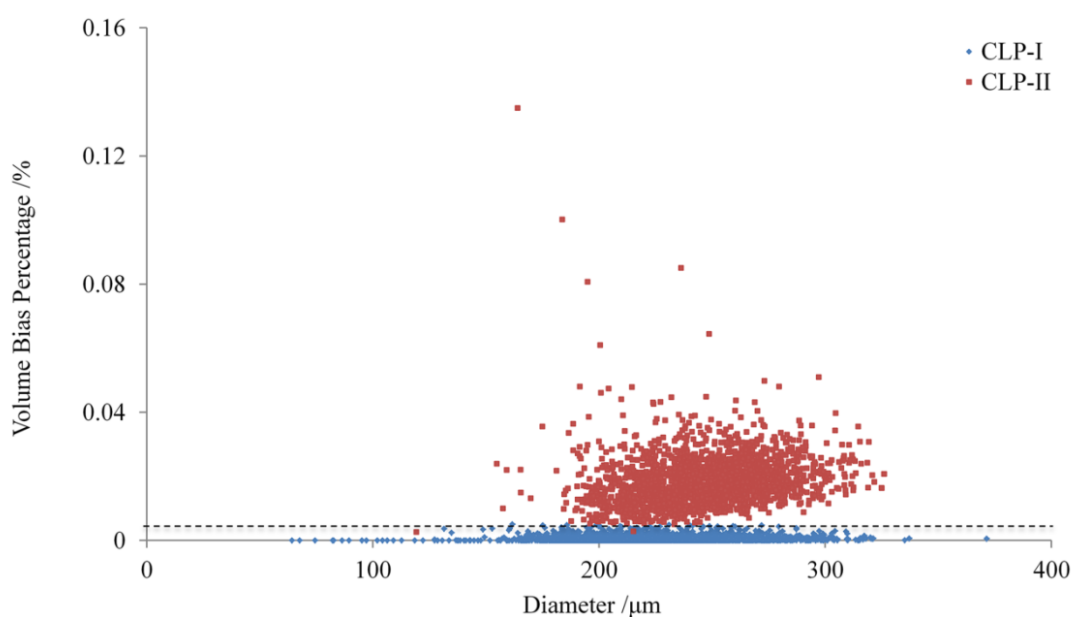
Figure 26 *Volume bias analysis of 4544 CLP I (n = 2710) and CLP II (n = 1834) particles*

With SR-µCT, the high resolution structure of every single particle can be visualized from the 3D X-ray CT images. With the N-in-One analysis, from only one CT scan, the 3D morphological information of hundreds even thousands of crystal particles can be obtained and a wide range of 3D quantitative parameters

can also be calculated. Generally, the solid form morphology of a chemical compound is defined in terms of its molecular structure and arrangement. Besides the crystal form, crystal habit describes the shape and aggregates that a certain compound is likely to form. The crystal morphology is also an important character for the identification of crystal form, whereas the challenge is the quantitative characterization of the 3D morphology of crystalline particles. In this research, the concept of volume bias percentage (VBP) has been proposed for the quantitative characterization of the surface roughness and the surface morphology pattern. Thus a new method has been developed for the quantitative identification of the crystal form of clopidogrel crystal at a high accuracy level (above 99.91%); in a wide particle size range of microcrystalline particles (the diameter of samples in our study covering from 150 μm to 400 μm). Importantly, interference of excipients, which is commonly found, can be avoided a fact which demonstrates an advantage of this technique over, other polymorph identification methods.

3.3 The internal micro-structure of tablets

3.3.1 Micro-structure of Osmotic Pump Tablets

The clinical performance of a drug molecule is not only dependent on its inherent therapeutic activity, but also largely dependent on the speed and extent with which it is delivered to the site of action by means of a drug delivery system (DDS) [48, 49] . Oral controlled release systems hold the major market share for modified release systems because of the ease of administration and patient compliance. The well-designed drug delivery systems provide desired drug

concentration at the absorption site, maintaining the plasma drug level within the therapeutic range for a period of time, and hence can reduce the dosing frequency and adverse side effects to a minimum [50-52].

Among the various oral controlled drug delivery systems, osmotic drug delivery systems (ODDS) delivering active agents by constant inner osmotic pressure, have received special attention [53]. ODDS' have many advantages over other oral controlled drug delivery systems. The zero-order drug release kinetics of ODDS is neither dependent on the drug chemical properties, nor the patient's physiological factors nor concomitant food intake [54]. The drug release kinetics of the ODDS shows dependency on formulation factors, including the solubility of drugs within the tablet core, the osmotic pressure of the core component(s), the semi-permeable membrane characteristics, and the delivery orifice size [55].

Recently, advances has been reported on the design of ODDS, from single chamber osmotic pumps to multiple chamber osmotic pumps [56]. More than thirty ODDS products have been developed and launched in the market [57] and more than two hundred patents and numerous publications have reported on formulation aspects, clinical results and safety aspects [58-62]. Whilst the tablet structure is obviously the primary physical characteristic of the ODDS, few research attempted to visualize the internal structure and the dynamic changes of the ODDS tablet core during the drug release process. Methods for detailed information please refer to S 6 Pre-treatment of felodipine osmotic pump tablet.

Visualization of the surface morphology and the internal 3D structure

Figure 27 shows the 2D monochrome X-ray CT images of felodipine MOTS at different sampling time (0.5, 1.0, 3.0, 6.0 and 8.0 h) during dissolution testing. The semi-permeable membrane, the tablet core, and the drug delivery orifices have been visualized. The small voids generated during the tablet processing are also visible at the tablet core (image A). From Figure 27 (image D at 3.0 h), it is also observed that the solid content is detached from the tablet core with associated erosion and swelling. The surface properties of the tablet shell maintain the original morphology up to 8.0 h, there is evidence of collapses at the surface of the tablet shells.

As shown in Figure 27, most of the tablet core remains as a solid or semi-solid form with cracks emerging at 0.5 and 1.0 h. At 3.0 and 6.0 h, the tablet core disaggregates and several voids are generated and become increasingly larger along the side adjacent to the drug delivery orifice. At 8.0 h, the majority of the content of the tablet core has dissolved and passed out of the orifice. It is interesting to observe that the shape of the remaining tablet core varies irregularly, a feature which is different from the concept a formulation scientist might imagine. It is also observed that some aggregates adhered to the internal wall of the tablet shell at 8.0 h and 10.0 h, a feature which partially correlated with the release percentages of felodipine at 8.0 h and 10.0 h as 73 % and 82.4 %.
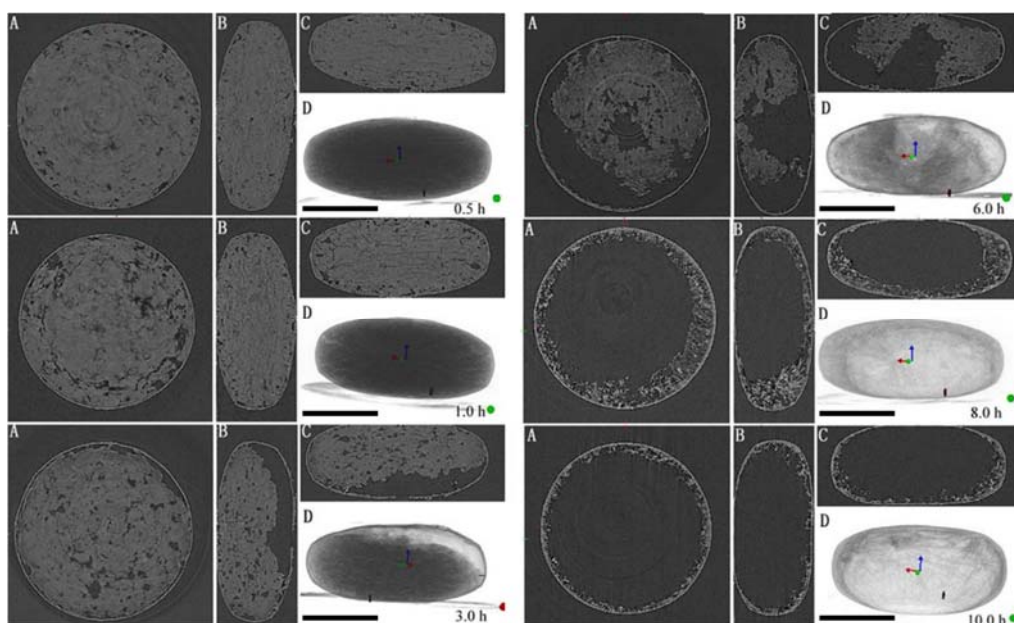
Figure 27 *2D monochrome X-ray CT images of felodipine MOTS viewing from different aspects*

(A: top; B: front; C: back; D: the reconstructed image; air appears dark, grey represents the solid moiety of the tablet core, grey edge represents the semi-permeable membrane, the scale bar is 5mm).

Figure 28 illustrates the reconstructed 3D tomographic images at different release time points, demonstrating the dynamic changing of the internal 3D structure characteristics of the felodipine MOTS. The shape of the tablet is elliptic at 0.5 and 1.0 h. With the continuing hydration of the tablet core, the initial regular shapes of the cores change into more irregular forms with several voids appearing after 3.0 h. Interestingly, the changes in shape at positions near the delivery orifices are more marked than that at other locations, suggesting the release of felodipine near the delivery orifices is faster than from other regions.
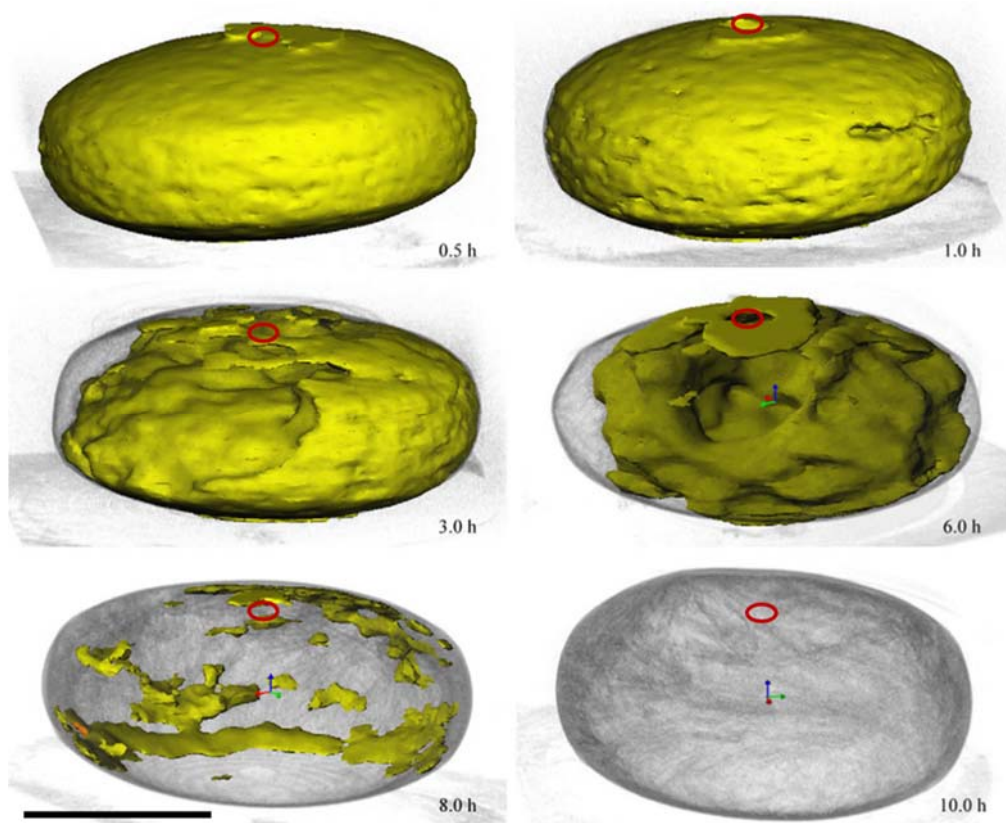
Figure 28 *Reconstructed three dimensional images of felodipine MOTS at different sampling time.*

(the red circles indicate the orifices, the scale bar is 5mm, yellow represents the solid moiety of the tablet core, air appears grey (after reconstruction, some moiety in Figure 27 is not seen in Figure 28)).

In summary, based on the SR-μCT technique, the surface morphology, the internal 3D structure of the MOTS and their changing characteristics are clearly visualized from the 2D monochrome X-ray CT images and the reconstructed 3D tomographic images.

3.3.2 Micro-structure of Swellable Sustained Release Matrix Tablets

Among a variety of oral controlled release drug delivery systems, water swellable matrix systems, particularly those containing hydroxypropyl

methylcellulose (HPMC), are widely used due to the relative simplicity of formulation compositions, ease of manufacturing, and low cost, as well as acceptance by regulatory authorities and applicability to drugs with a wide range of dose and solubility [63, 64].

Much attention has been given to the mechanism governing the transport of solutes. In recent articles, mathematical models have been reviewed which describe drug release from tablets with HPMC matrices [65]. Diffusion equations for a semi-infinite medium were also proposed [66, 67]. Subsequently, a model accounting for both the volume change of the swellable tablet upon contact with the aqueous medium and the countercurrent diffusion of the solute was developed [68]. Following the work on the swelling and dissolution behaviour of the polymeric matrix systems [69, 70], it was found that the thickness of the continuously forming hydration layer upon water penetration into the matrix was proportional to the square root of time when the swelling front was moved faster than the eroding front. Constant thickness of the hydration layer and zero order drug release could be achieved when swelling and erosion fronts synchronized their movements [71]. More recently, the importance of the diffusion front, the interface between the remaining undissolved drug and the dissolved drug in the hydration layer, has been highlighted [72]. The authors postulated that erosion of the matrix was the rate-limiting step for the release of poorly water-soluble drugs whilst for highly soluble drugs, the rate-limiting step was water penetration [73] or diffusion [74].

SR-μCT has also been employed to investigate tablet swelling in real time by following the movements of embedded glass microsphere tracers [75]. Axial expansion of tablets has been observed, which may be due to mechanical

relaxation of residual compaction stresses. This expansion appears to be accompanied by extensive bubble formation, which may retard water penetration into the tablets. Whilst this methodology can characterize the swelling behaviour of gel-forming formulations in real time, water in the swelling medium may interfere with the image acquisition.

A set of two dimensional monochrome projections are presented in Figure 29 A to show the surface morphology and the hydration layer of swollen felodipine HPMC matrix tablets. The hydration layer, the glassy tablet core, the relative movement of the erosion and swelling fronts with time, are clearly visible. The images also show the microstructures and the changes in the core with time. The HPMC matrix swells following absorption of water resulting in the increase of the matrix dimensions. After 0.5 h, the hydration layer is visible and grows gradually with time. After 5.0 h, the thickness of hydration layer is reduced. The size of the glassy core reaches a maximum at 6.0 h, and then reduces as the polymer hydrates to a greater extent. These phenomenon are consistent with the finding of the gravimetric analysis (Figure 29). After 8.0 h the matrix is entirely hydrated with no core remaining. Over the period from 1.0 h to 6.0 h, the thickness of the hydration layer exhibits only minor changes indicating the constant release rate of the felodipine HPMC matrix tablets over this time period.
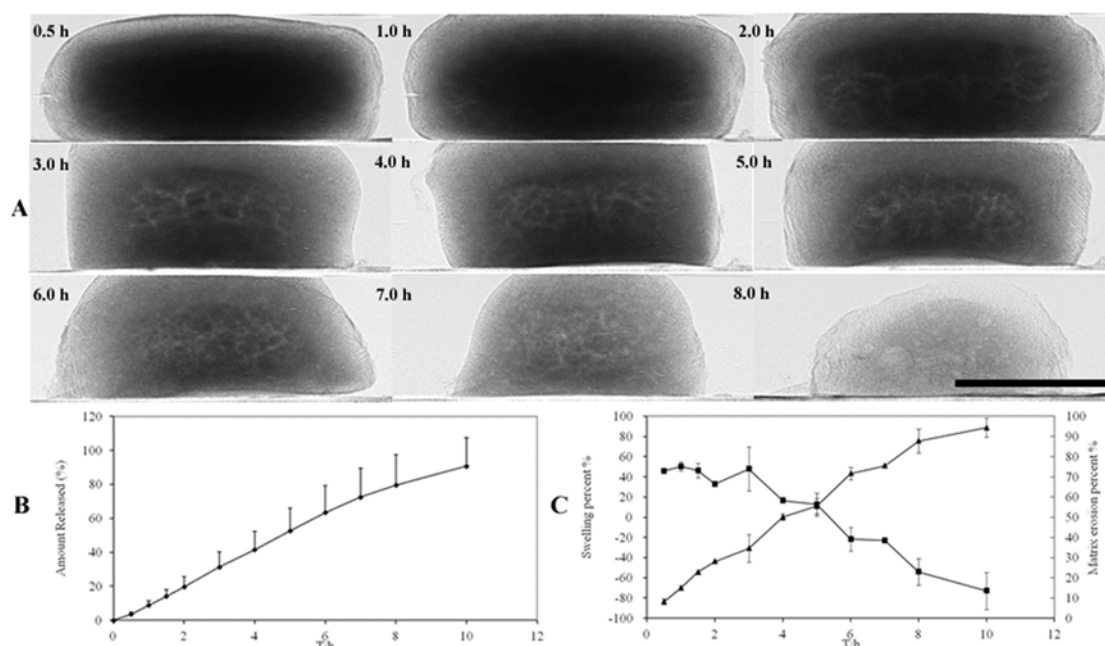
Figure 29 *In vitro dissolution, hydration and erosion of felodipine sustained release tablets.*

(*A*) Dissolution profile. Error bars indicate the SD (n=6). (*B*) Percentage of weight gain (■) and mass loss (▲). (*C*) 2D monochrome X-ray CT images during drug dissolution. Error bars indicate the SD (n=3), the scale bar is 5mm.

Reconstructed three dimensional structures of felodipine tablets are created with segmented slices, as shown in Figure 30 A. The length, width, height, volume and the surface area values of the whole tablet are shown in Figure 30 B. The length, width and height of the tablet all increase within the first 1.0 h as the tablet swells following its contact with the dissolution medium. The length and width then start to decrease from 2.0 h onwards as the HPMC matrix erodes. The height of the tablet, however, remains the same. The volume and surface area of the tablet reduced with time.
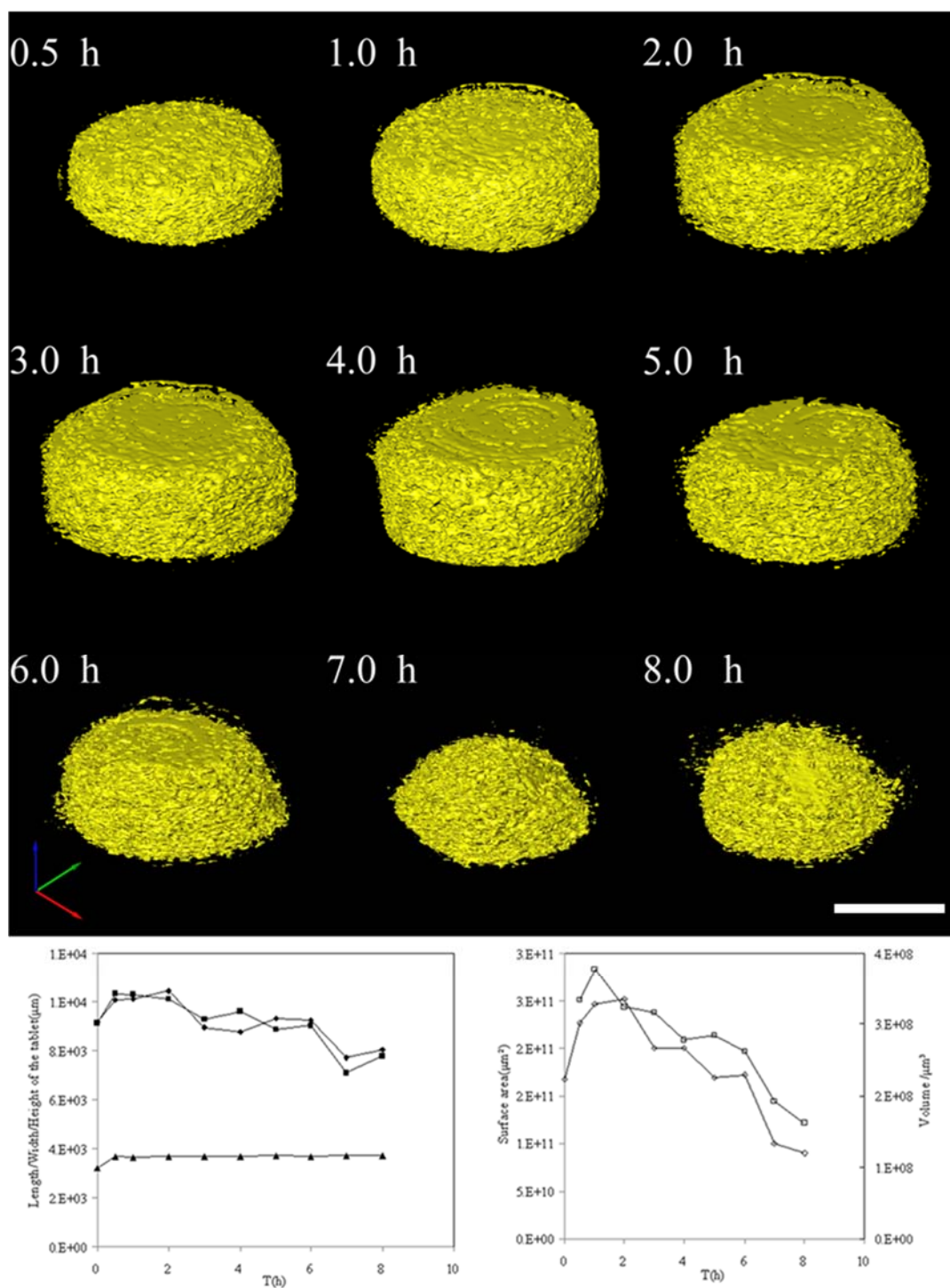
Figure 30 *Changes to internal structures of the whole tablet during drug dissolution.*

(*A*) Reconstructed three dimensional images. (*B*) Volume (*) and surface area (□) values. (*C*)

Length (◆), width (■) and height (▲), the scale bar is 5 mm.

The total projected images are reconstructed using the software developed by SSRF to perform a direct filtered back-projection algorithm [76]. In order to enhance the quality of reconstructed slices, the X-TRACT SSRF CWS x64 (Commonwealth Scientific and Industrial Research Organization, Australia, http://www.ts-imaging.net/Default.aspx) is used for phase contrast extraction. The reconstructed slice stack is converted into 8 bit greyscale format and re-sliced vertically. Then, the vertical slices of tablets at different time points (include the well hydrated tablets and the tablet with totally dried core) are analysed to determine the threshold grey values to distinguish the erosion diffusion, the diffusion front and the swelling front. The quantitative criterion to distinguish the erosion front, the diffusion front and the swelling front is exemplified by the sample at 0.5 h (Figure 31).
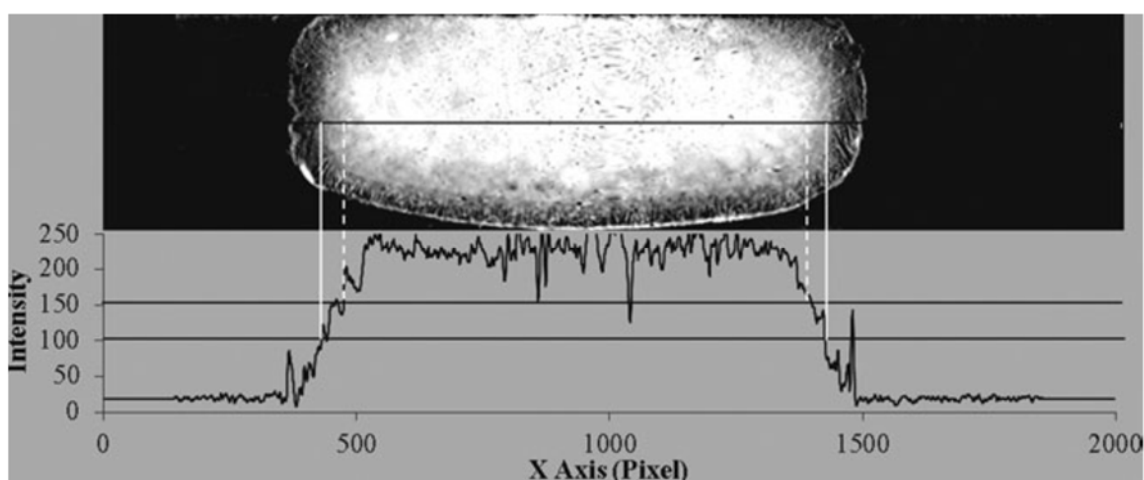
Figure 31 *The quantitative criterion to distinguish the erosion front, the diffusion front, and the swelling front*

(With the line profile of vertical slice of the sample at 0.5 h, the front with grey value of 18 is the erosion front, 100 is the diffusion front, and 150 is the swelling front; the intermediate portion between the erosion front and the swelling front is the hydration layer)

As shown in Figure 30, the completely hydrated erosion layer has a grey value from the background value from 18 to the value of 100; the grey value between 100 and 150 is the partially hydrated hydration layer and the glassy layer has a grey value above 150. Thus, the front with grey value of 18 is the erosion front, that with a value of 100 is the diffusion front, and the swelling front is shown by the layer with a grey value of 150. The intermediate portion between the erosion front and the swelling front is the hydration layer.

The quarter view of the hydration layer is shown in Figure 32 together with plots of the volume of the hydration layer and the surface area of the hydration layer with time. The reduction in the volume of the hydration layer is slower than that of the whole tablet, indicating that the drug release rate is influenced by matrix erosion.
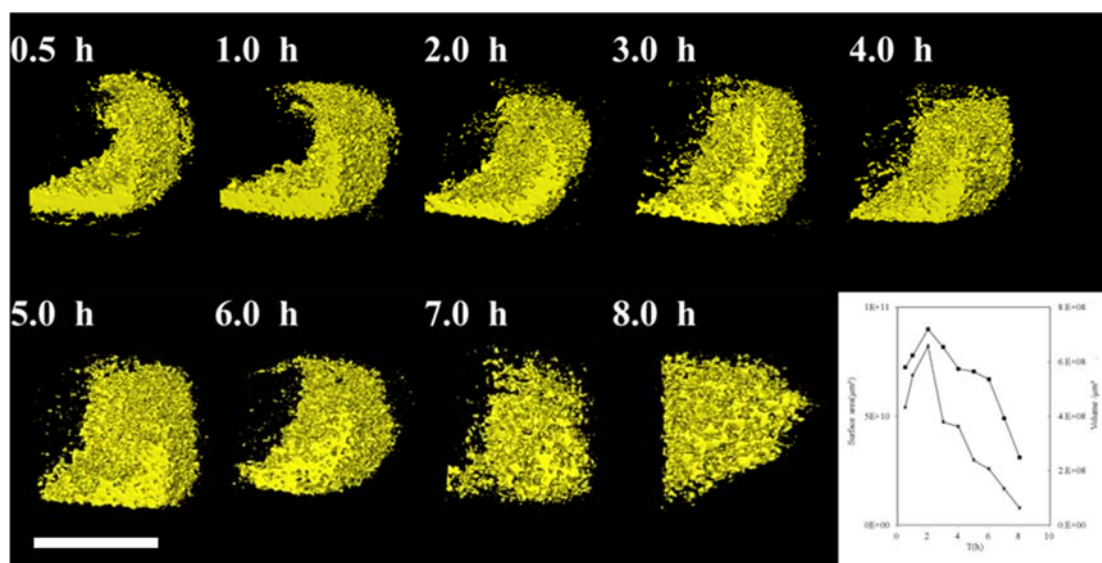
Figure 32 *Visualization and quantitative analysis of the hydration dynamics during drug dissolution.*

(*A*) Reconstructed three dimensional images of the hydration layer. (*B*) Volume (∗) and surface area (□) values of the hydration layer, the scale bar is 5 mm.

In summary, based on the SR-µCT technique, changes in the surface morphology, the internal 3D structure of the tablets and the hydration layer can be clearly visualized from the 2D monochrome X-ray CT images and the reconstructed 3D tomographic images.

General comments

The findings presented in this chapter demonstrate the great potential of SR-µCT for improving understanding of solid pharmaceutical structures in different kinds of tablets and granular materials during manufacturing. Granular samples of microcrystalline cellulose granules, starch granules, pellets and crystal particles were characterized with particle distribution by calculating many quantitative parameters and the frequency distribution. With a statistic method for testing sphericity, spherical cellulose and irregular starch granules were distinguished even though there's bare difference in grey values. Most challenging is that, with the high-precision quantitative parameters generated from the high resolved 3D structures, Volume Bias Percentage based on Surface Smoothing (VBP) was successfully developed. Based on the VBP method, minor differences between the two kinds of irregular rough crystal particles have been quantified for the identification of the polymorphs of clopidogrel bisulphate with a total matching rate of 99.91% and a lowest detectable limit of 1%. The microstructures and the surface morphology of osmotic pump tablets and swellable matrix tablets were investigated. The steric structures with high spatial complexity were visualized and characterized quantitatively. In chapter 4, studies are focused on pharmaceutical processes including mixing, tableting and laser

drilling. With the quantitative characterization method, the interactions between the microstructure and the processing parameters investigated to provide a further understanding of typical pharmaceutical manufacturing.

Chapter 4

Evaluation of Pharmaceutical Processes

-The Intermediate Structure during

Processing

4.1 Structure profiling of mixing and segregation of granules

In this section, synchrotron radiation X-ray computed microtomography (SR-µCT) was used to investigate mixing and segregation of a model two-component system, consisting of powdered microcrystalline cellulose and starch granules, blended in a cylindrical vessel. Compared with the conventional X-ray computed microtomography, the synchrotron radiation light source usually provides 2 higher orders of photon flux in relative parallel beam morphology. Moreover, SR-µCT permits the rapid acquisition of data with high intensity and strong collimation via a high specification detector [14, 77]. This investigation uses the results of SR-µCT to obtain characteristics of particles such as average size, sphericity and surface area collectively, with an in-situ 3D view to achieve a greater understanding of granular behaviour. Furthermore, statistical analyses of the particle parameters are used to investigate particle distribution and dynamics of granular systems. Thus, this study aims to develop a characterization method with SR-µCT, which can measure morphological characteristics and monitor blend homogeneity of the particle systems, for use in optimizing mixing processes of pharmaceutical production.

4.1.1 Homogeneity measurement of two-component systems

Details of the preparation and physical properties of the two sets of granules have been given in S 1. Prior to measuring the blend homogeneity, the microcrystalline cellulose and the starch granules were filled into the cylindrical vessel (with a diameter about 10.0 mm) with initially segregated fractions. They were loaded along the longitudinal axis, each with a volume of 0.5 ml and total

volume was 1.0ml. Two granular systems were composed of microcrystalline cellulose granules loaded first and the starch granules followed. The total height of sample after loading in the cylindrical vessel was 13.0 mm.

For further experiments, the longitudinal axis of the cylindrical container was inclined at an angle to a horizontal axis of rotation manually to simulate a pattern of mixing (Figure 33 a). Rotation speed (V_R) was set at 30 rotations per minute (rpm). To study the influence of the number of rotations, the cylindrical container was rotated for 5 and 20 seconds (s). Then, samples at the upper, middle and lower levels of the container were imaged in an upright position within the X-ray light beam Figure 33 b). In consideration of the maximum height of X-ray beam, both the heights of the acquisition window for the samples were set as 3315 μm.

(a)   (b)
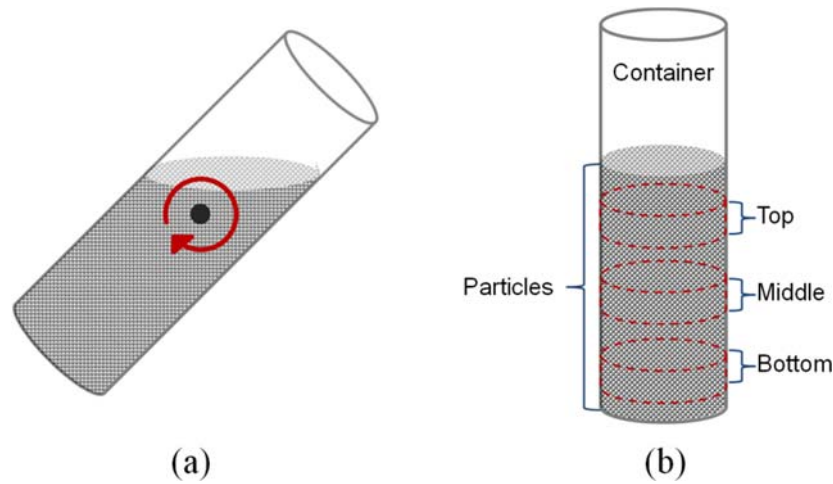
Figure 33 *The schematic diagram of sample pretreatment and image acquisition.*

 (a) mixing process, (b) imaging process.

The sample which was rotated for 20 s in the previous step was then vibrated by shaking to simulate a pattern of material handling. To investigate the influence of the time of vibration, the mixed granular system was vertically vibrated for 5 and 20 s by the shaker, with vibration speed (V_V) of 2000 rpm. Then, as before,

samples at the upper, middle and lower levels of the container were scanned in an upright position within the X-ray beam and each height of the acquisition window for the samples was set as 3315 µm.

Mixing index

A mixing index is frequently used to describe the degree of mixing in powder blends quantitatively. Many definitions and mixing indexes, usually based on the standard deviation of component content in samples of the mixture, have been proposed to describe the difference in composition throughout the mixture [22]. Considering Np particles in the upper, middle and lower levels in total, the arithmetic mean of sphericity value is given as follows:

$$\bar{s} = \frac{1}{N_P} \sum_{i=1}^{N_P} s_i \qquad\qquad \textbf{Eq. (2)}$$

where s_i is the ith value of s, which represents a sphericity of the particle, N_l particles in one level. The sample variance of a single level is given as follows:

$$\sigma^2 = \frac{1}{N_l-1} \sum_{i=1}^{N_l} (s_i - \bar{s})^2 \qquad\qquad \textbf{Eq. (3)}$$

In order to quantify the effect of mixing by image analysis, we calculated a numerical index S, defined as follows:

$$S = \frac{\sigma}{\bar{s}} = \sqrt{\frac{1}{N_l-1} \sum_{i=1}^{N_l} (s_i - \bar{s})^2} \Big/ \frac{1}{N_P} \sum_{i=1}^{N_P} s_i \qquad\qquad \textbf{Eq. (4)}$$

where $\bar{s}$ is the mean sphericity measured over the totality of the particles in all of the three levels of the container, σ is the standard deviation of the individual level. For a perfect mix value of S would be 0, and the higher value indicates a low degree of mix.

4.1.2 Result of mixing experiments

In order to characterize the mixing processes, the influence of the time of rotations was investigated, as described above. Images were taken at different times for a rotation speed of 30 rpm, and displayed with different colours depending on the sphericity of the particles after 3D reconstruction (see Figure 34). As these two different kinds of granules can be distinguished with sphericity (please refer to section 3.1.1). Resulting images show via a time series of 3D images that the homogeneity of the two-component system increases with increasing the time of rotations T_R. It can be seen that at time 0 that the mixture was initially segregated prior to rotation so that the colour boundaries are well defined in the middle level. As a consequence of rotation in the same direction, two types of particles separate along the cylinder axis for T_R= 5 s. The system tends towards homogeneity without any colour boundaries for T_R= 20 s.
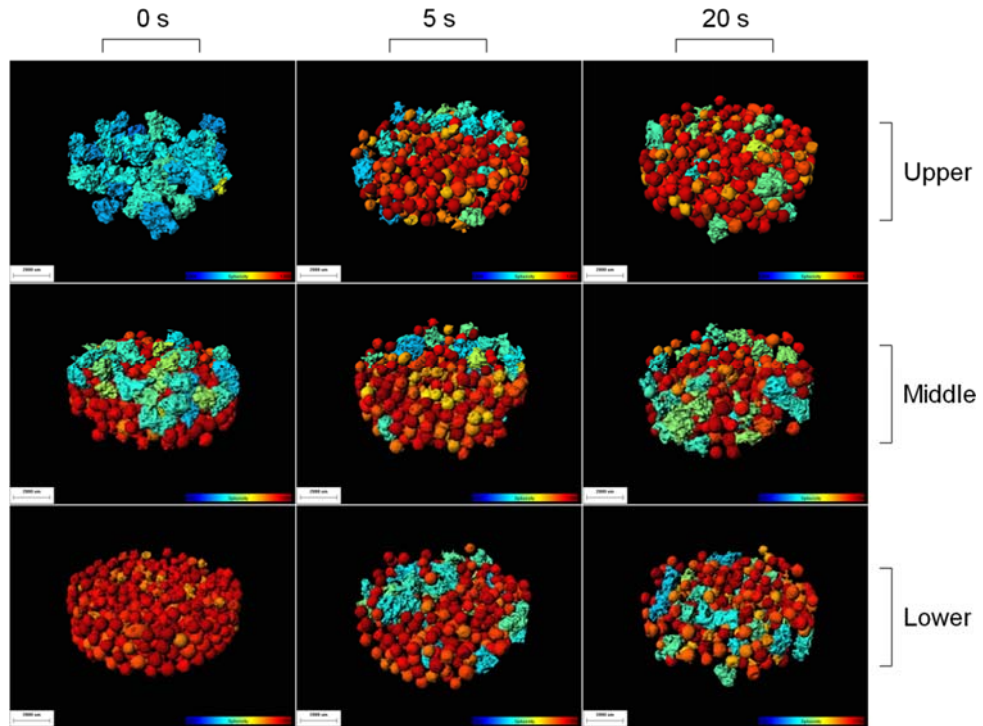
Figure 34 *Influence of the time of rotations T_R for the mixed granular system.*

V_R = 30 rpm. Each line corresponds to the same level of the cylindrical vessel. Images of each column correspond to the same time of rotation. The scale bar is 2000 μm, the standard jet color map reflects the sphericity value from 0.0 to 1.0.

Quantification of these images by normalized frequency distribution confirms these observations. The frequency distribution of particles according to the sphericity parameter in the two-component system is normalized such that different scales of each profile are unified. As can be seen from the profiles in Figure 35, in general, the degree of coincidence of three curves for upper, middle and lower levels tends to increase with time. However, the degree of a coincidence for 5 s appears higher than for 20 s. This might be confusing if this interpretation is accepted without further analysis. It has been shown that the homogeneity of the mixed system after 20 s rotation is better than after 5 s (Figure 34). This means that the sphericity statistical profiles do not totally capture the true pattern evolution after rotating the sample. It can, however, be used to some extent to evaluate the homogeneity of the mixed system, whereas the in-situ images are of particular importance to confirm the statistical estimates. These results also suggest that methods based on image–image correlations would improve the data analysis. Furthermore, due to the different particle sizes of the two types of granules, the number and frequency of starch granules are lower than those of microcrystalline cellulose granules. It can be seen in Figure 35 that the frequency of starch granules decreases in the upper level and increases in the middle and lower levels of the sample container with an increasing time of rotations T_R. Taking into account the relative amounts of the components, the frequency of microcrystalline cellulose granules with smaller particle size tends to increase in the upper level and decrease in the middle and lower level.

Considering the totality of the analyses, the results show that the homogeneity of the mixed system increases with increasing time of rotations T_R, in accordance with visualization of the 3D image (Figure 34).
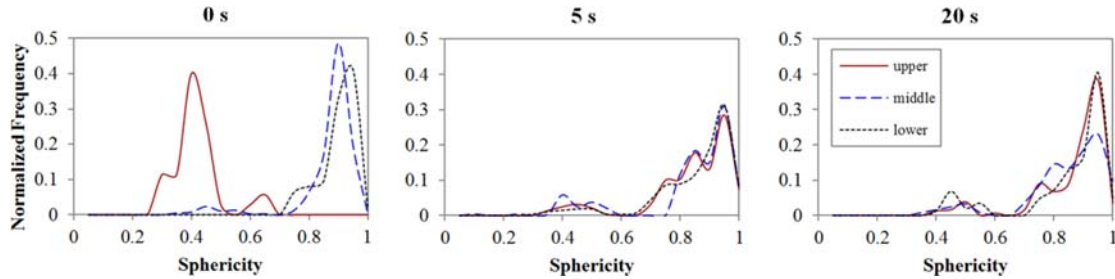
Figure 35 *The homogeneity of the two-component system increases with increasing the time of rotations T_R.*

A mixing index on the basis of standard deviation for the sphericity is calculated to evaluate quantitatively the mixing homogeneity of the samples. The mixing index value is strongly dependent on the particle size and 3D shape, i.e., an increasing number of microcrystalline cellulose granules lead to a decrease of mixture standard deviation, and the mixing index value rises with increasing number of starch granules.

All the particles are microcrystalline cellulose in the lower level for 0 s and the *S* is at its lowest value as described in connection with Figure 34 and Figure 36. If the value of mixing index is higher than that of the lower level for 0 s, some starch granules must be present in the level. Similarly, microcrystalline cellulose must be present in the level, if the value of mixing index is lower than that of the upper level for 0 s. As expected, the mixing index value of the upper level decreases with an increasing time of rotations T_R (Figure 36). The results illustrate that the number of microcrystalline cellulose granules rises in the upper level with an increasing T_R. Namely, the mixture homogeneity of the upper level increases.

Meanwhile, the mixing index value and homogeneity of the lower level rises with an increasing T_R. Compared with the middle level of 0 s, there are more starch granules in the middle level after 5 s and more microcrystalline cellulose after 20 s.

The upper, middle and lower levels can be regarded as three sampling zones in the container. The closer the mixing index values of three levels, the better the mixing will be. As can be seen from Figure 36, the mixing index values of the three levels become closer with increasing T_R. This finding also illustrates that the degree of homogeneity for the whole granular system rises with an increasing T_R, in accordance with the results shown in the 3D image (Figure 34).
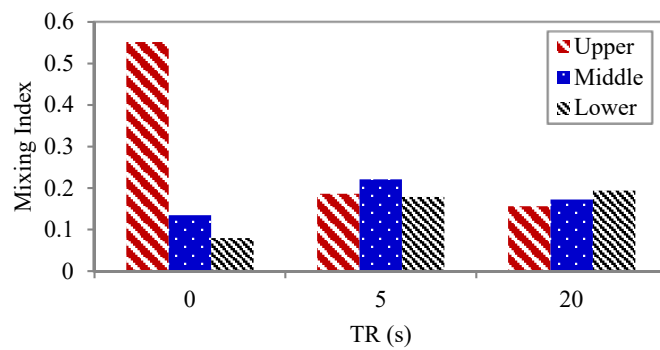
Figure 36 *The changes of mixing index in each level with an increasing T_R.*

4.1.3 Segregation experiments

For the two granules sets being studied with differences in size and shape, it was observed that segregation increased for the longer time of vibration at 2000 rpm (Figure 37). Compared with the initial mixed sample which was rotated for 20 s, segregation occurs at T_V = 5 s and increases at T_V= 20 s. For the granular mixture, the starch granules have a tendency to rises to the top of the sample. At

the same time, the microcrystalline cellulose granules move down to the bottom of the container.
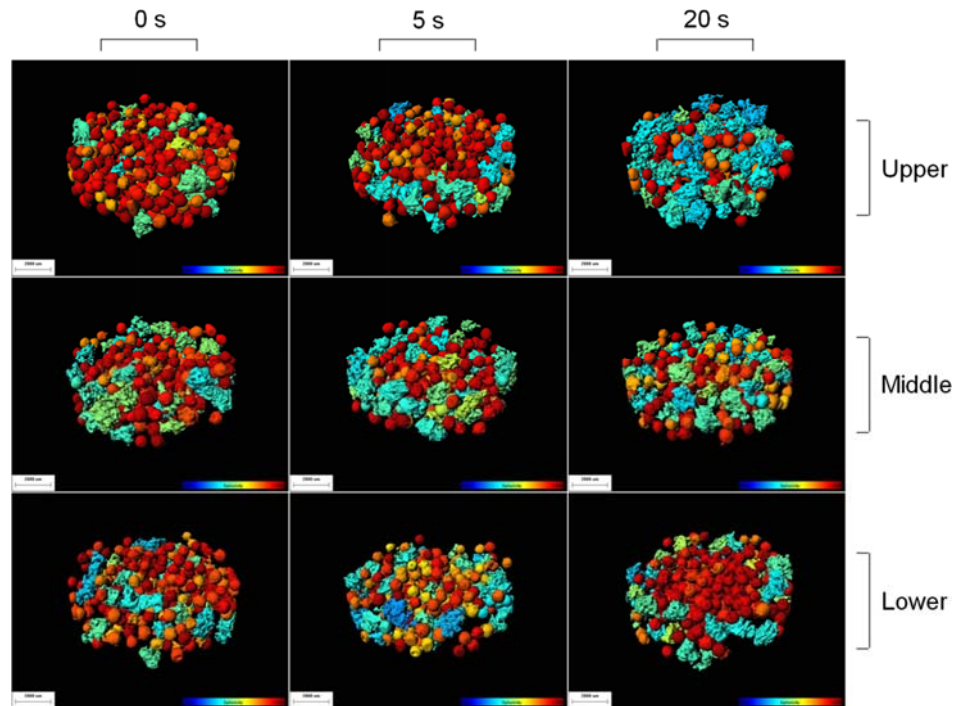
Figure 37 *Influence of the time of vibration T_V for the mixed granular system after T_R= 20 s at 30 rpm. V_V = 2000 rpm.*

Each line corresponds to the same level of the cylindrical vessel. Images of each column correspond to the same time of vibration. The scale bar is 2000 μm, the standard jet color map reflects the sphericity value from 0.0 to 1.0.

A time series of statistical sphericity profiles describing segregation of the mixed system shows that the degree of coincidence of the three curves for upper, middle and lower levels tends to decrease (Figure 38). These findings indicate that, as expected, the segregation increases with longer T_V. In addition, the frequency of starch granules rising in the upper level with longer T_V, corresponds to a decrease in the distribution of microcrystalline cellulose granules at the same level. In contrast, the relative amounts of starch granules reduce and the number of microcrystalline cellulose granules increases in the lower level. The results

illustrate that the starch granules preferentially rise to the top and the microcrystalline cellulose granules percolate down to the bottom of the container, confirming the previous visualization of the 3D images (Figure 37).
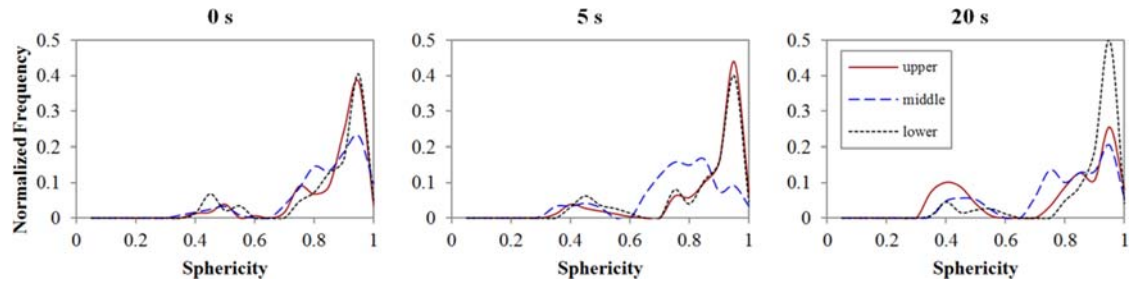
Figure 38 *The segregation of the two-component system increases with increasing the time of vibration T_V.*

As can be seen from the Figure 39, the mixing index of the upper level rises rapidly with increasing time of vibration T_V, which illustrates that the number of starch granules in the upper level increases with increasing T_V. In contrast, the increases in mixing index values of middle and lower levels are considerably lower with an increasing T_V. These results show that the number of starch granules increases to a small degree in the upper level over a long periods of T_V. Overall, the differences among the mixing index values of upper, middle and lower level tend to become larger with an increasing T_V. The quantitative results of mixing index are consistent with visualization of the 3D image (Figure 37).

100
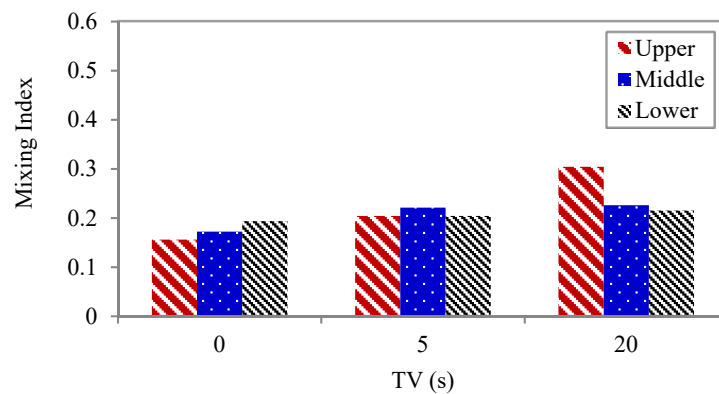
Figure 39 *The changes of mixing index in each level with an increasing T_V.*

The distributions of granular systems calculated by frequency analysis are in good agreement with the images obtained from SR-μCT for the mixtures examined. The shape information, such as sphericity and box ratio can be measured and utilized to explore systems of greater relative particle complexity. A mixing index on the basis of standard deviation for the sphericity is calculated to evaluate quantitatively the mixing homogeneity of the samples, which provide descriptions and visualizations of the imaging data. This model-based approach could, therefore, be used in other material processing challenges such as granular compaction or shear. This phenomenon may be associated with the larger size and non-spherical shape of the starch granules.

As a rapid and non-invasive technique, SR-μCT methods have great potential for clarifying the relationships between physical characteristics of granules and operation processes in the area of granular materials and provide the possibility for further investigation of pharmaceutical processes.

4.2 Deformation of clopidogrel bisulfate polymorphs during tableting

Powder compression represents an essential unit operation in the pharmaceutical industry since the compressed tablet represents the most common solid dosage unit used throughout the world for the delivery of medicines to patients. Mechanical properties, such as compactability, compressibility, elasticity, plasticity, and brittleness of the excipients and drugs as powders, dictate how formulations will behave during tablet processing and perform as drug delivery systems. The physicochemical and solid state properties of powders,

such as their polymorphism, moisture content, particle shape, particle size, and surface roughness, affect the mechanical properties of tablets formed from these constituent powders. Therefore, understanding the potential influence of these parameters on the properties of the products during and after compaction is important [78].

Many solid pharmaceuticals exhibit polymorphism resulting from the possibility of forming at least two crystalline arrangements of molecules in the crystal lattice [79, 80]. Generally, the polymorphs often exhibit different solid-state properties, density, habits, refractive index, melting properties, solubility, dissolution rate, and mechanical properties [81]. Moreover, under specific environmental conditions, such as pressure and temperature, as well as chemical purity the structure of polymorphs represents the packing of the molecules in the crystal lattice, which directs the solid-state properties of the crystals and also influences the compaction behaviour of powders [82].

During compaction, particles rearrange at the initial stage of compression and then deformation takes place during consolidation. Deformation behaviour of powder under stress depends primary on the mechanical properties - elastic, plastic, brittle fracture or a combination of these mechanisms. Elastic deformation is time independent, reversible and does not continuously influence tablet strength. However, plastic deformation is an irreversible process that contributes to the formation of particulate bonds that generate the tablet strength [83]. During the direct compaction process, the density distribution inside the tablets is often heterogeneous due to the inter particle friction and die wall friction. Since the shape of tablets used in pharmaceutical industry varies between flat-faced cylindrical tablets to more complex geometries with embossing, density variations

in pharmaceutical tablets may be important and affect the compact mechanical properties [84] as well as leading to non-uniformity of three dimension (3D) internal structure between individual tablets and consequently potential non-uniform drug release patterns. Density distribution has been investigated using NMR tomography [85] and autoradiography [86]. Recently, X-ray microtomography has been used successfully in pharmaceutical development studies [87].

The relationships between the mechanical properties, deformation behaviour and the molecule structure of the polymorphs have been studied for example ranitidine hydrochloride polymorphs. Powder X-ray diffraction (PXRD), differential scanning calorimetry (DSC), and optical and polarized microscopy were combined with compressibility plots and a Heckel analysis to confirm the greater plastic deformation of ranitidine form II over form I. The Heckel equation provides a method for transforming a parametric view of the force and the displacement data to a linear relationship for the materials undergoing compaction [88]. While studying the compression behaviour of orthorhombic paracetamol crystals, the resulting tablets were broken into small pieces, and 2D images of compressed crystals were obtained using SEM [89]. However, this approach has several disadvantages. The analytical method destroys the integrity of the tablet and might damage the structure of the individual crystal particles to some extent during tablet breakage. Moreover, SEM is not an in situ measurement and is unable to reflect the deformation behaviour of the crystals during and after the compaction process. Other current methods use various mechanical parameters include Young's modulus, Poisson's ratio, yield stress, and fracture toughness to reflect the deformation characteristics of powder [90]. Such approaches do not

provide high-resolution visualization of the in situ behaviour of individual crystals within the tablets. In addition, methods such as SEM that are used to probe the shape of a limited number of crystal particles do not provide a statistical confidence since all of the crystal particles in the intact tablets are not evaluated.

Within pharmaceutical material science and drug delivery research, SR-μCT has been used to visualize and quantify the microstructure of particles and the distribution of chemical composition for individual particles and their assemblies [23, 28, 91]. SR-μCT has also been used to distinguish clopidogrel bisulfate (I and II) in combination with multilayer perceptron. The polymorphs of the drugs could be identified and predicted through the numerical description of the 3D morphology [92]. However, to our knowledge, the visualization of the deformation behaviour of crystals in situ has never been reported as measured by SR-μCT.

In this study, the deformation behaviour of two polymorphs of clopidogrel bisulfate (CLP I and CLP II) was investigated by SR-μCT. As reported, these two polymorphs of CLP were investigated for in-die and out-of-die compaction behaviour using compressibility, tabletability and compactibility (CTC) profile, Heckel, and Walker equations, and the difference in compaction behaviour was explained in terms of the different molecular packing of two forms [90]. This study aims to develop a characterization method for SR-μCT that can determine the in situ deformation behaviour of the CLP polymorphs after compaction and to analyse the relationship between the polymorphic structures and mechanical behaviour during tableting.

(Detailed experimental information is provided in S 4 Reconstruction of compaction behaviours of CLP polymorphs)

4.2.1 Characterization of CLP crystal particles

The results of the PXRD measurements were consistent with those reported previously (Figure 40) showing PXRD patterns of both CLP I and CLP II [90]. There were clear differences in the X-ray diffraction peaks for CLP I and II polymorphs. The region 12-13º 2θ was characteristic for polymorph II while the peak at 21º signified form I, without any overlap of peaks from the other polymorph in these regions.
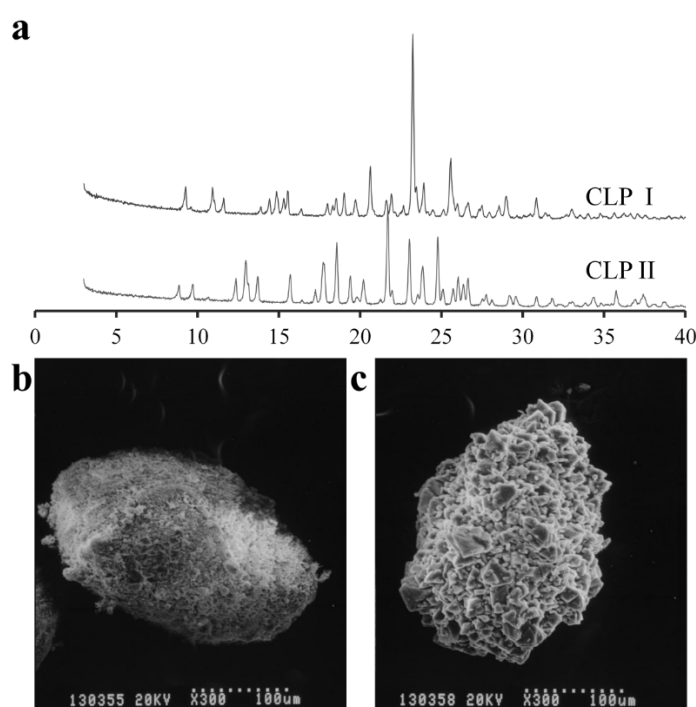
Figure 40 *PXRD and SEM of CLP I and II crystal particles. Powder X-ray diffraction overlay of CLP I and II.*

 (a). SEM (300×) of CLP I (b) and II (c).

Scanning electron microscopy.   As discussed in section 3.2, SEM was employed to characterize the surface morphology of the CLP polymorphs. And morphological differences were visible between CLP I and CLP II. The surface morphology of CLP II was rougher than CLP I. The images (b) and (c) in Figure

40 showed that a large number of individual crystals combined into a larger polycrystal. The subunits of CLP I particles were all smaller than those of CLP II, indicating that CLP I crystals were more densely packed compared to those of CLP II, and the larger subunit size of CLP II introduced a loose structure of the accumulated particles due to larger pore space between the particles.

Structure of CLP polymorphs particles measured by SR-µCT. CLP particles were distinguished from the excipients due to the noise reduction and phase retrieval. The grey value of the background was close to 0 for the excipients and the wall of the capsule as a container for the powders was between 80 and 120, and the CLP particles gave a grey value above 150. Two dimensional (2D) slices of the crystal particles are shown in Figure 41; the bright areas represent CLP particles and the PVP/VA are illustrated in grey.

Based on the analysis of grey values, all of the crystal particles in the samples were extracted. Afterward, highly resolved tomographic images of CLP I and CLP II with high quality phase contrast were derived for each single particle after 3D reconstructions (Figure 41, b and e). For the two samples, all of the crystal particles were included in the analysis, and individual particles were assigned a colour according to the volume of the individual particles. The morphological structure of the CLP I and CLP II particles were clearly different. Both crystal forms were irregular but the surface topography of CLP II showed greater roughness than CLP I (Figure 41, c and f).
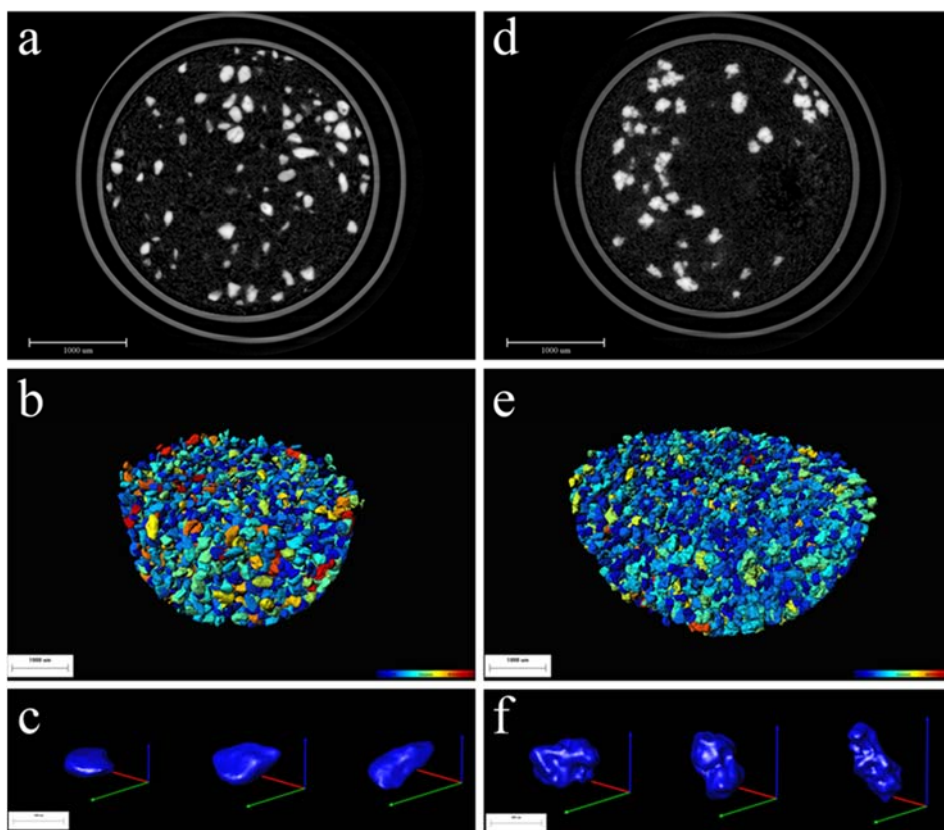
Figure 41 *Monochrome 2D slices and 3D morphology of CLP I and II crystal particles.*

2D slices of the samples contain CLP particles diluted with PVP/VA (a, d), 3D images of crystal particles in the capsule after extraction and construction (b, e), and the randomly selected individual CLP I (c) and CLP II (f). The colour gradients reflect particle volume, ranging from about 8.0E+4 μm^3 (dark blue) to 4.0E+7 μm^3 (red), the scale bars of a, b, d and e are 1000 μm and scale bars of c and f are 300 μm.

4.2.2 Visualization of the crystal deformation behaviour in tablets by SR-μCT

Tablets containing hundreds of pure particles of CLP I or CLP II diluted with PVP/VA were put into individual capsules with an internal diameter identical to that of the tablets. From the SR-μCT scan and the analysis of phase contrast extraction by X-TRACT, 2D slices were obtained (Figure 42), showing the individual crystal particles within the tablet distinguished from the PVP/VA by the

difference in the grey level, as discussed above. Compared to the powder samples in Figure 41, the CLP crystal particles showed a change in shape as a result of the compaction process. Specifically, the particles of CLP I exhibited a flatter morphology, while many CLP II particles were fractured into smaller sized particles.
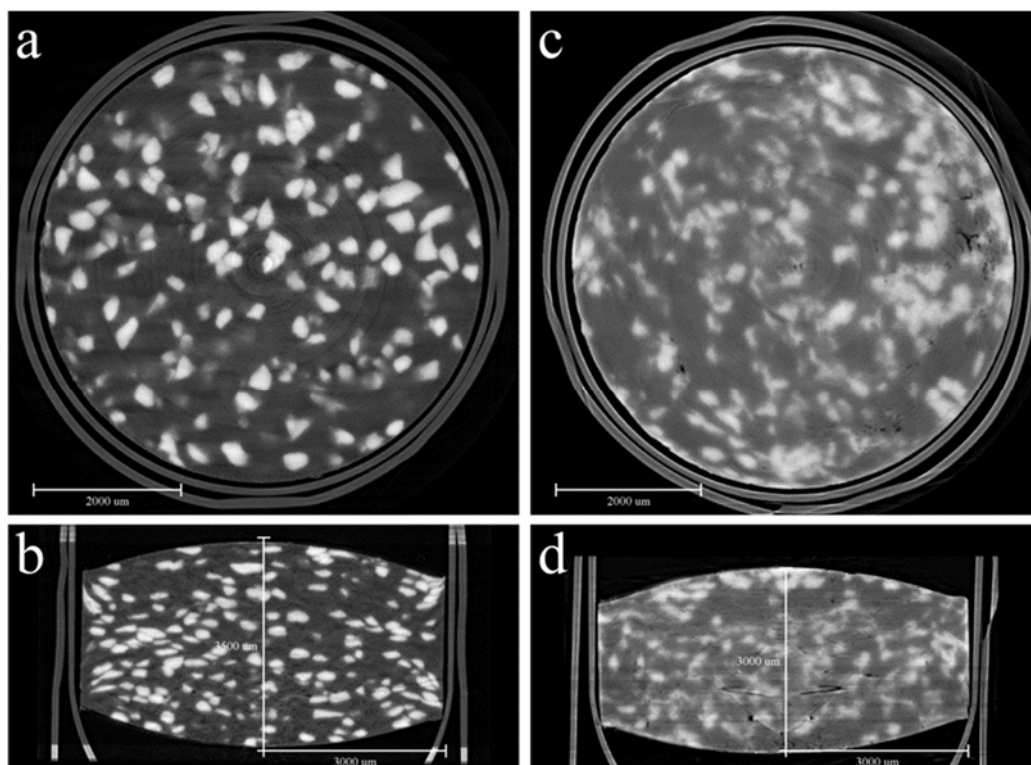
Figure 42 *Monochrome 2D slices of CLP tablets.*

CLP I (a, b) and CLP II (c, d). (a,c) and (b, d) are planes from the different angles (the outside border is the shell of the gelatin capsule, the container to fix the tablet on the objective table).

Both the tablets contained the same weight of CLP particles and excipients, compacted under the same conditions, and the same compression ratio. The true density of CLP I is 1.504 cm^3 and 1.471 cm^3 for CLP II. With the same mass weight of CLP in the compressed tablets, it might be expected that CLP II would have a larger volume than CLP I. However the final size, especially the thickness of the tablet was markedly different, namely, 3.5 mm for CLP I and 3.0 mm for

the CLP II. The tablet of CLP I exhibited 17% of elastic recovery following compaction when the pressure was released, but CLP II did not show such a high degree of elastic recovery.

All the 2D slices were processed by VGStudio Max and Image Pro Analyser 3D software, and the reconstructed 3D images of tablets obtained. Figure 43 shows the 3D morphological images of all particles within the tablet samples. In the surface regions of the tablets, the CLP I and CLP II particles exhibited large changes in morphology. The CLP I particles were flattened, while most of the CLP II particles were fragmented and lost their original shape. In the lower pressure regions, the CLP I particles remained well separated from each other and changed slightly in shape, while the CLP II particles fragmented, although less so when adjacent to the die wall.

By deleting particles that retained their original shape and could be distinguished from the other drug particles from the 3D-structure analysis, the reconstructed images of the deformed and fragmented particles in the tablets were obtained (Figure 43). The images reveal that the particles underwent extensive deformation at the surfaces of the tablets. The shapes of the particles were flattened and combined into agglomerates under pressure, particularly the particles of CLP II. Therefore, images prepared by SR-µCT clearly visualized the consequences of the different deformation behaviour of CLP I and CLP II. Although some particles of CLP I combined to form large agglomerates, it was still possible to identify their characteristic shape. In contrast, particles of CLP II were fragmented and compressed into a connected framework.
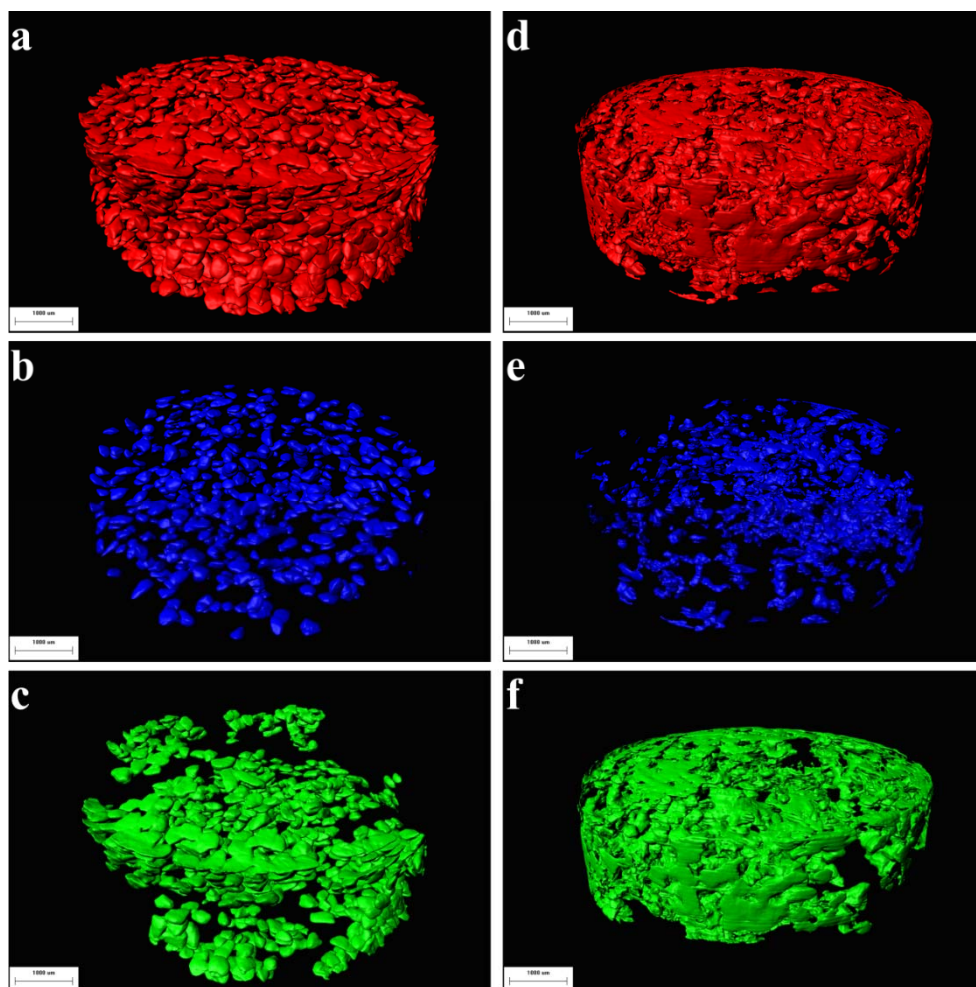
Figure 43 *3D models of CLP particles in tablets. Left insets represent CLP I particles, right insets represent CLP II particles,*

(a) and (d) are the 3D models of all particles in tablets, (b) and (e) are the 3D models of unattached particle clusters in the tablets, (c) and (f) are the 3D models of agglomerated particles in tablets. The scale bar is 1,000 μm.

The drug particles of CLP I that retained their original shape and remained separated from each other after compaction were distributed around the centre of the tablets (Figure 43). The degree of deformation for the particles separated from each other was markedly reduced compare with that for particles at the surface of the tablets. It is likely that these particles deformed under different applied pressures. In general, for the curved faced tablets, the highest density

110

regions were found to be close to the die wall, while the lower density regions were located in the centre of the tablets [93].

The different deformation behaviour in the various regions of the tablets reflects the heterogeneous density distribution within the tablet. The degree of particle deformation reveals how the particles reacted to the applied pressures during tableting. The greater degree of deformation, the greater forces the particles experienced. By considering the different deformation behaviours of the CLP I or CLP II particles, the tablets can be segmented into three sections. The area subjected to the high pressure tended to be close to the surface, while intermediate pressure regions remained in the central core of the tablets; the low force region is the middle layer between the surface and the central core of the tablets. Figure 44 (e) illustrates these sections of the pressure distribution spaces: section A as the intermediate pressure zone, section B as the lowest pressure area, and section C as the highest pressure section.

4.2.3 Quantification of crystal deformation behaviour in tablets

SR-µCT has been performed on the CLP I and CLP II tablets to extract single particle data for the visualization and quantitative characterization of the deformation behaviour of the two polymorphic forms. The shapes of particles and other 3D parameters changed during compaction providing data for further statistical analysis. The SR-uCT thus generates 3D quantitative data not generated by conventional detection methods available for powder compaction studies.

111
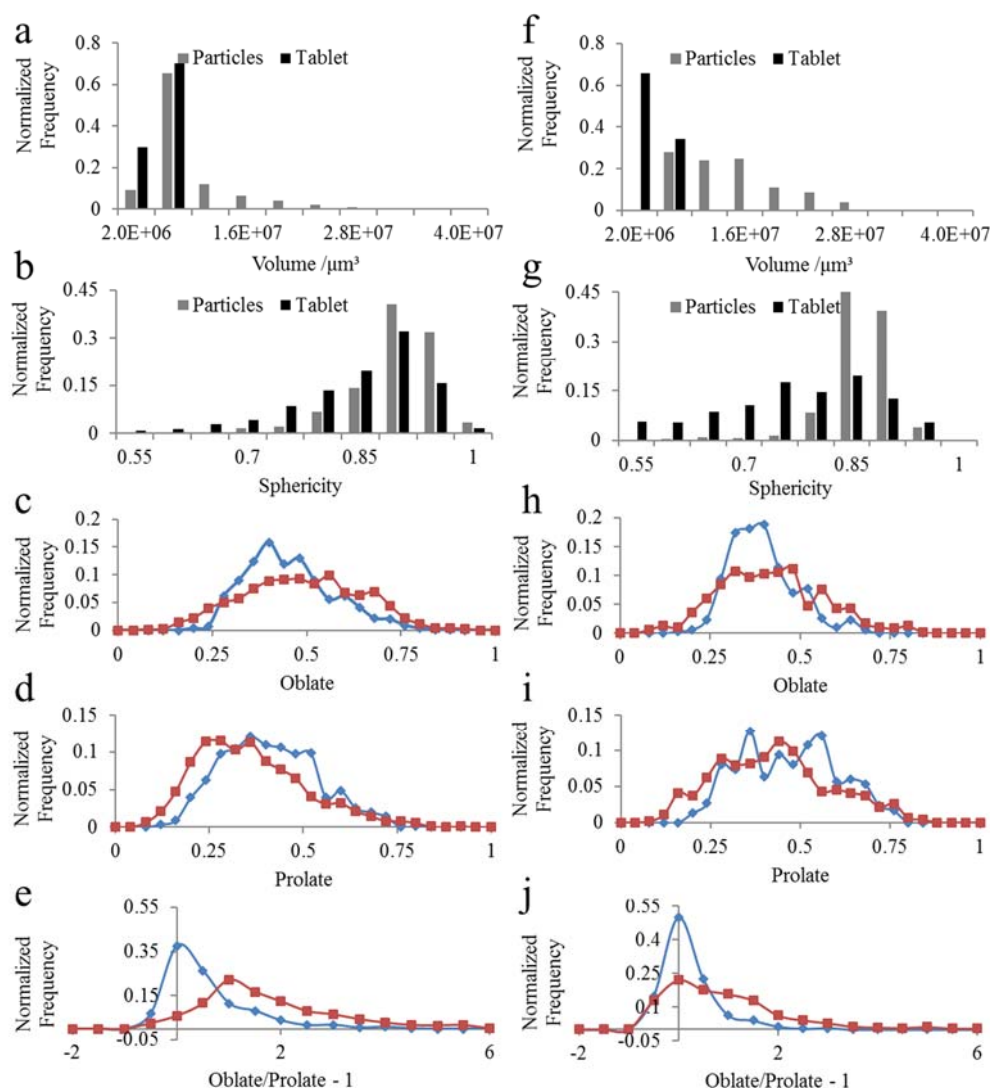
Figure 44 *3D quantitative parameters of CLP I and CLP II before and after compression.*

Particle volume and sphericity distribution changes during tableting of CLP I (a, b) and CLP II (f, g). (■ show the normalized volume/sphericity frequency of particles before tableting, ■ show the normalized volume/sphericity frequency of particles in tablets after tableting.) The ellipsoid parameters distribution of crystal particles before and after compaction (c, h. for oblate, d, i. for prolate and e, j. for oblate/prolate-1). (■ before compaction, ◆ after compaction). The left set of graphs represents CLP I, the right represents CLP II.

The volume distribution of the particles changed during tablet formation (Figure 44, Table 5). Before tableting, most of the particle volumes of CLP I and CLP II were distributed in the same range from 4.0E+06 μm³ to 1.2E+07 μm³. After

compaction, some particles were crushed and compressed into large clusters. When the clusters were rejected and eliminated from the analysis, the particle volume distribution of CLP I was filtered into from 3.2E+06 µm^3 to 4.0E+06 µm^3, while the particles volume distribution of CLP II was filtered into from 4.0E+06 µm^3 to 1.2E+07 µm^3. Generally, the particle volumes of both CLP I and CLP II were reduced. The different changes in the particles volume distribution reflected the difference in their deformation behaviours during tableting.

The sphericity distribution also changed after tableting (Figure 44, Table 4). Before tableting, most particles were distributed from 0.85 to 0.95. The sphericity of a small percentage of particles that originally exhibited low sphericity increased after compaction. This effect may be linked to the crushing of some particles. However, the sphericity of most particles in the tablet decreased. The degree of change in the sphericity was higher in CLP II compared to CLP I and the width of the distribution became wider. Sphericity of CLP II particles also showed large changes than for CLP I. In addition, the sphericity of CLP II particles was smaller than CLP I after tableting. These findings support the view that particles of CLP II are more readily deformed, exhibiting greater compressibility i.e. the ability to be reduced in volume at a given pressure.

Table 5 Sphericity of CLP I and CLP II before and after tableting.

Parameters	CLP I	CLP II
Sphericity-Before tableting	0.873 ± 0.056	0.840 ± 0.045
Sphericity-After tableting	0.826 ± 0.089	0.747 ± 0.011
Oblate-Before tableting	0.435 ± 0.005	0.375 ± 0.005
Oblate-After tableting	0.467 ± 0.005	0.400 ± 0.007
Prolate-Before tableting	0.392 ± 0.005	0.449 ± 0.008
Prolate-After tableting	0.341 ± 0.004	0.406 ± 0.007
Eclipse-Before tableting	0.354 ± 0.040	-0.030 ± 0.032
Eclipse-After tableting	1.616 ± 0.050	0.695 ± 0.059

Ellipsoid parameters of individual crystal particles were also calculated (Figure 44). Comparison of the morphology before and after compaction reveals the detailed deformation behaviour of single particle. Oblate and prolate describe the magnitude of change in shape of objects from an ideal sphere. When the oblate and prolate value equal zero, the object is a standard sphere. Higher values of the prolate parameters indicate object shape like a "cigar", while an increase of oblate value reflects a shape similar to a "disc". The value of Oblate/Prolate-1 was also evaluated as shown in Figure 44 and Table 5. The oblate and prolate values of CLP I original crystal particles were both larger than that of CLP II, indicating the particles of CLP I had a longer axis and flatter shape in comparison with CLP II. After the compaction, the average value of oblate increased and of prolate decreased for both CLP I and CLP II. The deformation during compaction made crystal particles flatter and the cracks developed against

the longest axis. During the compaction, the oblate/prolate-1 value for both CLP I and CLP II changed consistently. Detailed calculated value of the original oblate/prolate-1 of CLP I was 0.354, which specified a flat shape, whilst the value of -0.030 for CLP II was very close to 0, indicating a cylinder-like shape. After compaction, both oblate/prolate-1 value of CLP I and CLP II increased dramatically. For the CLP I, the increased with the oblate/prolate-1 reaching an average value of 1.616.

In combination with the result of volume change and height of tablet, the deformation processes of CLP I and CLP II can be illustrated. Under compression, the relative magnitude of three different deformation mechanisms which determines the consolidation of CLP I was Plastic ≥ Elastic > Brittle Fracture. Theoretically, plastic deformation facilitates the formation of permanent particle–particle contact regions during compaction, the binding between particles has also been observed in Figure 43 and Figure 45.e. The superior mechanical properties compared with CLP II could be due to the higher density and stronger interaction between the molecules, resulting in the most favourable packing of molecules in the crystal[90]. In contrast, the sequence of CLP II was Brittle Fracture > Plastic > Elastic. This rank order explains the good compressibility and higher densification of CLP II, for the crystal particles are readily fractured and this contribute to the reduction in volume as a result of an applied pressure. Owing to the plastic deformation and binding between particles under compression, CLP I shows great tabletability and compactibility, which can be observed in Figure 43 [90].

The sphericity, volume and position of particles in a tablet affect particle behaviour on compaction (Figure 45). This feature is clearly different between CLP

I and CLP II. After tableting, the particles of CLP II exhibited a smaller volume and a lower sphericity than particles of CLP I in the same regions, because the CLP II particle fragmented more readily than those of CLP I. Nevertheless, the importance of particles position and sphericity of CLP II was consistent with CLP I behaviour. The sphericity reduced, and the volume was decreased, particularly in section C of the tablets.
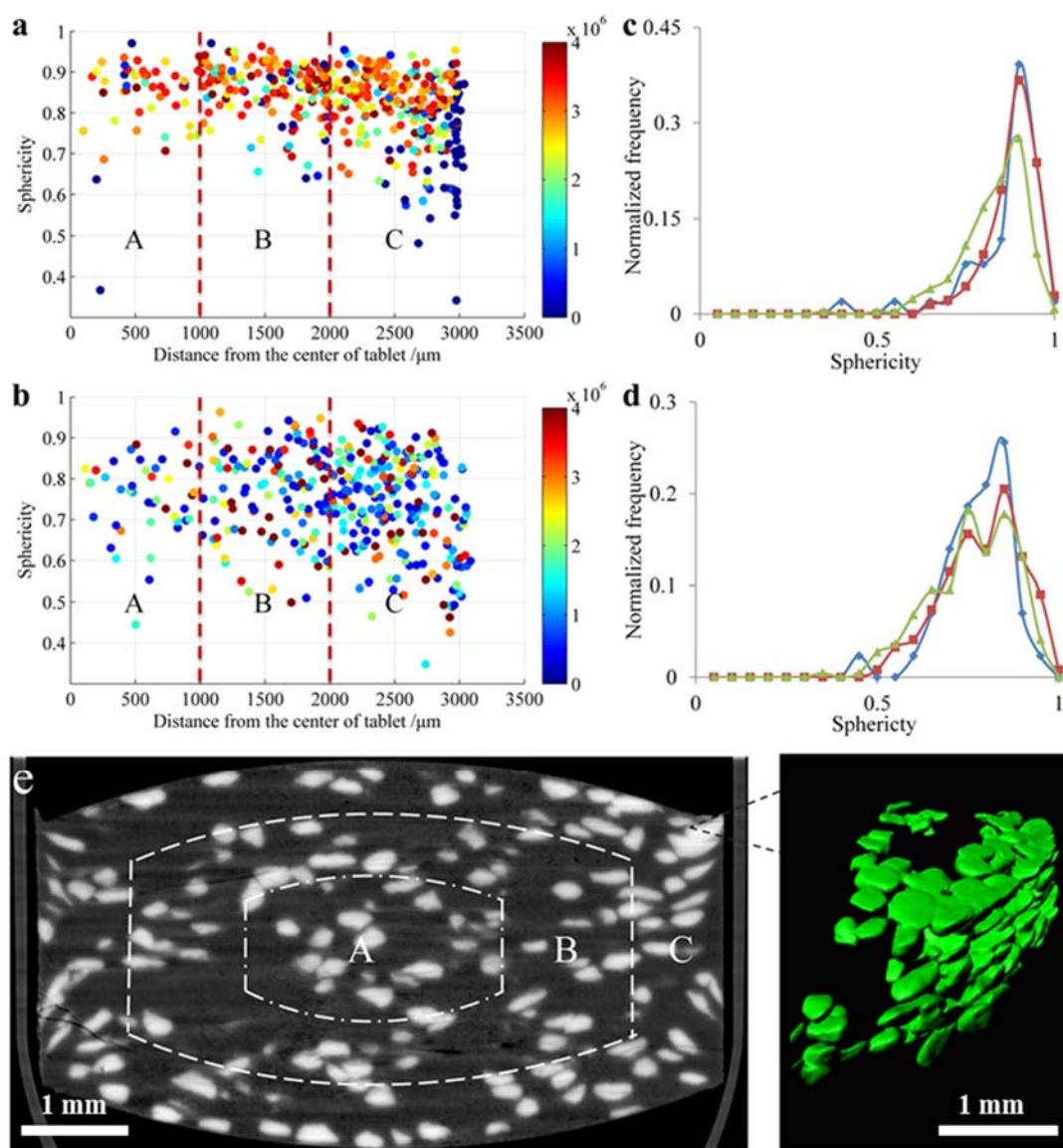
Figure 45 *Heterogeneous pressure distribution within the tablets.*

Particle position (a, b. distance from the centre of the tablet) and the sphericity coloured with volume (Section A: intermediate pressure, Section B: low pressure, Section C: high pressure. The chromatic stripes on the right side of the axis represent the volume, a. CLP I, b. CLP II); c, d. Sphericity distributions of CLP I and CLP II in different parts of a tablet. (c. CLP I, d. CLP II, ■ Section A (intermediate pressure), ◆Section B (low pressure), ▲Section C (high pressure)). e. The pressure distribution in a tablet was indicated by the distribution and agglomeration of crystal particles and divided into three sections (Section A: intermediate pressure, Section B: low pressure, Section C: high pressure. The enlarged part indicated the ultra-high pressure within the tablet with a dense cluster of crystals of CLP I).

In regions close to section C of the CLP I tablets, some small particles were observed due to the localized high pressure during compaction. The changes in sphericity were different in section A, section B and section C (Figure 45 and Table 6). The sphericity of CLP I and CLP II were the highest in section B, and the sphericity was the smallest in section C. The distribution range for the sphericity in section C was wider than that for the two other areas.

The relationship between the changes in sphericity, volume and particle position inside the tablets showed that the greater the pressure the particles were subject to greater change in sphericity and volume. Therefore, section C experienced high pressure, especially at the edges of the tablet, section A experienced the intermediate pressure, and section B experienced low pressure.

Table 6 Sphericity of CLP I and CLP II in section A (intermediate pressure), section B (low pressure) and section C (high pressure) regions.

Sphericity	CLP I	CLP II
Section A (intermediate pressure)	0.841 ± 0.099	0.754 ± 0.094
Section B (low pressure)	0.858 ± 0.067	0.767 ± 0.110
Section C (high pressure)	0.803 ± 0.096	0.735 ± 0.110

In this study, a new method combining synchrotron radiation X-ray microtomography and 3D reconstructions was developed to visualize and quantify the deformation behaviour of clopidogrel bisulfate polymorphs CLP I and CLP II. At the same compression ratio, CLP II deformed easily with higher compressibility and hence higher densification as compared with CLP I. Both CLP I and CLP II particles exhibited different deformation behaviour in the different pressure distribution regions within the tablets. At the surface of the tablets, the degree of deformation behaviour of particles was larger than other areas. The degree of deformation behaviour was linked to the changes of volume, sphericity and ellipsoid parameters. The different morphology of CLP I and CLP II particles showed different deformation behaviours after compaction. Plastic and elastic mechanisms dominated deformation behaviour for CLP I. With the disc shaped crystal particles flatterening under the pressure loading. The deformation of CLP II was dominated by the brittle fracture mechanism as the lower bonding strength did not prevent fracturing of the crystal particles. The direct observation and quantitative characterization of the deformation behaviour are in excellent agreement with the published results of mechanical test and molecular modelling of CLP I and II [90]. SR-µCT is shown as a powerful tool to provide in situ 3D

parameters of each particle in the tablets, enabling an improved understanding of particle behaviour during compression and tableting.

4.3 Structure of laser drilled delivery orifices in osmotic pump tablets

The controlled release of drugs has gained increasing attention in the pharmaceutical sector and drug delivery systems (DDSs) remain extremely important for optimizing pharmacological and therapeutic efficacy for many drugs [94]. Osmotic pump drug delivery systems (OP-DDSs) are regarded as one of the most reliable techniques for controlled delivery of therapeutic drugs, such as anti-hypertension, antidiabetic, and anti-angina compounds, as well as hormones and other agents [95, 96]. Compared with other approaches used in controlled release formulations, drug release from OP-DDS is independent of the external pH and hydrodynamics, which attributes minimal patient-to-patient variability and allows accurate prediction of in vivo performance from in vitro dissolution in many cases [97]. With such highly predictable drug release rates, OP-DDS generate various attractive biomedical advantages, e.g., reduced dosage and constant release rate leading to fewerside effects [98]. In terms of the clinical benefits and good in vivo-in vitro correlations (IVIVC), OP-DDS provide a promising technology for extending product life-cycles and optimization of therapeutic effects [95]. In addition, OP-DDS can be designed to deliver either highly soluble drugs or sparingly soluble drugs [95] in zero-order release profiles or other release behaviours, e.g., sigmoidal shape release [99] and pulsatile release [97].

The OP-DDS generally consist of a core tablet containing drug(s) mixed with osmotic agents and other excipients, and a semipermeable membrane with an

orifice(s) for the release of dissolved drug substance [54]. Release of the drug(s) is driven by the osmotic pressure gradient across the membrane from the inner-side to the outer-side as well as the solubility of the drug, the penetrability of the coating membrane to external aqueous liquids, and the size and the number of the delivery orifices [100]. A typical OP-DDS has at least one delivery orifice, for which the structure is critical for uniform drug release [55]. The size and number of the delivery orifices must be optimized in order to achieve the desired drug release rate. A tablet with an undersized delivery orifice may lead to the burst of the membrane and dysfunction of the OP-DDSs caused by internal high hydrostatic pressure. On the other hand, the delivery orifices with too large a size could result in solute diffusion dominated drug release through the orifices [54]. However, the effects of the shapes, depths and other structural parameters of delivery orifices on OP-DDSs have not been reported.

Methods used to create delivery orifices in the coating membranes of OP-DDSs include: mechanical drilling, passageways formed in situ, and laser drilling [55]. Mechanical drilling generally involves the use of a micro drill to create orifices on the surface of the tablets after coating [101-103] or modifying the upper punch of the tableting machine with a needle to produce an indentation at the centre of the surface of the tablet cores [104-106]. The orifices formed in situ are formed by adding a pore-forming agent to the semipermeable membrane composition [100, 107, 108] or by preparing the asymmetric membrane systems by controlled phase separation [109, 110]. However, the OP-DDSs prepared by inclusion of a pore forming agent and asymmetric membrane methods are usually limited by the solubility of active ingredients. Laser drilling is the most widely used

industrialized technique to create delivery orifices in the membrane of the OP-DDSs with high efficiency, accuracy and reliability.

The architecture of micro-structures formed after laser drilling contains not only the delivery orifices in the membranes, but also any melting and solidification in the tablet cores adjacent to the drilled orifices need to be examined. The effects of laser drilling parameters on the quality of delivery orifices and some structural parameters of the orifices have been reported in other fields, such as alumina ceramics and metals, using optical microscopic [111], and scanning electron microscopic methods [112]. However, for OP-DDS the evaluation of delivery orifices have been mainly limited to cross section two-dimensional (2D) observations to determine the cross section diameter of the delivery orifice by microscopes using a pre-calibrated ocular micrometer [113]. An alternative approach was to measure the delivery orifice microscopically using empty shells obtained after complete dissolution of the contents of OP-DDS [102], a techniques which is likely to introduce some errors or structural movement. In contrast, non-invasive imaging techniques are efficient tools which can reveal directly the internal structure and dynamic characteristics of OP-DDSs at different stages of the drug release process.

Although a critical structural feature of OP-DDSs, the structures of delivery orifices of OP-DDSs have been almost ignored in OP-DDSs development with an absence of published literature on this topic. The architectural detail extracted via SR-μCT can provide the real structures of laser drilled orifices with 3D visualization and enable quantitative assessment of the effects of laser drilling. Such structural detail will provide a deeper understanding in guiding the design of OP-DDSs to optimize their performance in controlled drug delivery to patients.

In this study captopril tablets and commercial felopidine tablets were studied using SR-uCT. Laser drilling was carried out on prepared captopril tablets, with cores composed of 42% captopril, 26% copovidone, 26% lactose, 5% sodium chloride and 1% magnesium stearate. Detailed information on the preparation of captopril tablets and the laser drilling of orifices is given in S 5

4.3.1 Visualization and 3D structure determination of drilled orifices

For OP-DDS, the ideal delivery orifice would be a controlled size of the circular opening in the semi-permeable membrane without any disturbance of the tablet core beneath the opening. In this study, an osmotic pump tablet containing captopril was selected to demonstrate the potential of SR-µCT 3D visualization and extraction procedures for examining laser drilled orifices (Figure 46). The slices of the reconstructed structure (Figure 46 a,b) show that the orifice has a border with readily distinguishable differences from the surrounding material. Additionally, the membrane, high density materials in the tablet core (e.g., the brightest particles are sodium chloride), are distinguished from each other.

Based on the recognized morphology and structure of the membrane and tablet core, the initial study was to determine whether the laser drilled orifice penetrated the membrane completely. The red coloured regions (Figure 46 e) showed the structure and form of the laser drilled orifices in the osmotic pump tablets. The rough surfaces of the architectures of drilled orifices, with some irregular protuberances attached, are attributed to the re-solidification of melted materials in the tablet cores after laser drilling (with melting points of cellulose acetate, polyethylene glycol, copovidone and captopril all less than 200ºC).

The overall shape of the drilled orifice was conical, with the cone angle inserted into the tablet core (Figure 46 c, the grey region). The unexpected conical shape, rather than an expected cylindrical structure, is thought to be due to one or more of a number of factors - i) any melted material as liquid re-solidify into a conical well; ii) the laser energy at the edge of the laser spot is weaker than that in the centre. However, it is regarded that the first factor is the primary cause for the conical shape of the orifice. Compared to the thickness of the membrane (approximately 50 μm), the depth of the drilled orifice was 575.61 μm, which indicated that the drilling penetrated through the membrane and into the tablet core. It is also shown that the membrane around the edge of the orifice protruded from the surface of the osmotic pump tablet. This feature was able to be identified due to the low reflection and good absorption of the coating and tablet core materials to the scanning laser, as well as the generation of thermal energy during their contact with the laser beam. It is hypothesized that the membranes in regions adjacent to the laser beam melted and re-solidified into curled circle edges after drilling.

The shape of the orifice opening resulting from the laser drilling was irregular and elliptical, although the original set shape for laser drilling was a regular circle. In addition to the potential melting event mentioned above which would have a major influence in the shaping of the orifice geometry [114], another explanation for the elliptical shape is that variation of directional control during the high speed movement of the laser beam led to the formation of an elliptical shape. It is also interesting to note that many very small micro-porous structures were observed around the edge of the drilled orifices, which might be due to thermally induced

vaporization of tablet core and membrane components during the drilling operation with subsequent re-solidification.
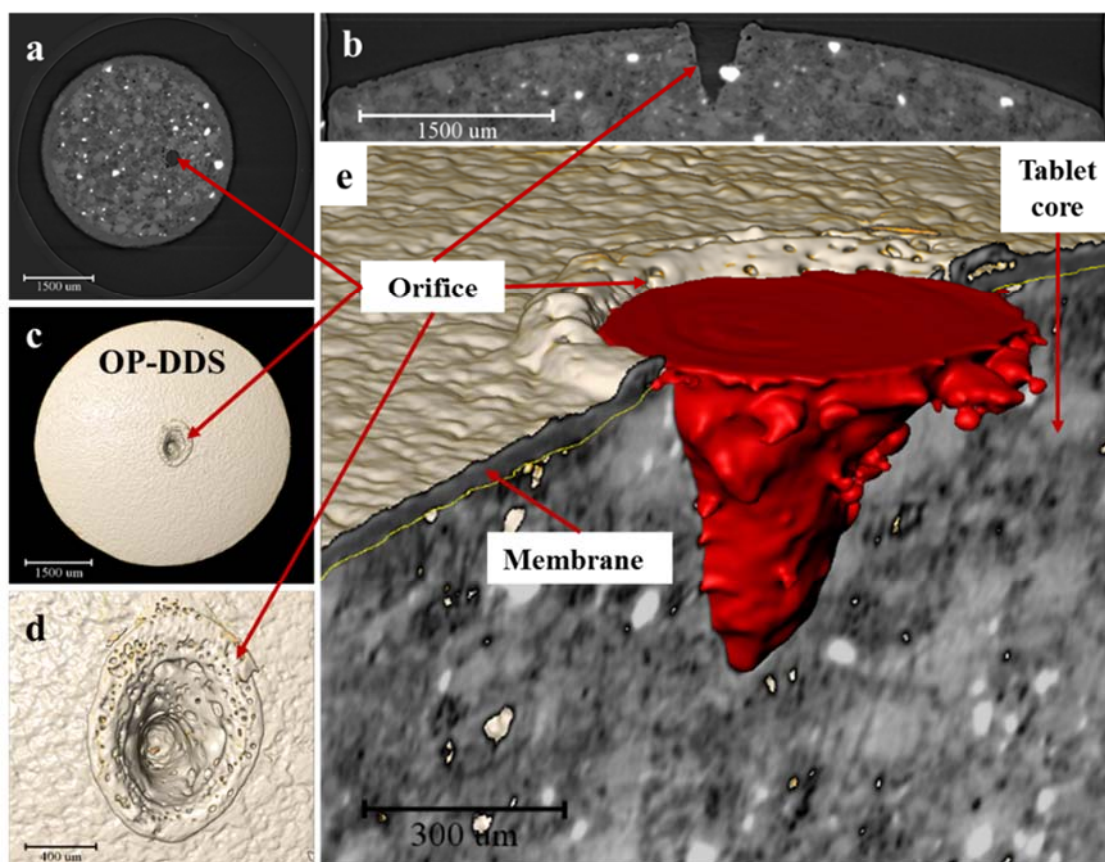
Figure 46 *Visualization and 3D structure determination of laser drilled orifices.*

Slice of the orifice (**a** and **b**, from different perspectives), 3D visualization of the orifice (**c** and **d**, **d** is the magnification of **c**), and extraction of architectures (**e**) of the laser drilled orifices from the osmotic pump tablet.

4.3.2 Drilling parameters and the structure of orifices

Reproducibility verification for 3D structural determination of drilled orifices

In order to assess the accuracy and reproducibility of the methodology, osmotic pump tablets subjected to the same laser drilling parameters were examined in triplicate. Architectures of the laser drilling orifices and the

corresponding cross section 2D and structural 3D parameters were extracted and analysed (Figure 47 a-c). In practice, it is challenging to produce uniform delivery orifices with laser drilling, which makes it difficult to achieve fabricating orifices with the desired orifice-geometry with industrial tolerances. It was reported that orifices with the same laser parameters generate different orifice geometries [114]. However, the results in our study revealed that the architectures of the orifices drilled by the same laser parameters had relatively good consistency in term of the cross section 2D structural parameters, with the area of 1.56 E6±0.01 E6 (±8.19%) μm^2, and aspect ratio of 1.30±0.06 (±4.71%). In contrast, there were much greater differences for the 3D structural parameters with average volume of 1.05 E7±0.04 E7 (±34.2%) μm^3, surface area of 4.33 E5±0.81 E5 (±18.7%) μm^2, depth of 214.29±26.04 (±12.2%) μm, and cone angle of 90.11±35.25 (±39.1%)° (Table 7). The relatively high variance of 3D parameters compared to the 2D parameter indicates that a 3D sensitive measurement uncovers more structural information of laser drilled orifices.
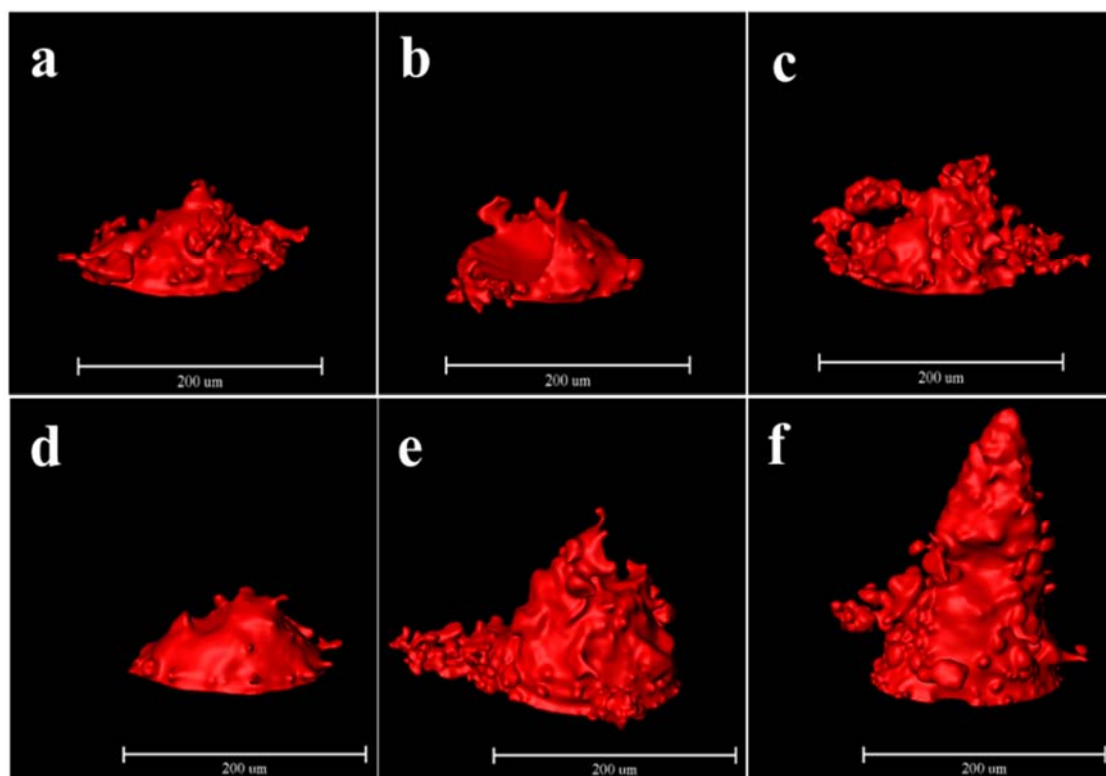
Figure 47 *Architectures of the laser drilled orifices.*

Generated by the same laser drilling parameters for the repeatability verification (**a-c**), and by one laser drilling (**d**), two laser drillings (**e**), and five laser drillings (**f**).

Intriguingly, in one example there was a large pore in the architecture (Figure 47 b), which was associated with the removal of a particle with a much higher melting point in the wall of the orifices. It was confirmed that the particle was sodium chloride (the osmotic pressure modulating agent, with the melting point of 804°C, Figure 46 b), as indicated by the brightness of X-ray image of the particle in the cross section. As a result, it can be argued that the presence of particles with a relatively large size and hardness close to the region of laser drilling will dramatically affect the architecture of the resulting orifices, especially the depth of the drilled orifices.

Table 7 Quantitative structural parameters of the laser drilled orifices generated by the same laser drilling parameters for the repeatability verification.

Orifice ID	Structural parameter					
	Cross section area (E6, μm^2)	Cross section aspect ratio	Depth (μm)	Cone angle (°)	Volume (E7, μm^3)	Surface area (E5, μm^2)
a	1.48	1.23	184.6	125.9	0.64	3.45
b	1.68	1.30	233.2	55.4	1.24	4.50
c	1.73	1.35	225.0	89.1	1.27	5.04

Effects of repeated laser drilling on orifices

The 3D structural changes of orifices occurring after repeated laser drilling were also observed. Under the identical laser operating parameters, three tablets were drilled for different number of times, namely, one, two and five drillings, respectively (Figure 47 d-f). It was found that whilst the 2D structural parameters remained almost unchanged, the 3D parameters were markedly different. For example, the 2D cross section areas of the architectures of orifices laser drilled one, two and five times were similar at 1.74 E5, 2.01 E5 and 1.75 E5 μm^2, respectively. In contrast, the depths of the orifices laser drilled for one, two and five times were in proportion to the number of drillings at 208.99, 428.01 and 675.27 μm, respectively.
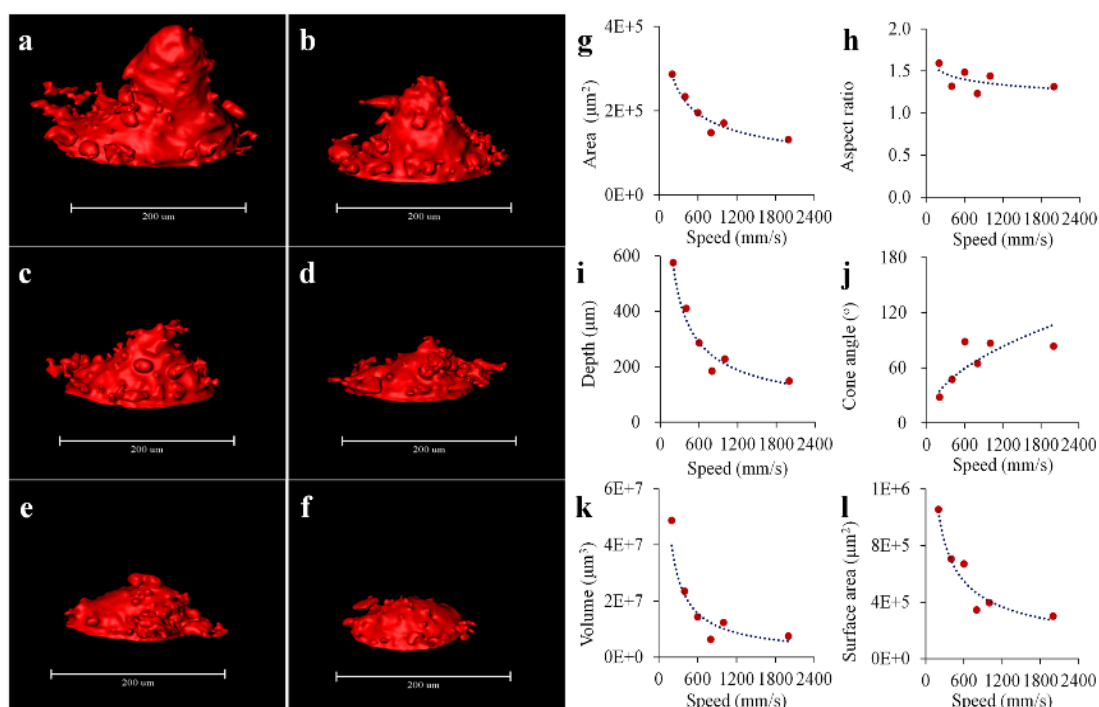
Figure 48 *Effects of laser powers on the architectures of the drilled orifice.*

3D visualization of architectures extracted from the osmotic pump tablets formed by different laser powers (**a-e**, **a**. 2 W, **b**. 6 W, **c**. 10 W, **d**.14 W, and **e**. 20 W), and the relationship between laser powers and structural parameters (**f-k**, **f**. cross section area, **g**. cross section aspect ratio, **h**. depth, **i**. cone angle, **j**. volume, and **k**. surface area).

Effects of scanning speeds of laser beam on orifices

If uniform orifice diameters can be formed with faster speeds, a shorter working time for laser drilling will occur. The orifice architectures resulting from speeds ranging from 600 mm/s to 2,000 mm/s, penetrated the membranes with minimum disturbance to the tablet core, with depths from 286.76 µm to 148.80 µm (Figure 48 c-f, i). The scatter diagrams and the exponential function fitting for the extracted structural parameters are shown in Figure 48 g-l. Architectures of the drilled orifices from faster speeds had smaller areas, volumes, surface areas and depths than for orifices formed at slower speeds. It was also clear that the reduction of speed values over the range of 200-1000 mm/s increased the cone

angle. Moreover, the relative standard deviations of the six drilled orifices for 3D parameters were larger than those determined from the 2D parameters. For example, the average 2D aspect ratio was 1.40±0.10 (±9.52%), ranging from 1.23 to 1.59 and the average area was 1.94 E5±0.58 E5 (±29.71%) μm^2, ranging from 1.32 E5 to 2.87 E5 μm^2. However, the average 3D determined depth, volume, surface area, and angle were 305.75±160.92 (±52.63%) μm, 1.88 E7±1.59 E7 (±84.50%) μm^3, 5.79 E5±2.89 E5 (±49.85%) μm^2, and 66.6±0.4 (±36.91%)º, respectively.

Effects of laser powers on the orifices

In general, the same orifice diameter formed under lower laser power involves a lower working energy or laser drilling. With the depth of 84.92 μm (Figure 49 h), the architecture of the orifice resulting from laser power of 2 W (Figure 49 a) was smaller and shallower than others (Figure 49 b-e), although, a low laser power often induces some instability into the drilling operation. The scatter diagrams and the exponential function fitting for the cross section 2D and 3D structural parameters are shown in Figure 49 f-k. The data show that the architectures formed by the higher laser power had larger cross section areas, depths, volumes and surface areas. However, the effects of laser power on the structural architecture of the orifices were more variable compared with those of the speed, especially for the 3D parameters of depth, cone angle, volume and surface area. The average aspect ratio was 1.40±0.11 (±7.54%). Apart from the lowest power (2 W), the cone angle widened with an increase in laser power. The steric morphologies of the architectures also changed when the laser power increased from 2 W to 6 W, but at a reduced rate over the power range 6-20 W.
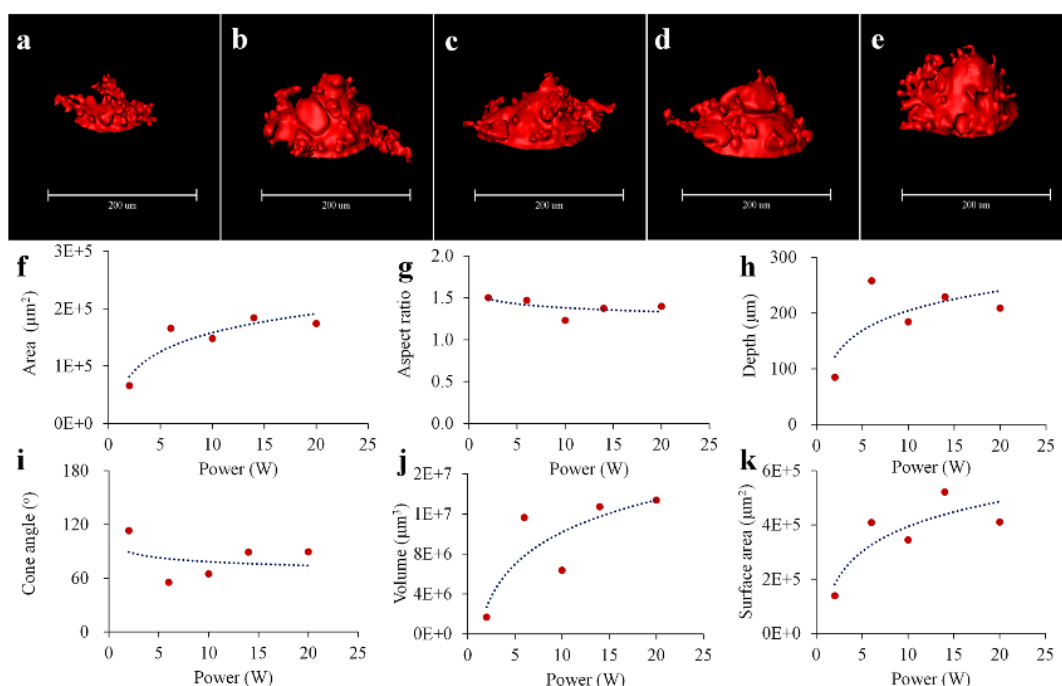
Figure 49 *Effects of scanning speeds of laser beam on the architectures of drilled orifices.*

3D visualization of architectures extracted from the osmotic pump tablets formed by different speeds (**a-f**, **a**. 200 mm/s, **b**. 400 mm/s, **c**. 600 mm/s, **d**. 800 mm/s, **e**. 1,000 mm/s, and **f**. 2,000 mm/s), and the relationship between speeds and structural parameters (**g-l**, **g**. cross section area, **h**. cross section aspect ratio, **i**. depth, **j**. cone angle, **k**. volume, and **l**. surface area).

Stability of chemical change around the orifices after laser drilling

The materials used as components of membranes and tablet cores of OP-DDSs may be sensitive to heat, and the laser drilling process is a high energy operation which can cause localized heating. Therefore, the materials within the membranes and close to the orifices may undergo some chemical change as a result of any melting and re-solidification of the membranes. Any such chemical changes and the chemical distribution can be identified by Fourier transformed infrared microspectroscopy (FTIR). Therefore, the regions close to the orifice in the membrane were mapped in situ by synchrotron radiation-based FTIR (SR-FTIR) (Figure 50 a). The region around the edge of the orifice was not transmittable

to the SR-FTIR if it was raised up to form a relatively high rim (approximately >100 µm). From the line mapping extraction SR-FTIR image (Figure 50 b), there was no dramatic difference among the microspectroscopy of the membranes from the edge of the orifice to the normal membrane region. However, the magnitude of absorbance of the regions adjacent to the normal membrane increased, due to the increased thickness of the membrane.
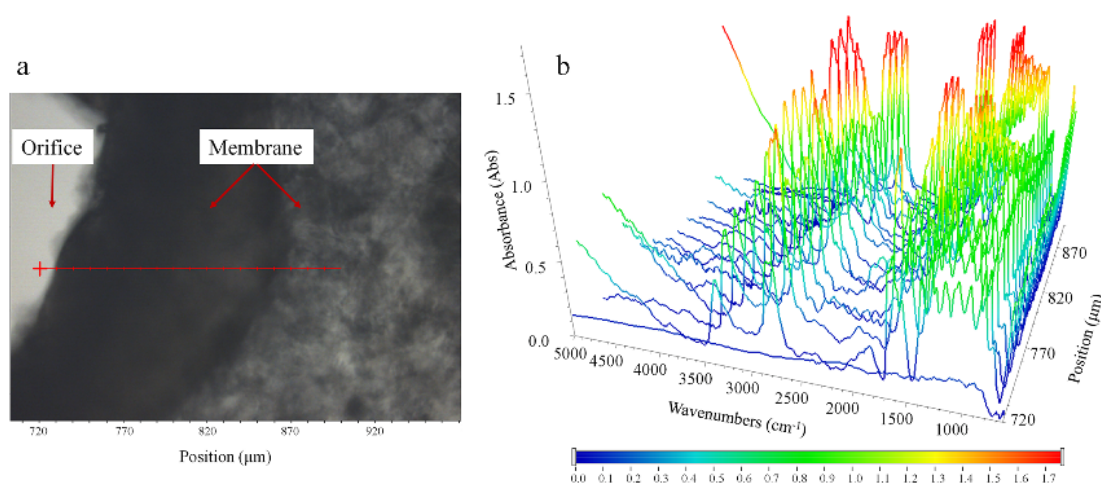
Figure 50 *SR-FTIR imaging of membranes around the laser drilled orifice.*

Morphologies of the membrane with an orifice (**a**). SR-FTIR spectra extracted from the line mapping image demonstrated there was no dramatic change from the edge of the orifice to the normal membrane (**b**).

4.3.3 Evaluation of the orifices on marketed OP-DDSs

The laser drilled orifices of felodipine OP-DDS (Linuo®, a marketed osmotic pump product in China) were evaluated using the above methodologies. However, the presence of a water-soluble crimson coloured coating outside of the cellulose acetate semipermeable membrane eliminated the opportunity to study any chemical feature of the membrane of felodipine OP-DDSs, since SR-FTIR imaging could not be carried out. The extra coating constituent did not, however,

interfere with the X-ray analyses for the SR-µCT measurement, and three felodipine sustained release tablets, providing six orifices, were measured (Figure 51). The architectures of the laser drilled orifices had similar 2D parameters, with an average cross section area of 2.48 E5±0.25 E5 (±10.03%) µm^2 and aspect ratio of 1.08±0.04 (±3.75%). As mentioned above, consistent and regular cross section areas and aspect ratios of laser drilled orifices would play an important role in achieving uniform and reproducible drug release profiles. In comparison, there were major differences in 3D parameters average volume of 3.27 E7±0.95 E7 (±29.05%) µm^3, the surface area of 7.85 E5±1.82 E5 (±23.25%) µm^2, depth of 394.18±257.57 (±65.34%) µm, and a cone angle of 68.10±28.38 (±41.67%)$^\text{o}$. All the depths of the orifices were larger than the average thickness (approximately 60 µm) of the membranes, penetrating into the tablet core. Although the effects of the orifice differences in 3D parameters on the drug release need to be further identified, it is considered that minimization of differences of the delivery orifices in 3D parameters could improve the consistency of drug release and the quality of the products in the future.
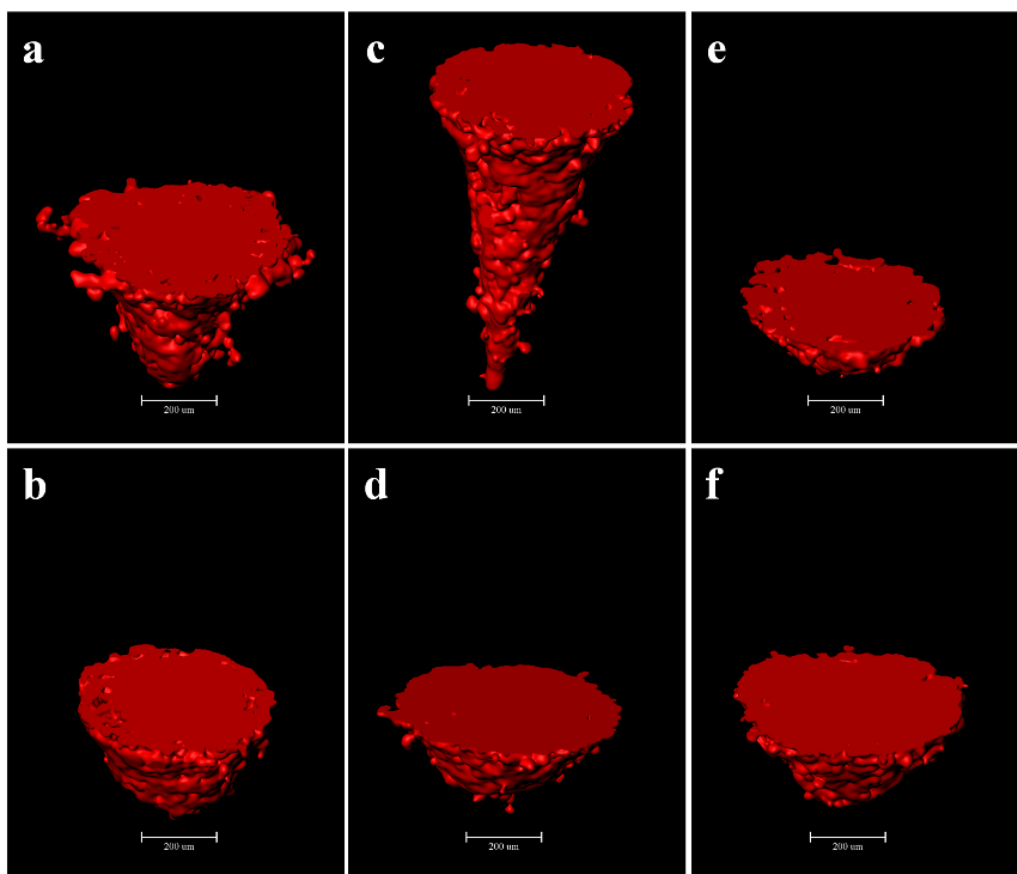
Figure 51 *Evaluation of the laser drilled orifices from the market product.*

Architectures of orifices (**a-f**) extracted from felodipine OP-DDS.

In this section, 2D and 3D visual and structural quantitative methods were established based on the SR-μCT to investigate the architectures of laser drilling orifices in the osmotic pump tablets. Results and findings using the new methodology have demonstrated the effects of laser drilling on the reproducibility and fine architecture of orifices, which are the key functional structure for the osmotic pump controlled drug release systems. The in situ SR-FTIR spectra and mapping have shown that there was no chemical change close to the delivery orifices when compared to the normal membrane. In conclusion, quantitative visualization by SR-μCT and structural reconstruction of the architectures on the semipermeable membranes and orifices generated by laser drilling provides

valuable information for improving the design and performance of osmotic pump drug delivery systems for controlled release.

General comments

In conclusion, studies reported in this chapter focused on the intermediate microstructures in pharmaceutical manufacturing processes. The blend of microcrystalline cellulose and starch granules was studied and the derived mixing index used to evaluate the mixture homogeneity of the particle system. Particle mixing and segregation as visualised in 3D images and found to be Influenced by the time of rotations and the time of vibration. Tableting of crystal particles was tested in situ non-invasively. With the advantages of SR-μCT to obtain the individual particle characteristics of CLP I and II polymorphs, the deformation behaviours of the two crystal forms was measured without destroying the integrity of the tablets and correlated closely to the published result of their mechanical properties. The quantified degrees of deformation illustrated the heterogeneous pressure distribution in various regions of the compacted tablet.

Examination of the laser drilled orifices in OP-DDS was also carried out. Rather than the conventional microscopic evaluations being limited to measurement of two-dimensional cross-section diameters, a novel method to measure quantitatively the three-dimensional architectures of orifices was established. Quantitative analysis of architectures of orifices drilled with different laser power and scanning speed revealed variation in cross section area, volume, surface area and depth of the orifices.

In the next chapter, chapter 5, various microstructures affected by swelling, dissolution, erosion and hydration to deliver drug release will be investigated

using in part DDS systems previously examined . In this way a correlation of the microstructure with drug release profile can be probed to provide insight into, and reveal details of, drug release mechanisms.

Chapter 5

Innovation of Novel Architecture Driven

Drug Release Mechanism

-Dynamic Structures during Release

5.1 Internal architectures correlated to release kinetics of particulate systems

Conventional dissolution testing is routinely performed using methods described in Pharmacopoeias. The solid dosing unit is placed in a suitable buffer, agitated under controlled conditions, and the results represent the amount of active pharmaceutical ingredient (API) that is released over time. The key components for optimizing the formulation and manufacturing processes, as well as the release mechanism, are the dose level of drug and the target release profile of the drug over time. However, this approach toward establishing a release profile does not provide the contributions of individual pellet, in case of multi-pellet products, due to the extremely tedious experiments required and the analytical constraints of quantifying very low levels of a substance. However, this strategy for multi-pellet product is insufficient because the release kinetics for ensembles is a composite profile of the individual units [115-117]. An ensemble of zero-order releasing units will exhibit first-order kinetics under certain conditions [118]. The results from single pellet experiments can also be used to simulate the release behaviour on the dose level [119-122].

The rate and mechanism of drug release from solid dosage forms depend strongly on their shape and microstructure. Lorck et al. found that rough pellets had a higher release rate than smooth pellets after approximately 2 h of release where spherical pellets were classified as smooth, and all other shapes were denoted as rough [123]. The internal micro-structure of pharmaceutical tablets can not only influence mechanical strength but also impact the rate at which APIs are released from some types of dosage forms [124]. For microcrystalline

cellulose (MCC)-carbopol pellets with a high proportion of carbopol, the size, shape, mechanical properties and release behaviour can be tuned by modulating the $CaCl_2$/carbopol ratio and the drying conditions due to the influence of these variables on the pellet microstructure [125]. In another study, a good correlation was also reported between the total porosity, mean pore diameter and drug release rate, while the porosity parameter was important when evaluating the in vitro performance of the multi-unit erosion matrix during the controlled release of an insoluble drug [126].

This section details SR-µCT investigations into the relationships between the microstructure parameters and single pellet drug release from a multi-pellet DDS (TSH sustained release pellets). The release behaviour of a single TSH pellet was analysed using a LC/MS/MS quantification analysis method, SR-µCT method to reveal the microstructure of TSH sustained release pellets: (i) visualise the surface morphology and internal 3D structure while investigating the drug release behaviour of the individual pellets; (ii) elucidate the release mechanism of individual pellets and probe relationships between the microstructure and release kinetics; (iii) correlate the release behaviour of single pellets and the pellet ensemble from a single-unit dose capsule.

5.1.1 Identifiable pellets preparation

To investigate the release behaviour of the individual pellets with the microstructures discussed above, samples containing identified pellets containing tamsulosin from a commercial multi-pellet controlled release DDS were prepared for a SR-µCT scan. PVP/VA was introduced and mixed with the pellets; five samples were examined. Therefore, three differently sized capsules

were filled with a specific number of tamsulosin hydrochloride (TSH) pellets (i.e., seven pellets for the largest size capsule and five pellets for the two smaller sizes); these capsules were closed to form a sample for CT scanning. Figure 52. a is a 2D synchrotron X-ray tomographic image showing how the two components of the capsule shells fitted together. Every capsule was identified using a specific code. The pellets in each capsule were easily distinguished by size and shape. The images of the pellets were acquired using a CCD camera (20× magnification) and analysed by software Image-Pro Plus (Version 7.0, Media Cybernetics, Inc., USA) to verify the differences for every pellet.

Identifying and matching the pellets with the reconstructed 3D model

Pellets separated from the PVP/VA were transferred to a black plastic board after the CT scan. Then, photos of each pellet were taken using the CCD camera (20× magnification times) and the digital images analysed using Image Pro Analyser 3D. The pellets on the image were sequenced according to their size and shape (Figure 52. b and c) and each pellet was identified with an ID by comparing the true pellet to the sequenced pellet image. Data from CT scan and 3D reconstruction, the reconstructed model and the pellet image were linked and compared. In this way, every pellet was successfully matched with the corresponding 2D image and 3D model.
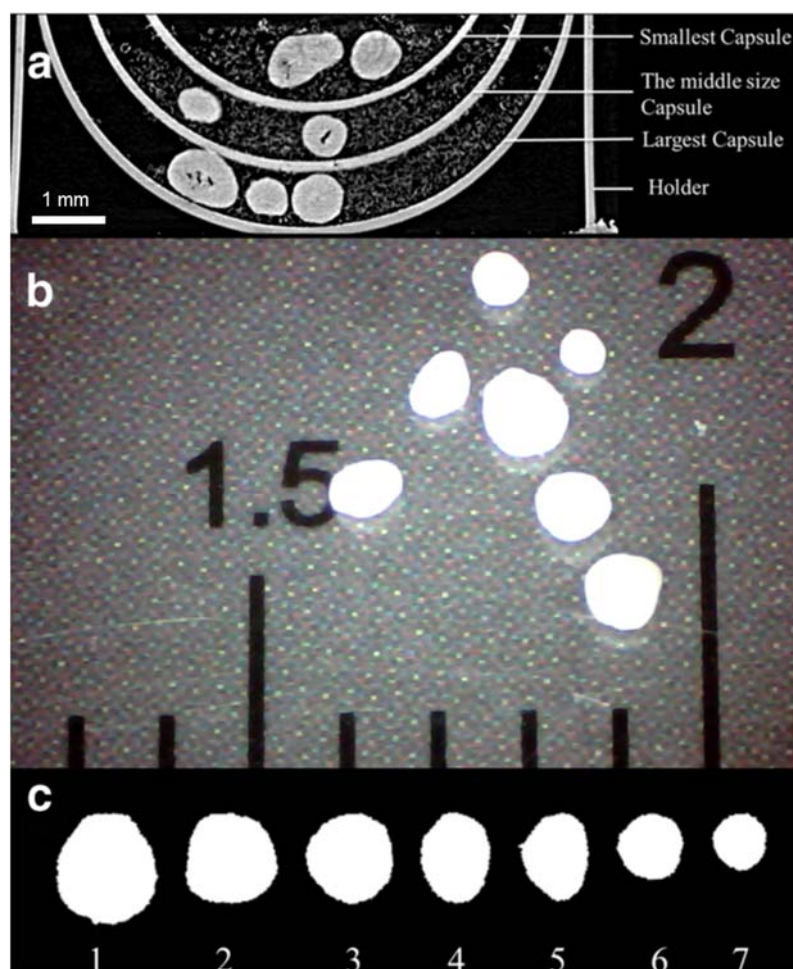
Figure 52 *Preparation and identifying of the pellets.*

 a Tomography of the prepared sample (TSH pellets (bright) and PVP/VA (grey)); b original image of the pellets from one typical capsule; c the sorted sequence with the corresponding label

5.1.2 Dissolution testing and data analysis

The dissolution testing included two parts - the original capsule at the unit dose level and single pellets. The dissolution testing with the original capsule was performed using a USP31-NF26 Apparatus II (paddle) at 100 rpm and 37 ℃ in 500 mL of phosphate buffer (pH 6.8) (n=6). Five mL samples were withdrawn at established time intervals (15, 30, 45, 60, 90, 120, 180, 240 and 300 min), and the amount of drug released was determined using LC/MS/MS analysis (see details below). After sampling, 5.0 mL of the fresh release medium was added to

each dissolution vessel. For the single pellets, the dissolution test was performed using a constant temperature oscillator at 100 rpm and 37 ℃ in a 10.0 mL release medium and 0.5 mL samples were withdrawn for quantification, as well as the other parameters tested for the single unit dose capsule. Ultrasonic processing was performed for 30 min before the concentration was determined to obtain the total amount of drug in each single pellet ($M\infty$ in Eq.(6)).

The cumulative amount of drug released over time was calculated using Eq. (5):

$$M_t = C_n \cdot V_2 + (C_{n-1} + \cdots + C_2 + C_1) \cdot V_1 \hspace{2cm} \textbf{Eq. (5)}$$

where Mt is the cumulative amount of the drug released at time t, C1 is the concentration of drug during the first sample collection, C2 is the concentration of the drug after the second sample was collected, Cn is the concentration of the drug at time t, V1 is the volume of sample withdrawn at different times, V2 is the volume of the dissolution medium.

The cumulative percentage of drug released over time was calculated using Eq. (6):

$$R_t = M_t / M_\infty \hspace{2cm} \textbf{Eq. (6)}$$

where Rt is the cumulative percentage of the drug released at time t, and M∞ is the total amount of drug.

LC/MS/MS analysis

The chromatographic experiments were performed on an Agilent 1260 series HPLC system (Agilent Technologies Inc., China). The separation was carried out

at 30 ℃ on a Luna C18 column (150 mm × 4.6 mm, 5 µm, Phenomenex). The mobile phase consisted of methanol-acetonitrile (30:40, v/v) and ammonium formate (10 mmol/L) (58:42, v/v, pH 4.2-4.5) flowing at 0.4 mL/min. The total run time for each sample was 8.0 min.

The mass spectrometric data were collected with a G6460 tandem mass spectrometer (Agilent Technologies Inc., China) equipped with an atmospheric pressure chemical ionisation (APCI) module. Nitrogen was used as the nebuliser gas at 20 psi and the drying gas at 6 L/min and 350 °C. The instrument was operated with a 3.5 kV capillary voltage. Multiple reactions monitoring (MRM) was employed during data acquisition. The optimised MRM fragmentation transitions for tamsulosin and the internal standard (IS, diphenhydramine) were m/z 409.0→m/z 228.1 with a fragment voltage of 135 V and a collision energy (CE) of 20 V and m/z 256.1→167.1 with a fragment voltage of 75 V and a CE of 6 V, respectively. The dwell time for each transition was 200 ms. Quadrupoles Q1 and Q3 were set to unit resolution.

The stock standard solution of TSH (0.2 mg/mL) was prepared by dissolving the drug in phosphate buffer (pH 6.8) before storage at 4 ℃. A standard calibration curve (peak area ratio of TSH/IS vs. known drug concentration) was built using standard solutions (1.00, 2.50, 5.00, 10.00, 25.00 and 50.00 ng/mL) prepared by diluting the stock standard solution with phosphate buffer. The IS (5.16 ng/mL) was prepared by dilution in acetonitrile. For the analyses, 40 µL of each sample was combined with 60 µL of IS solution (diphenhydramine, 5.16 ng/mL). After vortexing (2500 rpm, 1 min), a 2 µL aliquot of each sample was injected into the HPLC system.

The peak area ratios of the calibration standards were proportional to the concentration of Tamsulosin in each assay over the nominal concentration range (1.00-50.00 ng/mL). The calibration curves were linear and were well described by least-squares linear regression lines. Compared to the 1/x weighing factor, a weighting factor of 1/x2 achieved the homogeneity of variance and was used accordingly. The correlation coefficient was ≥ 0.9950. The validated linearity range justified the concentrations observed when analysing the real samples. The LLOQ (lower limit of quantification) of the method was 0.1 ng/mL at a signal-to-noise ratio (S/N) ≥ 32. The accuracy and precision for tamsulosin were 93.1-106.2% and 4.8%, respectively. The recovery for the analyte and the internal standard were obtained by comparing the peak areas at the low, medium and high quality control (LQC, MQC and HQC) concentration levels. The recovery of the analyte at the LQC, MQC and HQC samples was calculated: 99.1±7.0%, 103.6±5.3% and 96.8±6.4%, respectively.

5.1.3 Single pellet release kinetics

The total amount of drug in each single pellet was determined as mentioned above and additional data analyses were performed (Figure 53. a and b) to understand the drug release behaviour. The drug loading of the individual pellets was distributed across a wide range and was weakly correlated (R^2 =0.7790) to the pellet volume, as shown in Figure 53. a. In Figure 53 b, the points on the scatter plot spread further as the diameter increases, indicating that the drug loading on the small pellets with high sphericity show a higher homogeneity. Furthermore, the drug concentration in the pellet matrix (content in a unit of volume) of most pellets was approximately 1 to 2 ng/µm³. This concentration is markedly lower than the saturated solubility of TSH; this feature is important for understanding

the drug release mechanism. Several outliers are apparent in the plot showing the differences in the drug concentration in the pellet matrices because the manufacturing process is unable to provide a perfectly heterogeneous product. The drug concentration decreased slightly as the pellet diameter increased.
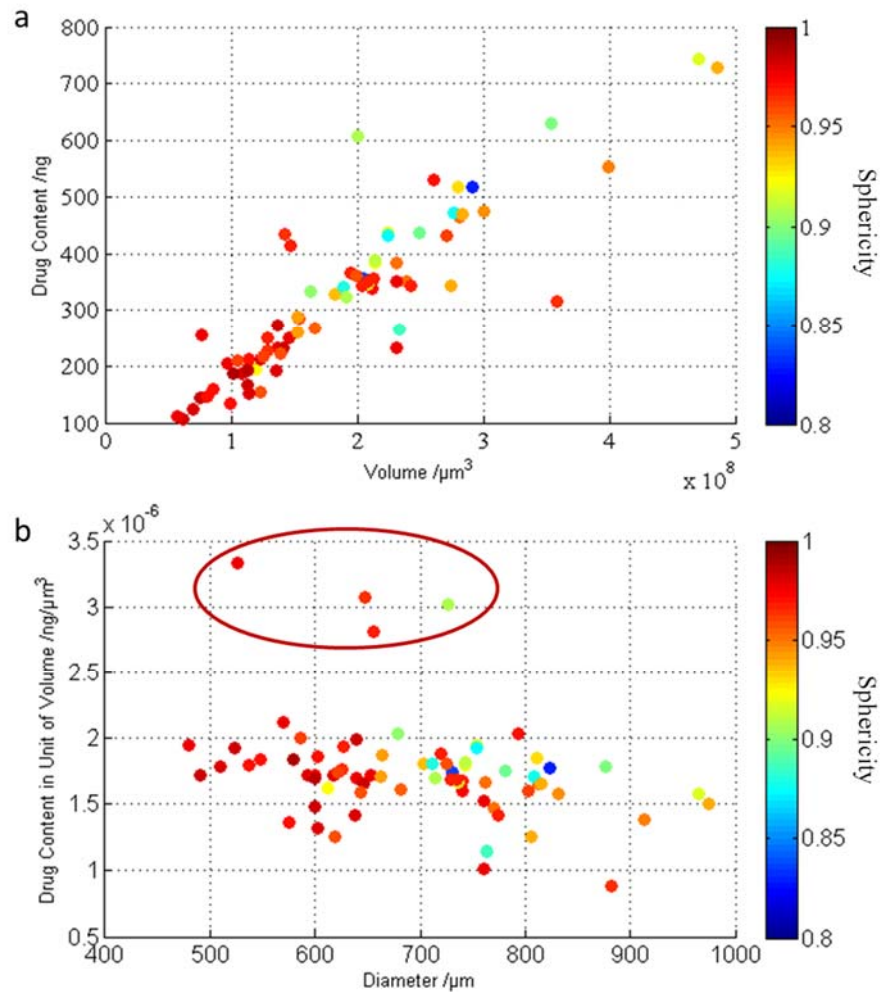
Figure 53 *Correlation between (a) volume and drug loading, (b) diameter and concentration of drug in the matrix.*

 The colour coding (bar on the right) has been chosen such that yellow to red illustrates an increasing and big value of sphericity whereas green to dark blue corresponds to a decreasing and small value of sphericity. Outliers were highlighted with elliptical.

A 3D map of the drug release profiles from 74 single pellets is shown in Figure 54. The IDs of the pellets were rearranged as the drug loading increased to facilitate visualisation in the graphical displays. The blue domains correspond to lower amounts of drug release, and the red domains correspond to the higher amount of drug release. The drug loading of individual pellets ranged from less than 100 ng to 700 ng. The amount of drug released from each pellet at various test points changed as the colour changed in Figure 54.b. The regularity of drug loading and release behaviour as the colour changed gradually is linked to the fact that the individual pellet data were rearranged according to the drug loading. Figure 54 e and f show the threshold of drug release. The rate gradually decreased during the release process. The number of pellets with the total drug content released at specific points was (cumulative release percent ≥ 85%) was 1, 1, 10, 37, 22, 3 at 60, 90, 120, 180, 240, 300 min, respectively. Therefore, after 240 min almost all of pellets had completed their release. The release distribution at each point appears similar.
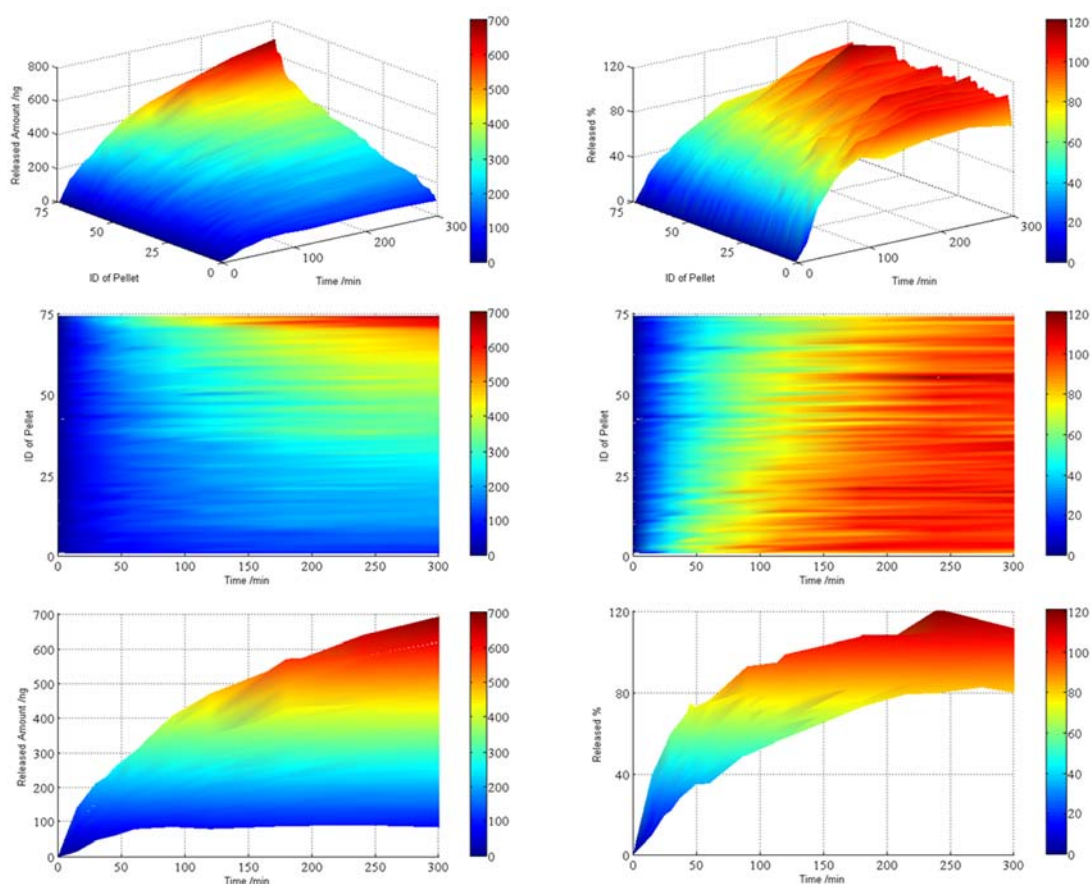
Figure 54 *Single pellet release profile for released amount (a–c) and released percent (d–f).*

3D surface plot (a, d), top view (b, e) and front view (c, f). The colour legend (bar on the right) refers to the amount of drug released (ng) in a–c and the cumulative release percentages (%) in d–f

5.1.4 Correlation between structural parameters and drug release

The rate and mechanism of the drug released from the pellets depend on their microstructure. The correlation between these parameters and the drug release was investigated further.

Correlation and release mechanism analysis

146

The nine subplots in Figure 55 show the correlations between the surface area of individual pellets and the cumulative amount of drug released at each sampling point. The 74 data points in each subplot correspond to the 74 individual pellets analysed. As shown in Figure 55, the cumulative amount released correlated well with pellet surface area, with particularly strong linear correlations observed from 45 to 120 min.
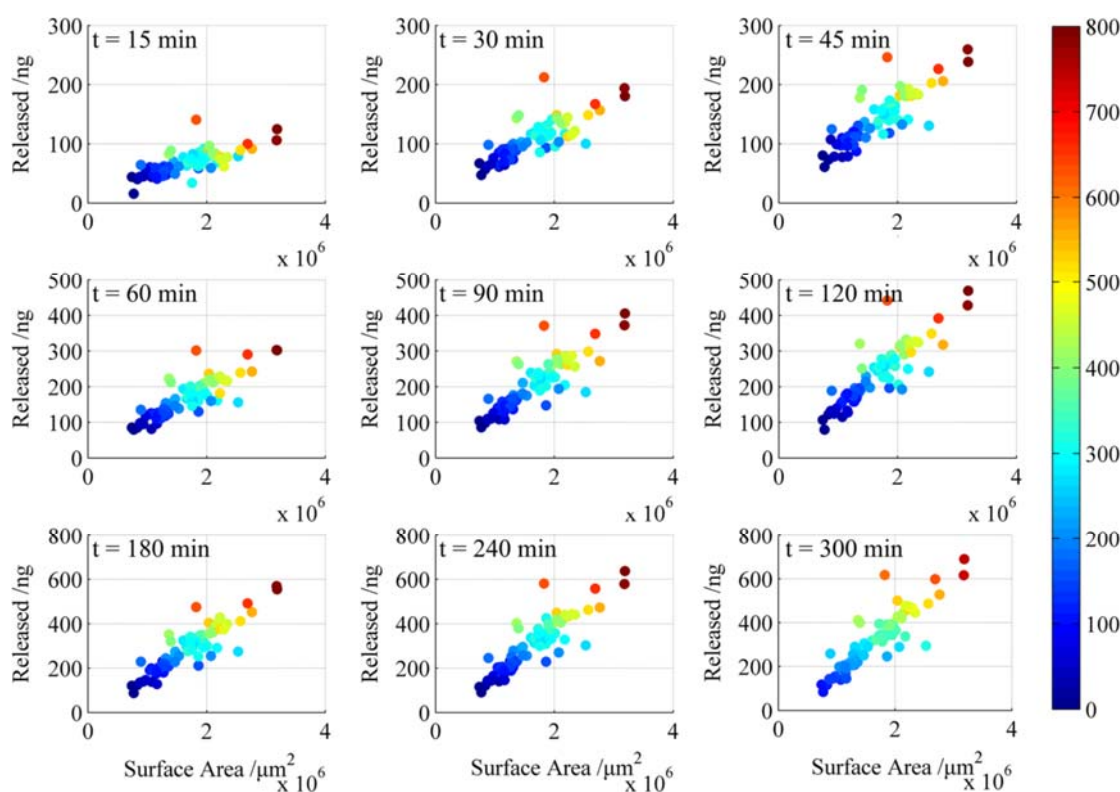
Figure 55 *Correlation between the surface area and cumulative amount released at different times.*

The colour legend (bar on the right) refers to the drug loading of the pellets (ng)

The above analysis shows that the surface area of the pellet represents a key steric parameter that determines the drug release profile. The drug release kinetics may also be controlled by the diffusion of the drug from the pellet. The pellets tested in this study contain microcrystalline cellulose (MCC) as a bulking excipient. MCC is insoluble in water but does swell. The van der Waals interaction

will be the main inter particle interactions between the drug particles and MCC and the sustained release of the drug will also be affected by the insolubility of MCC in water [127]. Thus in this case, the drug release mechanism of the MCC-based pellets can be classified as that occurring from an inert matrix [128]. In the inert matrix, the drug is released through both the initial, existing pores of the matrix and the pores formed when the drug has been dissolved [129]. MCC has a porous structure. From observations, it was noted that the drug-containing pellets maintained their original shape during the drug-release tests and no swelling or disintegration was observed.

The drug release patterns of single pellets from MCC matrices can be expressed as the well-known relationship reported by T. Higuchi in 1963 and reduced to Eq.(7) [130].

$$Q/A = \sqrt{\frac{DK}{\tau}(2 - KC_S)C_S t}$$
<div align="right">**Eq. (7)**</div>

where Q is the amount of drug released per unit of surface area for the matrix (mg/cm^2), A is the concentration of that component in the matrix (mg/cm^3), D is the diffusion coefficient (cm^2/min), т is the tortuosity factor, C_s is the concentration of a saturated solution of the drug or solubility (mg/cm^3), t is time (h) and K is the specific volume of each soluble component (cm^3/mg).

The release rate is controlled by the drug concentration, the dissolution speed and how fast the dissolved drug diffuses throughout the matrix. The largest value of M_∞/V is 3.5 µg/mm^3, a value which is considerably lower than the solubility of TSH. Therefore, if TSH dissolves fast during the first and middle periods of the drug release period, the drug concentration in the pellet is constant and equal to

M_∞/V. Because the matrix of the pellet formed by MCC remained throughout the release, the surface area of the pellets remained unchanged, allowing τ and the surface area to remain constant. For specific cases in this research where the D, K, C_s, and τ is constant, this equation can be reduced to form Eq. (8):

$$Q/A = \sqrt{\omega t} \qquad\qquad \textbf{Eq. (8)}$$

where ω is the slope of the square root of the time relationships, and Q can be rewritten as dM/S; A can be rewritten as M/V, allowing Eq. (8) to be rewritten as Eq. (9):

$$dM = \frac{M}{V} \cdot S \cdot \sqrt{\omega t} \qquad\qquad \textbf{Eq. (9)}$$

where M is the drug loading of the pellet, and V and S are the volume and surface area of the pellet, respectively. According to Eq. (9), the cumulative amount of drug released is a linear function of the square root of time.

Therefore, the level of correlation between M*(S/V) and drug release kinetics was investigated in this study. The results are shown in Figure 56. a and confirm a high level of correlation.
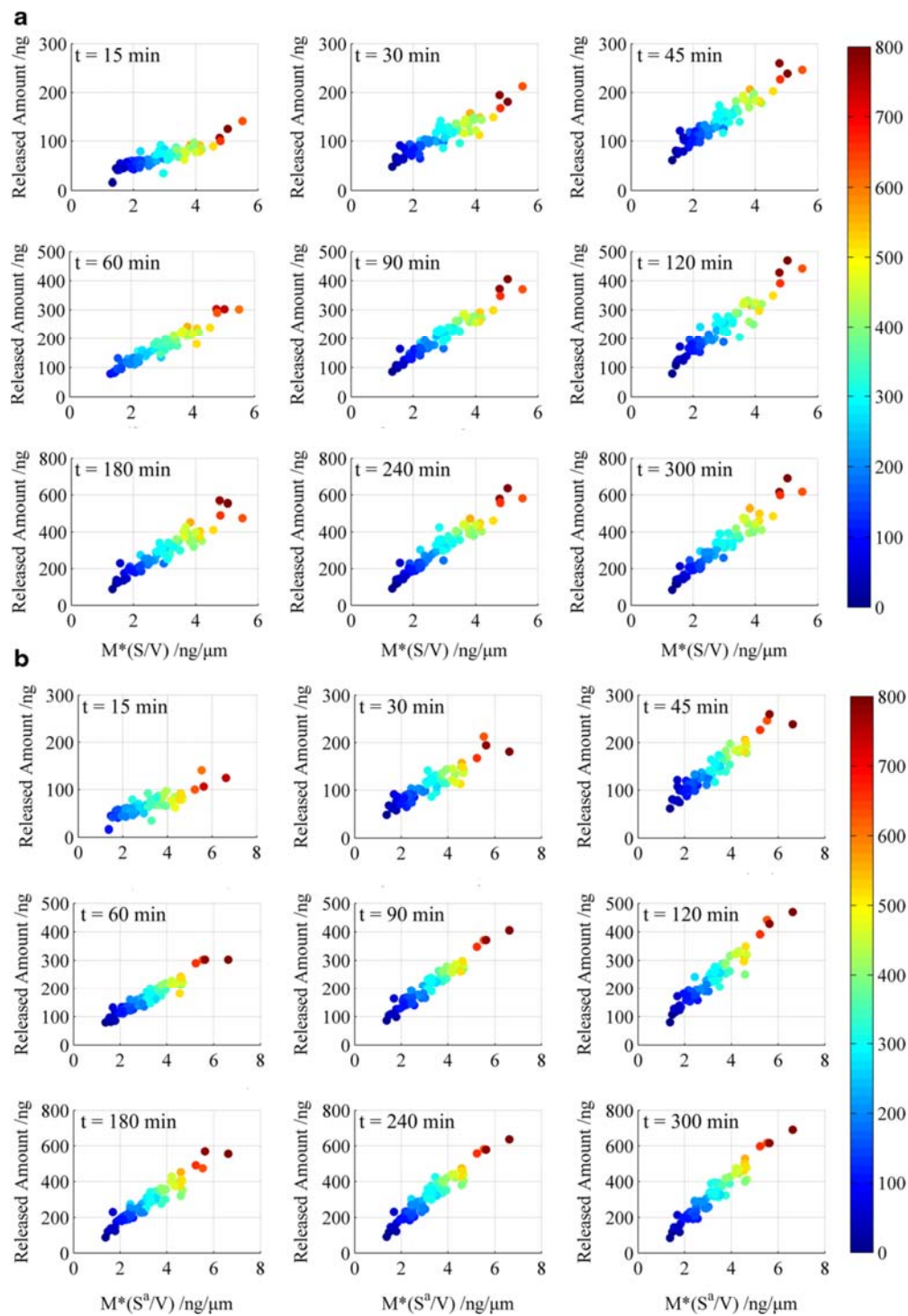
Figure 56 *Correlation between the newly defined parameters (M×(S/V))*

(a) and (M×(Sa/V)) (b) cumulative release amount. The colour legend (bar on the right) refers to the drug loading of the pellets (ng)

At the beginning of the drug dissolution process, only the outer surface of the pellet is infiltrated with dissolution medium. When the pellet is well hydrated, the

voids are also filled with dissolution medium and the surface area of the internal void will affect the dissolution and speed up the diffusion process. Take these factors into account, the surface area, an important steric parameter for the release profile, has been adjusted to Sa (Sa =surface area of pellet + surface area of void). The adjusted parameter ($M*(S_a/V)$) produced an improved correlation with higher R^2 values, as shown in Table 8 and Figure 56. b, demonstrating that the voids play a profound role during drug release.

Table 8 Correlation between the newly defined parameter and cumulative release amount at different release time points

Time(min)	$M*(S/V)$		$M*(S_a/V)$	
	Equation	R^2	Equation	R^2
15	y=18.6646x+14.6874	0.7620	y=15.5782x+19.0202	0.7290
30	y=31.2213x+19.7131	0.8414	y=26.6961x+24.9757	0.8448
45	y=42.3283x+21.2302	0.8944	y=36.2690x+28.1294	0.9019
60	y=53.5459x+14.2706	0.9172	y=45.8026x+23.2418	0.9216
90	y=63.6359x+7.2662	0.9306	y=59.7397x+18.3916	0.9406
120	y=79.7005x+6.6756	0.8964	y=68.8736x+17.8536	0.9193
180	y=101.7183x-9.8328	0.8912	y=88.1092x+3.7832	0.9183
240	y=120.8122x-35.6993	0.9184	y=103.9438x-17.3337	0.9337
300	y=131.6917x-57.3757	0.9204	y=113.7402x-38.7131	0.9429

Cluster analysis of release behaviour

During an attempt to categorise differences in drug release behaviour, a cluster analysis of the pellet release data was carried out using the k-means method (39) to force a three-group solution. Compared to the release profile of the unit dose capsules, the pellets were identified as quick (*n*=12), slow (*n*=24) and similar (*n*=38). The centre of cluster-1 shows similarities with the compositional release curve of all 74 tested pellets and the entire capsule at the dose level, as shown in Figure 57 a.
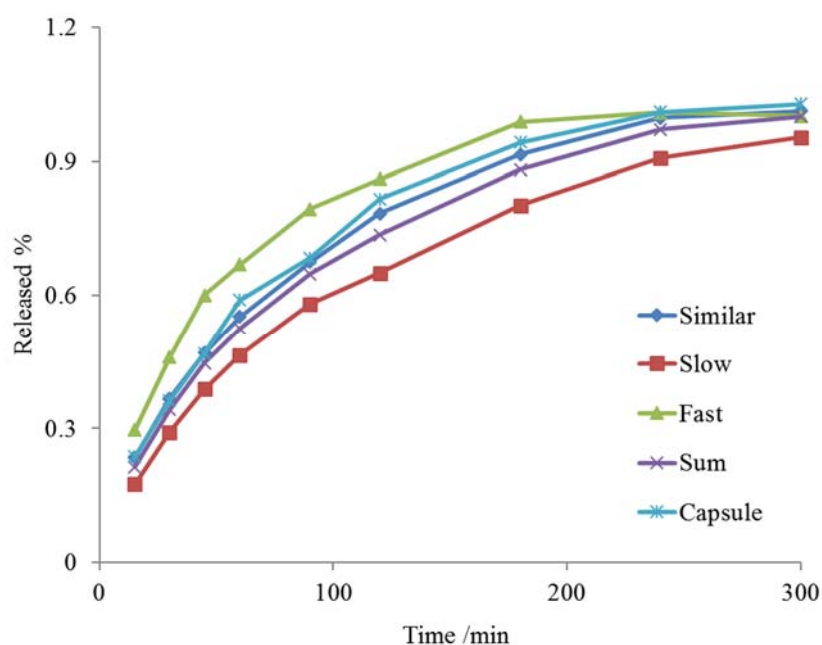
Figure 57 *Dissolution profile after clustering, the compositional release curve of all individually tested 74 pellets and the unit dose capsule dissolution*
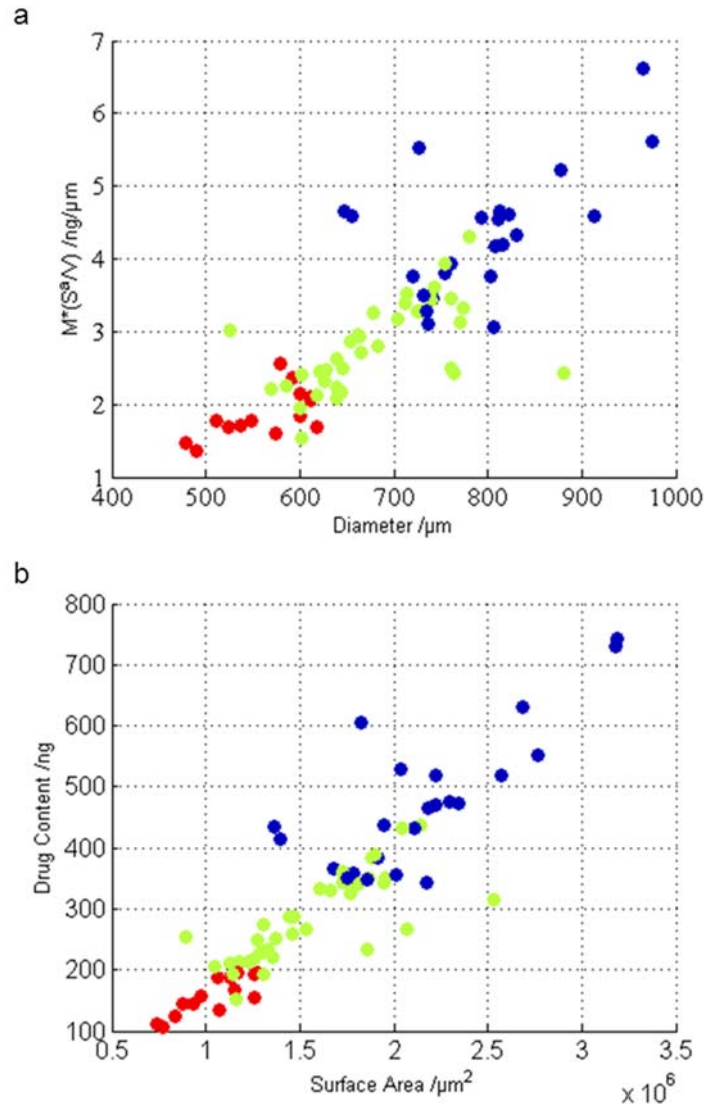
Figure 58 *Correlation between the diameter and M×(Sa/V)*

(a), surface area and drug loading (b) (green, Similar; blue, Slow; red, Fast)

The key structural parameters discussed above for the three groups are also clearly distinguished. In Figure 58 a, three colours (green, blue and red) represent clusters 1, 2 and 3, respectively. The three colours of the individual data points on the scatter plot (Figure 58 b) varied, demonstrating that the cluster result links strongly with the key structural parameters, such as diameter, surface area and drug loading.

These findings provide important knowledge regarding the investigation of drug delivery systems, specifically the visualization and quantification of the apparent morphology and internal void structure of the individual pharmaceutical pellets using SR-μCT imaging technology. This strategy also provides the opportunity to predict the effect of the pellet design parameters (e.g., shape, size and composition of pellets) on the resulting manufacturing process and drug release rate, thus facilitating the development of new pharmaceutical products. The proposed LC/MS/MS method yielded high quality single-pellet drug release data, even though the drug content of some pellets was as low as 100 ng. Experimental evidence has confirmed that the structure parameters that determine drug release are surface area, volume, and internal porosity. Further investigations using these methodologies can provide additional insight into the impact of other material and physicochemical properties on drug dissolution from solid dosing forms. Consequently, these analyses will provide knowledge and understanding of release mechanisms, thereby enabling the rational design, formulation and manufacture of solid dosing medicines with specific and controlled drug release profiles.

5.2 Fractal structure dependent release kinetics of osmotic pump tablets

The conventional in vitro dissolution tests for ODDS tablets with HPLC or LC/MS analysis can quantify the extent and rate of the drug release kinetics. The release profiles measured by conventional methods do not, however, provide the insight of the internal structure information of the ODDS tablet cores. Even though tight dissolution specifications are introduced to monitor the quality of the final

products, a number of batches of dosage forms often fail to meet in-house specifications, or even regulatory approval, and consequently have to be recalled from the market [21]. Thus, it is of interest to develop a new methodology to visualize the internal characteristics of the ODDS. When an internal structure method is established, the conventional in vitro release method can be calibrated. Modern in-vitro tomography techniques can directly reveal the internal structure and dynamic characteristics of ODDS tablet cores at different stages of the drug release process.

This section details studies of the internal 3D structure of commercially available monolith osmotic pump controlled release tablet containing the API of felopidine using SR-µCT, as used in chapter 4. The tablets tested in this study, Linuo®, are swelling monolithic osmotic tablets of felodipine with a viscous suspending agent(s) [131, 132]. The primary objectives are (i) to visualize the surface morphology, the internal 3D structure and their changing characteristics of the ODDS tablet core at different stages of the drug release process using a synchrotron radiation X-ray microtomography technique; (ii) to correlate the 3D steric data with the remaining percentages of the in the tablet core quantitatively and (iii) to elucidate the drug release mechanism of the monolith pump controlled release systems with the internal 3D steric data. Additional detailed experimental information is given S 6 Pre-treatment of felodipine osmotic pump tablets.

5.2.1 In vitro dissolution testing

In vitro drug release of the felodipine sustained tablet was measured using the basket method according to the Chinese Pharmacopoeia. The dissolution test was conducted with the rotation speed of 100 rpm, medium volume of 500 mL

and temperature of 37℃. 10 mL aliquot samples were withdrawn at 0.5, 1, 2, 3, 5, 6, 8, 10, 12h and equivalent volumes of fresh medium were added to maintain the sink condition. The samples were then filtered and analysed with the UV method at 361 nm (λ_{max} for felodipine).

In vitro release kinetics of felodipine from the ODDS

The dissolution profile of felodipine sustained release tablets showed a typical osmotic pump release profile (Figure 59). It was found that the zero-order model provides a good correlation coefficient for the test formulations (R = 0.9911), suggesting that the release rate of felodipine remains approximately constant.
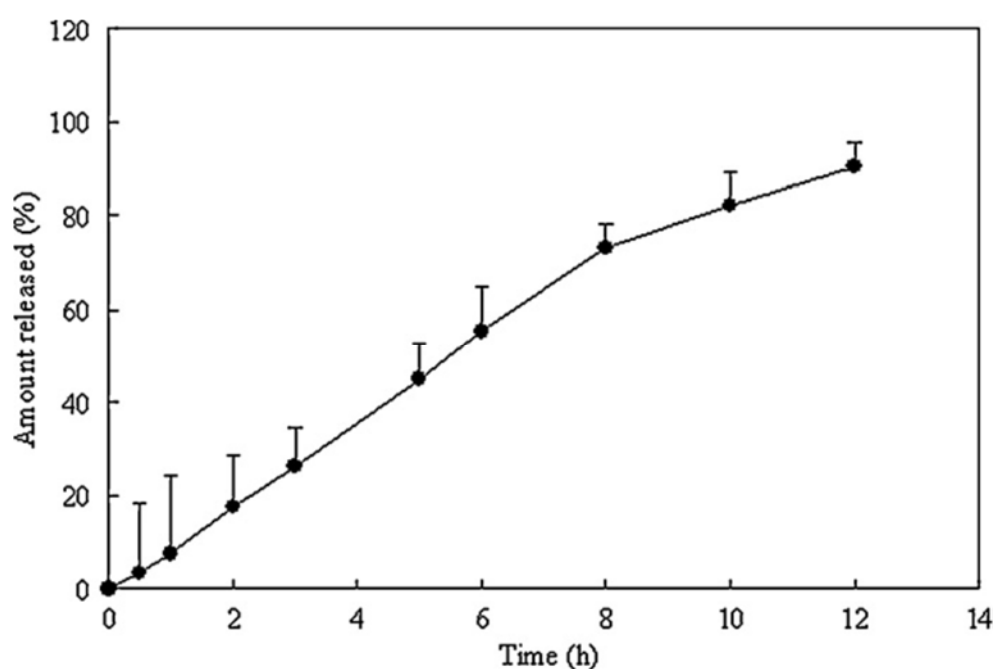
Figure 59 *The in vitro dissolution profiles of felodipine sustained release tablets (n = 6).*

Felodipine is a widely used antihypertensive drug with poor aqueous solubility, less than 10 µg/mL at ambient temperature [26]. For drugs with moderate or poor aqueous solubility, the osmotic delivery system delivers a portion of the drug as a suspension [27].

The drug release mechanism of MOTS is different from that of an elementary osmotic pump tablet (EOP) or a push-pull osmotic pump tablet (PPOP) [133]. In the dissolution medium, water is firstly imbibed from the environment through the difference of the osmotic pressure between the inside and outside of the semi-permeable membrane with the aid of the osmotic agent. Then, a viscous drug suspension is consequently formed in situ within the coated tablet, which is enabled by the presence of the suspending agent and the imbibed water. The suspension is subsequently pumped out through the orifices as a result of the swelling of the suspending agent. The drug release is co-controlled by both the osmotic mechanism and suspension mechanism, which can be expressed by the Poiseuille's law of laminar flow (Eq. 10)

$$\frac{dM}{dt} = \frac{\pi C}{8} \frac{R^4}{\eta} \frac{P_1 - P_2}{h}$$

Eq. (10)

Where dM/dt is the drug release rate, C is the concentration of drug in suspension, R is the radius of the orifice, η is the viscosity of the suspension, $(P_1 - P_2)$ is the pressure difference between two sides of the semi-permeable membrane and h is the thickness of the semi-permeable membrane. As shown in Eq. 10, the drug release rate is directly proportional to C, R^4 and $(P_1 - P_2)$, and inversely proportional to η and h. Values of $(P_1 - P_2)$ and η are dependent on the suspending agent. In summary, the dynamic process of the drug release from MOTS can be linked to the osmotic, suspending and expanding properties of the tablet.

5.2.2 Correlation between the 3D steric parameters and the remaining percents of felodipine in the tablet cores

The volume and surface area of the remaining tablets core are calculated from the reconstructed 3D images (Figure 60). The remaining percents of felodipine MOTS in the tablet cores at 0.5, 1.0, 3.0, 6.0 and 8.0 h are calculated by 100% minus the in vitro release percent of felodipine (Figure 60). As a result, the 3D volume values correlate well with the remaining percent of felodipine in the MOTS (R = 0.9988), suggesting that the 3D parameter accurately reflects the release characteristic of the felodipine MOTS.
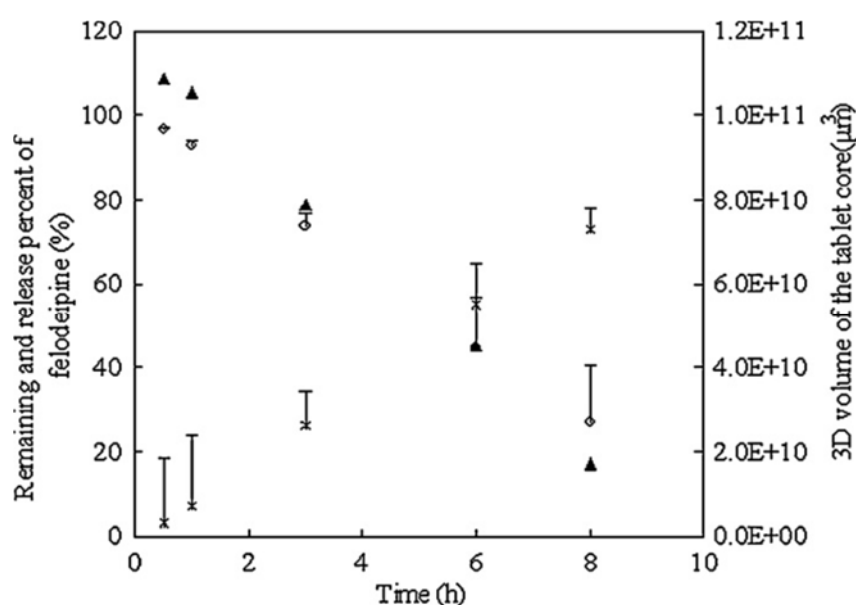
Figure 60 *Released percent and remaining percent of felodipine.*

Measured by in vitro dissolution testing plotted with 3D volume of the tablet core calculated from the reconstructed images ((*): the released percent; (○): the remaining percent; (△): 3D volume of the tablet core).

For MOTS, the release of felodipine is co-controlled by the osmotic pressure and suspension. Firstly, the pump is controlled by the osmotic mechanism, which is similar to the EOP systems. The water is imbibed and the suspension is created. Then, the core within the pump is covered by suspension liquid. The solid content of the tablet core (containing solid drug) is then eroded. Figure 61 illustrates the

two dimensional images of the cross-sections of felodipine MOTS acquired at 3.0 and 6.0 h, and the images are consistent with the occurrence of erosion of the solid content from the tablet core to the suspension. As a result of the osmotic pressure and suspension co-mechanism, the suspension is pumped out through the orifice, which is also similar to the EOP systems.
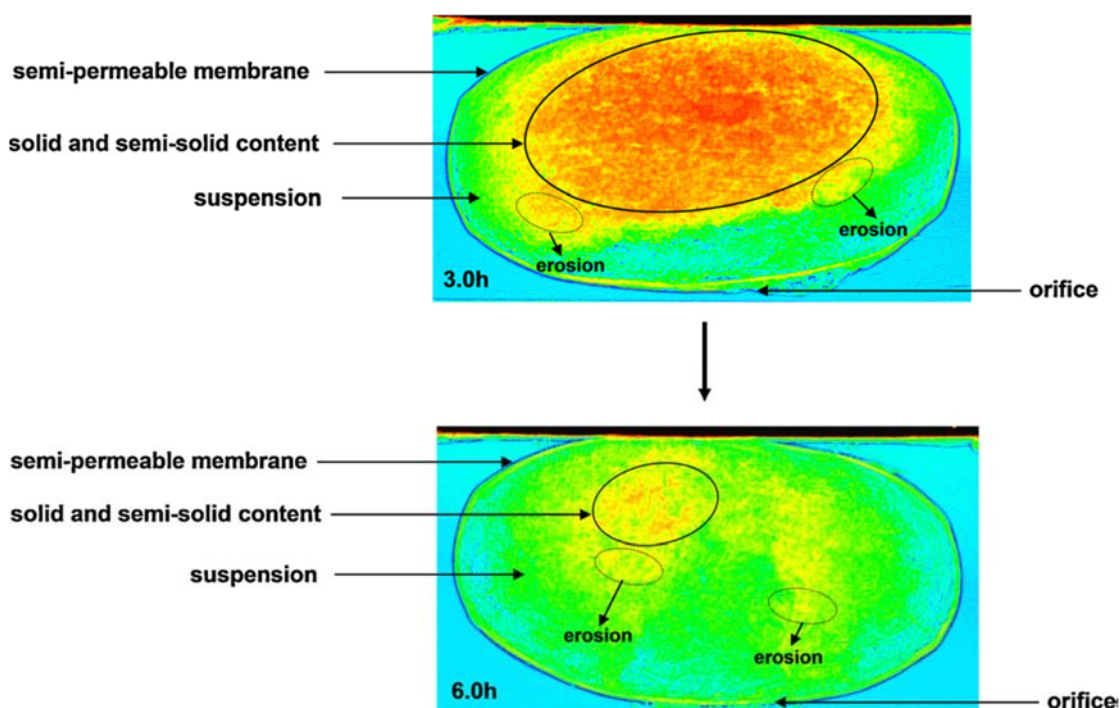
Figure 61 *Two dimensional images of the cross-sections of felodipine MOTS acquired at 3.0 and 6.0 h.*

Demonstrating the erosion of the solid content from the tablet core to the suspension, red represents the solid moiety of the tablet core, yellow represents the semi-solid moiety of the tablet core, air appears blue, and green represents the hydration layer.

Among these processes, the detachment of the solid content from the tablet core is complex. According to Eq. 9, for MOTS with zero-order drug release kinetics, values of R, η, (P_1-P_2) and h are nearly constant. However, the apparent value of C is dependent on the extent of solid content detached from the tablet

core to generate the suspension. It is the erosion controlled process and can be expressed as Eq. 11 [134].

$$\frac{dM}{dt} = \frac{DAC_s}{l}$$ **Eq. (11)**

Where D, A, C_s, and l are the diffusion coefficient, the surface area of diffusion or erosion, drug solubility, and the thickness of boundary layer, respectively. For a given drug and tablet, values of D, l and C_s in Eq. 10 are invariable parameters. The surface area of diffusion or erosion, namely, the surface area of the remaining tablet core.

Common sense might expect the surface area as well as the volume of the tablet core to decrease with the disappearance of the solid content during the drug release process. However, it is observed in our study that the surface area of the tablet core during the drug release process remains virtually unchanged whilst the shape of the internal solid content is changing markedly from ellipse to irregular shape with voids, which results in the 3D surface area values being almost constant.

In summary, values of C, R, η, (P_1-P_2) and h in Eq. 9 are all constant during the drug release process, which demonstrates the intrinsic mechanism of the drug release kinetics of the MOTS. Thus, the 3D surface area might be a key steric parameter for the quality control of the felodipine MOTS products

It has been shown that formulations with similar dissolution profiles can generate variable in vivo biological activities [135, 136]. This may be due to the dissolution profile lacking specificity and spatial resolution, which leads to an insufficient understanding of the intrinsic quality of drug delivery systems [21].

Tomographic imaging techniques, such as X-ray computed microtomography [22, 137], magnetic resonance imaging [138, 139] and terahertz imaging [140], offer a means to generate improved understanding of the structural characteristics of solid dosage forms. Further understanding of the hydration kinetics have been obtained through the imaging techniques, including the visualization of the surface morphology and internal structure (i.e. front position or layer thickness), the rate of water penetration into the polymer matrix, the polymer concentration across the formed hydrogel and the location of the drug substance in the hydrogel during swelling [141, 142]. In addition, mathematical models describing drug release mechanisms and critical parameters for successful formulation design have also been proposed [143].

Through 3D reconstruction in these studies, the calculated volume of the tablet core correlated well with in vitro drug release kinetics. The 3D surface area exhibited only minor changes during the dissolution process, which demonstrated the intrinsic mechanism of the controlled drug release. However, most of these studies provide only qualitative information on the surface morphology and internal structure of the tablets during drug dissolution, which are irregular, complex and continuously changing. A quantitative method or an indicator to define the complexity of the surface morphology and internal structure of tablets during drug dissolution is required.

5.2.3 Qualitative 3D fractal analysis of the tablet during drug release

Fractal analysis is a quantitative analytical method to characterize morpho-metric variability and complexity of an object in nature [144, 145]. Fractal analysis

has been applied in medical signal processing and pharmacokinetic modelling extensively. Using this concept, the irregular degree of the subject can be highly abstracted into a non-integer fractal dimensional value (Df) [146]. For solid pharmaceutical dosage forms, Df derived from surface imaging techniques have been employed to characterize the surface morphology of particles, mainly focusing on 2D static measurements, such SEM and AFM [147-150]. Information on surface roughness and shape for particles and tablets has been gained from the fractal dimension values. However, three dimensional fractal analysis and its relationship with controlled drug release has not been explored.

In this section, the concept of a three-dimensional fractal analysis based on box-counting method is explored with the aim of simultaneously quantifing the entire shape, interior porous channels and surface structure of felodipine osmotic pump tablets during the drug release process.

For fractal dimension calculation, the box-counting algorithm has been widely used in medical image processing due to the ease of implementation. Additionally, there is a strong correlation between this algorithm and classical geometry [151]. These factors indicate that using the box-counting algorithm can be a sound approach to generate fractal descriptors for the characterization of the internal complex structure of tablets during a release profile. Thus, the box-counting algorithm was employed to calculate the volumetric and surface fractal dimension using the reconstructions images acquired from SR-μCT.

3D objects were extracted from rendered data of solid tablet cores with Image-Pro 3D to obtain the mask of volume. From this volume, the sobel operator was performed to enhance the principle edges to obtain the mask of 3D surface

object. Then the bitmap information was extracted from the mask of 3D surface and volume to construct the point cloud matrix and the box-counting method was performed. Three dimensional fractal values of volume ($D_{f,\text{volume}}$) and surface ($D_{f,\text{surface}}$) of the solid core were calculated. The fractal dimension computing procedures are shown in Figure 62.
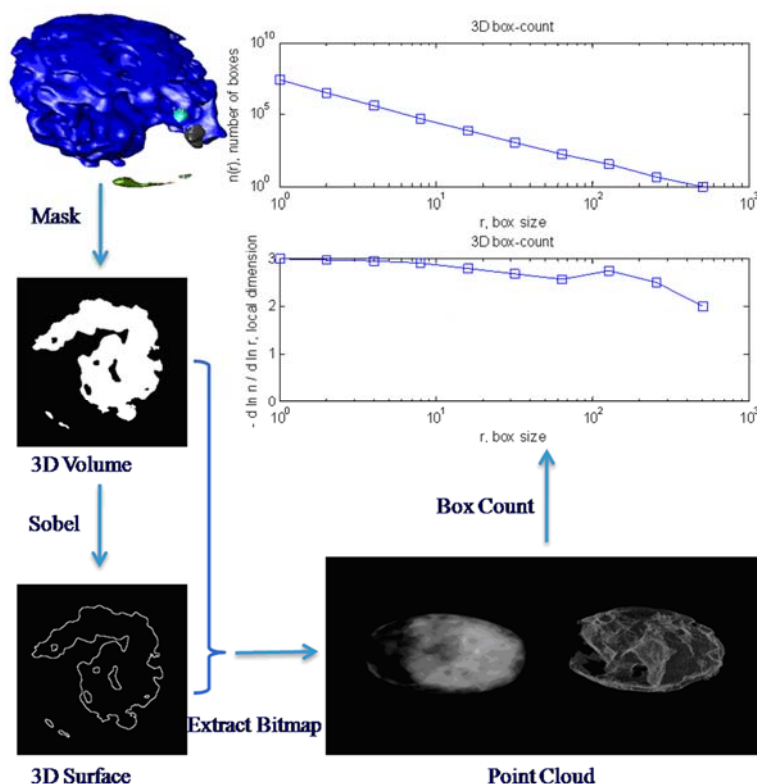
Figure 62 *Computing procedures for the fractal dimension values of the felodipine osmotic pump tablet core.*

 The computing sequence includes four steps: (1) 3D objects are extracted from rendered data of solid tablet cores with 3D reconstruction model in Image-Pro analyser software to obtain the mask of volume; (2) the sobel operator is performed to enhance the principle edges to obtain the mask of 3D surface object; (3) the bitmap information is extracted from the mask of 3D surface and volume to construct the point cloud matrix; (4) the box-counting method is performed and 3D fractal values of volume and surface of the solid core are calculated.

Due to the absence of solid fraction left after 10.0 h dissolution testing, the fractal analysis was carried out with the data between 0 and 8.0 h. $D_{f,volume}$ and $D_{f,surface}$ values of the osmotic pump tablet core during felodipine release are shown in Figure 63.

During felodipine release from the osmotic pump tablets, the values of $D_{f,volume}$ and $D_{f,surface}$ are both within the range of 2-3, indicating that the 3D structural complexity of the reconstructed tablet core was different from 2D fractal analysis derived form scanning imaging methods ($D_f \leq 2$). Values of $D_{f,volume}$ are maintained at 2.73 for the first three hours of drug dissolution, and then decrease, reaching a value of 2.3 after 8.0 h. However, for $D_{f,surface}$, values increase within the first three hours (from 2.28 (0.5 h) to 2.36 (3.0 h)) and then decrease to value of 2.25 at 8.0 h.
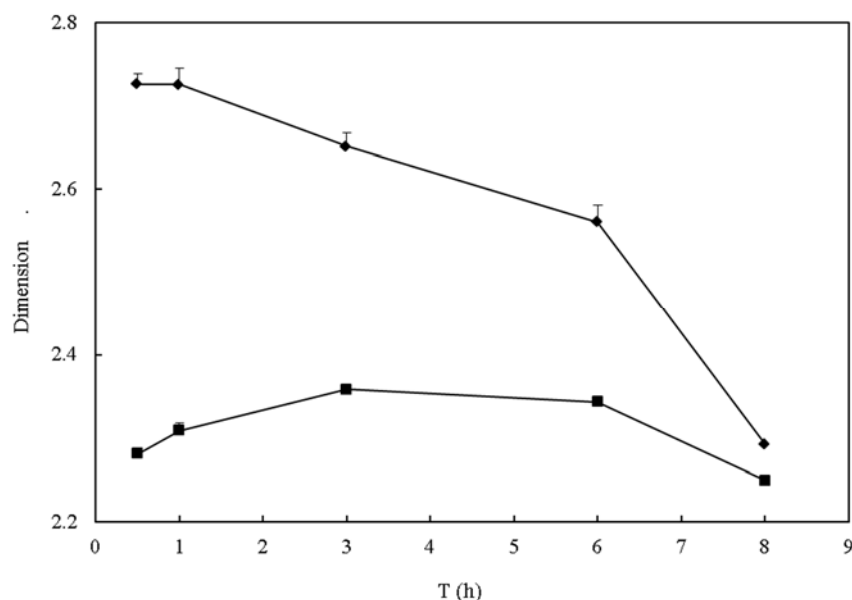
Figure 63 *The calculated Df,volume and Df,surface values of the reconstructed osmotic pump tablet core during felodipine release at sampling times of 0.5, 1.0, 3.0, 6.0 and 8.0 h.*

◆, Df,volume; ■, Df,surface. Error bars in these plots represent a range of standard deviations for triplicate samples, except for the time points of 1.0 h (n = 2) and 8.0 h (n = 1), due to the erosion of the tablet core and the variance of the drug release characteristics for the three tablets.

As can be seen from Figure 63, values of $D_{f,volume}$ and $D_{f,surface}$ change from 3.0 h, a time which corresponds to the extensive changes observed in the microstructure of the tablet core. This can be visualized from the 3D reconstructed images (Figure 64). The shape of the tablet is elliptic and some cracks can be seen at 0.5 and 1.0 h. As a result of the hydration of the tablet core, the shape of the core becomes more irregular with several voids present after 3.0 h. At 8.0 h, the solid content of the tablet core is approaching complete dissoluttion.
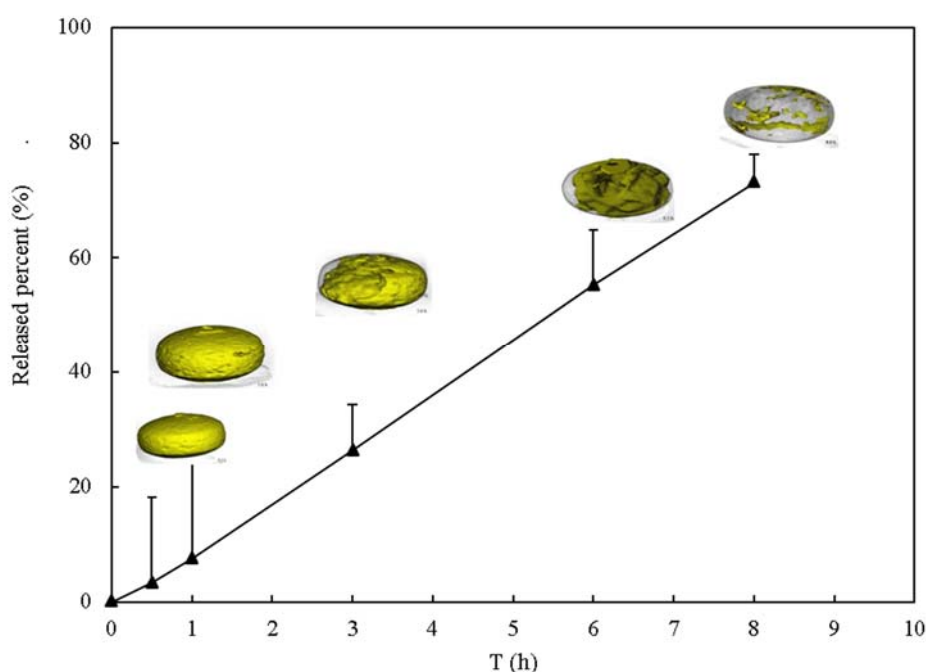
Figure 64 *The determined in-vitro dissolution profiles for felodipine osmotic pump tablets at sampling times of 0.5, 1.0, 3.0, 6.0 and 8.0 h (n = 6).*

The reconstructed 3D images for one of the three tablets in the imaging acquisition are shown (black represents the solid moiety of the tablet core, void appears grey).

165

5.2.4 Correlation between fractal dimension values and drug release

Correlations between $D_{f,volume}$ and the volume of the tablet core, $D_{f,surface}$ and the surface area of the tablet core have also been considered. As shown in Figure 65, the curve for $D_{f,volume}$ mirrors that of the volume of the tablet core, with a correlation coefficient (R) of 0.97 between $D_{f,volume}$ and the volume of the tablet core. However, the curve of $D_{f,surface}$ is different from that of the surface area of the tablet core, with the latter showing an initial upward profile followed by a decrease. In addition, no correlation is observed between $D_{f,surface}$ and the surface area of the tablet core. From these findings, it is proposed that the values of volume and surface area do not comprehensively represent the changes to the microstructure of the tablet core, which is especially complex during drug release. The value of fractal dimension reflects not only the size of object's volume (surface) but also the degree of spatial complexity of the object in 3D and provides an appropriate parameter to characterize the complexity of the dimensional changes of the tablet core during drug release.
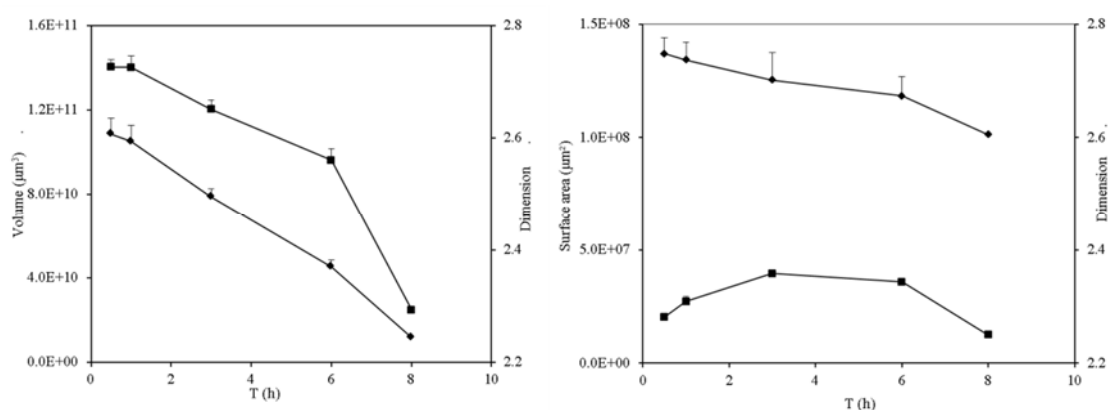
Figure 65 *The correlation between volume, surface and the corresponding Df.*

The calculated volume and Df,volume values (a, ◆, the volume of the reconstructed tablet core;

■, Df,volume) and the calculated surface area and Df,surface values (b, ◆, the surface area of

the reconstructed tablet core; ■, Df,surface) for the reconstructed osmotic pump tablet core during

felodipine release at sampling times of 0.5, 1.0, 3.0, 6.0 and 8.0 h. Error bars in these plots

represent a range of standard deviations for triplicate samples, except for the time point of 1.0 h

(n = 2) and the time point of 8.0 h (n = 1), due to the erosion of the tablet core and the variance

of the drug release characteristics for the three tablets.

As discussed in the previous section, the release of felodipine from a

monolith osmotic pump tablet is co-controlled by the osmotic pressure and drug

suspension. Also, the zero-order drug release kinetics is dependent on the extent

of solid content detached from the tablet core to the suspension, which can be

expressed as Eq. 11. The felodipine release from the tablet is determined by the

surface area of the tablet core.

The correlations between values of the fractal dimension and drug release

kinetics are shown in Table 9. A strong correlation exists between $D_{f,volume}$ and the

remaining percent of felodipine (R = 0.94), $D_{f,surface}$ and the felodipine release rate

(dM/dt, R = 0.99). No correlation is found when the $D_{f,volume}$ and $D_{f,surface}$ were

interchanged.

Table 9 Correlation between fractal dimension values and drug release kinetics

Time (h)	Released percent (%)	Remaining percent (%)	$D_{f,volume}$	dM/dt	$D_{f,surface}$
0.5	3.3	96.7	2.73	8.57	2.28
1	7.5	92.5	2.73	8.88	2.31
3	26.3	73.7	2.65	9.65	2.36
6	55.2	44.8	2.56	9.38	2.34
8	73	27	2.29	8.26	2.25
Correlation Coefficient		0.94[a]		0.99[b]	

[a]Correlation between the percentage of drug remaining in the tablet core and Df,volume.

[b]Correlation between the drug release rate and Df,surface.

The correlation between $D_{f,surface}$ and drug release rate can be expressed by Eq. 12.

$$\frac{dM}{dt} = 12.78 \cdot D_{f,surface} - 20.54$$ **Eq. (12)**

Therefore, $D_{f,surface}$ is an efficient fractal parameter that can be used to characterize the complex changes to the tablet core during drug release and can be regarded as a key indicator for assessing the quality control of felodipine osmotic pump tablets.

The 3D volume and surface area related fractal dimensional values were then calculated and correlated with drug release kinetics. Finally, the mechanism of drug release for felodipine controlled release system was elucidated through 3D fractal data.

In summary, a new method combining 3D fractal analysis and SR-µCT was developed to research the drug release kinetics of felodipine monolithic osmotic tablets. The values of $D_{f,volume}$ and $D_{f,surface}$ are both within the range of 2-3 and $D_{f,surface}$ correlated well with the felodipine release rate, which indicates that the 3D fractal analysis is not only able to characterize the microstructural changes to the tablet core during drug release process but also provide information on the final drug release performance of the product.

5.3 Quantification of swelling and erosion in hydrogel matrix tablets

5.3.1 Erosion studies testing

Detailed experimental information related to this section can be found in S 7 Pre-treatment of felodipine HPMC gel matrix tablet.

Felodipine extended release tablets (Plendil®, eachtablet containing 5 mg of felodipine) produced by AstraZeneca PLC has been investigated. In addition to the active ingredient felodipine, the tablets contained the following inactive ingredients: cellulose, red and yellow oxide, lactose, polyethylene glycol, sodium stearyl fumarate, titanium dioxide, and other ingredients. The rate of uptake of the dissolution medium by the tablets and the rate of polymer erosion were determined by gravimetric analysis methods. Dry matrix tablets were accurately weighed using a Mettler-Toledo ML-203 electronic balance (Mettler-Toledo, Inc.). In separate experiments, tablets were removed from the dissolution medium at 0.5, 1.0, 1.5, 2.0, 3.0, 4.0, 5.0, 6.0, 7.0, 8.0 and 10.0 h following exposure to the dissolution medium and lightly blotted with filter paper to remove excess water. The swollen tablets were weighed to determine the extent of water uptake and then dried in a convection oven at 40 °C. After 12 h the tablets were cooled to ambient temperature and then weighed This measurement was termed the dried weight. All studies were conducted in triplicate. The percent increase in tablet weight that can be attributed to the uptake or absorption of water was calculated at each time point using Eq. 13. The percent matrix erosion was estimated at each time point using Eq. 14.

$$\text{Swelling percent} = \frac{W_s - W_i}{W_i} \times 100\%$$ Eq. (13)

$$\text{Matrix erosion percent} = \frac{W_i - W_t}{W_i} \times 100\%$$ Eq. (14)

where W_s is the weight of swollen samples at sampling times, W_i is the initial weight of tablet and W_t is the weight of dried matrices at sampling times.

In vitro release kinetics of felodipine from the HPMC matrix tablets

Much attention has previously been paid to the mechanism governing drug release from hydrophilic matrices, where it has been suggested that the diffusion front at the interface between the undissolved drug and the dissolved drug in the hydration layer influences the rate of drug release from cellulose ether based systems. In addition, water penetration and/or diffusion are postulated to be the rate limiting steps for the release of highly water-soluble drugs. For poorly water-soluble drugs, matrix erosion is considered to provide a major contribution to the mechanism of the drug release [152]. Compared with studies on water soluble drugs, few quantitative analyses have been reported on the detailed contribution of swelling and erosion to the release mechanism of poorly soluble drugs.

In vitro dissolution profiles of felodipine tablets are shown in Figure 66 *B*. In order to describe the drug release mechanism, *n* values are obtained from the following well known equation proposed by Ritger and Peppas [153], as shown in Eq. 15.

$$\frac{M_t}{M_\infty} = kt^n$$ Eq. (15)

where M_t is the moiety of the drug released at time t, M_∞ is the moiety of drug released over a very long time that corresponds in principle to the initial loading, k is the kinetic constant and n is an exponent dependent on the release mechanism.

Since drug release occurs through the hydrophilic gel barrier created around the tablets, the rate of drug release from the matrix is dependent on the formation and viscosity of the hydration layer and its swelling or erosion rate. For a cylindrical matrix, values of $n \leq 0.45$ indicate Fickian release, values $0.45 < n < 0.89$ indicate anomalous release kinetics (coupled diffusion/relaxation) and $n \geq 0.89$ indicate a zero order release also known as purely relaxation controlled (erosion controlled) drug release. Studies of drug release from cylindrical matrices containing HPMC obtained values of the exponent n approximately 0.6 [154]. When a soluble polymer is used, linear drug release is obtained and the value of the exponent n is close to 1.0, implying an erosion controlled mechanism. In our study, the n value for the felodipine tablet is 1.09, indicating that erosion of the hydration layer is the dominant factor determining the extended release of felodipine. Our results are also in full agreement with the reported findings that erosion is the controlling factor for poorly water-soluble drugs in hydrophilic HPMC matrices [73, 74].

Hydration and erosion studies by gravimetric analysis

The gravimetrical analysis is a conventional procedure to study the hydration and erosion of tablets, although data obtained always exhibit relatively large errors. As a consequence, this methodology generally only provides qualitative information with regard to swelling and erosion. Thus in this study, the

gravimetrical analysis is used primarily as a qualitatively supplementary method to verify that erosion is a critical factor in the controlled release of felodipine from the tested tablets.

Figure 29 *C* (section 3.3.2) shows the results of weight gain and mass loss of felodipine tablets. The swelling rapidly increases to a plateau, and then decreases over the course of the dissolution test. The curves of swelling and erosion intersect at the time point between 5.0 and 6.0 h, after which the tablets do not demonstrate any further swelling. However, mass loss occurs throughout the entire time course of the dissolution process. Furthermore, erosion kinetics appears to follow a similar pattern to those of drug release, suggesting that erosion is a critical factor influencing the controlled release of felodipine from the tablets tested.

5.3.2 Correlation of the 3D hydration parameters with drug release kinetics

X-ray absorption of the glassy core is stronger than that of the hydration layer for the matric tablet. The density of the hydration layer is lower than that of the glassy core as the hydrated matrix is much more porous after the uptake of the dissolution medium. From these observations, it is possible to distinguish the hydration layer from the glassy core based on the X-ray intensity. Thus, the hydration layer has been extracted from the 3D models and quantitative steric parameters have been calculated accordingly.

23 three dimensional steric parameters have been calculated based on the extracted Iso-Surface models in this study. The names, descriptions and the units of these parameters are listed in Table 10.

Table 10 The names, descriptions and the units of the 3D parameters

3D Parameters	Description	Units
Volume of tablet	Volume of the whole tablet	μm^3
Volume of core	Volume of the unhydrated core	μm^3
Volume of hydration layer	Volume of the hydrated gel layer	μm^3
Surface of tablet	Surface area of whole tablet	μm^2
Surface of core	Surface area of unhydrated core	μm^2
surface of hydration layer	Surface area of the hydrated gel layer	μm^2
Specific surface of tablet	Surface area of tablet / Volume of tablet	μm^{-1}
Specific surface of core	Surface area of core / Volume of core	μm^{-1}
Specific surface of hydration layer	Surface area of tablet / Volume of tablet	μm^{-1}
Porosity of hydration layer	The volume of voids over the total volume	%
Length of whole tablet	Size of bounding box in Y direction	μm
Width of whole tablet	Size of bounding box in X direction	μm
Height of whole tablet	Size of bounding box in Z direction	μm
Box ratio of whole tablet	Ratio between the maximum and the minimum size of the bounding box	dimensionless

Box ratio of core	Ratio between the maximum and the minimum size of the bounding box	dimensionless
Sphericity of whole tablet	A measure of how spherical an object is	dimensionless
Sphericity of core	A measure of how spherical an object is	dimensionless
Surface deviation of tablet	Deviation of normal vectors on surface	dimensionless
Surface deviation of core	Deviation of normal vectors on surface	dimensionless
Volume fraction of tablet	Ration of object's volume to the box volume	Dimensionless
Volume fraction of core	Ration of object's volume to the box volume	Dimensionless
Diameter of tablet	Equivalent diameter of whole tablet	µm
Diameter of core	Equivalent diameter of unhydrated core	µm

With regard to correlations between single parameters and drug release kinetics, it is reported that the volume and surface area related parameters of the tablet are key variables in controlling drug release from HPMC matrix tablets [155]. Therefore, correlation between volume and cumulative release percent has been investigated, as shown in Figure 66 *A*, *B* and *C*. All the volume parameters, including volume of the whole tablet, volume of the glassy core and volume of the hydration layer, correlate well with percentages of drug release (R^2 = 0.90, 0.94, and 0.81 respectively). Generally, the correlation of the volume parameter to the cumulative release percentages are higher than that for those of single surface area parameters.
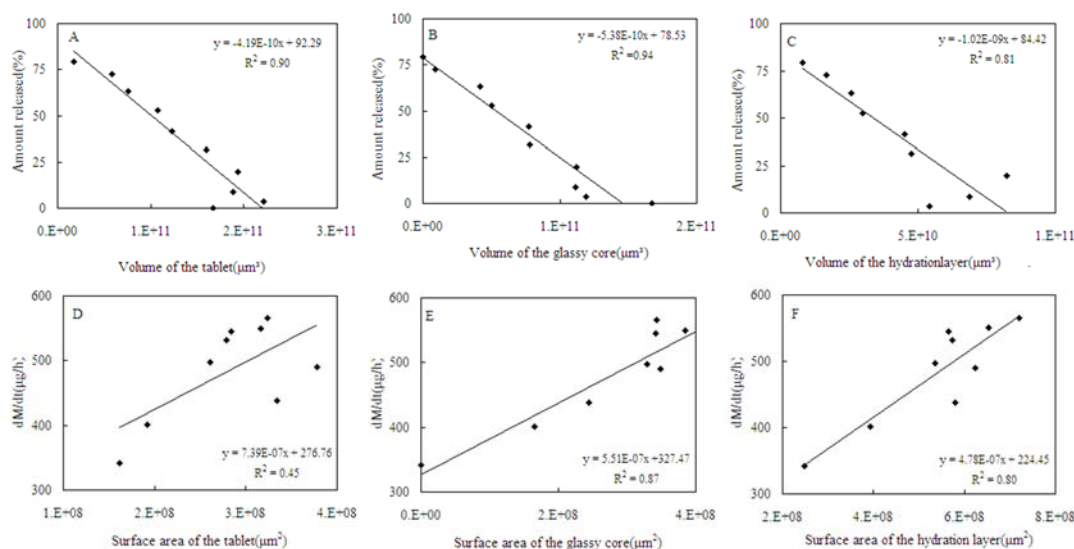
66 *Correlation between steric parameters and drug release kinetics.*

In contrast to the routine quality control indicators of the cumulative release percentages, drug release rate (dM/dt) values provide the key characteristics of drug delivery systems. Thus, the correlations between surface area parameters and drug release rate are shown in Figure 66 *D*, *E* and *F*. The R^2 values for these correlations are 0.45 for the surface area of the tablet and 0.80 for the surface area of the hydration layer, whilst the R^2 value between the surface area of the glassy core and the release rate is 0.87, indicating that the surface area of the glassy core is one of the key factors determining constant drug release rate. Namely, the matrix swelling has an important and controlling effect on the drug release kinetics.

In addition, a statistical model was constructed using SPSS PASW statistics (version 18.0) for multivariate analysis, using drug release rate as the dependent variable (n = 9). The sample of 0 h was excluded as the value of specific surface area of hydration layer at 0 h is not available. Independent variable reduction was carried out with the consideration of the value of R^2, the equation significance,

175

the parameter coefficient significance and physical meaning of the variables. Three parameters with marked influence on the drug release from felodipine matrix tablets were identified from 23 three dimensional structural parameters by independent variable reduction. There three parameters are surface area of hydration layer, surface area of glassy core and specific surface area of hydration layer.

Based on these three selected parameters, a multiple-linear regression model was established, as given in Eq. 16.

$$\frac{dM}{dt} = 420.4 \cdot SA_{hydration\ layer} + 128.4 \cdot SA_{glassy\ core} + 214.9 \cdot SSA_{hydration\ layer} - 23.4 \qquad \textbf{Eq. (16)}$$

The $SA_{hydration\ layer}$ is the surface area of the hydration layer, which includes the areas of pores and channels inside the hydration layer. The $SA_{glassy\ core}$ is the surface area of the non-hydrated glassy core, which is the interface where the glassy core swells into gel and hydration occurs. The $SSA_{hydration\ layer}$ is the specific surface area of the hydration layer (as shown in Table 9 and Figure 67), which reflects the magnitude of the hydration layer. All the relevant parameters in Eq. 16 have been normalized to ensure that all parameters have equal determinant strength to drug release rate. The statistical model exhibits relatively good predictability, with $R^2 = 0.96$ and significant p values (< 0.001).

5.3.3 Relative importance of swelling and erosion in controlled release of felodipine

Few researches have discussed the relative importance of swelling and erosion to the controlled release of poorly water-soluble drugs. Bettini et al. have studied the release mechanisms of drugs with different solubilities (buflomedil

pyridoxalphosphate with water solubility of 65% (w/v), sodium diclofenac with water solubility of 3.1% (w/v), nitrofurantoin with water solubility of 0.02% (w/v)) from HPMC matrices [156]. The role played by polymer swelling in drug transport was demonstrated with two different swelling/release experiments. The results showed that the tendency of the matrix to erode increased as drug solubility decreased. In swellable matrixes loaded with sparingly or slightly soluble drugs, solid drug particles can be transported within the hydration layer by polymer swelling. The presence of solid particles in the gel reduced the swelling and the entanglement of polymer chains and affected the resistance of gel towards erosion. As a consequence, the matrix became more erodible. The rate and amount of drug released from swellable matrices were dependent not only on the drug dissolution and diffusion but also on solid drug translocation in the gel due to polymer swelling.
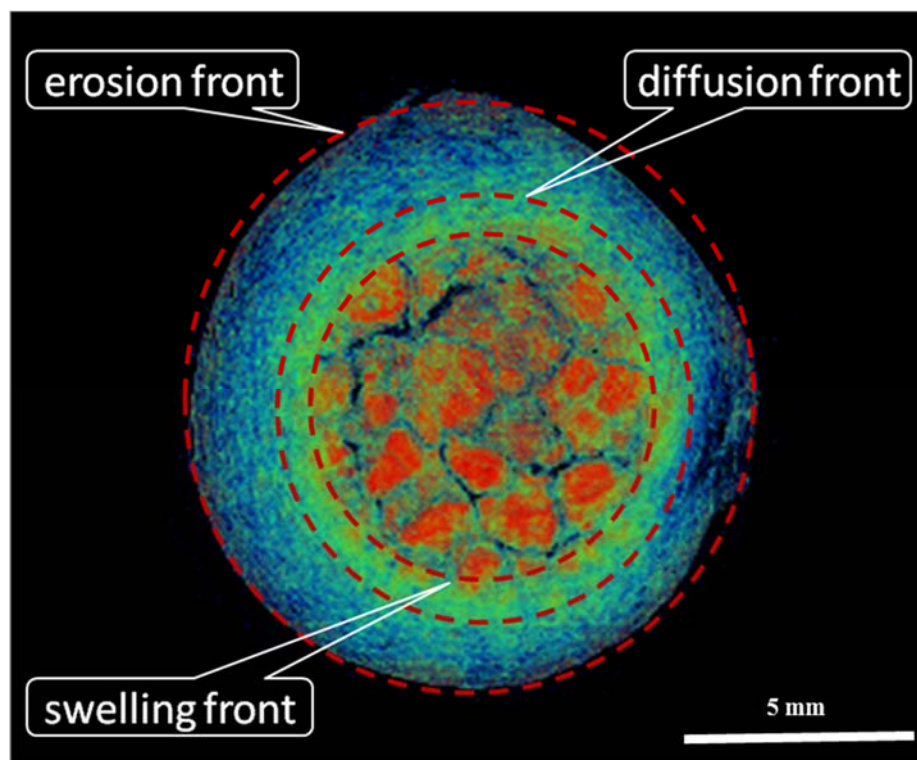
Figure 67 *Schematic of the layers of felodipine HPMC tablet during drug dissolution*

It can be observed from Eq. 16 that the rank order of the independent variables is $SA_{\text{hydration layer}} > SSA_{\text{hydration layer}} > SA_{\text{glassy core}}$. These three parameters represent the interface where the erosion and swelling of the hydrophilic matrix occur. The first two parameters represent the contribution of matrix erosion to controlled drug release, while the third represents the contribution of matrix swelling. Based on the quantitative relationship between 3D hydration parameters and drug release kinetics, drug release rate is determined primarily by matrix erosion. This finding is in accordance with the reported evidence that the matrix erosion governs the transport of poorly soluble drugs from the hydrophilic controlled drug release systems. Importantly, this model provides details of the quantitative contribution of matrix erosion and swelling to drug release rate for poorly water-soluble drugs with 3D hydration parameters that cannot be measured by conventional methods. Thus, the release mechanism is identified as a combination of erosion and swelling.

In this study, the relative importance of swelling and erosion in the controlled release of felodipine is quantified through the application of a statistical model and SR-μCT. The solubility of felodipine in the dissolution medium is 970 μg/mL (0.097%, w/v), which is relatively closer to the low level solubility of API (0.02%, w/v) in Bettini et al.'s study [156]. Although different techniques are used in these two studies, consistent results are obtained, the release of poorly water-soluble drugs from HPMC matrix being dominated by erosion and swelling. Furthermore, three dimensional structures of the hydration layer revealed in our study by SR-μCT with high resolution (9-micron) provides additional insight into the internal architecture of the swellable matrices as well as additional quantification of events controlling drug release. The 3D reconstruction and structural parameter

calculation methods detailed above are effective tools to visualize and quantify the translocation of drug particles in HPMC matrix hydration layers from a structural point of view.

Among 23 structural parameters, three key parameters were selected with a variable reduction to establish and optimize the statistical regression model, which covers nine data points over the release profile. For the constant release of felopidine during the sampling time period and limited SR-uCT beam time available, samples were obtained at nine time points to obtain as much data as possible from the imaging acquisition. Thus only a small sample model has been established. A large scale model or a real-time structure reconstruction, although challenging, would provide further in-depth information and knowledge. Nevertheless, the correlation coefficient (R^2) and the significance value (p) for the regression model are statistically significant.

Several imaging approaches have been employed to explore the hydration layer change during drug release. Among them, SR-μCT provides high spatial resolution. However, as the X-ray attenuation coefficient of water is similar to that of polymer material in the tablet, the image contrast would be affected when tablet is placed in aqueous dissolution media. To overcome this drawback in our study, the tablets were dried with the method caused minimal change to the structure of the tablet core. In addition, it is desirable to employ complementary methods to clarify chemical composition for the structural information obtained by SR-μCT, such as using MRI to identify the water content change or using matrix-assisted laser desorption/ionization (MALDI) to identify the drug position in the tablet core and the gel layer.

5.4 Dynamic Computed Tomography Reveals a Novel Release Mechanism Driven by Droplets

Novel controlled drug delivery systems are being explored to overcome the limitations of conventional formulations, which include sustained/controlled drug delivery system. The challenges involved are substantial but not insurmountable [157]. The osmotic system tablet that delivers constant release rates and is presented as a solid dosage unit with a laser-drilled hole in the surface of a polymer coating has been an attractive option [158]. 30 years of development and clinical use prove that these systems offer a promising technology for product life-cycle strategies [56].

Osmotic pump drug delivery systems with their versatility and highly predictable drug release rates offer various advantages and hold a prominent place in human medicines, such as reducing the risk of adverse reactions, independence from the environment pH of absorption site, and exhibiting a high degree of *in vitro/in vivo* correlation. As one of the most important formulations of controlled release preparation in the pharmaceutical field, various structures have been developed since the concept, "osmotic pump", was first invented by Rose and Nelson in 1955 [53]. From the Rose-Nelson elementary osmotic pump, design in structures has advanced markedly such as osmotic drug delivery using swellable-core technology, micro-osmotic pumps, asymmetric membrane capsule osmotic pump (ACM) and other new approaches. However it is not always desirable that a controlled release formulation provides zero-order drug release, and alternative release profiles are preferred, such as pulsatile drug delivery.

Despite the extensive research carried out on osmotic pump drug delivery system with various structures, tuning the internal structures and understanding the release mechanisms remain a challenge, especially for understanding the role of fine micro-structures. With most research focusing on the macro scale, it is thought that innovation in the design of new osmotic pump drug delivery systems will result from examination of internal micro-structures. As demonstrated above it has been established that a drug release profile is closely related to dynamic changes in microstructure, and fractal structure determines the controlled release kinetics of monolithic osmotic pump tablets. The values of $D_{f,surface}$ correlated well with the drug release rate and $D_{f,surface}$ was found to be an efficient fractal parameter that could be used to characterize the complex changes in the tablet core that take place during drug release [159].

Tools which directly reveal the internal structure and dynamic characteristics of the osmotic pump tablets at different stages of the drug release process, such as benchtop-magnetic resonance imaging (BT-MRI) [160], terahertz pulsed imaging (TPI) [161], magnetic resonance imaging (MRI) [162] and X-µCT [163] are some of the popular techniques can be applied to reveal deeper understanding of dosage form static structures. SR-µCT imaging technique, is able to provide quantitative details of the internal three dimensional (3D) structures of various objects as demonstrated above.

During studies for this thesis with 3D reconstructions of an osmotic tablet containing PVP/VA, numerous micro-droplets were observed. After contact with solution media, the structure of micro-droplet presented a certain evolution regularity. Whilst not all osmotic pump tablets will possess this kind of structure, a hypothesis is proposed that there will be a relationship between the micro-

droplets structure and the drug release behaviour. The following study details which research into how the micro-droplets are formed and how to adjust the evolution of the micro-droplets to achieve zero-order controlled release of drugs using the dynamic CT.

Detailed methodology of these studies is provided in S 8 Preparation and structural analysis of droplet generated tablet)

5.4.1 Discovery of droplet like structures in osmotic pump tablets

Ketoprofen, a nonsteroidal anti-inflammatory drug (NSAID) regarded as a nonselective cyclooxygenase (COX) inhibitor and described as practically insoluble in water (<1 g in 100,000 ml) [164, 165]. The design of a ketoprofen osmotic pump tablets aimed to deliver well-controlled drug release over 12 hours. The tablet composition was 50.0 mg of ketoprofen, 58.1 mg of copovidone (PVP/VA S630), 10.7 mg of sodium phosphate (Na_3PO_4) and 1.2 mg of magnesium stearate. of The powders for the osmotic pump cores were passed through 100# sieve and mixed in geometric proportion to form a uniform blend of powder, prior to direct compression on a rotary tablet machine (ZP-5, Shanghai Tianjiu Machinery Factory) using 6.0-mm-diameter punches. CA in acetone containing plasticizer (PEG 4000) was used as a coating solution. The coating was carried out in a pan coater (BY 300A, Shanghai Huanghai Drug Instrument Co., Ltd., China). The temperature of the coating pan was 40℃, rotating at 25rpm. The coated tablets were dried to remove the residual solvent acetone at 40℃ for 24 h, and laser machines drilled (CRS-C20D, Ceres Wuhan Photoelectric

Technology Co., Ltd., China) a single 0.8-mm-diameter orifice on the membrane surface on one of the faces of the tablet.

During the drug released process, the dynamic structure of tablets was investigated with 2D X-Ray Imaging for tablets removed at different times during the drug release process. Droplet-like structure were observed (Figure 68) as well as internal structure of stationary ketoprofen osmotic pump tablets in water with the drug release orifice upward using SR-μCT. As water was taken up by the tablet through the semipermeable membrane, numerous micro-droplets were generated *in situ* continuously in the osmotic pump tablet with the core, also containing fluid, suspension and/or gel. All the micro-droplets migrated to the drug release orifice close to the semipermeable membrane and those generated opposite the orifice chose the shorter way to reach the orifice (Figure 68). Ultimately, the micro-droplets which exited from the orifice gradually diffused and mixed in the bulk aqueous dissolution medium outside of the semipermeable membrane and the majority of the micro-droplets appeared to have uniform size and shape.
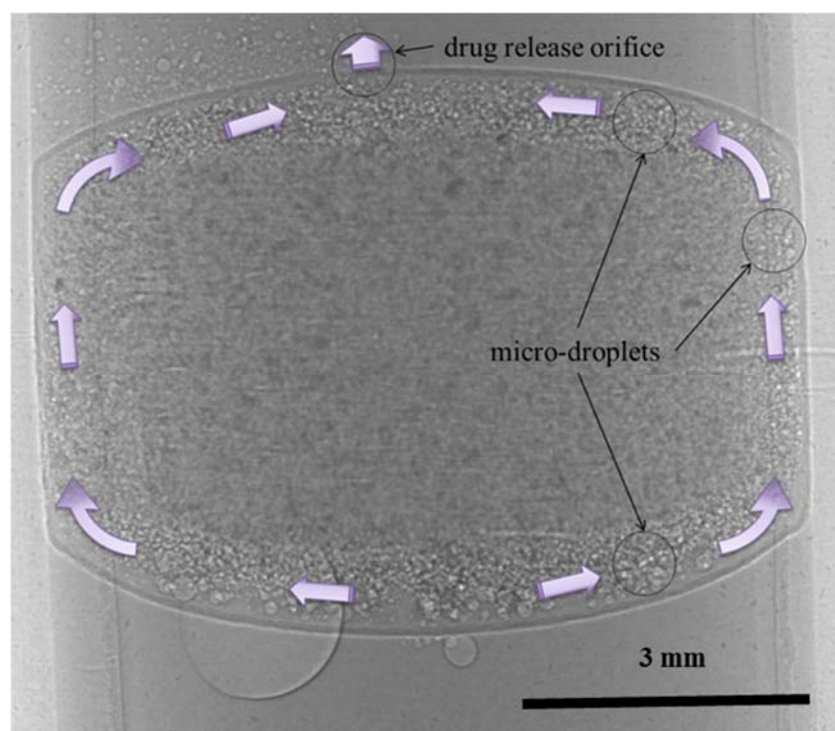
Figure 68 *Numerous micro-droplets generated in the ketoprofen osmotic pump tablets and moved to the drug release orifice through the shorted way when set in water.*

After the first observations of the droplet-like structure in the laboratory made ketoprofen osmotic pump tablets, different formulation compositions were prepared in an attempt to identify the key factors that cause the formation of micro-droplets. Four kinds of osmotic pump tablet were prepared according to the formulations shown in Table 11. All tablets were coated with the same semipermeable membrane and the same size of laser drilled orifice.

Table 11 Composition of the core of osmotic pump tablets

Core (tablet)	Per tablet (mg)			
	A	B	C	D
Na_3PO_4	10.7	0.0	0.0	10.7
PVP/VA	58.1	58.1	58.1	58.1
ketoprofen	0.0	50.0	0.0	50.0
MS	1.2	1.2	1.2	1.2

(* Note: Formulation D is the tablet core formulation described and discussed above)
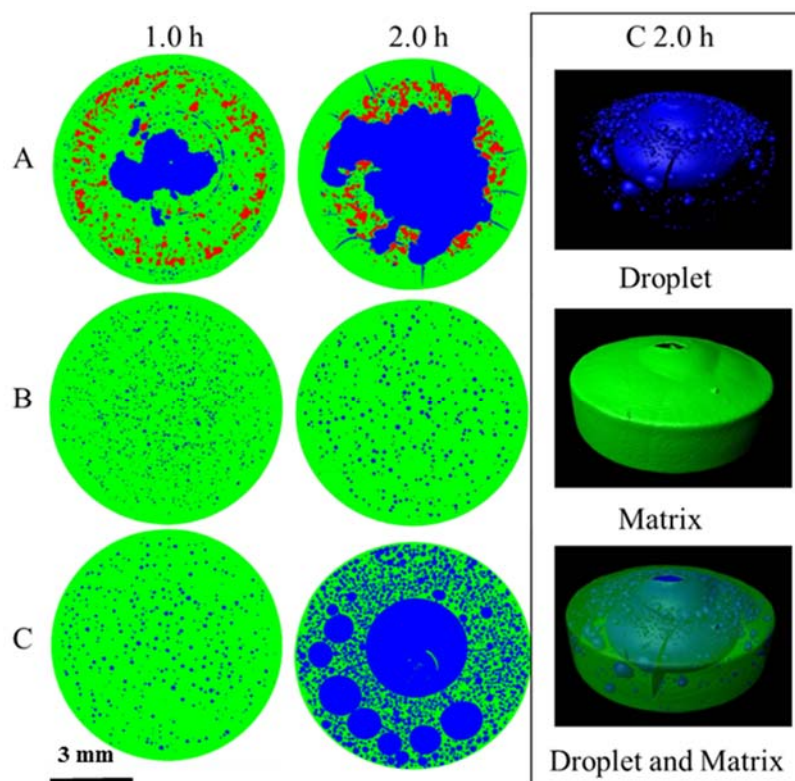
Figure 69 *2D and 3D internal structure of three kinds of osmotic pump tablets at 1.0 h and 2.0 h.*

(Blue represents the micro-droplets, green represents the remaining matrix, red represents NaCl). (*A*) Osmotic pump tablets containing copovidone and sodium phosphate (*B*) ketoprofen and copovidone and (*C*) copovidone.

Formulations A, B and C osmotic pump tablets were tested with SR-μCT after immersion in water for 1.0 h and 2.0 h. The plane slices (Figure 69) indicated difference in the degree of droplet generation for these three osmotic pump tablets formulations. Droplets in osmotic pump tablets containing PVP/VA and sodium phosphate are irregular. Droplets in tablets containing ketprofen and PVP/VA appear slowly and the sizes of droplets are small. Tablets containing PVP/VA contain many and multi-sized spherical droplets. From one plane slice of osmotic pump tablet only containing PVP/VA at 2.0 h in Figure 69, 1950 fine

spherical micro-droplets formed in the tablet with the min and max diameters of 4 μm and 2054 μm. These structral information indicates the PVP/VA might be the material base of the generation of droplet.

Cumulated dissolution release profile and release rate of ketprofen osmotic pump tablets of formulation D are demonstrated in Figure 70. The zero-order kinetic model provides a strong correlation coefficient for the test formulations (R^2 = 0.9796) over the period 0 - 10 hours and the cumulative release after 12 hours was over 93%.
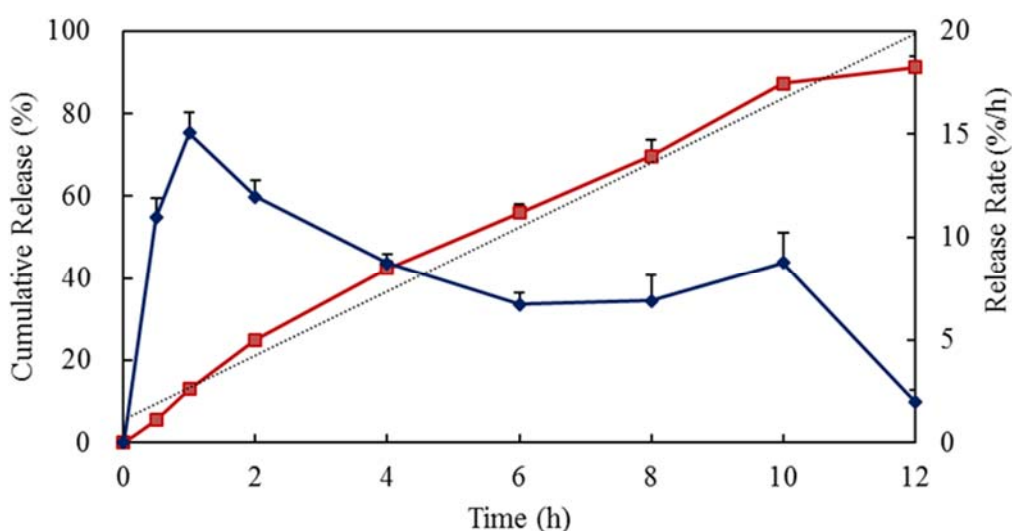
Figure 70 *Drug release profiles of ketoprofen osmotic pump tablets of formulation D with a nearly zero-order controlled release behaviour, n = 6.*

5.4.2 Quantitative evolution regularity of droplet-like structure

To understand the evolution regularity of droplets in the osmotic pump tablets, ketoprofen osmotic pump tablets of formulation D were examined after different periods of time immersed in water at 37℃ by SR-μCT. To describe and quantify the internal structure accurately, all the tablets were dried naturally to avoid the influence of water on the measurement. Numerous micro-droplets were detected

at 0.5 h, and with increasing time, the micro-droplets gradually move toward the table core and merged into a few larger droplets. From one slice at 0.5 h, 537 micro-droplets with 33 µm mean diameter were detected. As the core hydrated further at 1.0 h, the mean diameter and number of micro-droplets increased slightly with one plane slice at 1.0 h, 544 micro-droplets with a mean diameter of 37 µm. A smaller number of bigger micro-droplets with the max diameter of 132 µm, also emerged in the zone of the fully hydrated core and several micro-droplets were observed in the centre of the core. Whilst the number of micro-droplets decreased at 1.5 h due to coalescence, a single droplet with the diameter of 1592 µm was present. At 2.0 h, the mean diameter of micro-droplets and the largest droplet further increased to 58 µm and 2730 µm, respectively. Droplets could be seen concentrated at the core centre at 3.0 h with the largest micro-droplets occupying approximately 30% volume of the tablet. At 4.0 h, one large droplet with a diameter of 4531 µm with surrounding microdroplets surrounding was identified and at 6.0 h and 8.0 h, all the micro-droplets had coalesced into a single droplet occupying the whole region of the dissolved core. This sequence is illustrated in Figure 71. As displayed with Figure 71. D, the co-localization demonstrate micro-droplets and Na_3PO_4 are associated in deposits. This phenomenon indicate the recrystallization of dissolved Na_3PO_4 in micro-droplet might take place during the drying of tablet.
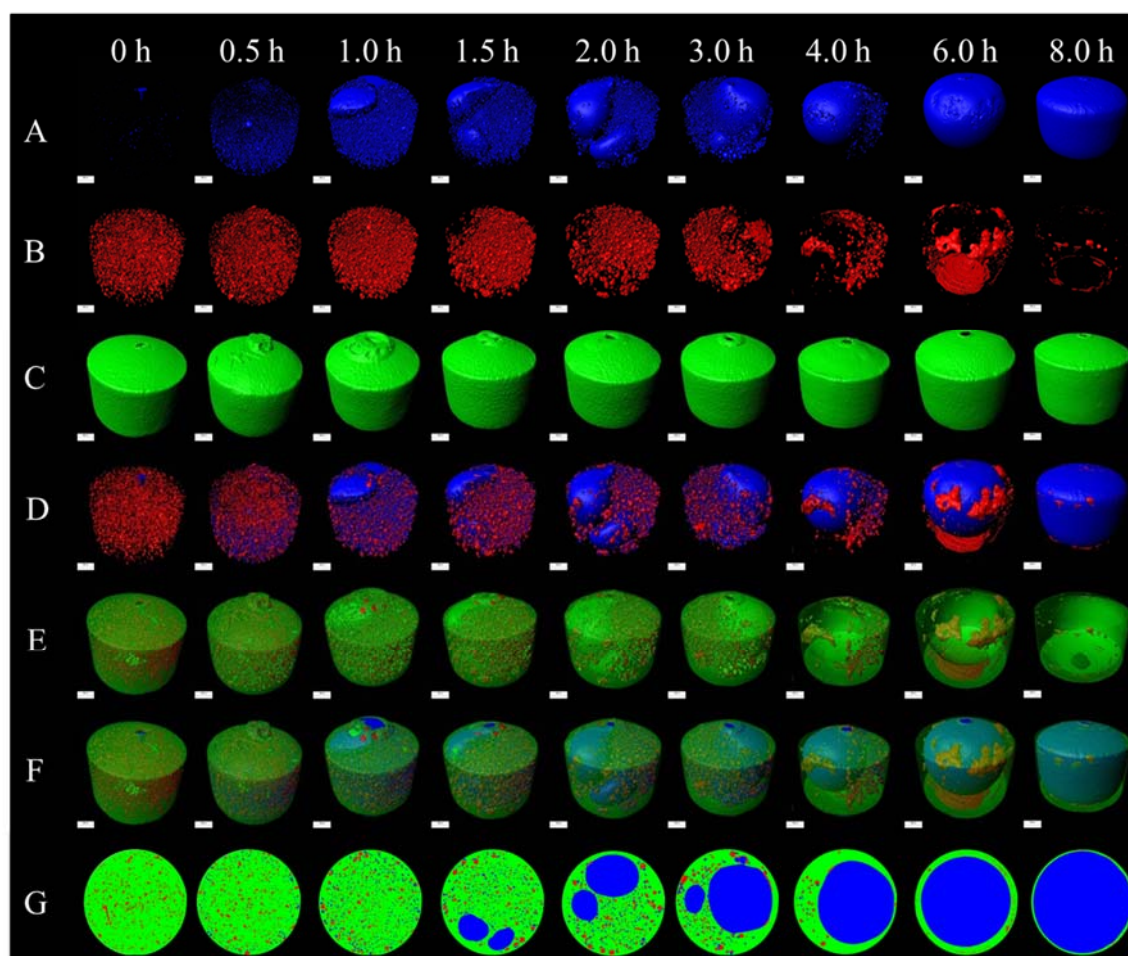
Figure 71 *Internal structure of ketoprofen osmotic pump tablets at different time*

(blue represents the micro-droplets, red represents the Na_3PO_4, green represents the remaining matrix). Time interval observations of (A) generation and evolution of micro-droplets, (*B*) distribution of Na_3PO_4, (*C*) morphology of the matrix, (D) relationship of micro-droplets and Na_3PO_4,(*E*) distribution of Na_3PO_4, (*F*) distribution of micro-droplets with Na_3PO_4 and(*G*) plane slices of ketoprofen osmotic pump tablets, the scale bar is 2000 μm.

The quantitative tracking of the micro-droplets at a different time reveals was obtained from collected data (Figure 71. From these tracks, droplets are identified and seen to move to the core centre in diminishing number as time increase (Figure 72). Although the position of micro-droplets is not the same in the different tablets examined, the evolution tendency is consistent.
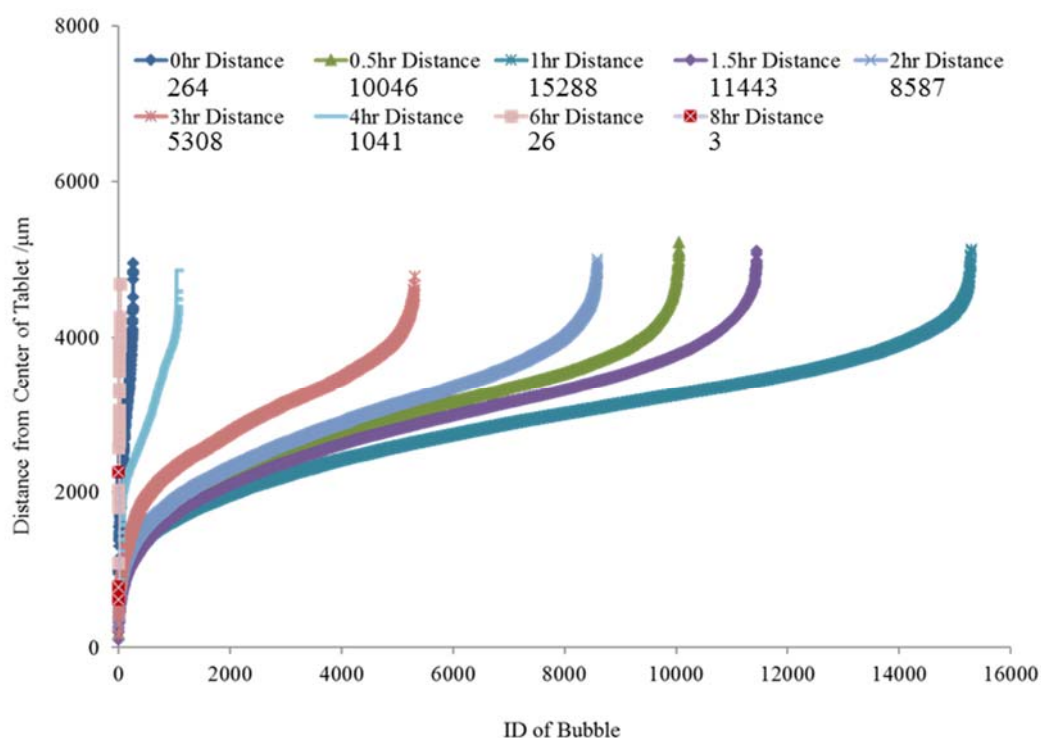
Figure 72 *Distribution of micro-droplets in the ketoprofen osmotic pump tablet at different time (labelled with the total number of micro-droplets)*

The correlation of micro-droplets volume and drug release

In probing correlations between drug release and 3D structure parameter, the area and volume of micro-droplets, Na_3PO_4, matrix and Na_3PO_4-matrix were choosen for analysis (Figure 73). Using surface area as the 3D structure parameter, the area of Na_3PO_4 showed a relatively good correlation with the cumulative drug release ($R^2 = 0.9006$). The correlation index (R^2) between the drug release and the micro-droplets volume, matrix and Na_3PO_4-matrix were all weaker ($R^2 < 0.90$). When using volume as the 3D structure parameter, the correlations with the drug release improved, ($R^2 > 0.95$) with a correlation index of $R^2 = 0.3184$. Over all, the total volume of micro-droplets with drug release showed the best index ($R^2 = 0.9803$).
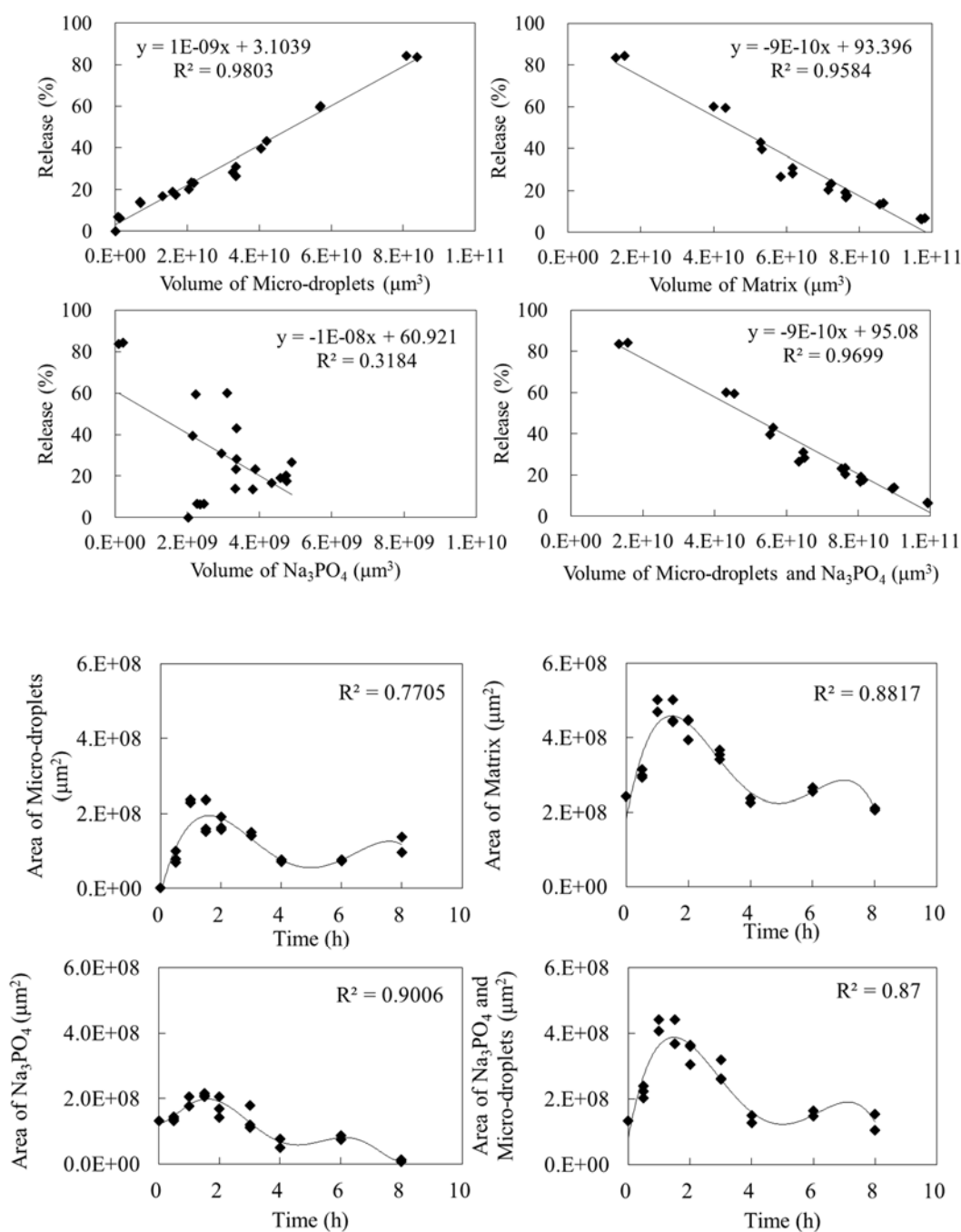
Figure 73 *Correlation between drug release and total area/volume of micro-droplets, Na₃PO₄ and matrix of ketoprofen osmotic pump tablets.*

5.4.3 Release mechanism revealed by dynamic computed tomography

The internal structure is a critical factor in the design of drug delivery systems. In osmotic pump formulations. Microporous, sandwiches, mixed pass,

asymmetric membrane osmotic pumps, and other osmotic pump varieties have appeared in recent years. These forms expressed unique dosage form structural complexity and diversity and provided different drug release characteristics and beneficial clinical outcomes. These innovative structures have promoted the development of other sustained and controlled release dosage forms. For any new structured dosage form designs based on internal fine dynamic droplet-containing structures, an important requirement is a theoretical demonstration and application value to investigate of any new drug release mechanism and potential application benefit in therapeutics.
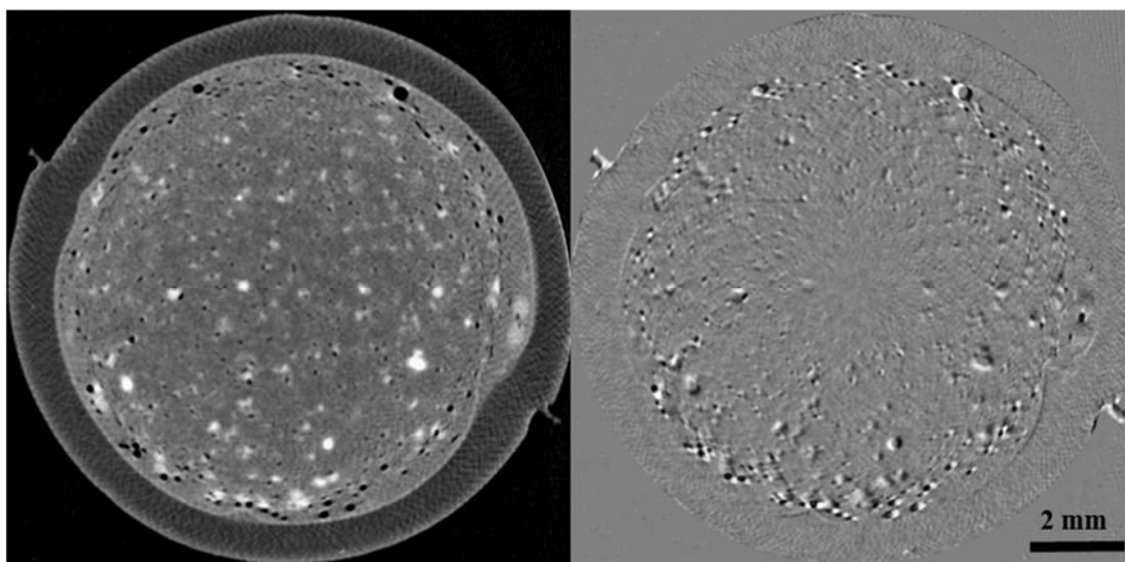
Figure 74 *Reconstructed slice after phase retrieval and the position correction by alignment*

After the phase retrieval and position correction, quantification of the dynamic evolution of the 3D structure of osmotic pump tablets, based on the optimized reconstruction algorithm was performed (Figure 74) on data obtained from formulation D. Droplets present at different dissolution times were quantified according to the following list of parameters:

a) **Area.** *The sum of the triangle surfaces.*

b) Centre Position X Y Z

c) Ellipsoid Axis

In mathematics, an ellipsoid is a type of quadric that is a higher dimensional analogue of an ellipse.

The equation of a standard ellipsoid in an x-y-z Cartesian coordinate system is:

$$\frac{x^2}{a^2} + \frac{y^2}{b^2} + \frac{z^3}{c^2} = 1 \qquad\qquad \text{Eq. (18)}$$

where a, b and c (the lengths of the three semi-axes) are fixed positive real numbers determining the shape of the ellipsoid.

Ellipsoid
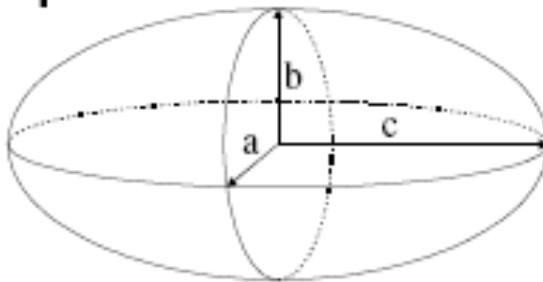
Surfaces - Ellipsoid (oblate)

Surfaces - Ellipsoid (prolate)

If we assume $a \leq b \leq c$*, then when:*

- *a = 0   it is an Ellipse*

- *a = b = c   it is a Sphere (three equal sides)*

- *a ≠ b ≠ c   it is a scalene Ellipsoid (three unequal sides)*

If two of these sides are equal, the Ellipsoid is a Spheroid:

- $a = b < c$ *it is a prolate Spheroid (cigar-shaped)*

- $a < b = c$ *it is an oblate Spheroid (disk-shaped)*

$$e_{prolate} = \frac{2a^2}{a^2+b^2} * \left(1 - \frac{a^2+b^2}{2c^2}\right)$$ **Eq. (19)**

$e_{prolate}$ = *prolate Ellipsoid*

$$e_{prolate} = \frac{2b^2}{c^2+b^2} * \left(1 - \frac{2a^2}{c^2+b^2}\right)$$ **Eq. (20)**

e_{oblate} = *oblate Ellipsoid*

d) **Speed,** *is the instantaneous speed of the object.*

$$S(t) = \frac{\sqrt{D_X(t,t-1)^2 + D_Y(t,t-1)^2 + D_Z(t,t-1)^2}}{T(t)-T(t-1)}$$ **Eq. (21)**

S(t) = TrackSpeed

$$D_X(t_1, t_2) = P_X(t_1) - P_X(t_2)$$ **Eq. (22)**

$P_X(t)$ = x-position of object at time index t

T(t) = time in seconds at time point t

e) **Track Sphericity,** *is a measurement parameter that tells how spherical an object is. Defined by Wadell in 1932, the sphericity, Ψ, of a particle is the ratio of the surface area of a sphere (with the same volume as the given particle) to the surface area of the particle:*

$$\Psi = \frac{\pi^{\frac{1}{3}}(6V_p)^{\frac{2}{3}}}{A_p}$$ **Eq. (23)**

Vp = volume of the particle

Ap = surface area of the particle

f) **Time Index,** *number indicates the current time point in the series for the selected object.*

g) **Track Duration,** *is the duration between the first and last time point within the Track.*

$$\text{Duration} = T(t_L) - T(t_F)$$

Duration = TrackDuration

T(t) = time in seconds at time point t

t_L = last time index of track

t_F = first time index of track

h) **Track Length,** i*s the total length of displacements within the Track.*

$$L = \sum_{t=t_F+1}^{t_L} \sqrt{D_X(t,t-1)^2 + D_Y(t,t-1)^2 + D_Z(t,t-1)^2} \qquad \textbf{Eq. (24)}$$

L = TrackLength

t_L = last time index of track

t_F = first time index of track

$$D_X(t_1, t_2) = P_X(t_1) - P_X(t_2) \qquad \textbf{Eq. (25)}$$

$P_X(t)$ = x-position of object at time index t

i) **Track Straightness**

$$Straightness = \frac{\text{Displacement}}{\text{Length}} \qquad \textbf{Eq. (26)}$$

j) Volume, *is a quantification of how much space an object occupies.*
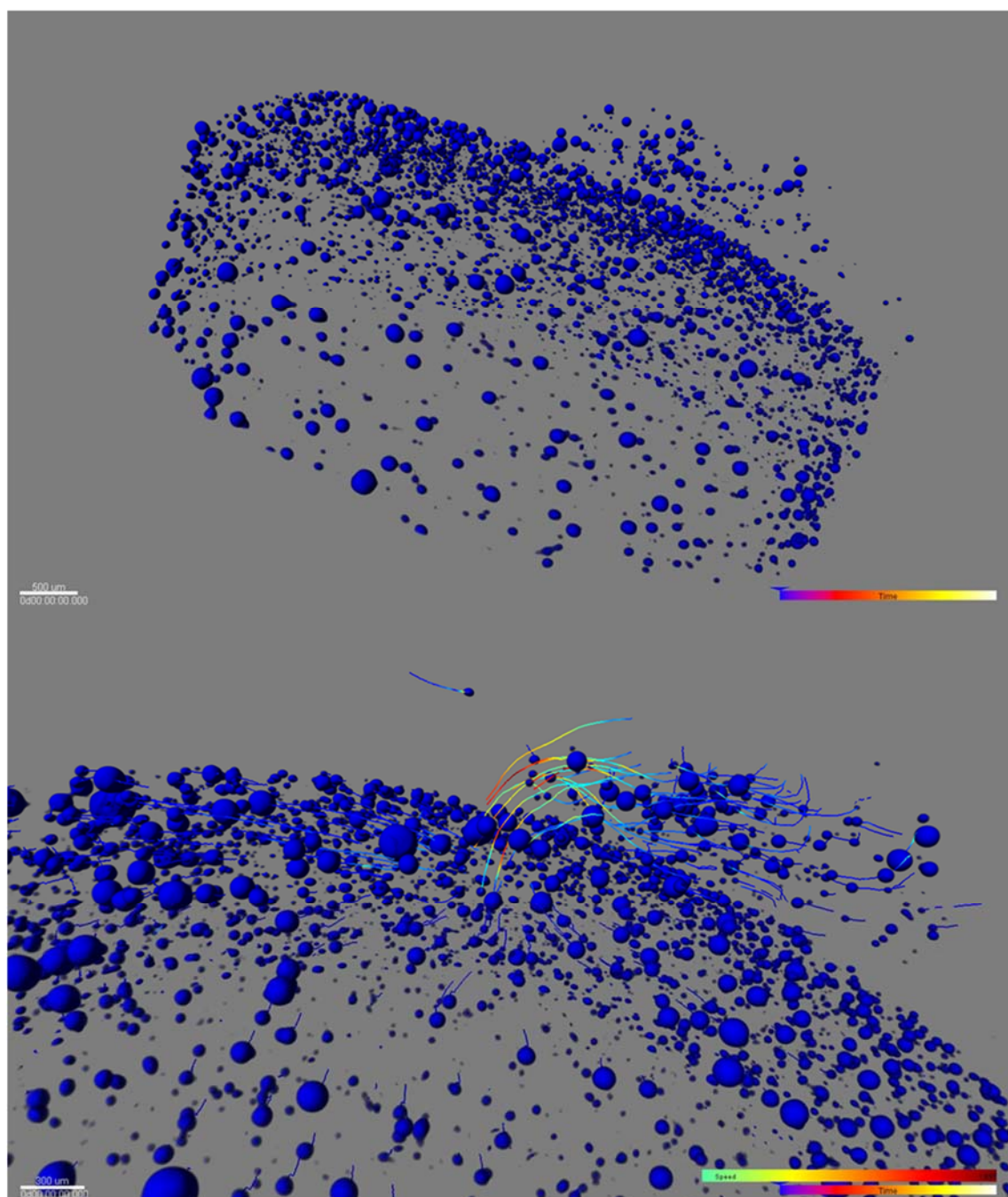
Figure 75 *The dynamic computed tomography   tracking the numerous droplet-like structure quantitatively*

The structure and drug delivery system characteristics of an osmotic pump film coated tablet with laser drilled orifice that is determined by *in situ* generated micro-droplets is now considered. By tracing the position, size and distribution of

every micro-droplet at different stages of the drug dissolution from the tablet, this analysis is now possible. Result indicate that the structure of micro-droplets was predominant in determining the drug release behaviour. The total volume and area of micro-droplets correlated well with the drug release percentage and drug release rate, respectively.
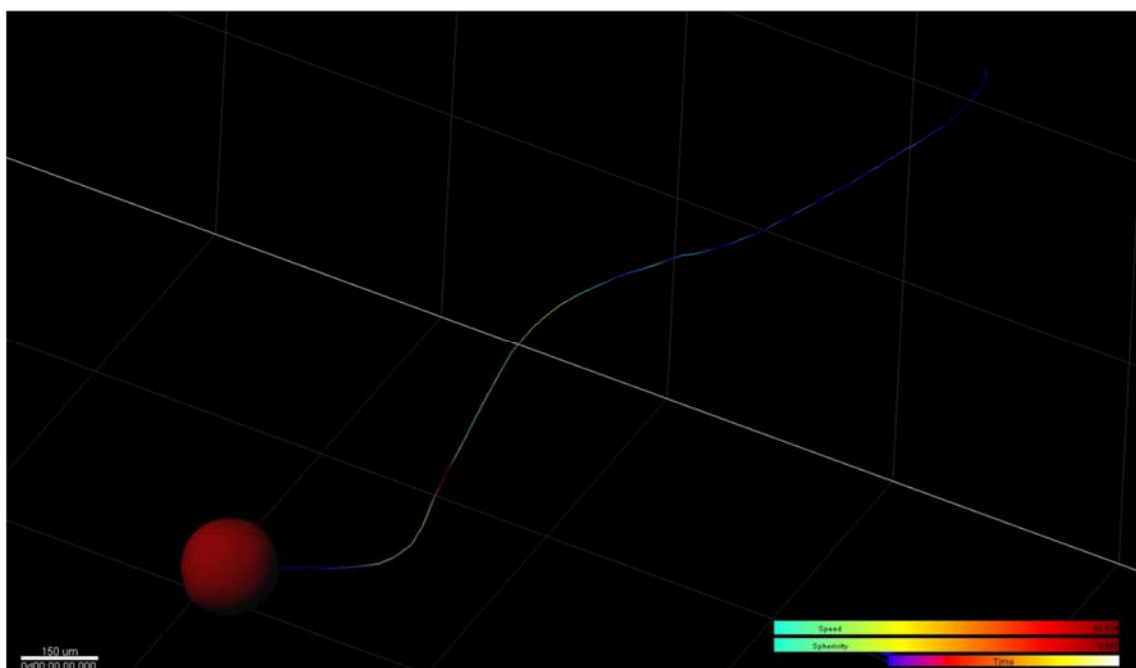
Figure 76 *The quantitative tracking of single droplet*

As highlighted above, a key factor of droplets formation in the tablet was the presence of PVP/VA in the tablet core. Via segmentation of the formulation components, without the semipermeable membrane coating, a number of droplets on the surface of the tablets were found. However, these droplets appeared static due to the lack of pressure caused by the film. It is concluded that the droplet-like structures form due to the unique property of matrix of PVP/VA with appropriate viscosity, Morphological changes of the micro-droplets are observed especially near the drug release orifice (Figure 75, Figure 76). Around the orifice, the shape of droplets changes from spherical to elliptical shape due

to the different local pressures. Results also show that the droplets deform markedly after moving to the orifice and recover a spherical shape after migrating from the orifice. According to the strong correlation between the volume of droplets and the release of drug and also the associated presences of recrystallized Na_3PO_4 with the droplets, the droplet is composed of drug in solution or suspension embodied in the swelling PVP/VA.

General comments

In this chapter, the diffusion controlled drug release mechanism of pellets was revealed with SR-μCT and a sensitive LC/MS/MS method at single pellet level. The microstructures and drug release behaviours of 76 single pellets were investigated individually. Correlations indicated that the dissolution rate of the individual pellets depended on the combined effects of the drug loading, volume and surface area of the pellets. Most important is that the inner void microstructures were critical to the drug release profiles whereas the microstructure characteristics of the hydration layer and the glassy determined the release profile. Thus, the investigation of the hydration dynamics of felodipine HPMC matrix tablet verified that the release of felodipine was dominated by a combination of erosion and swelling. The structural investigation of monolith osmotic drug delivery system also indicated that the hydration, swelling and changing surface morphology of internal structure played a key role in the sustained-release. Finally, the droplet related structure research revealed a unique type of drug delivery system. With further studies, it is proposed that specific drug release patterns can be designed and optimized by regulating the evaluation rate of micro-droplets to achieve targeted pharmacokinetics and therapeutic performance. This new evidence of micro-droplets in osmotic pump

controlled release systems provides wide opportunities perspectives in pharmaceutical sciences.

Chapter 6

General Discussion

Definition of Four Levels of Drug Delivery System Architectures

Diverse range of dosage forms and drug delivery systems have been developed for the care and welfare of patients. The development of dosage forms draws on the discipline of pharmaceutics, which integrates an understanding of numerous topics including solid state properties, material science, formulations, drug dissolution, stability, and processing technologies. The resulting architectures of the dosage form determine the drug release characteristics and thereby the clinical efficacy and safety of the drug. The design of optimised dosage forms and the optimization of formulations require a comprehensive understanding of the structure and microstructure of the dose units. To date, the role and characterisation of dosage form microstructure is unusual, primarily due to a lack of suitable non-invasive tools. The research and findings of this thesis point to the benefits offered by SR-uCT in providing the required details of microstructures of DDS.

Apart from pure solutions for injection or oral delivery, drugs are usually given in structured dosage forms of solid dosage forms as the vast majority of marketed medicines. The architecture of solid dosage forms can be categorised into four levels according the spatial scale and the lifespan (Figure 7):

Primary level, the static structure of the whole dosage form

Size ranges from microns to centimetres

The final structure after formulation

a) Oral solids dosage forms (tablets, capsules, powders, granules, premixes, and medicated blocks) or semi-solids (creams, ointments, and pastes).

b) Parenteral dosage forms and drug delivery systems include injectable powders, intravaginal delivery systems, and implants.

c) Transdermal delivery systems that elicit clinical responses by carrying medications across the skin barrier to the bloodstream.

Secondary level, formation of DDS using intermediate structures during pharmaceutical processing

Size distribution is from nanometres to millimetres

The materials exposed to processes such as mixing, grinding, granulation, tableting, packing, coating and etc.

a) Powders: a mixture in which a drug particle is mixed with other powdered excipients for processing. Particle size distribution and particle shape, along with selected chemical and solid-state material properties, usually constitute the critical variables of a pharmaceutical manufacturing process.

b) Granules or pellets: a solid particle consisting of powder particles that have been aggregated to form a larger mass, usually 1–4 mm in diameter.

c) Crystal or crystalline: a solid material whose constituent atoms, molecules, or ions are arranged in an ordered pattern extending in all three spatial dimensions.

Tertiary level, the dynamic structure during drug release after administration

Size distributed from nanometres to millimetres

The changing structure during drug release due to dissolution, swelling, erosion, diffusion

a) Dissolution: the soluble contents of DDS form a solution in a solvent. The solute has its crystalline structure disintegrated as separate ions, atoms, and molecules form. Dissolution is a kinetic process, and is quantified by its rate.

b) Swelling: when a polymer is in contact with the solvent, it starts swelling and dissolution simultaneously due to the penetration of the solvent. There are two distinct regions. One is the liquid solution wherein the dissolved polymer molecules are carried away by diffusion; the other one is the gel layer of the polymer in which the solvent diffuses. The gel/liquid interface separates the diffusion of the dissolved polymer in the liquid solution from that of the solvent in the polymer.

c) Erosion: the process by which the solid contents are removed from the DDS's surface by exogenetic processes such as liquid flow, and then transported and deposited into the solvent.

d) Diffusion: the transport phenomenon that occurs in a release. A distinguishing feature of diffusion is that it results in mixing or mass transport, without requiring bulk motion. The transport mechanism is that contents move from one position to another.

Quaternary level, the meso or micro scale architectures of active and non-active molecules within a DDS

Size distribute from Å to nanometres

The molecular structure of drug and excipients

The drug molecule is the basic element of DDS, the smallest structural unit during absorption, metabolism and pharmacodynamics performance.
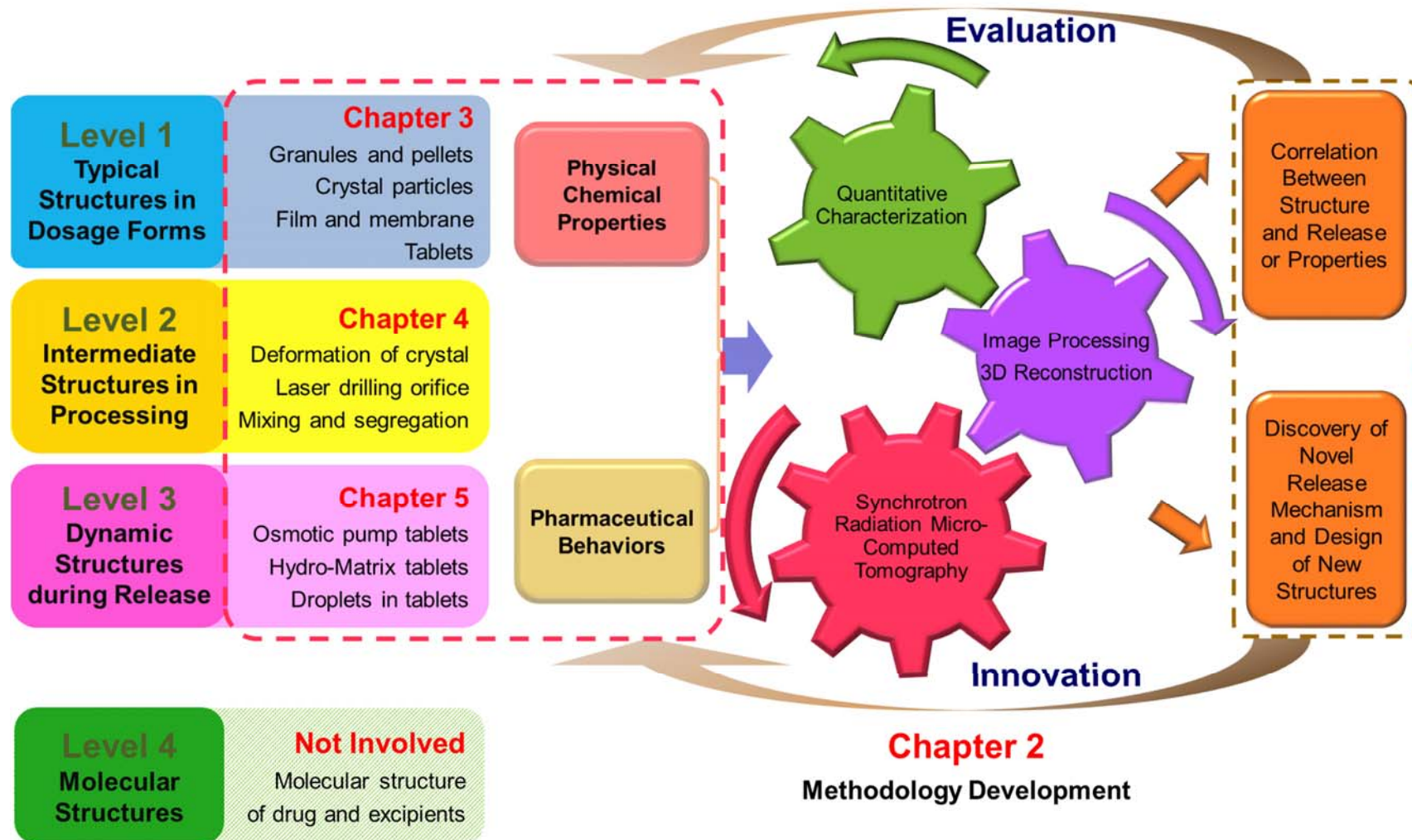
Figure 7 *Framework of thesis and the four levels of drug delivery system architectures*

As shown in Figure 7, the major knowledge gap between input and output target product is the microstructure of intermediate and dosage form structures across the size range from of nanometres to millimetres. As defined above for the four levels of drug delivery system architectures, much attention has been given to computer simulation at the molecular level. For the other three levels of architecture, highly sophisticated and advanced techniques provide full chemical, 2 dimensional and mechanical profiles. However, the internal architecture and microstructure are not well understood. This is true across the various scales of scrutiny relevant for solid dosage forms - from nanometres to millimetres. The poor investigation and characterization of internal microstructure is due to the lack of suitable in situ imaging techniques and methodologies to quantify the features of three dimensional structures.

In Chapter 2, SR-µCT imaging methodology was designed for quantitative characterization of microstructures. Principles of the synchrotron radiation imaging include the preparation of samples, optimization of imaging parameters and the evaluation of image quality. Protocols and workflows of data analysis especially image processing and 3D reconstruction, were devised tested and established. The developed methodologies were then applied to generate quantitative evaluation of the irregular micro-structures of DDS as well as particles from intermediate processing, demonstrating the potential of the new methods for presentation the full details of the surface morphology and the internal 3D structure of solid pharmaceutical structures.

In Chapter 3, the SR-µCT imaging method was employed for the visualization of typical pharmaceutical structures includes particulates, polymorph crystals, and tablets. 1) Granules of spherical microcrystalline cellulose and irregular

starch were characterized quantitatively and individually. Particle distribution was investigated by calculating the frequency distribution of steric parameters. Microstructures of pellets of multi-unit DDS were investigated. The volume, surface area and the internal void structure of every single pellet were characterized individually.   2) Polymorphic crystal particles of clopidogrel bisulphate were analysed by a range of calculated structural parameters. With the irregular surface patterns of CLP II and CLP I, crystals and agglomerated crystal forms, an accurate and sensitive detection method was devised to identify the polymorphs based on the quantitative morphological property of particles. The term of volume bias percent (VBP) was devised, defined and successfully used for the identification of single polymorphic particle, with a total matching rate of 99.91% for 4544 particles and a lowest detectable limit of 1%. 3) Based on the SR-µCT technique, the surface morphology, the internal 3D structure of the osmotic pump tablet core and their changing characteristics were clearly visualized from the 2D monochrome X-ray CT images and the reconstructed 3D tomographic images. These researches provide strong evidence that SR-µCT is a powerful non-invasive and quantitative technique with great potential for quantitative investigation of solid pharmaceutical structures. Based on the quantitative parameters, the methodology should be considered for the routine testing of pharmaceutical materials, the evaluation of formulations and act as a conventional test for the quality control of pharmaceutical products.

In Chapter 4, pharmaceutical processes include mixing, tableting and laser drilling of orifices for osmotic pump tablets were evaluated by the investigation of intermediate structures during processing. The various outcomes of these research studies were 1) Deep understanding of the dynamics of granular

materials hehavious during mixing. The blend homogeneity of binary granular mixtures of microcrystalline cellulose and starch was monitored non-invasively. Influences of the time of rotations and the time of vibration on the mixture homogeneity were investigated with statistical evaluation. A mixing index was also adopted to evaluate the mixture homogeneity of the particle system. The results showed that mixture homogeneity was improved with increasing the time of rotations. Furthermore, segregation increased with longer time of vibration. 2) The in situ 3D deformation of two polymorphs (I and II) of clopidogrel bisulphate particles under pressure was determined to illustrate pressure distribution profiles within the tablet by the deformation of the crystalline particles for the first time. SR-μCT was utilized to visualize and quantify the morphology of thousands crystalline particles of CLP I and CLP II before and after compression. As a result, the deformation was examined for quantitative comparison to CLP I and CLP II. The different degrees of deformation under the same compression conditions of CLP I and CLP II were observed and characterized quantitatively. The map of degree of deformation within the tablet illustrated the heterogeneous pressure distribution in various regions of the compacted tablet. 3) A novel method to measure quantitatively the three-dimensional architectures of orifices drilled in the membrane based on SR-μCT has been established. Quantitative analysis of architectures drilled by a range of operating parameters indicated that laser power correlated with the cross section area, volume, surface area and depth of the orifices, while scanning speed of laser beam showed inverse relationships with the above structure characteristics. The first three-dimensional structural insight of orifices in osmotic pump tablets by SR-μCT and structural reconstruction for the architectures has provided deeper insight into improving

the design of advanced osmotic pumps for controlled drug release. As demonstrated, the 3D structural insight of intermediate microstructures in processing provides valuable information for the optimization of manufacturing processes and design of drug delivery systems.

In Chapter 5, the dynamic structures during release were characterized and correlated quantitatively with the release behaviours to reveal the mechanisms controlling drugrelease. Single pellets, osmotic pump tablets and hydrogel matrix tablets have been investigated. Important finding were 1) The release profiles of single tamsulosin hydrochloride pellets correlated well with the combined effects of the drug loading, volume and surface area of the pellets and the void microstructures within the pellet were critical during drug release. 2) At different stages of the drug release process, the surface morphology, the hydration, the swelling, and the structure changing of the felodipine osmotic tablets were visualized. The volumes of the remaining tablet core correlated well with the release profile with the surface area of the core remaining almost unchanged during the drug release process. The 3D fractal values of volume ($D_{f,volume}$) and surface ($D_{f,surface}$) of the tablet core calculated based on the box counting method and the values of $D_{f,surface}$ correlated well with the drug release rate which reflecting the drug release performance and could be regarded as a key indicator for the quality control of oral controlled drug delivery systems. 3) Investigations provide quantitative detail on the relative importance of swelling and erosion in the release of poorly soluble drugs, and 3D structures of the hydration layer, which plays a key role in the controlled drug release of gel-forming matrix tablets. A statistical model of the hydration layer was conceived and developed based on the reconstructed 3D rendering of tablets. The surface area hydration layer

($SA_{hydration\ layer}$ and $SSA_{hydration\ layer}$) and of the glassy core ($SA_{glassy\ core}$), were identified to establish the statistical model. The order of significance of independent variables was $SA_{hydration\ layer}$ > $SSA_{hydration\ layer}$ > $SA_{glassy\ core}$, which indicated that the release of felodipine was dominated by a combination of erosion and swelling. 4) Dynamic computed tomography methods have been developed for *in-situ* testing in the dissolution medium during release. With the discovery of a new micro-droplet architecture driven release mechanism, a novel osmotic pump tablet was designed.

In this thesis, new methods for SR-µCT imaging of the pharmaceutical dosage forms have been created, developed and employed, including the image processing method, 3D reconstruction method and construction of 3D models. Methods for the quantitative evaluation of the irregular micro-structures of DDS as well as the intermediate particles has been established. The powerful 3D research tool has been applied to explore the world of pharmaceutical structures. High resolved 3D images present full details of the surface morphology, the internal 3D structure and the dynamic behaviours in architecture oriented release kinetics. All of the above provide a basis for the concept of structure pharmaceutics, which enables fundamental understanding of formulations, manufacturing processes and drug release mechanisms, broadens the vision of pharmaceutical scientists and ultimately promotes the design of novel drug delivery systems with innovative structures.

Bibliography/References

[1] M.N.V.R. Kumar, Handbook of Particulate Drug Delivery (2-Volume Set), American Scientific Publishers, 2008.

[2] N. Bertrand, J.-C. Leroux, The journey of a drug-carrier in the body: an anatomo-physiological perspective, Journal of controlled release, 161 (2012) 152-163 %@ 0168-3659.

[3] B.Y. Shekunov, P. Chattopadhyay, H.H.Y. Tong, A.H.L. Chow, Particle size analysis in pharmaceutics: Principles, methods and applications, Pharm Res, 24 (2007) 203-227.

[4] L.X. Yu, G. Amidon, M.A. Khan, S.W. Hoag, J. Polli, G.K. Raju, J. Woodcock, Understanding Pharmaceutical Quality by Design, Aaps J, 16 (2014) 771-783.

[5] S. Westermarck, A.M. Juppo, L. Kervinen, J. Yliruusi, Pore structure and surface area of mannitol powder, granules and tablets determined with mercury porosimetry and nitrogen adsorption, Eur J Pharm Biopharm, 46 (1998) 61-68.

[6] R.C. Lyon, D.S. Lester, E.N. Lewis, E. Lee, L.X. Yu, E.H. Jefferson, A.S. Hussain, Near-infrared spectral imaging for quality assurance of pharmaceutical products: analysis of tablets to assess powder blend homogeneity, AAPS PharmSciTech, 3 (2002) E17.

[7] K.C. Pingali, T. Shinbrot, A. Cuitino, F.J. Muzzio, E. Garfunkel, Y. Lifshitz, A.B. Mann, AFM study of hydrophilicity on acetaminophen crystals, Int J Pharmaceut, 438 (2012) 184-190.

[8] Q.L. Zhang, L. Gladden, P. Avalle, M. Mantle, In vitro quantitative H-1 and F-19 nuclear magnetic resonance spectroscopy and imaging studies of fluvastatin (TM) in Lescol (R) XL tablets in a USP-IV dissolution cell, Journal of Controlled Release, 156 (2011) 345-354.

[9] B. Vajna, I. Farkas, A. Szabo, Z. Zsigmond, G. Marosi, Raman microscopic evaluation of technology dependent structural differences in tablets containing imipramine model drug, J Pharmaceut Biomed, 51 (2010) 30-38.

[10] J.A. Zeitler, Y. Shen, C. Baker, P.F. Taday, M. Pepper, T. Rades, Analysis of coating structures and interfaces in solid oral dosage forms by three dimensional terahertz pulsed imaging, Journal of pharmaceutical sciences, 96 (2007) 330-340.

[11] M. Haaser, K. Naelapaa, K.C. Gordon, M. Pepper, J. Rantanen, C.J. Strachan, P.F. Taday, J.A. Zeitler, T. Rades, Evaluating the effect of coating equipment on tablet film quality using terahertz pulsed imaging, Eur J Pharm Biopharm, 85 (2013) 1095-1102.

[12] M. Niwa, Y. Hiraishi, Quantitative analysis of visible surface defect risk in tablets during film coating using terahertz pulsed imaging, Int J Pharm, 461 (2014) 342-350.

[13] D.M. Cooper, A.L. Turinsky, C.W. Sensen, B. Hallgrimsson, Quantitative 3D analysis of the canal network in cortical bone by micro-computed tomography, Anatomical record. Part B, New anatomist, 274 (2003) 169-179.

[14] S.R. Stock, X-ray microtomography of materials, Int Mater Rev, 44 (1999) 141-164.

[15] F.R. Elder, A.M. Gurewitsch, R.V. Langmuir, H.C. Pollock, Radiation from Electrons in a Synchrotron, Phys Rev, 71 (1947) 829-830.

[16] J. Schwinger, On the Classical Radiation of Accelerated Electrons, Phys Rev, 75 (1949) 1912-1925.

[17] E. Rowe, F.E. Mills, Tantalus. 1. A Dedicated Storage Ring Synchrotron Radiation source, Part. Accel., 4 (1973) 211-227.

[18] H. Wiedemann, Synchrotron radiation, Springer, 2003.

[19] N.X. Wang, H.A. von Recum, Affinity-Based Drug Delivery, Macromol Biosci, 11 (2011) 321-332.

[20] C. Redenbach, R. Ohser-Wiedemann, R. Loffler, T. Bernthaler, A. Nagel, Characterization of Powders using Micro Computed Tomography, Part Part Syst Char, 28 (2012) 3-12.

[21] J.A. Zeitler, L.F. Gladden, In-vitro tomography and non-destructive imaging at depth of pharmaceutical solid dosage forms, Eur J Pharm Biopharm, 71 (2009) 2-22.

[22] P.M. Young, K. Nguyen, A.S. Jones, D. Traini, Microstructural Analysis of Porous Composite Materials: Dynamic Imaging of Drug Dissolution and Diffusion Through Porous Matrices, Aaps J, 10 (2008) 560-564.

[23] L. Farber, G. Tardos, J.N. Michaels, Use of X-ray tomography to study the porosity and morphology of granules, Powder Technol, 132 (2003) 57-63.

[24] X. Fu, M. Dutt, A.C. Bentham, B.C. Hancock, R.E. Cameron, J.A. Elliott, Investigation of particle packing in model pharmaceutical powders using X-ray microtomography and discrete element method, Powder Technol, 167 (2006) 134-140 %@ 0032-5910.

[25] Y.M. Wang, P.A. Heng, F.M. Wahl, Image reconstructions from two orthogonal projections, Int J Imag Syst Tech, 13 (2003) 141-145.

[26] E. Karakosta, P.M. Jenneson, R.P. Sear, P.J. McDonald, Observations of coarsening of air voids in a polymer-highly-soluble crystalline matrix during dissolution, Phys Rev E, 74 (2006).

[27] G. Chauve, F. Raverielle, R.H. Marchessault, Comparative imaging of a slow-release starch exciplent tablet: Evidence of membrane formation, Carbohyd Polym, 70 (2007) 61-67.

[28] X.Z. Yin, H.Y. Li, Z. Guo, L. Wu, F.W. Chen, M. de Matas, Q. Shao, T.Q. Xiao, P. York, Y. He, J.W. Zhang, Quantification of Swelling and Erosion in the Controlled Release of a Poorly Water-Soluble Drug Using Synchrotron X-ray Computed Microtomography, Aaps J, 15 (2013) 1025-1034.

[29] Y.D. Wang, Y.S. Yang, I. Cole, A. Trinchi, T.Q. Xiao, Investigation of the microstructure of an aqueously corroded zinc wire by data-constrained modelling with multi-energy X-ray CT, Mater Corros, 64 (2013) 180-184.

[30] Z. Tian, X. Jia, K.H. Yuan, T.S. Pan, S.B. Jiang, Low-dose CT reconstruction via edge-preserving total variation regularization, Phys Med Biol, 56 (2011) 5949-5967.

[31] P. Roy, A. Shahiwala, Multiparticulate formulation approach to pulsatile drug delivery: Current perspectives, Journal of Controlled Release, 134 (2009) 74-80.

[32] P.H. Emmett, S. Brunauer, K.S. Love, The measurement of surface areas of soils and soil colloids by the use of low temperature van der waals adsorption isotherms, Soil Sci, 45 (1938) 57-65.

[33] Y. Li, P.S. Chow, R.B.H. Tan, Quantification of polymorphic impurity in an enantiotropic polymorph system using differential scanning calorimetry, X-ray powder diffraction and Raman spectroscopy, Int J Pharmaceut, 415 (2011) 110-118.

[34] N. Rodriguez-Hornedo, D. Murphy, Significance of controlling crystallization mechanisms and kinetics in pharmaceutical systems, Journal of pharmaceutical sciences, 88 (1999) 651-660.

[35] P. Aldridge, S. áSonja Sekulic, Determination of end-points for polymorph conversions of crystalline organic compounds using on-line near-infrared spectroscopy, Analyst, 122 (1997) 549-552.

[36] I. Karabas, M.G. Orkoula, C.G. Kontoyannis, Analysis and stability of polymorphs in tablets: The case of Risperidone, Talanta, 71 (2007) 1382-1386.

[37] G.G.Z. Zhang, D. Law, E.A. Schmitt, Y.H. Qiu, Phase transformation considerations during process development and manufacture of solid oral dosage forms, Adv Drug Deliver Rev, 56 (2004) 371-390.

[38] S. Alam, S. Patel, A.K. Bansal, Effect of sample preparation method on quantification of polymorphs using PXRD, Pharm Dev Technol, 15 (2010) 452-459.

[39] H.G. Brittain, Methods for the Characterization of Polymorphs: X-Ray Powder Diffraction, Polymorphism in Pharmaceutical Solids, (1999) 235-238.

[40] B. Shah, V.K. Kakumanu, A.K. Bansal, Analytical techniques for quantification of amorphous/crystalline phases in pharmaceutical solids, Journal of pharmaceutical sciences, 95 (2006) 1641-1665.

[41] N. Chieng, T. Rades, J. Aaltonen, An overview of recent studies on the analysis of pharmaceutical polymorphs, J Pharm Biomed Anal, 55 (2011) 618-644.

[42] V. Uvarov, I. Popov, Development and metrological characterization of quantitative X-ray diffraction phase analysis for the mixtures of clopidogrel bisulphate polymorphs, J Pharmaceut Biomed, 46 (2008) 676-682.

[43] V. Koradia, G. Chawla, A.K. Bansal, Qualitative and quantitative analysis of clopidogrel bisulphate polymorphs, Acta pharmaceutica, 54 (2004) 193-204.

[44] Z. Nemet, A. Demeter, G. Pokol, Quantifying low levels of polymorphic impurity in clopidogrel bisulphate by vibrational spectroscopy and chemometrics, J Pharm Biomed Anal, 49 (2009) 32-41.

[45] M.R. Singh, J. Chakraborty, N. Nere, H.-H. Tung, S. Bordawekar, D. Ramkrishna, Image-Analysis-Based Method for 3D Crystal Morphology Measurement and Polymorph Identification Using Confocal Microscopy, Crystal Growth & Design, 12 (2012) 3735-3748.

[46] M.D. Eddleston, K.E. Hejczyk, E.G. Bithell, G.M. Day, W. Jones, Polymorph identification and crystal structure determination by a combined crystal structure prediction and transmission electron microscopy approach, Chemistry, 19 (2013) 7874-7882.

[47] A. Bousquet, B. Castro, J. Saint-Germain, Polymorphic form of clopidogrel hydrogen sulphate, in, Google Patents, 2003.

[48] W.N. Charman, H.K. Chan, B.C. Finnin, S.A. Charman, Drug delivery: A key factor in realising the full therapeutic potential of drugs, Drug Develop Res, 46 (1999) 316-327.

[49] P.D. Reddy, D. Swarnalatha, Recent Advances in Novel Drug Delivery Systems, International Journal of PharmTech Research, 2 (2010).

[50] E. Mehuys, C. Vervaet, [Oral controlled release dosage forms], Journal de pharmacie de Belgique, (2010) 34-38 %@ 0047-2166.

[51] H. Gupta, D. Bhandari, A. Sharma, Recent trends in oral drug delivery: a review, Recent patents on drug delivery & formulation, 3 (2009) 162-173 %@ 1872-2113.

[52] B.N. Singh, Modified-release solid formulations for colonic delivery, Recent patents on drug delivery & formulation, 1 (2007) 53-63 %@ 1872-2113.

[53] S. Rose, J.F. Nelson, A continuous long-term injector, The Australian journal of experimental biology and medical science, 33 (1955) 415-419.

[54] R.K. Verma, B. Mishra, S. Garg, Osmotically controlled oral drug delivery, Drug Dev Ind Pharm, 26 (2000) 695-708.

[55] R.K. Verma, D.M. Krishna, S. Garg, Formulation aspects in the development of osmotically controlled oral drug delivery systems, Journal of Controlled Release, 79 (2002) 7-27.

[56] V. Malaterre, J. Ogorka, N. Loggia, R. Gurny, Oral osmotically driven systems: 30 years of development and clinical use, Eur J Pharm Biopharm, 73 (2009) 311-323.

[57] R.K. Verma, S. Arora, S. Garg, Osmotic pumps in drug delivery, Crit Rev Ther Drug, 21 (2004) 477-520.

[58] G. Santus, R.W. Baker, Osmotic Drug-Delivery - a Review of the Patent Literature, Journal of Controlled Release, 35 (1995) 1-21.

[59] A.M. Kaushal, S. Garg, An update on osmotic drug delivery patents, Pharmaceutical technology, 27 (2003) 38-44 %@ 0147-8087.

[60] P. Kumar, B. Mishra, An overview of recent patents on oral osmotic drug delivery systems, Recent Pat Drug Deliv Formul, 1 (2007) 236-255.

[61] R. Conley, S.K. Gupta, G. Sathyan, Clinical spectrum of the osmotic-controlled release oral delivery system (OROS), an advanced oral delivery form, Current medical research and opinion, 22 (2006) 1879-1892.

[62] D.M. Bass, M. Prevo, D.S. Waxman, Gastrointestinal safety of an extended-release, nondeformable, oral dosage form (OROS (R))(1) - A retrospective study, Drug Safety, 25 (2002) 1021-1033.

[63] K. Tahara, K. Yamamoto, T. Nishihata, Overall mechanism behind matrix sustained release (SR) tablets prepared with hydroxypropyl methylcellulose 2910, Journal of controlled release, 35 (1995) 59-66 %@ 0168-3659.

[64] C.F. Rodriguez, N. Bruneau, J. Barra, D. Alfonso, E. Doelker, D.L. Wise, L. Brannon-Peppas, Handbook of Pharmaceutical Controlled Release Technology, Handbook of Pharmaceutical Controlled Release Technology, (2000).

[65] P.I. Lee, Modeling of drug release from matrix systems involving moving boundaries: Approximate analytical solutions, Int J Pharmaceut, 418 (2011) 18-27.

[66] H. Lapidus, N.G. Lordi, Some factors affecting the release of a water‐soluble drug from a compressed hydrophilic matrix, Journal of pharmaceutical sciences, 55 (1966) 840-843 %@ 1520-6017.

[67] H. Lapidus, N.G. Lordi, Drug Release from Compressed Hydrophilic Matrices, Journal of pharmaceutical sciences, 57 (1968) 1292-&.

[68] N.A. Peppas, R. Gurny, E. Doelker, P. Buri, Modeling of Drug Diffusion through Swellable Polymeric Systems, J Membrane Sci, 7 (1980) 241-253.

[69] P.I. Lee, Diffusional Release of a Solute from a Polymeric Matrix - Approximate Analytical Solutions, J Membrane Sci, 7 (1980) 255-275.

[70] P.I. Lee, N.A. Peppas, Prediction of polymer dissolution in swellable controlled-release systems, Journal of Controlled Release, 6 (1987) 207-215 %@ 0168-3659.

[71] R.S. Harland, A. Gazzaniga, M.E. Sangalli, P. Colombo, N.A. Peppas, Drug Polymer Matrix Swelling and Dissolution, Pharm Res, 5 (1988) 488-494.

[72] P. Colombo, R. Bettini, G. Massimo, P.L. Catellani, P. Santi, N.A. Peppas, Drug Diffusion Front Movement Is Important in Drug-Release Control from Swellable Matrix Tablets, Journal of pharmaceutical sciences, 84 (1995) 991-997.

[73] K. Tahara, K. Yamamoto, T. Nishihata, Application of model-independent and model analysis for the investigation of effect of drug solubility on its release rate from hydroxypropyl methylcellulose sustained release tablets, Int J Pharmaceut, 133 (1996) 17-27 %@ 0378-5173.

[74] M.C. Bonferoni, S. Rossi, F. Ferrari, M. Bertoni, R. Sinistri, C. Caramella, Characterization of three hydroxypropylmethylcellulose substitution types: rheological properties and dissolution behaviour, Eur J Pharm Biopharm, 41 (1995) 242-246 %@ 0939-6411.

[75] P.R. Laity, R.E. Cameron, Synchrotron X-ray microtomographic study of tablet swelling, Eur J Pharm Biopharm, 75 (2010) 263-276 %@ 0939-6411.

[76] F. Shen, R.C. Chen, T.Q. Xiao, GPU-based parallel computing for fast image reconstruction in micro CT, Nucl Tech, 34 (2011) 401-405.

[77] S.H. Yalkowsky, S. Bolton, Particle-Size and Content Uniformity, Pharm Res, 7 (1990) 962-966.

[78] M. Celik, C.E. Driscoll, An Overview of the Effects of Some Physicochemical and Mechanical Characteristics of Particulates on the Compaction and Post-Compaction Properties of Compacts, Drug Dev Ind Pharm, 19 (1993) 2119-2141.

[79] S. Jain, Mechanical properties of powders for compaction and tableting: an overview, Pharm Sci Technol To, 2 (1999) 20-31.

[80] J. Scholl, D. Bonalumi, L. Vicum, M. Mazzotti, M. Muller, In situ monitoring and modeling of the solvent-mediated polymorphic transformation of L-glutamic acid, Crystal Growth & Design, 6 (2006) 881-891.

[81] C.Q. Sun, D.J.W. Grant, Influence of crystal structure on the tableting properties of sulfamerazine polymorphs, Pharm Res, 18 (2001) 274-280.

[82] Y.S. Feng, D.J.W. Grant, Influence of crystal structure on the compaction properties of n-alkyl 4-hydroxybenzoate esters (Parabens), Pharm Res, 23 (2006) 1608-1616.

[83] S. Patel, A.M. Kaushal, A.K. Bansal, Compression physics in the formulation development of tablets, Crit Rev Ther Drug, 23 (2006) 1-65.

[84] V. Busignies, B. Leclerc, P. Porion, P. Evesque, G. Couarraze, P. Tchoreloff, Quantitative measurements of localized density variations in cylindrical tablets using X-ray microtomography, Eur J Pharm Biopharm, 64 (2006) 38-50.

[85] G. Nebgen, D. Gross, V. Lehmann, F. Muller, H-1-Nmr Microscopy of Tablets, Journal of pharmaceutical sciences, 84 (1995) 283-291.

[86] H.M. Macleod, K. Marshall, Determination of Density Distributions in Ceramic Compacts Using Autoradiography, Powder Technol, 16 (1977) 107-122.

[87] I.C. Sinka, S.F. Burch, J.H. Tweed, J.C. Cunningham, Measurement of density variations in tablets using X-ray computed tomography, Int J Pharmaceut, 271 (2004) 215-224.

[88] P. Upadhyay, K.S. Khomane, L. Kumar, A.K. Bansal, Relationship between crystal structure and mechanical properties of ranitidine hydrochloride polymorphs, Crystengcomm, 15 (2013) 3959-3964.

[89] E. Joiris, P. Di Martino, C. Berneron, A.M. Guyot-Hermann, J.C. Guyot, Compression behavior of orthorhombic paracetamol, Pharm Res, 15 (1998) 1122-1130.

[90] K.S. Khomane, P.K. More, A.K. Bansal, Counterintuitive Compaction Behavior of Clopidogrel Bisulfate Polymorphs, Journal of pharmaceutical sciences, 101 (2012) 2408-2416.

[91] B. Crean, A. Parker, D. Le Roux, M. Perkins, S.Y. Luk, S.R. Banks, C.D. Melia, C.J. Roberts, Elucidation of the internal physical and chemical microstructure of pharmaceutical granules using X-ray micro-computed tomography, Raman microscopy and infrared spectroscopy, Eur J Pharm Biopharm, 76 (2010) 498-506.

[92] L. Chen, L.Y. Wang, X.Z. Yin, J.C. Wang, R.H. Liu, D. Wang, H.Y. Li, W.F. Zhu, J.W. Zhang, [Identification of the polymorphs of clopidogrel bisulfate based on the steric morphology parameters of crystals], Yao xue xue bao = Acta pharmaceutica Sinica, 48 (2013) 1459-1463.

[93] B. Eiliazadeh, B.J. Briscoe, Y. Sheng, K. Pitt, Investigating density distributions for tablets of different geometry during the compaction of pharmaceuticals, Particul Sci Technol, 21 (2003) 303-316.

[94] H. Rosen, T. Abribat, The rise and rise of drug delivery, Nat Rev Drug Discov, 4 (2005) 381-385.

[95] V. Malaterre, J. Ogorka, N. Loggia, R. Gurny, Oral osmotically driven systems: 30 years of development and clinical use, Eur J Pharma Biopharm, 73 (2009) 311-323.

[96] S. Herrlich, S. Spieth, S. Messner, R. Zengerle, Osmotic micropumps for drug delivery, Adv Drug Deliv Rev, 64 (2012) 1617-1627.

[97] A.M. Kaushal, S. Garg, An update on osmotic drug delivery patents, Pharmaceutical Technology, 27 (2003) 38-44.

[98] R. Sareen, N. Jain, D. Kumar, An Insight to Osmotic Drug Delivery, Curr Drug Deliv, 9 (2012) 285-296.

[99] S. Narisawa, M. Nagata, Y. Hirakawa, M. Kobayashi, H. Yoshino, An organic acid-induced sigmoidal release system for oral controlled-release preparations. 3. Elucidation of the anomalous drug release behavior through osmotic pumping mechanism, Int J Pharm, 148 (1997) 85-91.

[100] S. Tuntikulwattana, A. Mitrevej, T. Kerdcharoen, D.B. Williams, N. Sinchaipanid, Development and optimization of micro/nanoporous osmotic pump tablets, AAPS PharmSciTech, 11 (2010) 924-935.

[101] N. Ozdemir, J. Sahin, Design of a controlled release osmotic pump system of ibuprofen, Int J Pharmaceut, 158 (1997) 91-97.

[102] D. Prabakaran, P. Singh, P. Kanaujia, S.P. Vyas, Effect of hydrophilic polymers on the release of diltiazem hydrochloride from elementary osmotic pumps, Int J Pharmaceut, 259 (2003) 173-179.

[103] A.G. Thombre, L.E. Appel, M.B. Chidlaw, P.D. Daugherity, F. Dumont, L.A.F. Evans, S.C. Sutton, Osmotic drug delivery using swellable-core technology, Journal of Controlled Release, 94 (2004) 75-89.

[104] L. Liu, X. Xu, Preparation of bilayer-core osmotic pump tablet by coating the indented core tablet, Int J Pharm, 352 (2008) 225-230.

[105] L. Liu, B. Che, Preparation of monolithic osmotic pump system by coating the indented core tablet, Eur J Pharm Biopharm, 64 (2006) 180-184.

[106] L. Liu, J. Wang, S. Zhu, Delivery of prazosin hydrochloride from osmotic pump system prepared by coating the core tablet with an indentation, Drug Deliv, 14 (2007) 219-224.

[107] P. Kanagale, B.B. Lohray, A. Misra, P. Davadra, R. Kini, Formulation and optimization of porous osmotic pump-based controlled release system of oxybutynin, AAPS PharmSciTech, 8 (2007) 7.

[108] A. Patel, T. Mehta, M. Patel, K. Patel, N. Patel, Recent patent in controlled porosity osmotic pump, Recent Pat Drug Deliv Formul, 7 (2013) 66-72.

[109] A. Patel, T. Mehta, J. Patel, M. Patel, K. Patel, N. Patel, Recent advances in asymmetric membrane capsule based osmotic pump: a patent overview, Recent Pat Drug Deliv Formul, 6 (2012) 66-72.

[110] Y. Yang, Y. Wang, J. Li, W. Pan, Manufacture and characteristics of asymmetric membrane capsule shells with a novel wet phase inversion method, Drug Dev Ind Pharm, 40 (2014) 1704-1708.

[111] J. Tu, A.G. Paleocrassas, N. Reeves, N. Rajule, Experimental characterization of a micro-hole drilling process with short micro-second pulses by a CW single-mode fiber laser, Opt Laser Eng, 55 (2014) 275-283.

[112] A. Bharatish, H.N.N. Murthy, B. Anand, C.D. Madhusoodana, G.S. Praveena, M. Krishna, Characterization of hole circularity and heat affected zone in pulsed CO2 laser drilling of alumina ceramics, Opt Laser Technol, 53 (2013) 22-32.

[113] R.N. Gupta, R. Gupta, P.K. Basniwal, G.S. Rathore, Osmotically controlled oral drug delivery systems: a review, Int J Pharm Sci, 1 (2009) 269-275.

[114] G.K.L. Ng, L. Li, Repeatability characteristics of laser percussion drilling of stainless-steel sheets, Opt Laser Eng, 39 (2003) 25-33.

[115] A. Hoffman, M. Donbrow, S.T. Gross, S. Benita, R. Bahat, Fundamentals of Release Mechanism Interpretation in Multiparticulate Systems - Determination of Substrate Release from Single Microcapsules and Relation between Individual and Ensemble Release Kinetics, Int J Pharmaceut, 29 (1986) 195-211.

[116] A. Hoffman, M. Donbrow, S. Benita, Direct Measurements on Individual Microcapsule Dissolution as a Tool for Determination of Release Mechanism, J Pharm Pharmacol, 38 (1986) 764-766.

[117] S. Benita, D. Babay, A. Hoffman, M. Donbrow, Relation between Individual and Ensemble Release Kinetics of Indomethacin from Microspheres, Pharm Res, 5 (1988) 178-182.

[118] S.T. Gross, A. Hoffman, M. Donbrow, S. Benita, Fundamentals of Release Mechanism Interpretation in Multiparticulate Systems - the Prediction of the Commonly Observed Release Equations from Statistical Population-Models for Particle Ensembles, Int J Pharmaceut, 29 (1986) 213-222.

[119] C. Sirotti, I. Colombo, M. Grassi, Modelling of drug-release from poly-disperse microencapsulated spherical particles, J Microencapsul, 19 (2002) 603-614.

[120] C. Sirotti, N. Coceani, I. Colombo, R. Lapasin, M. Grassi, Modeling of drug release from microemulsions: a peculiar case, J Membrane Sci, 204 (2002) 401-412.

[121] P. Borgquist, G. Zackrisson, B. Nilsson, A. Axelsson, Simulation and parametric study of a film-coated controlled-release pharmaceutical, Journal of Controlled Release, 80 (2002) 229-245.

[122] P. Borgquist, P. Nevsten, B. Nilsson, L.R. Wallenberg, A. Axelsson, Simulation of the release from a multiparticulate system validated by single pellet and dose release experiments, Journal of Controlled Release, 97 (2004) 453-465.

[123] C.A. Lorck, P.C. Grunenberg, H. Junger, A. Laicher, Influence of process parameters on sustained-release theophylline pellets coated with aqueous polymer dispersions and organic solvent-based polymer solutions, Eur J Pharm Biopharm, 43 (1997) 149-157.

[124] P.A.C. Gane, C.J. Ridgway, E. Barcelo, Analysis of pore structure enables improved tablet delivery systems, Powder Technol, 169 (2006) 77-83.

[125] A. Gomez-Carracedo, C. Souto, R. Martinez-Pacheco, A. Concheiro, J.L. Gomez-Amoza, Microstructural and drug release properties of oven-dried and of slowly or fast frozen freeze-dried MCC-Carbopol (R) pellets, Eur J Pharm Biopharm, 67 (2007) 236-245.

[126] K.A. Mehta, M.S. Kislalioglu, W. Phuapradit, A.W. Malick, N.H. Shah, Effect of formulation and process variables on porosity parameters and release rates from a multi unit erosion matrix of a poorly soluble drug, Journal of Controlled Release, 63 (2000) 201-211.

[127] N. Kallai, O. Luhn, J. Dredan, K. Kovacs, M. Lengyel, I. Antal, Evaluation of Drug Release From Coated Pellets Based on Isomalt, Sugar, and Microcrystalline Cellulose Inert Cores, AAPS PharmSciTech, 11 (2010) 383-391.

[128] R.E. Oconnor, J.B. Schwartz, Drug Release Mechanism from a Microcrystalline Cellulose Pellet System, Pharm Res, 10 (1993) 356-361.

[129] I. Caraballo, M. Fernandezarevalo, M.A. Holgado, A.M. Rabasco, Percolation Theory - Application to the Study of the Release Behavior from Inert Matrix Systems, Int J Pharmaceut, 96 (1993) 175-181.

[130] T. Higuchi, Mechanism of Sustained-Action Medication - Theoretical Analysis of Rate of Release of Solid Drugs Dispersed in Solid Matrices, Journal of pharmaceutical sciences, 52 (1963) 1145-&.

[131] J. Kerc, S. Srcic, B. Kofler, J. Smidkorbar, Molar Solubility of Felodipine in Different Aqueous Systems, Int J Pharmaceut, 81 (1992) R1-R4.

[132] H. Wen, K. Park, Oral controlled release formulation design and drug delivery: Theory to practice, John Wiley & Sons, 2011.

[133] E. Lu, Z.Q. Jiang, Q.Z. Zhang, X.G. Jiang, A water-insoluble drug monolithic osmotic tablet system utilizing gum arabic as an osmotic, suspending and expanding agent, Journal of Controlled Release, 92 (2003) 375-382.

[134] L.X. Liu, G. Khang, J.M. Rhee, H.B. Lee, Monolithic osmotic tablet system for nifedipine delivery, Journal of Controlled Release, 67 (2000) 309-322.

[135] T. Sawada, K. Sako, M. Fukui, S. Yokohama, M. Hayashi, A new index, the core erosion ratio, of compression-coated timed-release tablets predicts the bioavailability of acetaminophen, Int J Pharmaceut, 265 (2003) 55-63 %@ 0378-5173.

[136] K. Sako, T. Sawada, H. Nakashima, S. Yokohama, T. Sonobe, Influence of water soluble fillers in hydroxypropylmethylcellulose matrices on in vitro and in vivo drug release, Journal of controlled release, 81 (2002) 165-172 %@ 0168-3659.

[137] P.R. Laity, M.D. Mantle, L.F. Gladden, R.E. Cameron, Magnetic resonance imaging and X-ray microtomography studies of a gel-forming tablet formulation, Eur J Pharm Biopharm, 74 (2010) 109-119.

[138] H. Metz, K. Mader, Benchtop-NMR and MRI-A new analytical tool in drug delivery research, Int J Pharmaceut, 364 (2008) 170-175.

[139] P.P. Dorozynski, P. Kulinowski, A. Mlynarczyk, G.J. Stanisz, Foundation review: MRI as a tool for evaluation of oral controlled release dosage forms, Drug Discov Today, 17 (2012) 110-123.

[140] J.A. Zeitler, Y.C. Shen, C. Baker, P.F. Taday, M. Pepper, T. Rades, Analysis of coating structures and interfaces in solid oral dosage forms by three dimensional terahertz pulsed imaging, Journal of pharmaceutical sciences, 96 (2007) 330-340.

[141] M.D. Mantle, Quantitative magnetic resonance micro-imaging methods for pharmaceutical research, Int J Pharmaceut, 417 (2011) 173-195.

[142] U. Mikac, J. Kristl, S. Baumgartner, Using quantitative magnetic resonance methods to understand better the gel-layer formation on polymer-matrix tablets, Expert Opin Drug Del, 8 (2011) 677-692.

[143] J.A. Kimber, S.G. Kazarian, F. Stepanek, Microstructure-based mathematical modelling and spectroscopic imaging of tablet dissolution, Comput Chem Eng, 35 (2011) 1328-1339.

[144] B.B. Mandelbrot, Self-affine fractals and fractal dimension, Physica Scripta, 32 (1985) 257 %@ 1402-4896.

[145] R. Lopes, N. Betrouni, Fractal and multifractal analysis: A review, Med Image Anal, 13 (2009) 634-649.

[146] G. Mabilleau, M.F. Basle, D. Chappard, Evaluation of surface roughness of hydrogels by fractal texture analysis during swelling, Langmuir, 22 (2006) 4843-4845.

[147] Z. Jelcic, K. Hauschild, M. Ogiermann, K.M. Picker-Freyer, Evaluation of tablet formation of different lactoses by 3D modeling and fractal analysis, Drug Dev Ind Pharm, 33 (2007) 353-372.

[148] A. Fini, F. Ospitali, G. Zoppetti, N. Puppini, ATR/Raman and Fractal Characterization of HPBCD/Progesterone Complex Solid Particles, Pharm Res, 25 (2008) 2030-2040.

[149] C. Cavallari, L. Rodriguez, B. Albertini, N. Passerini, F. Rosetti, A. Fini, Thermal and fractal analysis microparticles obtained by of diclofenac/Gelucire 50/13 ultrasound-assisted atomization, Journal of pharmaceutical sciences, 94 (2005) 1124-1134.

[150] T.L. Li, K. Park, Fractal analysis of pharmaceutical particles by atomic force microscopy, Pharm Res, 15 (1998) 1222-1232.

[151] D.A. Russell, J.D. Hanson, E. Ott, Dimension of Strange Attractors, Phys Rev Lett, 45 (1980) 1175-1178.

[152] M. Efentakis, I. Pagoni, M. Vlachou, K. Avgoustakis, Dimensional changes, gel layer evolution and drug release studies in hydrophilic matrices loaded with drugs of different solubility, Int J Pharmaceut, 339 (2007) 66-75.

[153] P.L. Ritger, N.A. Peppas, A simple equation for description of solute release II. Fickian and anomalous release from swellable devices, Journal of Controlled Release, 5 (1987) 37-42 %@ 0168-3659.

[154] P. Colombo, R. Bettini, P. Santi, N.A. Peppas, Swellable matrices for controlled drug delivery: gel-layer behaviour, mechanisms and optimal performance, Pharm Sci Technolo Today, 3 (2000) 198-204.

[155] T.D. Reynolds, S.A. Mitchell, K.M. Balwinski, Investigation of the effect of tablet surface area/volume on drug release from hydroxypropylmethylcellulose controlled-release matrix tablets, Drug Dev Ind Pharm, 28 (2002) 457-466.

[156] R. Bettini, P.L. Catellani, P. Santi, G. Massimo, N.A. Peppas, P. Colombo, Translocation of drug particles in HPMC matrix gel layer: effect of drug solubility and influence on release rate, Journal of Controlled Release, 70 (2001) 383-391.

[157] T.M. Allen, P.R. Cullis, Drug delivery systems: Entering the mainstream, Science, 303 (2004) 1818-1822.

[158] R. Langer, New Methods of Drug Delivery, Science, 249 (1990) 1527-1533.

[159] X.Z. Yin, H.Y. Li, R.H. Liu, J. Chen, J.Q. Ji, J. Chen, Q. Shao, T.Q. Xiao, P. York, Y. He, J.W. Zhang, Fractal structure determines controlled release kinetics of monolithic osmotic pump tablets, J Pharm Pharmacol, 65 (2013) 953-959.

[160] V. Malaterre, H. Metz, J. Ogorka, R. Gurny, N. Loggia, K. Mader, Benchtop-magnetic resonance imaging (BT-MRI) characterization of push-pull osmotic controlled release systems, Journal of controlled release : official journal of the Controlled Release Society, 133 (2009) 31-36.

[161] V. Malaterre, M. Pedersen, J. Ogorka, R. Gurny, N. Loggia, P.F. Taday, Terahertz pulsed imaging, a novel process analytical tool to investigate the coating characteristics of push-pull osmotic systems, Eur J Pharm Biopharm, 74 (2010) 21-25.

[162] A.L. Broadbent, R.J. Fell, S.L. Codd, K.A. Lightley, S. Konagurthu, D.G. Koehler-King, J.D. Seymour, Magnetic resonance imaging and relaxometry to study water transport mechanisms

in a commercially available gastrointestinal therapeutic system (GITS) tablet, Int J Pharm, 397 (2010) 27-35.

[163] W. KEY, X-ray computed microtomography for the study of modified release systems, Microscopy and Analysis, (2008) 13.

[164] I.R. The United States Pharmacopeial Convention, MD, , United States Pharmacopeia and National Formulary, (2012) 3621.

[165] E.D.f.t.Q.o. Medicines, European Pharmacopoeia, (2013).

[166] T. Gureyev, S. Mohammadi, Y. Nesterets, C. Dullin, G. Tromba, Accuracy and precision of reconstruction of complex refractive index in near-field single-distance propagation-based phase-contrast tomography, J Appl Phys, 114 (2013).

[167] M. Wang, X. Lu, X. Yin, Y. Tong, W. Peng, L. Wu, H. Li, Y. Yang, J. Gu, T. Xiao, M. Chen, J. Zhang, Synchrotron radiation-based Fourier-transform infrared spectromicroscopy for characterization of the protein/peptide distribution in single microspheres, Acta Pharm Sin B, 5 (2015) 270-276.

[168] B. Abrahamsson, D. Johansson, A. Torstensson, K. Wingstrand, Evaluation of Solubilizers in the Drug-Release Testing of Hydrophilic Matrix Extended-Release Tablets of Felodipine, Pharm Res, 11 (1994) 1093-1097.

S 1 Granule sample preparation and reconstruction

SR-µCT Morphology for Granule Characterization

Granular samples of microcrystalline cellulose and starch were imaged individually using SR-µCT. To avoid overfilling perturbation, the two individual particle systems were filled to a volume of 1 mL separately into the cylindrical container with a filling level F = 66%. If Oz represents the axis of the cylindrical vessel (vertical), segmented regions of Z-axial images were used to obtain characteristics of particles because the sample size of the container was excessively large for the image acquisition process. Using this experimental design, samples at the upper and lower levels of the container were scanned in upright position. In consideration of the maximum height of X-ray beam line, the heights of the acquisition window for the samples were set as 3315 µm.

SR-µCT scans and 3D reconstruction

Samples were scanned with synchrotron radiation X-ray at 13.0 keV. After penetration through the sample, images were recorded with an X-ray digital camera with direct coupled (micro) fiber-optic (photonics Science Ltd, Robertsbridge, UK). The pixel size was 13.0 µm, the exposure time was 1.0 s and the sample-to-detector distance was 25.0 cm. For each acquisition, 630 projection images over 180°were taken. Light field images (i.e. X-ray illumination on the beam-path without the sample) and dark-field images (i.e. X-ray illumination off) were also collected during each acquisition procedure to correct for the electronic noise and variations in the X-ray source brightness.

The total projected images were reconstructed using the software developed by SSRF to perform a direct filtered back-projection algorithm (Shen et al., 2012). In order to enhance the quality of reconstructed slices, the X-TRACT SSRF CWS x64 (Commonwealth Scientific and Industrial Research Organization, Australia, http://www.ts-imaging.net/Default.aspx) was used for phase contrast extraction. The 3D rendered data were analysed with commercially available software VGStudio Max (Version 2.1, Volume Graphics GmbH, Germany) and Image Pro Analyser 3D (Version 7.0, Media Cybernetics, Inc., USA) to obtain qualitative and quantitative data respectively. The reconstruction and phase contrast extraction process are shown in Figure 77.
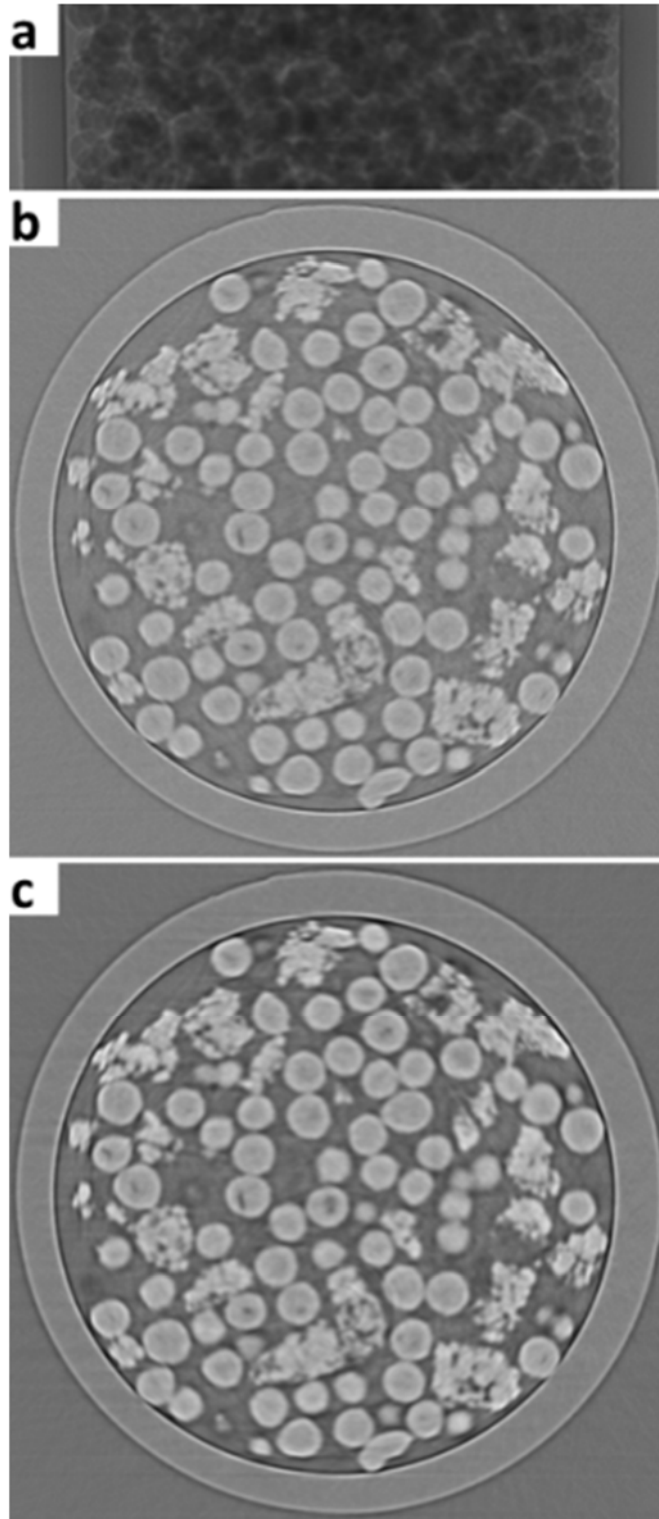
Figure 77 *The reconstruction and phase contrast extraction process for the two-component system.*

(a) tomography after background correction, (b) reconstructed slice, (c) reconstructed slice with phase contrast extraction.

S 2 Imaging and quantitative characterization of single pellet

Sample preparation

When using µCT to characterise a material, the sample size is roughly proportional to the image resolution; in addition, the sample must be entirely contained within the field of view. Due to the limitation on sample maximum height, 10 mg of TSH pellets were used to fill a capsule with 10 mg of PVP/VA. PVP/VA is widely used as an excipient in solid dosing forms and was introduced as a diluent to enable the extraction of data for each pellet for individual characterisation from a sample including many pellets. Due to the stability, small size, good flow ability and X-ray absorption contrast of this diluent, the extraction of data for the individual pellets during image processing was facilitated. Before analysis, the filled capsule was manually rotated horizontally at 30 rotations per minute (rpm) for 30 s to ensure that the pellets and PVP/VA were well mixed. The height of the acquisition window used to cover the pellets in the capsule was adjusted, and the CT scan was carried out.

SR-µCT scans

The samples were scanned with synchrotron radiation X-rays at 16.0 keV. After penetrating the sample, the projections were magnified using diffraction-limited microscope optics (2× magnification) and digitised using a high-resolution 2048 pixel× 2048 pixel CCD camera (pco.2000, PCO AG, Kelheim, Germany). The pixel size was 3.7 µm, the exposure time was 2.0 s and the sample-to-detector distance was 12 cm. For each acquisition, 720 projections over 180° were collected. Light field images (i.e., X-ray illumination on the beam-path

without the sample) and dark-field images (i.e., X-ray illumination off) were also collected during each acquisition to account for the electronic noise and variations in the brightness of the X-ray source.

3D reconstruction

The CT scan was a 3D map of the X-ray phase contrast. Further analysis of the data was needed for a quantitative description of the microstructure. The total projected images were reconstructed using software developed by SSRF to perform a direct filtered back-projection algorithm. To enhance the quality of reconstructed slices, X-TRACT SSRF CWS x64 (Version 6.5, Commonwealth Scientific and Industrial Research Organisation, Australia, http://www.ts-imaging.net/Default. aspx) was used to extract the phase contrast. The 3D rendered data were analysed with the commercially available VG Studio Max (Version 2.1, Volume Graphics GmbH, Germany) and Image Pro Analyser 3D software (Version 7.0, Media Cybernetics, Inc., USA) to obtain the qualitative and quantitative data, respectively.

After the 3D reconstruction, the resolved images had a high quality phase contrast. It was found that nearly one third of pellets were hollow. Based on the 2D slices, all of the pellets in the scanned sample were individually examined. Then a 3D model of each pellet was selected from rendered objects, and the ROIs (region of interest) were re-sliced to determine the surface morphology. The void in the pellet was extracted using grey value based segmentation with a self-programed algorithm; the extracted slices of the inner void and the pellet were merged when characterising the entire pellet; 3D models of both the pellet and

the inner void were rendered to calculate the quantitative parameters. The modelling procedures are shown in Figure 78.
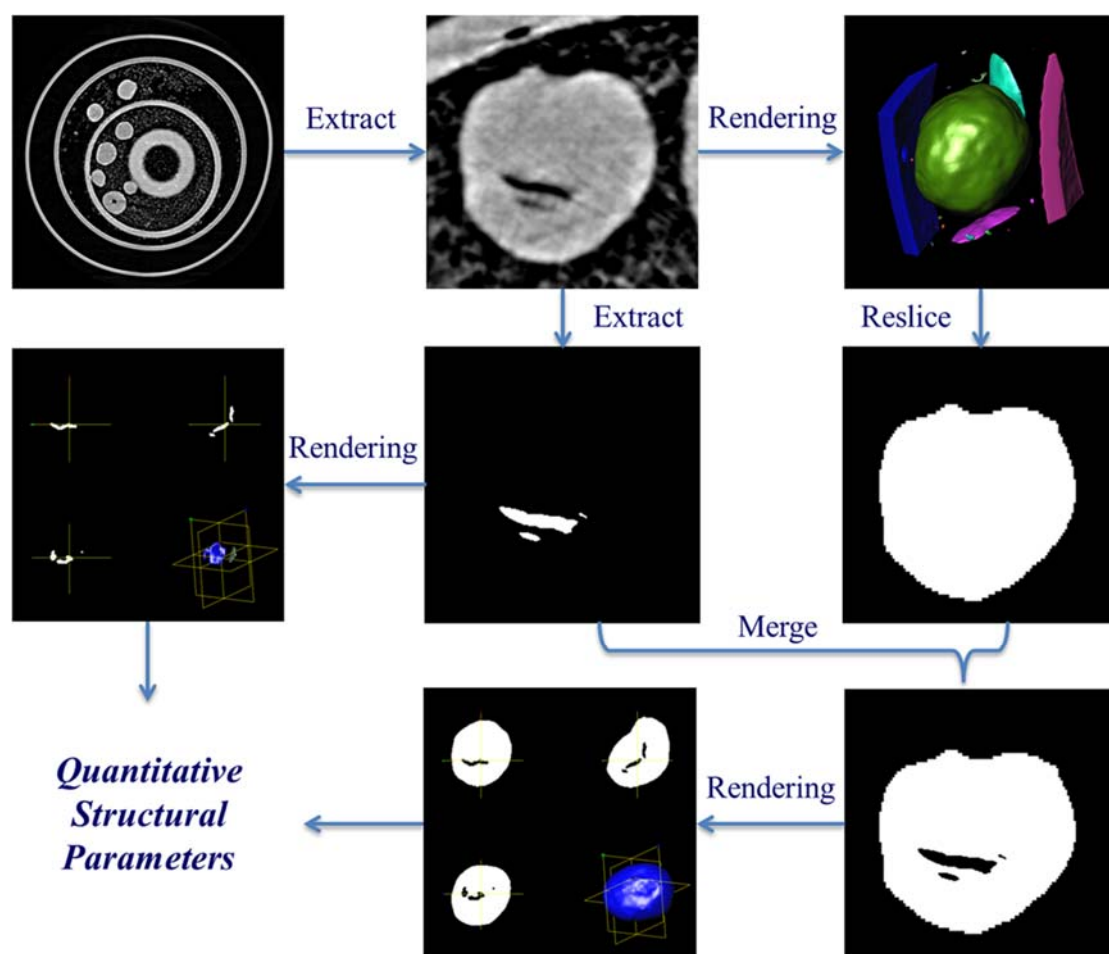
Figure 78 *Structural characterisation procedures for the TSH sustained release pellet.*

The procedure includes four steps: (1) the segmented slice is extracted from the reconstructed slice; (2) the void extraction is performed to derive the slice of the void; (3) the 3D model is acquired by reconstructing a series of slices from the void; (4) the slice and without void are merged together

S 3 Crystallographic analysis and reconstruction of CLP polymorphs particles

CLP polymorphs characterization. The PXRD was performed to verify the crystal form of the two polymorphs following pulverization (<5 μm) and

homogenization. PXRD scans were acquired using a Bruker D8 Advance (Siemens) powder diffractometer equipped with a 2.2 kW sealed Cu X-ray source, a graphite monochromator to filter out the Cu K β radiation, and a NaI (Tl) scintillation detector. The scans were performed between 3° and 40° 2θ with a 0.01° step size and a counting time of 0.1s per step.

The morphological information of CLP particles was also acquired using optical microscopy and SEM. The optical microscopy images were acquired with magnification at 200×(1280×960 pixels and pixel size was 0.450 μm), and for the SEM test all polymorph samples were scanned at 300×(800×900 pixels and pixel size was 0.450 μm) and 3000×(800×900 pixels and pixel size was 0.045 μm) respectively to capture the full surface morphological detail of particles.

Sample preparation. In order to simulate the real capsule dosage form, and to extract and characterize every particle individually from a mixture sample with hundreds of particles, PVP/VA was introduced as typical and widely used excipient. The stable, smaller size, good flowability, and X-ray absorption contrast of this diluent facilitates the CLP particle extraction during image processing.

5 mg of CLP I and CLP II (-60 mesh~ +80 mesh, sieve sizes between 180-280 μm) were weighed and filled into the capsule with 10 mg of PVP/VA respectively. In order to ensure the CLP crystals and excipients were blended thoroughly, the capsule was rotated manually and horizontally at a speed of 30 rotations per minute (rpm) for 30 seconds. The capsule was then fixed at the centre of the stage positioned in the synchrotron beam line, then the heights of the experimental acquisition window were adjusted to cover the whole sample in the capsule and then the CT scan was carried out.

SR-µCT scans and 3D reconstruction. SR-µCT tomographic images were acquired with beam line BL13W1 at SSRF. Samples were scanned with synchrotron radiation X-ray at 16.0 KeV. After penetration through the sample, the projections were magnified by diffraction-limited microscope optics (2 × magnification). Then X-rays were converted into visible light by a Lu2SiO5: Ce scintillator (10 µm thickness) and digitized by a high-resolution 2048 pixel × 2048 pixel CCD camera (pco.2000, PCO AG, Kelheim, Germany). The pixel size was 3.7µm, the exposure time was 2.0 s and the sample-to-detector distance was 12 cm. For each acquisition, 720 projection images over 180°were taken. Light field images (i.e. X-ray illumination on the beam-path without the sample) and dark-field images (i.e. X-ray illumination off) were also collected during each acquisition, for the correction of electronic noise and variations in the X-ray source brightness.

The projected images were reconstructed using the software developed by SSRF to perform a direct filtered back-projection algorithm[76]. In order to enhance the quality of reconstructed slices, the X-TRACT SSRF CWS x64 (Version 6.5, Commonwealth Scientific and Industrial Research Organization, Australia, http://www.ts-imaging.net/Default.aspx) was used for phase contrast extraction. The 3D rendered data were analysed with commercially available software VGStudio Max (Version 2.1, Volume Graphics GmbH, Germany) and Image Pro Analyser 3D (Version 7.0, Media Cybernetics, Inc., USA) to obtain qualitative and quantitative data respectively.

Quantitative characterization and classification of the polymorphs. After segmentation, image slices were all converted into black and white images by removal of the background and noise. Then 3D ISO-Surface models were

constructed with segmented slices. The surface level, surface range and the simplification parameters were adjusted to optimize the models. Then all of the CLP particles in the samples were extracted and characterized quantitatively. Finally, in order to classify CLP I and II quantitatively, several steric parameters were calculated and the overall surface patterns of the two polymorphs were presented by the new designed quantitative parameter, Volume Bias Percentage based on Surface Smooth (VBP).

Validation of the quantitative polymorph classification methods based on VBP. For the previously mentioned samples in the section of Sample Preparation, the sample of CLP II particles and excipient was transferred into the capsule with CLP I after the CT scans, and the capsule were mixed and the capsule positioned in the beam line as detailed above. Then, another CT scan was performed. In total 27 samples have been examined, and details are shown in Table 12.

Table 12 Detail information of CLP samples.

Sample ID	CLP I (mg)	CLP II (mg)	Excipients (mg)	Description
CLP-1	2.50	0.00	10.0	Pure CLP I
CLP-2	0.00	2.50	10.0	Pure CLP II
CLP-3	2.50	2.50	20.0	CLP-1+CLP-2
CLP-4	1.00	0.00	10.0	Pure CLP I
CLP-5	0.00	4.00	10.0	Pure CLP II
CLP-6	1.00	4.00	20.0	CLP-4+ CLP-5
CLP-7	4.00	0.00	10.0	Pure CLP I
CLP-8	0.00	1.00	10.0	Pure CLP II
CLP-9	4.00	1.00	20.0	CLP-7+ CLP-8
CLP-10	0.50	0.00	10.0	Pure CLP I
CLP-11	0.00	4.50	10.0	Pure CLP II
CLP-12	0.50	4.50	20.0	CLP-10+ CLP-
CLP-13	4.50	0.00	10.0	Pure CLP I
CLP-14	0.00	0.50	10.0	Pure CLP II
CLP-15	4.50	0.50	20.0	CLP-13+ CLP-
CLP-16	0.25	0.00	10.0	Pure CLP I
CLP-17	0.00	4.75	10.0	Pure CLP II
CLP-18	0.25	4.75	20.0	CLP-16+ CLP-
CLP-19	4.75	0.00	10.0	Pure CLP I
CLP-20	0.00	0.25	10.0	Pure CLP II
CLP-21	4.75	0.25	20.0	CLP-19+ CLP-
CLP-22	0.05	0.00	10.0	Pure CLP I
CLP-23	0.00	4.95	10.0	Pure CLP II
CLP-24	0.05	4.95	20.0	CLP-22+ CLP-
CLP-25	4.95	0.00	10.0	Pure CLP I
CLP-26	0.00	0.05	10.0	Pure CLP II
CLP-27	4.95	0.05	20.0	CLP-25+ CLP-

After 3D reconstruction the samples were divided into 3 groups: group A (CLP-1, 4, 7, 10, 13, 16, 19, 22, and 25) with pure CLP I, group B (CLP-2, 5, 8, 11, 14, 17, 20, 23 and 26) with CLP II and group C (CLP-3, 6, 9, 12, 15, 18, 21, 24 and 27) with mixtures of polymorphs. For every sample, all particles were extracted and the Volume Bias Percentage based on Surface Smooth calculated individually. Then the distribution of VBP values for group A and group B was compared, and threshold values for the classification of crystal forms were

calculated. The number of misclassified particles was also considered to provide an estimate of the accuracy of the method.

For samples in group C, particles in the polymorphs mixture were extracted one by one. After the classification of the crystal form with the VBP value, every particle was matched with the corresponding pure crystal form sample based on the surface morphological information and quantitative parameters such as volume, surface area and sphericity. By counting the number of mismatched particles, a method was developed to determine the lowest detectable limit of the experimental procedure.

Grey value analysis

After the reconstruction based on the filtered back-projection algorithm and phase contrast extraction with X-TRACT, the reconstructed slice stack was converted into 8 bit greyscale format and re-sliced vertically. Then the vertical slices of samples were analysed to determine the threshold grey values to distinguish the excipients, clopidogrel particles and capsule shell (Figure 79).
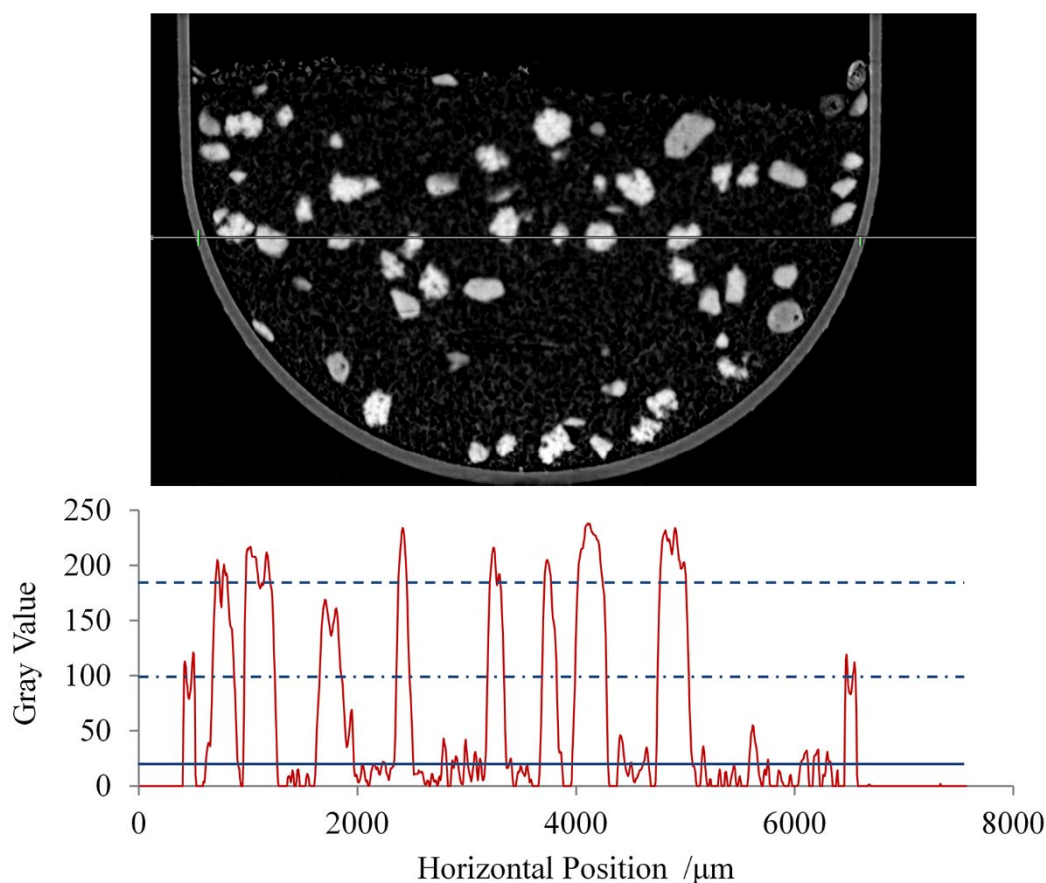
Figure 79 *Line profile of vertical slice of sample in the capsule for the distinguish of crystal particle*

(after background correction and noise reduction the grey value of background is near 0, the ▬ line at 25 shows the grey value of excipients (in this sample PVP/VA), the ▬▬ line at the value of 100 is the grey value of the capsule film, the line indicates that the average grey value of clopidogrel crystal is 185).

As shown in Figure 79, clopidogrel can be distinguished from the excipients and most of the clopidogrel crystal particles were separated by diluents. Owing to the successful noise reduction and phase retrieval procedures, the grey value of background is close to 0, the excipients have a grey value of 50, the grey value between 80 and 120 is the shell of the capsule, and the clopidogrel particles have the grey value above 150.

Definition of important quantitative parameters

In order to characterize the morphological information of particles, more than thirty parameters were calculated, most important ones as follow:

Size: *could be derived from volume, surface area.*

Equivalent diameter: *is defined as the diameter of a ball of equivalent volume. Volume fraction: Ratio of object's volume to the bounding box volume (R = Vobj / Vbox).*

Sphericity: *6 volumes of object divided by equivalent diameter and surface area of object. For a spherical object this parameter equals 1, for all other shapes it is less than 1.*

Surface deviation: *The deviation of endpoints of triangle normal vectors. Uniform surface will have deviation of 0. The maximum deviation of 1.336 will have a sphere.*

Radius Min: *Minimum distance between an object's centroid and surface.*

Radius Max: *Maximum distance between an object's centroid and surface.*

Radius Ratio: *Ratio between Radius (max) and Radius (min).*

Feret Min: *Minimum distance between two parallel planes enclosing an object.*

Feret Max: *Maximum distance between two parallel planes enclosing an object.*

Feret Ratio: *Ratio between Feret (max) and Feret (min).*

Box ratio: *Ratio between maximum and minimum size of the bounding box (R = Max / Min).*

Note. 3 Validation of the quantitative polymorph identification methods based on VBP

As all the microcrystalline particles have been scanned twice in pure and mixed samples, and a quantitative method has been devised and introduced to recognize particles in polymorph mixture, it is possible to track each individual particle in different scanned samples. For the sample containing the mixed particles of CLP I and CLP II, after the CT scan, reconstruction and 3D model construction, particles in the sample have been extracted and quantitative parameters calculated. Subsequently, particles were analysed one by one to classify the crystal form with the VBP value. Then for each particle with classified crystal form, a matching process has been performed on particles in corresponding individual sample of CLP I or CLP II with the lower proportion in the mixture to find the matched particle based on size related and morphological parameters such as volume, surface area, diameter, sphericity and radius min (Figure 80).
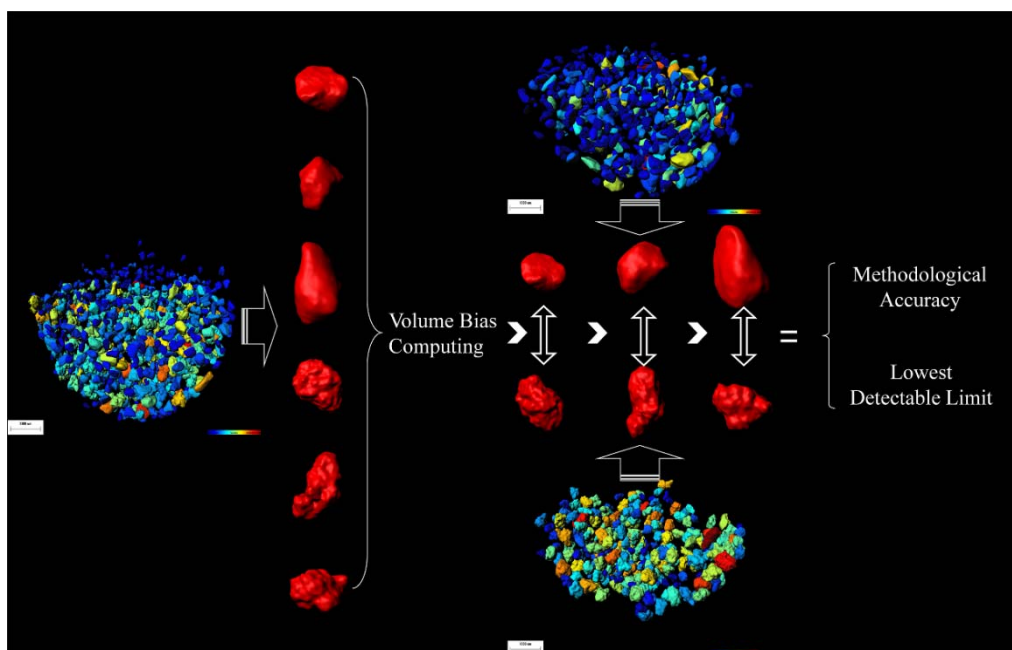
Figure 80 *One by one CLP crystal particle identification and matching.*

For the validation, 4544 particles have been analysed and the volume, surface area and sphericity selected as key parameters for matching (Figure 81). The results are shown in Table 13. In total 4540 particles were matched. The matching rate was 99.91%.
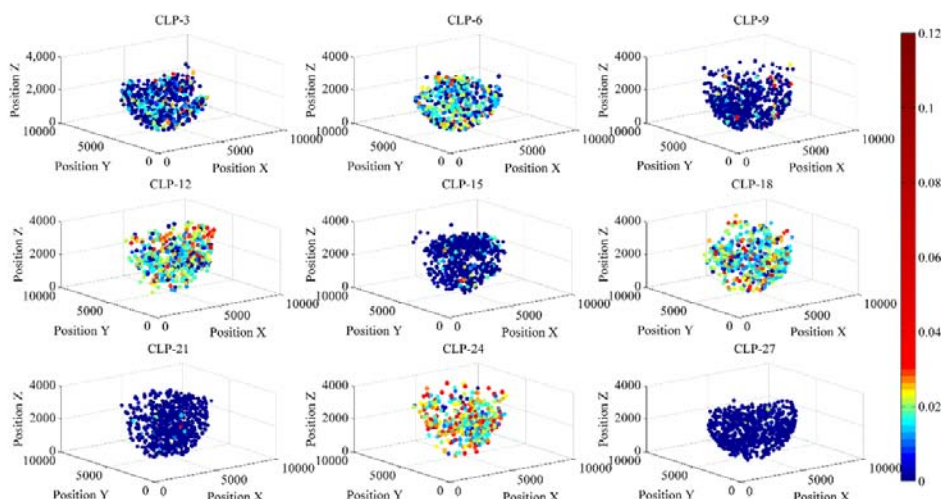
Figure 81 *VBP value based in situ crystal form identification for polymorphic mixture (n = 4544).*

Table 13 Accuracy and lowest detectable limit.

Sample ID	Content (mg)		Identified		Matched		Accuracy %
	CLP I	CLP II	CLP I	CLP II	CLP I	CLP II	
CLP-3	2.50	2.50	297	202	297	202	100.00
CLP-6	1.00	4.00	99	313	99	313	100.00
CLP-9	4.00	1.00	498	68	497	69	99.64
CLP-12	0.50	4.50	48	380	49	379	99.53
CLP-15	4.50	0.50	518	47	518	47	100.00
CLP-18	0.25	4.75	30	413	31	412	99.54
CLP-21	4.75	0.25	576	17	575	18	99.71
CLP-24	0.05	4.95	9	390	9	390	100.00
CLP-27	4.95	0.05	635	4	635	4	100.00

S 4 Reconstruction of compaction behaviours of CLP polymorphs

Tablets of CLP I and II each containing 25 mg of sieved (180-250 μm) CLP I and II particles respectively and 75 mg PVP/VA particles were prepared. The PVP/VA powder was sieved to obtain samples with an average size of 150 μm. Although CLP particles were sieved by the same mesh sieve, CLP particles may

have different size due to their different morphology. A rotary tablet presser (ZP-5; Tianjiu Machinery factory, Shanghai, China) was equipped with 5 mm D-tooling with concave-faced punch tips and a feed frame was used to fill the die uniformly. The position of the bottom punch was adjusted, and the distance between the two punches at peak loading was set at 3 mm. During the compaction process, the rotation speed was set at 8 rpm. Tablets were compacted under the same conditions to ensure that the compression ratio was the same, and the deformation behaviour of different CLP particles was dominated by the morphology of different CLP particles. The weight for each tablet was adjusted before tableting and was set at 100 ± 5 mg. The height of the acquisition window during SR-μCT scanning was 4.5 mm, covering the whole side of the tablet while performing the CT scan.

PVP/VA S630 was proven to be a good diluent for CLP particles in the tablets. By experimental verifications, when excipients like lactose, cornstarch, and microcrystalline were used, the CLP particles were easy to be compacted into large particles, which made it unable to detect CLP particles easily by SR-μCT.

Details about Powder X-ray diffraction, Scanning electron microscopy as given in S 3.

SR-μCT. The SR-μCT tomographic images of prepared samples were acquired using the BL13W1 beam line at the Shanghai Synchrotron Radiation Facility (SSRF). X-rays were derived from an electron storage ring with an accelerated energy of 3.5 GeV, and an average beam current of 180 mA. The samples were scanned with a photon energy of 16.0 keV. The size of the beam was approximately 45 mm (horizontal) × 5 mm (vertical) and a double-crystal

monochromator with Si (111) and Si (311) crystals was used to monochromatize the X-rays. The monochromatized has a flux density about 5.8×10^{10}ph/s/mm2 and the energy resolution was $\Delta E/E = 5 \times 10^{-3}$. After penetrating the sample, the X-rays were converted into visible light by a YAG:Ce scintillator (200 μm thickness). The projections were magnified by diffraction-limited microscope optics (2 × magnification) and digitized using a high-resolution 2,048 pixel × 2,048 pixel CCD camera with a physical pixel size of 7.4 μm (pco.2000, PCO AG, Kelheim, Germany). The effective pixel size was 3.7 μm, the exposure time was 2.0 s, and the sample-to-detector distance was 12 cm. For each acquisition, 720 projection images were captured with an angular step size of 0.15° for 180°. Flat-field and dark-field images were also collected during each acquisition procedure, in order to correct the electronic noise and variations in the X-ray source brightness.

The projected images were reconstructed using direct filtered back projection algorithm. To enhance the quality of reconstructed slices, the X-TRACT SSRF CWSx64 (Commonwealth Scientific and Industrial Research Organization, Australia, http://www.ts-imaging.net/Default.aspx) was used for phase contrast extraction. The 3D rendered data were analysed with commercially available software (VGStudio Max (Version 2.1, Volume Graphics GmbH, Germany) and Image Pro Analyser 3D (Version 7.0, Media Cybernetics, Inc., USA) to obtain the qualitative and quantitative data, respectively.

S 5 Laser drilling and the reconstruction of orifices

Captopril and excipients were passed through a 100 mesh sieve (mesh size of 150 μm), weighed accurately, and mixed in geometric proportions to form a

uniform blend of powders prior to direct compression. The mixed powders were compressed on a rotary tablet press (ZP-5, Shanghai Tianjiu Machinery Factory) using 6.0-mm-diameter shallow concave punches. An acetone solution containing cellulose acetate and polyethylene glycol (3:1), at 2% w/w concentration was used in the coating process to form a semipermeable membrane on the surface of core tablet. The coating was carried out by spraying the coating solution in a high efficiency coating machine (BGB-5F, Zhejiang Xiaolun Pharmaceutical Machinery Co., Ltd., China) equipped with a hot air blower. The stainless steel and peristaltic pump were both set a rotating speed of 12 rpm. The temperatures of air intake and outlet were 40°C and 30°C, respectively. The rotate speed of air intake and outlet were set at 500 rpm and 1,450 rpm, respectively, with coating continuing until a 4% weight increase in tablet weight was reached. The coated tablets were then dried to remove any residual solvent at 40°C for 16 h. An orifice was then drilled through the coating membrane with laser drilling machine (CRS-C20D, Ceres Wuhan Photoelectric Technology Co., Ltd., China).

Since laser drilling involves selecting a set of operating conditions, including laser power, pulse width, pulse frequency, focus plane position, and number of pulses[112], laser drilling parameters that markedly affected the quality of orifices were investigated using the above mentioned laser drilling machine and the software Mark Studio (0x0001.1946) setting, developed by Shenzhen Earain (China). Power for laser drilling (2, 6, 10, 14 and 20 W) and movement speeds of laser spot (namely, scanning speeds of the laser beam, 200, 400, 600, 800, 1,000 and 2,000 mm/s) that can be set in the software by user were investigated. The CRS-C20D laser drilling machine was assembled with the ultra-pulsed laser (max

power of 20 W, Access, USA), optical offset mirror (Ceres, China), optical focusing mirror (Wavelength, USA), and control card (Ceres, China). The frequency of laser was 5 KHz. For the drilling, the coated tablets (diameter of 6 mm and thickness of 2 mm) were positioned in wells of a board and then placed in the operational stage 12.5 cm away from the laser light source.

The slight shake of samples during the data acquisition process can result in the poor image quality, so it is necessary to apply an appropriate method to fix the samples. In the present study, two osmotic pump tablets were positioned separately orifice to orifice in a plastic pipe with a diameter of 6 mm. The pipe was then firmly attached to the sample stage in the beam line. For the marked Felodipine OP-DDSs with diameters of 7 mm, the tablets were cut along with the edges carefully to avoid disturbance to the orifices and reduce the diameters to about 6 mm and then fixed in the plastic pipes.

The SR-μCT measurements were carried out at beamline BM13W1 of Shanghai Synchrotron Radiation Facility (SSRF, China). X-rays were derived from an electron storage ring with an accelerated energy of 3.5 GeV, and an average beam current of 180 mA. The size of the beam was approximately 45 mm (horizontal) × 5 mm (vertical) and a double-crystal monochromator with Si (111) and Si (311) crystals was used to monochromatize the X-rays. The energy resolution was $\Delta E/E < 5\times10^{-3}$. The photon energy of 18.0 keV was selected for the CT scan. After penetration through the sample, the X-rays were first converted to visible light by a Lu_2SiO_5: Ce scintillator (10 μm thickness) cleaved single crystal scintillator. Data were acquired with the sample placed 34 m downstream of the synchrotron source. Projections were magnified by diffraction-limited microscope optics (magnification of 2) and digitized by a high-resolution

2,048 pixel × 2,048 with a physical pixel size of 6.5 µm (ORCA Flash 4.0 Scientific CMOS, Hamamatsu K.K, Shizuoka Pref., Japan). The effective pixel size was 3.25 µm and the exposure time was 1 s. The distance from the detector to sample was set at 10 cm. For each acquisition, 720 projection images were captured with an angular step size of 0.25° for 180°. Flat-field and dark-field images were also collected during each acquisition procedure, in order to correct for the electronic noise each other and variations in the X-ray source brightness.

The projected images for the samples were reconstructed using the X-TRACT SSRF CWSx64 (CSIRO, Commonwealth Scientific and Industrial Research Organization, Australia, http://www.ts-imaging.net) to perform a direct filtered back projection algorithm. To enhance the quality of reconstructed slices, propagation-based phase contrast extraction was carried out. As described in the paper [166], the larger sample-to-detector distances increased the contrast primarily due to the contribution from differences in the refractive properties across the sample in addition to the differential absorption. In combination with homogeneous Transport of Intensity equation (TIE-Hom) phase retrieval can achieve high quality reconstructed 3D images. During phase extraction, the parameter of δ/β was adjusted at 400 for the best contrast between different materials. After phase retrieval and reconstruction, the calculated images were truncated and rescaled to a grey value of 0 to 255 (8 bit grey level). The 3D rendered data were analysed with commercially available software Amira (version 6.01, FEI, USA) and Image Pro Analyser 3D (Version 7.0, Media Cybernetics, Inc., USA) to obtain qualitative and quantitative data, respectively.

Images were processed to reduce noise and enhance the contrast. All radiograph images were normalized based on the intensity within the selected

rectangular reference region which was never occluded by the sample in any of the images for the correction of varied illumination, and a simple median smoothing filter was performed for the noise reduction. During the TIE-Hom phase retrieval, zingers filter has been applied to remove isolated pixels or small clusters of pixels in which the signal was much higher than that in the surrounding part of the input frame files or dark and flat field files for the correction of artefacts. Brightness, contrast and gamma settings were also adjusted for the contrast enhancement of reconstructed slices. After the optimization, the crystal particles, membranes and delivery orifices could be distinguished due to the noise reduction and phase retrieval. The grey value of the background was about 0 to 50, while the grey value of excipients were between 70 and 150, and the crystal particles gave a grey value above 150.

From the analysis of grey values, X-ray CT data from all of the delivery orifices in the OP-DDSs were examined. Highly resolved tomographic images with high quality phase contrast were then derived after 3D reconstructions. Based on the difference of grey value, the matrix of OP-DDSs and orifices had been segmented and the constructed 3D models were used for the calculation of quantitative parameters.

Recently, synchrotron radiation-based Fourier transformed infrared microspectroscopy (SR-FTIR) has been developed as a rapid, direct and non-destructive chemical microprobe with high flux and brightness, high coherence, high signal-to-noise ratio at high-spatial resolutions and allow for smaller regions within a specimen to be analysed [167]. In this study, SR-FTIR microspectroscopy was performed in the BL01B beamline at SSRF (Shanghai Synchrotron Radiation Facility). Spectra of the membrane samples were

recorded on a Nicolet Continµm XL microscope (Thermo Fisher Scientific, Inc.) equipped with a 250 × 250 µm^2 liquid nitrogen cooled MCT/A detector, a 32X/NA0.65 Schwarzschild objective, a motorized knife-edge aperture, and a Prior XYZ motorized stage and coupled with Nicolet 6700 spectrometer (Thermo Fisher Scientific, Inc.) equipped with a Michelson interferometer. After peeled from the OP-DDS, the membranes with the orifice attached was mapped in transmission mode between 600 cm^{-1} and 5,000 cm^{-1}, with 64 scans at 4 cm^{-1} resolution, 10 µm ×10 µm aperture dimension, 10 µm × 10 µm step size, and 26 × 6 points (coving the part of orifices) on the BaF$_2$ substrate. With the OMINIC software 9.2.86 (Thermo Fisher Scientific, Inc.), chemical distribution maps were created and analysed after smoothing and baseline correction.

S 6 Pre-treatment of felodipine osmotic pump tablet

Samples pretreatment

Follow the instruction about sample preparation in Section 2.2. For the SR-µCT test, 18 tablets were divided into six groups and three tablets in each group. The dissolution medium was a phosphate buffer (pH 6.5) with 1% sodium lauryl sulfate and was prepared as follows: transfer 206 mL of 1 mol/L monobasic sodium phosphate monohydrate, 196 mL of 0.5 mol/L dibasic sodium phosphate anhydrous and 20g of cetyltrimethylammonium bromide to a 5000 mL volumetric flask, diluted with water to volume, and mix well, adjust the pH to 6.5. A standard dissolution test was carried out. At 0.5, 1.0, 3.0, 6.0, 8.0 and 10 h, three tablets were taken out from the dissolution medium gently and put on a piece of flat, dry filter paper. In order to keep the intrinsic structure of the tablet, the liquid on the surface and inside the tablet was absorbed as completed as possible by the filter

paper. Then, the tablet was kept at room temperature for 24 hours to remove the residual liquid. The tablet was not reused for the dissolution test, nor put back into the dissolution medium again.

SR-μCT tomography

SR-μCT tomographic images were acquired with beam line BL13W1 at Shanghai Synchrotron Radiation Facility (SSRF). Samples were scanned with synchrotron radiation at 13.0 keV. After the penetration through the sample, the X-rays were converted into visible light by a YAG:Ce scintillator (200 μm thickness). Projections were magnified by diffraction-limited microscope optics (1.25 × magnification) and digitized by a high-resolution 2048 × 2048 pixel CCD camera (pco.2000, PCO AG, Kelheim, Germany). The pixel size was 5.92μm, the exposure time was 4s and the sample-to-detector distance was 25 cm. For each acquisition, 900 projection images were taken. Light field images (i.e. X-ray illumination on and the specimen out of the beam-path) and dark-field images (i.e. X-ray illumination off) were also collected during each acquisition procedure, in order to correct the electronic noise and variations in the X-ray source brightness.

The projected images at each time point of dissolution (0.5, 1.0, 3.0, 6.0, 8.0 and 10.0 h), were reconstructed using the software developed by SSRF to perform a direct filtered back-projection algorithm. The 3D rendered data were analysed with VGStudioMax and Image-Pro 3D to obtain the qualitative and quantitative data, respectively.

S 7 Pre-treatment of felodipine HPMC gel matrix tablet

In Vitro Release test

In vitro drug release of the felodipine extended release tablets was measured using the paddle method according to the Chinese Pharmacopoeia. The dissolution test was conducted at a rotation speed of 100 rpm, medium volume of 500 mL at 37 ℃. The dissolution medium was a phosphate buffer (pH 6.5), which was prepared as follows: 206 mL of 1 mol/L monobasic sodium phosphate monohydrate, 196 mL of 0.5 mol/L dibasic sodium phosphate anhydrous and 20g of cetyltrimethylammonium bromide were transferred to a 5000 mL volumetric flask, diluted with distilled water to volume, and mixed well (pH = 6.5). Following addition of the tablet to the dissolution vessel, aliquot samples 10 mL were withdrawn from the dissolution vessel at 0.5, 1.0, 1.5, 2.0, 3.0, 4.0, 6.0, 7.0, 8.0, 10.0 h and then replaced with equivalent volumes of fresh medium in order to maintain sink conditions since the solubility of felodipine in phosphate buffer (pH = 6.5) containing 0.4% cetyltrimethylammonium bromide was 970 μg/mL [168]. The samples were then filtered with 0.45 μm microporous membrane and analysed using a validated HPLC method to calculate the percent of felodipine released at different stages of the dissolution test. The HPLC analysis was performed on a Diamonsil C_{18} column (150×4.6 mm, 5 μm) (Dikma Technologies, China) using methanol-water (80:20) as mobile phase, with a flow rate of 1.0 mL/min and injection volume of 20 μL. The detection wavelength was 238 nm. Calibration curves were prepared over the concentration range of 0.1, 1.0, 2.0, 5.0, 10.0 and 20.0 μg/mL. The linearity regression coefficient exceeded 0.995, showing a good linearity over this concentration range. Precision results revealed that the intra- and inter-assay RSD were below 1.0 %, and the sample was stable over 24 h, with RSD below 1.0 %.

Pre-treatment of Samples

In order to evaluate temporal changes in the microstructure of the matrix tablets during drug release by SR-µCT test, 18 tablets were taken and divided into nine groups, each containing two tablets and a standard dissolution test was carried out. At 0.5, 1.0, 2.0, 3.0, 4.0, 5.0, 6.0, 7.0 and 8.0 h, two tablets were removed from the dissolution medium and prepared for further testing.

As discussed in Section 2.2, samples have been prepared and pre-treated. In order to maintain the original shape of the tablets, swollen tablets were carefully removed using small spoons together with about 2 mL of the medium and placed individually in 24-well plates with 2 mL of the corresponding dissolution medium added to maintain the original shape of the tables. The 24-well plates containing the tablets in various states of hydration and erosion were then immediately placed into the ultra-low temperature refrigerator at -80 ℃ for 12 hour. After this process, the tablets were freeze-dried over a period of 24 hours at -50℃ and 10 mTorr using a freeze dryer (FD5-3, China-GOLD SIM (Beijing) International Co. Ltd., China). These tablets were then kept in the dry cabinet under ambient temperature (relative humidity of 20%) for further SR-µCT tests and were not reused in dissolution tests.

Tomography

SR-µCT tomographic images of prepared samples were acquired using beam line BL13W1 at the Shanghai Synchrotron Radiation Facility (SSRF). Samples were scanned with synchrotron radiation at 13.0 keV. Images were recorded with an X-ray digital camera with direct coupled (micro) fiber-optic (Photonics Science Ltd, Robertsbridge, UK). The pixel size was 9 µm, the exposure time was 4s and the sample-to-detector distance was 10 cm. For each

acquisition, 720 projection images over 180º were taken. Flat field images and dark-field images were also collected during each acquisition procedure, in order to correct the electronic noise and variations in the X-ray source brightness.

The projection sets of tablet for each time point of dissolution (0.5, 1.0, 2.0, 3.0, 4.0, 5.0, 6.0, 7.0 and 8.0 h) were reconstructed using developed software based on a filtered back-projection algorithm [76]. The 3D rendered data were analysed with VGStudio Max and Image-Pro 3D to obtain qualitative and quantitative data, respectively. Statistical models were constructed with PASW Statistics version 18.0 (Polar Engineering and Consulting).

Three dimensional parameter calculations

After segmentation, slices were all converted into black and white images by removal of the background and noise. Then, three dimensional Iso-Surface models were constructed with segmented slices. The surface level, surface range and the simplification parameters were adjusted to optimize the models and to extract objects for further calculation of quantitative steric parameters.

S 8 Preparation and structural analysis of droplet generated tablet

Tablet Preparation. All powder components of the osmotic pump cores were passed through the 100 mesh sieve (150 µm), weighted accurately, and mixed in geometric proportion to form a uniform blend of powder ready for direct compression. The uniform blend of powder was direct compression on a rotary tablet machine (ZP-5, Shanghai Tianjiu Machinery Factory) using 6.0-mm-

diameter punches. Cellulose acetate (CA) in acetone containing plasticizer (PEG 4000) was used as coating solution. The coating was carried out in a pan coater (BY 300A, Shanghai Huanghai Drug Instrument Co., Ltd., China). The temperature of coating pan was 40 °C, pan-rotating rate was 25 rpm. The coated tablets were dried to remove the residual solvent acetone at 40 °C for 24 h, and laser machines drilled (CRS-C20D, Ceres Wuhan Photoelectric Technology Co., Ltd., China) a 0.8-mm-diameter orifice on the membrane surface.

In Vitro Release Test. In vitro drug release test was conducted in a dissolution apparatus (ZRS-8G, Haiyida Co., Ltd, China) using the paddle method. The release medium was 900 mL distilled water. The temperature of the release medium was maintained at 37 ± 0.5 °C and the rotation speed of the paddle was adjusted to 75 rpm. Samples of 5.0 mL were withdrawn at 0.5, 1.0, 2.0, 4.0, 6.0, 8.0, 10.0 and 12.0 h and replaced 5.0 mL fresh release media to each vessel. The solution was filtered through a 0.45 μm membrane filter, suitably diluted and determined by Ultraviolet Spectrometer (UV-4802，Shanghai Unico Instruments Co., Ltd., China).

Sample Preparation for SR-μCT Test. Prior to the SR-μCT scanning, the sample positioned in a dissolution apparatus using the paddle method. The temperature of the release medium, 900 mL deionized water, was maintained at 37 °C. The rotation speed of the paddle was adjusted to 75 rpm. The tablets were taken out at a set time, and carefully placed on a piece of flat, dry filter paper. The liquid on the surface and inside the tablet was absorbed as much as possible by the filter paper. Then the tablets were kept in an amber-coloured drying

container holding the drug releasing orifices upward at room for 24 h to remove the remaining residue liquid as possible. Experiment were carried out in triplicate.

SR-µCT Tomography. SR-µCT analysis were performed using BM13W beam line at Shanghai institute of applied physics, Chinese academy of science (SSRF) with a resolution of 3.7 microns per pixel. The rotation step was fixed at 0.25 µ, the range of angel was -5 ° to 175 ° and exposure time was 2 s. For each sample, totally a stack of 720 2D tomographic sections was obtained. The X-TRACT software was used for 3D reconstruction. X-TRACT is a powerful software package for reconstruction and analysis of X-ray tomographic data, which has been parallelised to run on GPU clusters enabling great gains in speed and the ability to process larger image files. One of the unique features of X-TRACT is its ability to process phase-contrast images to improve the quality of the reconstructed data.

3D Reconstruction and Quantitative Analysis. The Image Pro Analyser 3D 7.0 was used for the building, rendering, visualization and measurements. 3D models were constructed from the stacks of 2D images after threshold of the objects of interest from the relevant objects and background noise. After selecting volume of interest (VOI), multiple iso-surface has been rendered based on segmentation of selected intensities and colours. For each tablet, the areas of the Na_3PO_4 and the matrix were first segmented respectively based on the difference in the grey value. As after drying, the bubbles in the tablets are all full with air and cannot be distinguished with the air out of the tablets by intensities. Algorithm base on the software platform of Image Pro Analyzer 3D was designed which can pick out micro-droplets in an image intelligently and segment them with specific colour. After the segmentation, images were divided into three regions and coloured. The

Na$_3$PO$_4$ area was dyed red, the matrix area was green and the micro-droplets were blue. These three regions of different colour were regarded as three channels and reconstructed into three models in the Image Pro Analyser 3D software. Then the quantitative measurements will be carried out based on these 3D models and computed parameters will also be correlated with the drug release kinetics.

Sample Preparation for In Situ Test. The film coated tablet was fixed inside the self-controlled device, which was made by plastic pipe. After deionized water was added in the device, the in situ test started.

To gain insight into the most authentic internal fine-structure dynamic change in the course of drug release and understand the release mechanism, it is necessary to monitor the real-time drug release behaviour of the tablets in situ. However, in vitro dissolution testing of tablets is usually carried out in large volumes of dissolution medium and acquisition of the internal refined information about structure requires high resolution. It is a major challenge for the conventional testing methods to record the real-time data. In the present study, the internal refined static structure change of the tablets in the previous release phase was successfully real-time monitored using the advanced SR-µCT.

Drug release mechanism of the film coated tablets driven by in situ generated numerous micro-droplets

The strong correlation between the volume of micro-droplets and drug release could be explained by the following mechanism: When the osmotic pump drug delivery system come in contact with the aqueous environment, water imbibitions by the active agents take place dissolving the core and the micro-droplets

generate. The total volume of micro-droplets increase from 0 to V_b. However, the outline volume (V_m) formed by the semipermeable membrane may be increased slightly but maintain constant in whole the release process. So,

$$\lim_{t=t_{max}} V_b = V_m$$

<div align="right">Eq. (27)</div>

At one bar pressure, that is in the osmotic pump tablet which is not totally hydrated, and if the solid content contacts the medium, this situation is equivalent to the "concentration" of the semi solid content extruded from the release orifice. If the volume is V_d. then：

$$a = \frac{V_d}{V_m}$$

<div align="right">Eq. (28)</div>

Clealy, at t, the percentage of the solid content discharged to the tablet is equivalent to the release R. That is:

$$R \approx \frac{a}{V_d} V_b$$

<div align="right">Eq. (29)</div>

Where, a and V_d are both constants. Thus, the drug release of this kind of osmotic pump has a positive correlation to the volume of the micro-droplets structure. That can be simplified as the drug release R has a positive correlation to the total volume of the bubble structure formed in the tablet:

$$R = kV_b$$

<div align="right">Eq. (30)</div>

When ketoprofen was included in the osmotic pump tablets only containing copovidone without sodium phosphate (formulation C), spherical micro-droplets remained. But, only 2% of ketoprofen was released at 1.0 h. Absence of sodium

phosphate could therefore play a vital role in increasing the drug release. When sodium phosphate was added based on the osmotic pump tablets only containing copovidone without drug (formulation C), the original spherical micro-droplets changed markedly. Due to the presence of sodium phosphate, the 'salting-out' reduced the solubility of copovidone, thus the hydration was delayed and the number of micro-droplets decreased and the size of the micro-droplets was smaller compared with the formation that only containing copovidone (formulation C). Simultaneously, the presence of sodium phosphate increased the osmotic pressure and surface tension of the solutions, resulting in the non-uniform and low sphericity of micro-droplets. Also, water entering into the core under the osmotic pressure led to the radial distribution of dissolved sodium phosphate. After the cores were in contact with water, copovidone absorbed water resulted in a saturated solution of sodium phosphate. Under the effect of the osmotic pressure, water accumulated in the centre area. Thus, the droplet formed by dissolved Na_3PO_4 pointed to the centre of the core. Fully dissolved sodium phosphate accelerated the dissolution of copovidone. Salt ions enhanced the polarity of the solution, thereby increasing the solubility of water-soluble polymer. Containing of sodium phosphate in the core made a large number of spherical aqueous micro-droplet not formed when contacting water. It could be explained that the existence of sodium phosphate solution leaded the increase of surface tension and solubility of polymer materials, resulting in the spherical micro-droplet could not be formed and exist stably.

Size, shape and evaluation rate control of micro-droplets

249

Table 14 Size and shape of micro-droplets in the film tablets at different drug release time

Stats	Area	Aspect	Diameter (mean)
0.5 h			
Min	137	1	13
Max	19714	6	166
Range	19577	5	153
Mean	1165	1	33
Std.Dev	1692	0	19
Sum	625606	795	17679
Samples	537	537	537
1.0 h			
Min	137	1	13
Max	14333	9.7488108	133
Range	14197	8.7488108	120
Mean	1487	1.330917	38
Std.Dev	1435	0.58254772	18
Sum	809147	724.0188	20501
Samples	544	544	544
1.5 h			
Min	137	1	13
Max	2019111	6	1592
Range	2018974	5	1579
Mean	9538	1	53
Std.Dev	111589	0	94
Sum	4463556	678	24971
Samples	468	468	468

2.0 h			
Min	137	1	13
Max	5924128	5	2731
Range	5923992	4	2717
Mean	21949	1	58
Std.Dev	308299	0	155
Sum	9130792	599	24227
Samples	416	416	416
3.0 h			
Min	137	1	13
Max	11640771	6.	3845
Range	11640634	5	3832
Mean	50797	2	64
Std.Dev	712172	1	245
Sum	13715149	453	17317
Samples	270	270	270
4.0 h			
Min	137	1	13
Max	16183538	10	4532
Range	16183401	9	4519
Mean	319168	2	129
Std.Dev	2243562	1	623
Sum	16277561	79	6558
Samples	51	51	51

Tablet Preparation. All compositions of the osmotic pump cores were passed through the 100 mesh sieve, weighted accurately, and mixed in geometric proportion to form a uniform blend of powder ready for direct compression. The uniform blend of powder was direct compression on a rotary tablet machine (ZP-5, Shanghai Tianjiu Machinery Factory) using 6.0-mm-diameter punches. Cellulose acetate (CA) in acetone containing plasticizer (PEG 4000) was used as coating solution. The coating was carried out in a pan coater (BY 300A, Shanghai Huanghai Drug Instrument Co., Ltd., China). The temperature of coating pan was 40 ℃, pan-rotating rate was 25 rpm. The coated tablets were dried to remove the

residual solvent acetone at 40 ℃ for 24 h, and laser machines drilled (CRS-C20D,

Ceres Wuhan Photoelectric Technology Co., Ltd., China) a 0.8-mm-diameter orifice on the membrane surface.

In Vitro Release Test. In vitro drug release test was conducted in a dissolution apparatus (ZRS-8G, Haiyida Co., Ltd, China) using the paddle method. The release medium was 900 mL distilled water. The temperature of the release medium was maintained at 37 ± 0.5 ℃ and the rotation speed of the paddle was

adjusted to 75 rpm. Samples of 5.0 mL were withdrawn at 0.5, 1.0, 2.0, 4.0, 6.0, 8.0, 10.0 and 12.0 h and replaced 5.0 mL fresh release media to each vessel. The solution was filtered through a 0.45 μm membrane filter, suitably diluted and determined by Ultraviolet Spectrometer (UV-4802，Shanghai Unico Instruments Co., Ltd., China).

Sample Preparation for SR-μCT Test. For the SR-μCT test, the sample preparation was conducted in a dissolution apparatus using the paddle method.

The temperature of the release medium, 900 mL distilled water, was maintained at 37 ℃. The rotation speed of the paddle was adjusted to 75 rpm. The tablets were taken out at a set time, three times in parallel experiments, and carefully placed on a piece of flat, dry filter paper. The liquid on the surface and inside the tablet was absorbed as much as possible by the filter paper. Then the tablets were kept in an amber-coloured drying container holding the drug releasing orifices upward at room for 24 h to remove the remaining residue liquid as possible.

SR-μCT Tomography. SR-μCT analysis were performed using BM13W beam line at Shanghai institute of applied physics, Chinese academy of science (SSRF) with a resolution of 3.7 microns per pixel. The rotation step was fixed at 0.25 u, the range of angel was -5 ° to 175 ° and exposure time was 2 s. For each sample, totally a stack of 720 2D tomographic sections was obtained. The X-TRACT software was used for 3D reconstruction. X-TRACT is a powerful software package for reconstruction and analysis of X-ray tomographic data, which has been parallelised to run on GPU clusters enabling great gains in speed and the ability to process larger image files. One of the unique features of X-TRACT is its ability to process phase-contrast images to improve the quality of the reconstructed data.

3D Reconstruction and Quantitative Analysis. The Image Pro Analyser 3D 7.0 was used for the building, rendering, visualization and measurements. 3D models were constructed from the stacks of 2D images after a threshold of the objects of interest from the relevant objects and background noise. After selecting volume of interest (VOI), multiple iso-surface has been rendered based on segmentation

of selected intensities and colours. For each tablet, the areas of the salt and the matrix were first segmented respectively based on the difference in the grey value. As after drying, the bubbles in the tablets are all full with air and cannot be distinguished with the air out of the tablets by intensities. Another software was programmed which can pick out micro-droplets in an image intelligently and segment them with a specific colour. After the segmentation, images were divided into three regions and coloured. The salt area was dyed red, the matrix area was green and the micro-droplets were blue. These three regions of different colour were regarded as three channels and reconstructed into three models in the Image Pro Analyser 3D software. Then the quantitative measurements will be carried out based on these 3D models and computed parameters will also be correlated with the drug release kinetics.